

DISSERTATION

DEVELOPING AND INVESTIGATING COPPER AND IRON CHALCOGENIDE NANOPARTICLE
SYNTHESES TO ELUCIDATE THE UNDERLYING PROCESSES OF FORMATION

Submitted by
Lily June Moloney
Department of Chemistry

In partial fulfillment of the requirements
For the Degree of Doctor of Philosophy
Colorado State University
Fort Collins, Colorado
Summer 2021

Doctoral Committee:

Advisor: Amy L. Prieto
Justin Sambur
Amber Krummel
Kristen Buchanan

Copyright by Lily June Moloney 2021

All Rights Reserved

ABSTRACT

DEVELOPING AND INVESTIGATING COPPER AND IRON CHALCOGENIDE NANOPARTICLE SYNTHESSES TO ELUCIDATE THE UNDERLYING PROCESSES OF FORMATION

Nanoparticle technology is rapidly growing field due to the unique, tunable properties of nanoparticles (NPs) as compared to their bulk counterparts, enabling a wide range of new applications. The key step, however, to applying NP systems to new areas is developing high quality syntheses. Specifically, solution-based methods for synthesizing NPs offer many synthetic handles for tuning structure/property relationships by controlling composition, size, morphology and capping agents. To effectively design syntheses to control the resulting properties, in depth investigation of the underlying fundamental processes are required. Elucidation of these processes would allow trends to be illuminated and a toolkit of synthesis methods could be built. However, a myriad of interactions (organic, inorganic, solid-state) occur during these reactions, and often these interactions are intertwined with each other. Therefore, careful examination of nanoparticle synthesis for various systems are necessary to advance the NP field.

In Chapter 1, we review literature reports that exemplify the careful examination of underlying mechanisms and pathways required for developing synthesis methods that allow for control over composition, size, morphology. This chapter is split into two major sections; 1) balancing precursor reactivities and elucidating mechanisms and 2) understanding reaction pathways. The first section is split into anion and cation speciation/reactivity. The anion section focuses on the development of chalcogenide reactivity trends and how these trends have led to advanced nanoparticle control. The cation section considers the use of metal-amide complexes to increase and balance reactivities of cations to produce small, phase pure NPs. In depth mechanism studies of these metal-amide reactions in model unary and binary system led to the utilization of this reagent in more complex ternary systems. The second section

focuses on investigation of reaction pathways, discussing how exploration of the reaction phase space as well as determination of intermediates is important for achieving a full picture. We end with a brief discussion on the importance of thorough characterization for describing these reaction mechanisms and pathways accurately.

The importance of investigating the reaction pathway was inspiration for the research described in Chapter 2. Few solution-based techniques to synthesize Cu_3Si , a material with applications in electronics, batteries, and photovoltaics, exist. This could stem from the limited number of Si precursors viable in solution-based techniques. This led us to explore the reaction between Mg_2Si and CuCl_2 in oleylamine, as a solution-based metathesis route to form Cu_3Si particles. The reaction pathway and the role of the solvent were characterized and elucidated. It was found that the reaction proceeds through a two-step pathway, where a Si matrix, Cu particles, and MgCl_2 initially form. Then, the Cu particles diffuse into the Si matrix to form Cu_3Si particles encased in a Si matrix ($\text{Cu}_3\text{Si}@$ Si matrix). Additionally, various solvents are tested to understand the importance of the solvent for the reaction to proceed successfully. The coordinating ability of the solvent was important, where an overly non-coordinating or coordinating solvent limited the production of $\text{Cu}_3\text{Si}@$ Si matrix particles. Oleylamine was found to be a “goldy-locks” solvent as the coordination supported both steps of the reaction.

In Chapter 3, the mechanistic metal-silylamide studies described in Chapter 1 offered inspiration. Specifically, Rebecca C. Miller in our group was recently able to synthesize Fe_2GeS_4 by utilizing lithium bis(trimethylsilyl)amide (LiHMDS). The increased understanding of the Fe-Ge-S phase space and the role of the LiHMDS gained from this previous study led to the research presented in Chapter 3. In this chapter, we report the first nanoparticle synthesis of Fe_2GeSe_4 and $\text{Fe}_2\text{GeS}_{4-x}\text{Se}_x$ ($x = 0.8$ and 1) via a LiHMDS-assisted hot-injection method. This system allowed the role of LiHMDS in balancing not only the cationic but also anionic species to be investigated. This was done by exploring the synthesis parameters, the pre-injection chalcogen speciation, and the reaction pathways.

Finally, in Chapter 4, synthesis methods attempted toward Cu_2SiSe_3 formation are described and a future direction for this project is proposed. Copper-based chalcogenides have gained much attention due to their exemplary intrinsic and structural properties. Cu_2SiSe_3 has been theorized to be a potential photovoltaic material, yet a NP synthesis of this material has not been realized. Exploration of hot injection, metathesis, and solvothermal solution phase methods are reported. However, all efforts resulted in binary Cu/Se phases over the formation of the desired ternary. A future direction for this project could be instead focusing on investigating reactivity trends of the group IV elements, Si, Ge, and Sn, using an amide-assisted synthesis of the Cu_2IVSe_3 materials.

ACKNOWLEDGEMENTS

I first want to thank the Prieto Group, both past and present, as this research would not be as enriched without the numerous scientific conversations that occurred during group meetings, office chats, and beer outings. Specifically, Drs. Jennifer Lee and Rebecca Miller have always been my role models in lab and I could always go to them for anything I needed help with. We spent many long days and nights completing a review on “The Development of Strategies for Nanoparticle Synthesis: Considerations for Deepening Understanding of Inherently Complex Systems” and I appreciate the scratch paper science chats we frequently had during the writing process.

The Prieto Group would obviously not be the Prieto Group without Dr. Amy Prieto, both because of the name but also because the type of mentor and work environment she created and sustained. Amy allows you to make your own path during your PhD and supports you along the way. On top of guiding you on your scientific journey, Amy knows when pausing science discussions to talk about personal or societal issues is needed and I am very appreciative of that quality.

The friends I made in graduate school made my time at CSU memorable and kept me sane. My writing group crew that helped keep me motivated both through setting goals and providing accountability while also providing a space to make writing not so stressful. My baking crew/ go-to for any event (science or fun related) crew are all unique and amazing people who celebrate each other’s successes and help you vent when you are frustrated. My hockey team where I could skate it out and each one of the women on my team create a welcoming and caring environment. Also, to quote a song by Ben Rector, “But truth is there’s nothing like old friends”. I have several old friends from high school and college that are people that can snap me back to the “good ole times” in an instant and they were always there when I needed that.

I don’t think I even know how to thank my family because they have done so much for me. My mom and dad taught me to be curious about my surroundings and that I could do whatever I wanted as long as I

put the work into it. I am incredibly close with my siblings, Maddy and Max; we have inside jokes on inside jokes (sullen), and they know exactly how to cheer me up or see the rational side of a situation. The best part about my family is I never have to ask, they just know.

I was fortunate to find my partner in life, Patrick, in graduate school. Graduate school pushes you to your limits and Patrick helped me from tipping over that ledge. He knows how to keep me laughing, is understanding, encourages me on any of my endeavors, and will call me out when I am being ridiculous. I am grateful to have a person that is always there for me. Most importantly he knows donuts and camping fixes everything. Finally, my fur babies Willow and Iris provided me with snuggles and love at all times, and really what is better than that!

TABLE OF CONTENTS

ABSTRACT.....	ii
ACKNOWLEDGEMENTS.....	v
CHAPTER 1: THE DEVELOPMENT OF STRATEGIES FOR NANOPARTICLE SYNTHESIS: CONSIDERATIONS FOR DEEPENING UNDERSTANDING OF INHERENTLY COMPLEX SYSTEMS	1
1.1 Overview.....	1
1.2 Introduction.....	1
1.3 Balancing Precursor Reactivities and Elucidating Reaction Mechanisms.....	6
1.3.1 Anionic Precursors: The Case of Chalcogenides	6
1.3.1.1 Phosphine Chalcogenides	7
1.3.1.2 Diorganyl Dichalcogenides.....	10
1.3.1.3 Elemental Chalcogen with Reaction Solvent.....	12
1.3.1.4 Perspective	15
1.3.2 Cationic Speciation.....	16
1.3.2.1 The Hard Soft Acid Base Principle.....	17
1.3.2.2 Metal Amides in NP Synthesis: Unary and Binary Systems	19
1.3.2.3 Metal Amides in NP Synthesis: Ternary Systems	22
1.3.2.4 Outlook on Cationic Speciation and Use of Metal Amides in NP Synthesis.....	28
1.4 Understanding Reaction Pathways.....	28
1.4.1 Reaction Pathway Studies in Bulk Solid-State Synthesis	29
1.4.2 Reaction Pathway Studies in Nanoparticle Synthesis	33
1.4.2.1 Exploring Reaction Phase Space by Altering Synthetic Parameters	34
1.4.2.2 The Evolution of Intermediates in NP Reaction Pathways: A Complex Multinary (CIGSe) System	37
1.4.2.3 Reaction Pathway Studies Through the Identification of Intermediates and Varying Reaction Parameters	39
1.4.2.3.1 Reaction Pathway Study of In ₂ O ₃	39
1.4.2.3.2 Reaction Pathway Study of CuInSe ₂	42
1.4.2.3.3 Reaction Pathway Study of Cu-Sb-Se System	45
1.4.3 Outlook for Solution-Based NP Reaction Pathways.....	47
1.4.3.1 Pathway Exploration of Li-Zn-Sb Using WANDA.....	47

1.4.3.2 Reaction Coordinate Plot of InP QD Synthesis	48
1.4.4 Conclusions for Understanding Reaction Pathways.....	50
1.5 Characterization of NP Syntheses.....	51
1.6 Conclusions.....	52
1.7 References.....	55
CHAPTER 2: EXPLORING THE SOLUTION-BASED METATHESIS PATHWAY TOWARD Cu ₃ Si FORMATION.....	60
2.1 Overview.....	60
2.2 Introduction.....	60
2.3 Experimental	63
2.4 Characterization.....	65
2.5 Results and Discussion	66
2.5.1 Material Synthesis Overview: Development and Optimization of Cu ₃ Si@Si matrix Particles	66
2.5.2 Examining the Effect of the Solvent Employed	71
2.5.3 Pathway Study of Cu ₃ Si@Si matrix: Confirming a Two-Step Reaction	74
2.5.4 Further Characterization of the Matrix.....	81
2.6 Conclusions.....	84
2.7 References.....	86
CHAPTER 3: CONTROLLING THE CHALCOGEN REACTIVITY IN THE Fe ₂ GeS _{4-x} Se _x System with LiHMDS	90
3.1 Overview.....	90
3.2 Introduction.....	90
3.3 Results and Discussion	92
3.3.1 Describing the Resulting Fe ₂ GeS _{4-x} Se _x , x=0.8, 1, 4 Particles.....	93
3.3.2 Altering the LiHMDS Amount.....	95
3.3.3 Investigating the Chalcogenide Speciation	97
3.3.4 Elucidating the Reaction Pathway.....	97
3.4 Conclusions.....	100
3.5 References.....	101
CHAPTER 4: EXPLORING SOLUTION PHASE SYNTHESIS EN ROUTE TO Cu ₂ GeSe ₃ : A POTENTIAL PHOTOVOLTAIC MATERIAL	103

4.1 Overview.....	103
4.2 Introduction.....	103
4.3 Experimental.....	105
4.4 Results and Discussion	108
4.4.1 Cu ₂ SiSe ₃ Nanocrystal Hot-Injection Synthesis	108
4.4.2 Cu ₂ SiSe ₃ Nanocrystal Metathesis Synthesis.....	110
4.4.3 Cu ₂ SiSe ₃ Nanocrystal Solvothermal Synthesis	118
4.5 Conclusions.....	119
4.6 Outlook and Possible Future Directions	120
4.7 References.....	122
APPENDIX A-SUPPLEMENTAL INFORMATION FOR CHAPTER 2: EXPLORING THE SOLUTION-BASED METATHESIS PATHWAY TOWARD Cu ₃ Si FORMATION.....	124
APPENDIX B-SUPPLEMENTAL INFORMATION FOR CHAPTER 3: EXAMINING THE ROLE OF LiHMDS IN THE Fe ₂ GeS _{4-x} Se _x SYSTEM WHERE PRECURSOR REACTIVITY IS INHERENTLY ALTERED	142

CHAPTER 1

THE DEVELOPMENT OF STRATEGIES FOR NANOPARTICLE SYNTHESIS: CONSIDERATIONS FOR DEEPENING UNDERSTANDING OF INHERENTLY COMPLEX SYSTEMS¹

1.1 Overview

In order to effectively exploit nanoparticles for a range of new applications, researchers strive to understand structure-property relationships, as well as develop expedient methods to discover and control new materials. Nanoparticle synthesis is complex, and the field is currently experiencing a significant growth of deepening understanding and increasing sophistication. Herein, we review examples from the literature where insight about a synthesis can be exploited to catalyze new discoveries. The focus is on synthetic reports on nanoparticles of increasing complexity.

1.2 Introduction

The study of nanoparticles (NPs) has developed tremendously since the concept of nanotechnology was introduced.¹ The development of new syntheses for nanostructured materials continues to be a thriving field of innovation and exploration, driven by the vast number of potential applications. For instance, NPs are used in battery, thermoelectric, nutritional, luminescence, agricultural, photovoltaic, and biomedical technologies.^{2,3} The great success of NPs in a wide range of applications generally stems from nanomaterials having unique properties compared to their bulk counterparts. Specifically, solution-based NP synthesis can offer the potential to tune properties and access novel materials. Solution-based syntheses have a number of synthetic handles, such as synthesis method, temperature, time as well identity of precursors and solvents/reagents, that can be modified to control morphology, composition, and size.^{4,5} Moreover, the area of NP synthesis provides an exciting opportunity for elucidating a deeper understanding reaction pathways because their synthesis draws from the disciplines of solid state, organometallic, coordination, and organic chemistry.

¹This chapter was adapted and expanded from a review article published (*J. Solid State Chemistry*, **2019**, 273, 243-286) by Jeniffer M. Lee, Rebecca C. Miller, Lily J. Moloney, and Amy L. Prieto. All chapters from the review were written and edited collaboratively between all authors. Section 2.3 from the review was majorly written by Lily J. Moloney with insights and edits from all authors. To represent the ideas of this dissertation, new sections have been added and the review has been adapted.

Over the last thirty years, much has been discovered about how the components of a reaction can lead to the composition, size and morphology of NPs. Building off of the knowledge gained by careful work on CdE (E = chalcogenide) systems,^{6,7} the field is striving to move past reports of cause and effect. Upon tuning the reaction variables, understanding is extrapolated from characterization of the final products. Understanding the pathways of a reaction may inform rational planning. It is currently very difficult to predict the results of a known targeted reaction if the reactants are new. Classic examples from the CdSe literature over the years show how the evolution of precursors can lead to greater control over the rate of nucleation and growth, as well as how the subtle interplay between closely related structures can lead to control over morphology.⁷ Even very simple cases of reactions focused on a single element, such as Co NPs, for example, highlight how complex these reactions can be.⁶

These unary and binary systems can act as model systems, where understanding the complexity at this simpler level can reveal trends and methods to manipulate and control the result of the reaction, whether that be morphology, size, composition, etc. As we move to multinary systems, the trends seen in model systems can act as a guide. However, as systems move to increased complexity the underlying reaction mechanisms and pathway are difficult to elucidate due to the widened phase space and convoluted species interactions, as depicted in Fig. 1.1. Investigation of these system would allow the desired ability to build a synthetic toolkit to predict, design, and understand reactions that ultimately achieve control over a wider phase space and structure/property relationships.

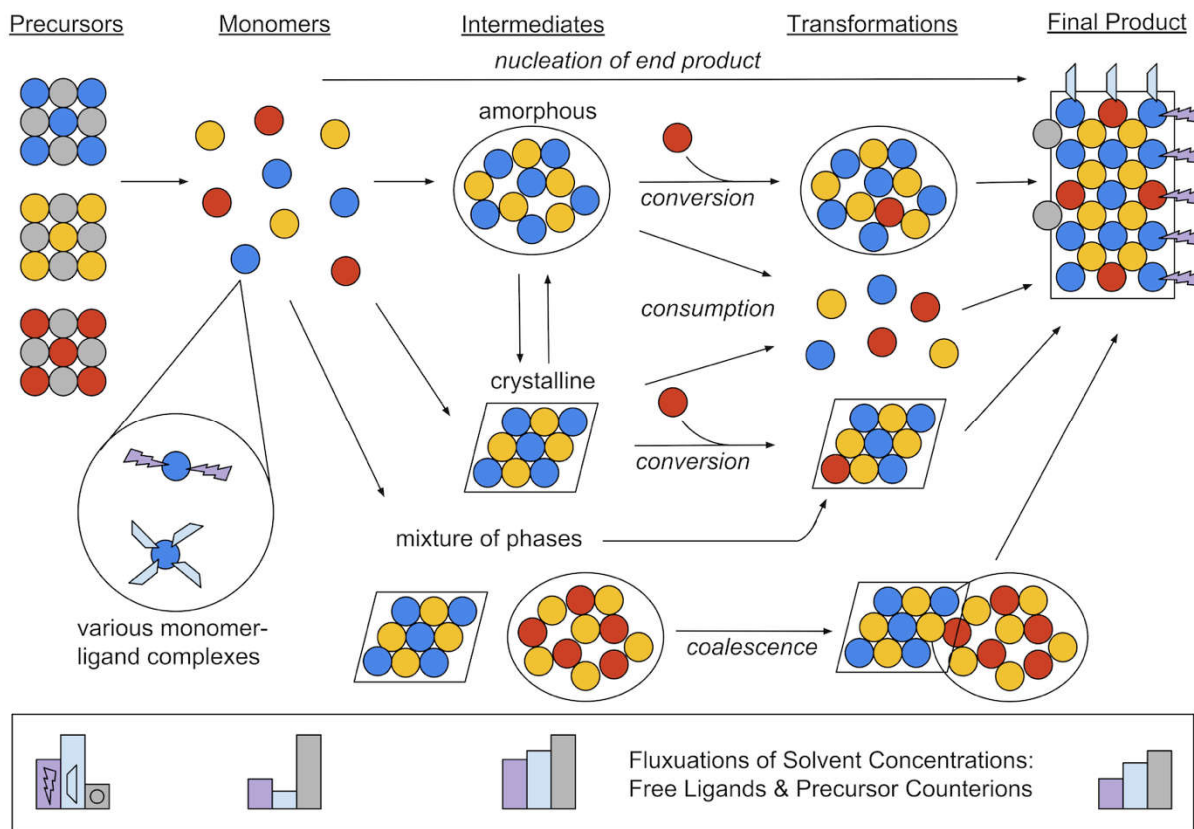


Figure 1.1. A general scheme depicting the transformation of NP precursors to end products, with possible reaction routes identified. Generally, syntheses follow the evolution of the underlined components, but may involve multiple simultaneous processes, and are inherently dynamic, complex systems. Constituent elements of the end product are depicted as red, yellow, and blue circles. Solvent molecules capable of complexation to the constituent elements (ligands) are depicted in purple lightning bolts and light blue trapezoids. Processes labeled between components are italicized. A simplistic description of the dynamic nature of the solvent system is shown in bar graphs at the bottom, with exaggerated concentration changes of the two ligands and the precursor material counterions.

In Fig. 1.1, we have depicted a simplistic overview of possible routes for the transformation of NP precursors to end products. These processes can be highly complex, with many important, dynamic components and the possibility for multiple pathways to simultaneously exist. As viewed from left to right, we typically think of NP precursors being introduced into the solvent system and reacting or dissolving to form active species or monomers. The blue, yellow, and red-atom containing compounds are depicted to dissociate from their gray counterions. Moieties from the solvent system may complex the NP constituent element and alter their reactivity, as shown in the circular inset labeled “various monomer-ligand complexes” with purple lightning bolt and light blue trapezoid shapes on the darker blue atoms.

Thus, due to dissociation or reaction of precursors and complexation by solvent molecules, the composition of the solvent system may change. Throughout the course of the reaction, these solvent concentrations are constantly in flux, depicted in an oversimplified manner by the purple, light blue, and gray bar graphs at the bottom of Fig. 1.1. The active species may then proceed along various routes to eventually precipitate the final product. These include the possibilities of direct multibody nucleation of the end product or the formation of any number of solid-state intermediates (crystalline or amorphous particles or clusters). Possible intermediates may then transform in different ways: (1) “consumption” as dissolution to produce elemental active species once more (though under different reaction conditions and possibly with different complexation), (2) “conversion” as incorporation of an active species into an intermediate, or (3) “coalescence” as attachment of solid intermediates prior to end product arrangement. The intricacy of this depiction also functions to highlight the convoluted impact each synthetic parameter may have.

A large part of the challenge for understanding NP synthetic strategies and adapting knowledge to new material systems lies in their inherent complexity. However, common language may also play a role. General terms are sometimes used to imply differing meaning, depending on the context of the study. Thus, we wish to define a few terms we will use in our discussion of NP syntheses and characterization. They are as follows.

- ❖ “**Nanoparticles (NP)**” as solid-phase particles with nanoscale dimensions. Specifically, the term nanocrystal (NC) should imply single crystallinity, but the term nanoparticle encompasses a wider range of nanostructures, including those which are polycrystalline.
- ❖ “**Precursors**” as the starting compounds for the constituent elements of the final NP
- ❖ “**Active species**” or “**Monomers**” as the compounds that undergo nucleation
- ❖ “**Precursor Conversion**” for the reaction(s) taking place during the transformation of precursors to active species

- ❖ **“Precursor Reactivity”** is a general term for describing a precursors qualitative kinetics or affinity to react/transform to the end product. The term **“Balanced Reactivity”** is used to describe when the reactivities of all precursors are tuned correctly to achieve the desired end phase.
- ❖ **“Solvent System”** as the non-precursor components of the reaction solution. These are typically high boiling point solvents, but could include additive compounds. We won’t use “surfactant” because it implies that this compound necessarily interacts with the surface of the NP, and this isn’t always known.
- ❖ **“Bound Ligand”** and **“Free Ligand”** for describing molecular interactions with the NP surface. Bound ligands are at the NP interface whereas free ligands are molecules with potential for being ligated but are solubilized and unattached to NP surfaces.
- ❖ **“Reaction Mechanism”** refers to the chemical processes occurring between specific species within the reaction system. In Fig 1.1, this could refer to the chemical equations that describe each of the arrows.
- ❖ **“Reaction Pathway”** refers to the route(s) taken by the reaction system from precursors to end products or the evolution of the solid phase components.
 - **“Conversion”** pathway refers to the preservation of a solid-state intermediate followed by end product formation via incorporation or expulsion of elemental species. Note: the word “conversion” is also commonly used to describe the transformation of precursors to active species.
 - **“Consumption”** pathway refers to the dissolution of a solid state intermediate, providing active monomers in solution, usually at different conditions (temperature, coordination, concentration, etc.) than the conditions during the intermediates’ initial nucleation(s).
 - **“Coalescence”** refers to the adhesion and/or merging of two solid state intermediates in solution followed by transformation to the end product.

Note: deconvolution of some of these terms is onerous; however, these descriptions are our best attempt at clarity of speech and meaning.

In this chapter, often model unary or binary systems are used to exemplify achievements as well as challenges in the NP field toward investigating or understand reaction mechanisms and pathways. However, we constantly have an eye toward future development and control over the synthesis of increasingly complex NPs. By complexity we mean either accessing multiple polymorphs in a single system or increasing complexity in composition or morphology.

1.3 Balancing Precursor Reactivities and Elucidating Reaction Mechanisms

1.3.1 Anionic Precursors: The Case of Chalcogens

Many technologically relevant materials are semiconductor metal chalcogenides. Selection of a chalcogen (E) precursor for solution-based NP synthesis is typically based on solubility, ease of use, and desired reactivity. However, this often becomes a game of trial-and-error in order to balance the reactivities of all species in the desired end compound and to avoid unintended byproducts. Further, in systems with an increased number of elements or solid-solutions, where two chalcogens must synchronously react, the balance of reactivities becomes more challenging. Discussed herein are some of the considerations we believe to be important not only when selecting a chalcogen precursor, but also in understanding its role and behavior when investigating the reaction system as a whole. While selection of the chalcogen precursor is a parameter that can be tuned, it may affect the identity of the active chalcogenide monomers and/or the interactions between the dissolved chalcogen monomers and other reaction components. These interactions could affect the system reactivity, the reaction mechanism to describe how the chalcogenide species are evolved and subsequently delivered, and the reaction pathway in which solid phase components are formed.

Reactivity trends and mechanism for common chalcogenide precursors are presented. The variety of different chalcogenide precursors suitable for NP synthesis is historically quite limited, however reports

are beginning to expand. Phosphine chalcogenides are frequently employed⁸⁻¹⁰ but, due to these precursors cost and toxic nature, reports of phosphine-free chalcogenide delivery system such as diorganyl dichalcogenides and dissolution of elemental chalcogens in organic solvents are also becoming more widely utilized.¹¹⁻¹³ Within these chalcogen precursor types, reports have begun to investigate reactivity trends. We will briefly summarize those trends as well as give some perspective on how these trends could be further explored and utilized.

1.3.1.1 Phosphine Chalcogenides

In general, basic structural properties, the mechanism of delivery, and reactivity trends of tertiary phosphine chalcogenides are well-reviewed by García-Rodríguez et al.¹⁴, Reiss et al.¹⁵, and Alvarado et al.¹⁶ Here, we briefly summarize a few key points. For the phosphine chalcogenide series, the reactivity order via bond dissociation energies (BDEs) of the phosphine chalcogenides follows $S < Se < Te$. Although Te will not be compared in this section, it is reviewed by García-Rodríguez et al.¹⁴ and Reiss et al.¹⁵

Determination of mechanistic details on the delivery of the chalcogen (E) from a tertiary phosphine chalcogenide (R_3PE) was pioneered by the Bawendi and Alivisatos groups using nuclear magnetic resonance (NMR).^{17,18} For phosphine chalcogenides, chalcogen atoms can be cleaved by two mechanisms¹⁴: (1) an acid/base reaction in which the chalcogen transfers as reduced E^{2-} and (2) a redox reaction in which it transfers as E^0 . Both mechanisms are known to be important in metal chalcogenide NP syntheses depending on the reaction conditions. In 2017, mechanism 1 was further probed by Frenette et al. who characterized the expected anhydride and tertiary phosphine oxide byproducts but additionally observed H_2Se generated by phosphine selenide decomposition.¹⁹ The headspace was collected into carbon disulfide (CS_2) by cannula transfer and analyzed via ^{77}Se NMR. Interestingly, the authors discovered that binary quantum dots (QDs) could be synthesized by cannula transfer of this gaseous Se species into a separate flask of cadmium carboxylate, suggesting that phosphine selenide activation by a metal complex is not solely necessary for phosphine-chalcogenide bond cleavage. However, the authors

acknowledge this observation does not necessarily disprove the previously proposed mechanism but provide it as an alternative route to QD formation. This highlights the difficulty in pinpointing an active precursor and identifying all interactions in even binary, but still complicated, NP systems.

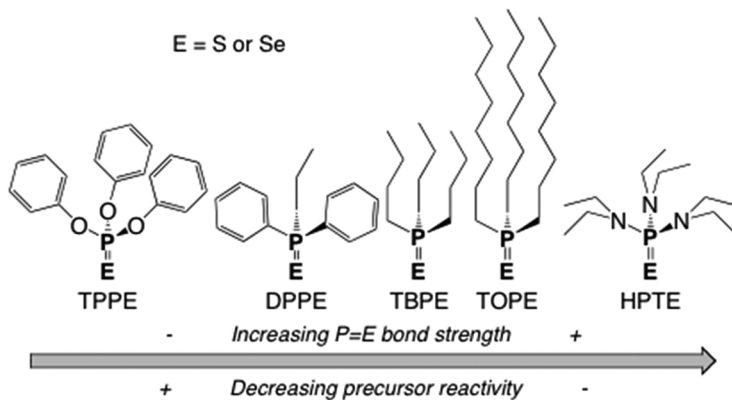


Figure 1.2. Reactivity trend of tertiary phosphine chalcogenides: triphenylphosphite (TPP), diphenylpropylphosphine (DPP), tributylphosphine (TBP), trioctylphosphine (TOP), hexaethylphosphorustriamide (HPT). Reprinted with permission from ref 20. Copyright 2012 American Chemical Society.

The Vela Group has made significant strides toward understanding the reactivity trends of tertiary phosphine chalcogenide families as they performed thorough work in which empirical evidence complemented their theoretical calculations.^{16,20} From DFT calculations, they rationalized that the BDE of the phosphorus-chalcogen (P=E) bond in tertiary phosphine chalcogenides determined its reactivity such that an increasing P=E BDE gave rise to lower reactivity of the phosphine chalcogenide precursor. For any given phosphine, the Se reactivity is greater than that of S because S is smaller, more electronegative, and therefore, forms stronger bonds. Moreover, P=E bond strength increases with increasing electron-donating ability of the R functional groups as this helps stabilize the partial positive charge on the P atom. This theoretical model was supported by empirical CdS and CdSe syntheses in which the aspect ratio of the nanorods were tuned by the reactivity of the P=E bond (Fig. 1.2).²⁰ Here, they see the production of low aspect ratio NPs with diphenylpropylphosphine chalcogenide (DPPE), where the functional group is electron-withdrawing. When trioctylphosphine chalcogenide (TOPE) with a more electron-donating group was used, high aspect ratio particles form. The general trend followed that as the P=E BDE decreased, thereby increasing reactivity, the aspect ratio and length of the NPs also decreased, meaning

shorter and wider nanorods (Fig. 1.3). This trend was explained by the heightened reactivity of the phosphine chalcogenide, initiating faster and more uncontrollable reaction with the cadmium precursor, which led to lower selectivity for anisotropic 1D growth. The authors hypothesized this outcome to be a nucleation-dominated phenomenon as more reactive precursors will nucleate more rapidly and in greater concentration, leading to less precursor for growth. Further, high precursor concentrations were also reported to favor anisotropic growth, so the rate of chalcogen release during growth may also contribute. Finally, the elucidation of the reactivity trend for both the Se and S phosphine precursors allowed the authors to successfully synthesize the $\text{CdS}_{1-x}\text{Se}_x$ solid-solution as well as manipulate the reactivity to instead produce core-shell CdSe@CdS .

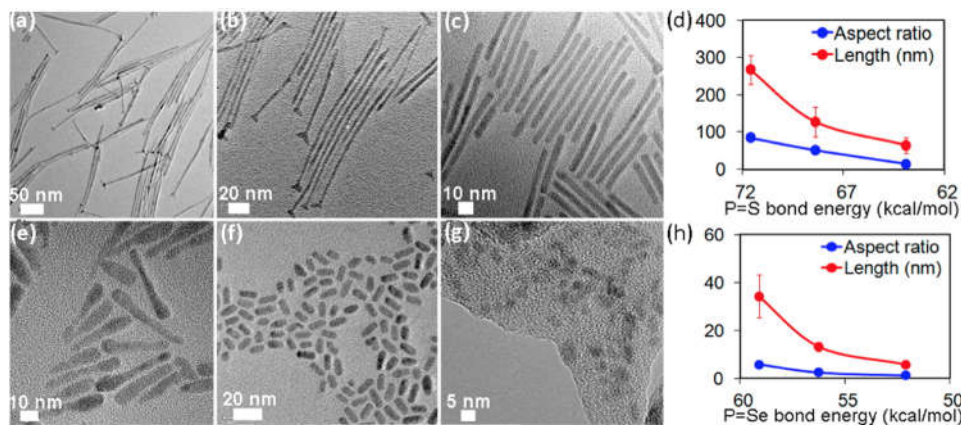


Figure 1.3. Change in nanorod aspect ratio as a function of precursor reactivity. CdS nanorods made with (a, b, c) TOPS, TBPS, and DPPS. (d) Plot of CdS nanorod length (nm) and aspect ratio as a function of calculated P=S bond strength. CdSe nanorods made with (e, f, g) TOPSe, TBPSe, and DPPSe. (h) Plot of CdSe nanorod length (nm) and aspect ratio as a function of calculated P=Se bond strength. Reprinted with permission from ref 20. Copyright 2012 American Chemical Society.

The strength of this report lies in establishing reactivity trends for the different series of tertiary phosphine chalcogenides. This enables selection of a chalcogen precursor due to the assignment of a quantitative value, e.g. BDE, instead of arbitrarily selecting a chalcogen precursor because it is common in the literature. This can be viewed as analogous to tuning a reaction with temperature and time parameters as they can be treated as “continuous” parameters (as in, there are no gaps in identifying a quantifiable value). As our knowledge of reactivity trends of tertiary phosphine chalcogenides expands, instead of these trends looking “step-wise,” we are now filling in gaps so that a precursor can be

A 2018 report from the Brutchey group corroborated and extrapolated these findings to a ternary system, CuInSe_2 , synthesized from diorganyl diselenide precursors.²² The group also demonstrated that the kinetics of diselenide precursor conversion were dependent on the C–Se BDEs and that, interestingly, the strength of this bond was phase directing (Fig. 1.5). It was found that the chalcopyrite phase forms from precursors with weaker C–Se bonds via a fast-nucleating Cu_{2-x}Se NP intermediate, while the metastable wurtzite-like phase forms from precursors with stronger C–Se bonds through a slow-nucleating umangite Cu_3Se_2 phase. While a range of dichalcogenides were tested en route to the formation of thermodynamically stable chalcopyrite and metastable wurtzite phases of CuInSe_2 , more mechanistic insight is required for the general use of dichalcogenides for ternaries. While ex situ X-ray diffraction (XRD) enabled the discovery of these respective reaction pathways, rigorous studies analogous to those presented in phosphine chalcogenide section would be useful to apply dichalcogenides to rational synthesis principles. However, tertiary phosphine chalcogenides have the advantage of being monitored by the P nuclei. NMR spectroscopies such as ^1H , ^{13}C , and most importantly, ^{77}Se could be used in addition, although we acknowledge this is not always an accessible technique.

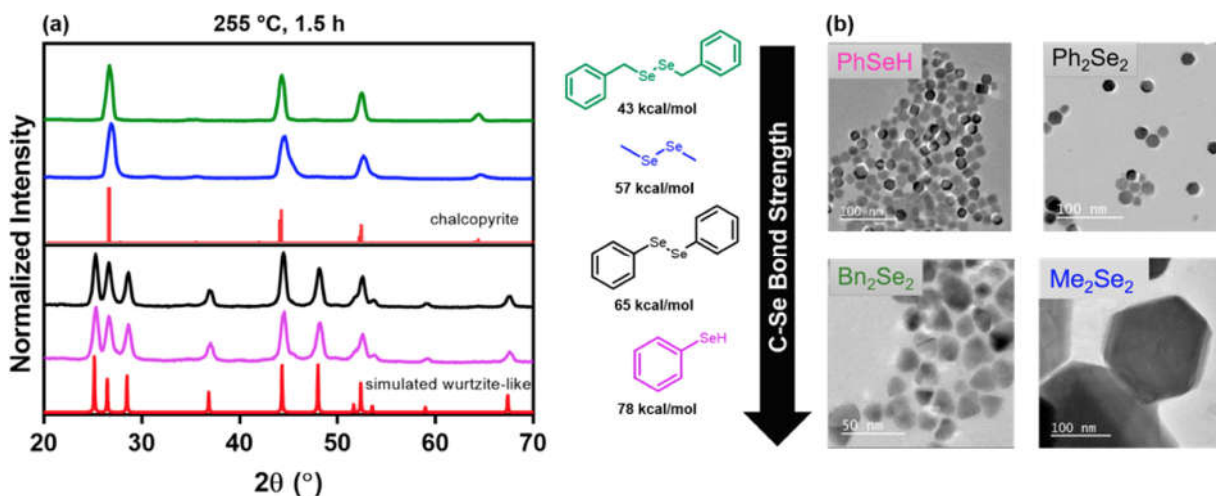


Figure 1.5. (a) Powder X-ray diffraction (PXRD) patterns of CuInSe_2 NPs derived from the corresponding diselenide and benzeneselenol (PhSeH) precursors, and the reactivity scale and DFT calculated BDE of C–E bond. (b) TEM of the resulting NPs synthesized by the corresponding diselenide. Reprinted with permission from ref 22. Copyright 2018 American Chemical Society

1.3.1.3 Elemental Chalcogen with Reaction Solvent

Generally, the simplest method to prepare a chalcogen precursor is mixing elemental powders of S or Se powders, which can exist respectively as S_8 and Se_8 rings as well as polymeric chains, with a high boiling point organic solvent. Solvents such as primary alkylamines, octadecene, dodecane thiol, or a combination are common. However, the chalcogen speciation in these solvents are still being explored due to the possible complexity of these solvent-chalcogen interactions and the difficulty in being able to directly characterize the active species. Additionally, the speciation vastly differs depending on the solvent, making the elucidation of reactivity trends near impossible.

Within the alkylamines family, oleylamine (OLA) is desirable and widely used due to its multiple roles: (1) as a reducing agent, from either its olefin or amine functional groups; (2) as a neutral, labile coordinating ligand group through the lone pair on the amine; and (3) as a long chain alkylamine affording controlled NP growth and a high boiling point synthetic parameter.²³ However, delivery of the chalcogen in these cases is not straightforward as the possible identities of active and non-active species are difficult to detect and categorize. Efforts to achieve mechanistic insight into these intermediate species and potential side products exist, with the aim to uncover how these might affect the reaction pathway of NP formation.

While several mechanisms have been proposed for the case of sulfur, seminal work from the Ozin group proposed that sulfur solubilized in a primary alkylamine (via sonication at 80 °C), specifically octylamine, existed mainly as alkylammonium polysulfides.²⁴ Octylamine was studied as a model compound for other common alkylamines because it can be bought commercially at a higher purity. OLA is typically used at 70% tech grade purity, for reference. Upon heating (2 h at 130 °C), the polysulfide ions reacted with excess alkylamine to liberate H_2S , indicated indirectly by the transformation of PbO-coated paper to PbS in the presence of the reaction flask headspace. Byproducts of the H_2S liberation reaction, such as thioamides, reacted further to continue evolving H_2S , although it remained unclear how and if these species contributed to the reaction pathway. Although studying octylamine instead of oleylamine afforded simplification of data, OLA has further functionality in the C-9 alkene²³ that we

suspect could contribute to the identity of the reaction byproducts. Moreover, the composition and grade of OLA can influence the outcome of a reaction. While this study is a valuable resource for initial understanding of the potential reaction mechanisms in which S could interact with a primary alkylamine, it cannot account for all the unexpected side reactions that might occur as a result of OLA's impurities.

Regarding selenium dissolution in alkylamines, earlier literature suggested that it was difficult to control the reactivity of directly dissolved Se powder in OLA as this often resulted in uncontrolled reactivity.¹³ A couple of alternative routes were developed. In 2010, Wei et al. demonstrated sodium borohydride, NaBH₄, was key in balancing the reactivities of many constituent elements, synthesizing not only binary but also ternary NPs (Fig. 1.6).²⁵ In the presence of OLA, the authors speculate that NaBH₄ reduces Se to generate some

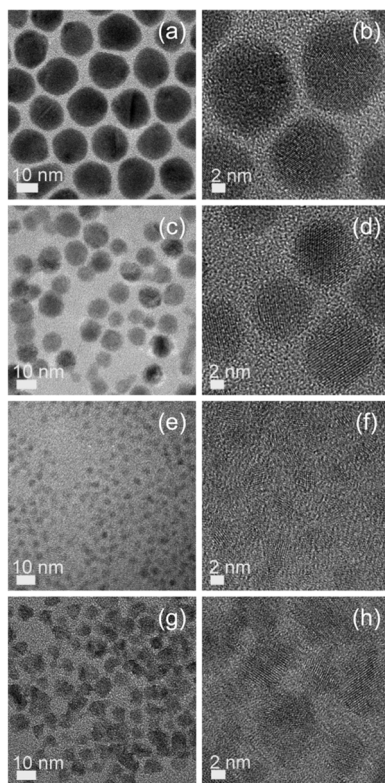


Figure 1.6. Versatility of Se-OLA precursor in the presence of NaBH₄. (a, c, e, g) Transmission electron microscopy (TEM) and (b, d, f, h) high-resolution TEM (HRTEM) images of (a, b) Ag₂Se, (c, d) PbSe, (e, f) ZnSe, and (g, h) CuInSe₂ NPs synthesized with Se-OLA-NaBH₄ precursor. Reprinted with permission from ref 25. Copyright 2010 American Chemical Society.

general alkylammonium selenide species in situ. Although the exact speciation was not well characterized, Se powder was dissolved with ease at RT. In a report from our group by Riha et al., the authors were able to achieve the balanced reactivities of five different constituent elements through the use of NaBH₄ to dissolve both S and Se in OLA, which resulted in compositionally controlled CZTS_{1-x}Se_x NPs.²⁶

Moreover, in 2012 Liu et al. showed that the inclusion of DDT with Se and OLA resulted in a soluble Se precursor.¹³ It was predicted that similarly to the reason for NaBH₄ incorporation, the reduction of Se was required for dissolution. By NMR, they observed a disulfide species suggesting that DDT oxidized to disulfide, releasing 2e⁻ to reduce the Se, which then coordinates with the OLA. The authors demonstrated this active precursor led to small and monodisperse CZTSe, CIGSe, and CdSe particles. However, this study lacked in-depth characterization of the Se speciation. This was somewhat rectified by Walker et al.²⁷ who investigated the addition of different alkyl thiols to the OLA/Se solution by GCMS, which acts as a complimentary technique supporting an alkylammonium selenide species formed, as was hypothesized by Liu et al. report. Despite the lack of true understanding of the actual speciation, the versatility of using NaBH₄ or DDT in the presence of OLA to dissolve Se and somewhat balance reactivities demonstrates the value of its extrapolated use to other systems.

Contrarily to OLA, the literature for the colloidal nanoparticle community has typically cited ODE as a non-coordinating and innocent bystander in NP reactions as a motivation for its use. However, this is not the case in the presence of a chalcogen. Bullen et al. extensively characterized Se as a chalcogen source in ODE to standardize and optimize its use.¹² The preparation of Se-ODE has varied through the literature in terms of time and temperature. Studies with its use have lacked close monitoring of the evolution of Se species, its mode of delivery in NP formation, and its efficacy as a Se precursor. The Bullen et al. report exhaustively measured efficacy by ultraviolet-visible (UV-Vis) spectroscopy, reaction yields of CdSe, inductively coupled plasma atomic emission spectroscopy (ICP-AES), photoluminescence excitation (PLE), X-ray absorption spectroscopy (XAS), NMR, and mass spectrometry (MS).¹² These techniques demonstrated that the most effective use of Se-ODE required

heating for 5 h at 180 °C as these were the minimum conditions required for complete Se dissolution. PLE was especially useful, in which the deepest color indicated the highest percentage of Se dissolution in ODE and thus activation. However, prolonged heating at higher temperatures and/or longer times resulted in significant loss of Se in solution, hypothesized to be a competitive reaction forming H₂Se. They tested their prediction by performing ICP-AES on active (5 h at 180 °C) and aged (48 h at 180 °C) samples. Although it was confirmed there was a loss in solubilized Se, the reaction yield was observed to reduce by a greater extent. This alongside the observation of a reduction in color intensity of the solution, rationalized to originate from Se precursor in solution, led the authors to suggest the speciation change of Se as a result of aging. This study exemplifies the in-depth characterization needed to begin to understand the possible speciation occurring between the solvent and elemental chalcogen powder, yet even with this breadth of characterization it is difficult to know the exact active species as there could be multiple or depend on the synthesis conditions.

In summary, while ease of dissolution is motivation for any use of a chalcogen precursor, this rarely results in simplicity of active precursor identity. It is still important to understand the mechanism of chalcogenide precursor evolution and delivery to aid in understanding the reaction pathway. This can be accomplished by careful characterization of all components. This is further important for these elemental chalcogen powders dissolved in a solvent as, unlike tertiary phosphine chalcogenides, S and Se may not possess analogous reactivities to one another. Additionally, each solvent the chalcogen powder is dissociated in can produce vastly different speciation.

1.3.1.4 Perspective

While we cannot expect that these chalcogenide precursors in a binary nanoparticle system will behave in an extrapolated manner to more complicated multinary systems, the body of literature demonstrates that the field is tending toward identifying reactivity trends of related chalcogenide precursors and that these scales can help direct NP synthesis and serve as strategies for rational precursor selection. Ideally, while we would like to make direct, quantifiable reactivity comparisons between the different types of chalcogen precursors and between different solvent systems, the property trends would

be hard to define because there are often many processes occurring that involve transformations of both the chalcogen and solvent system into different and hard to identify species.

1.3.2 Cationic Speciation

Considering cation precursors in NP syntheses, metal salts such as halides, oxides, and acetates, among others, are commonly used. Solubility of the starting materials plays an obvious role, but complexation in solution, whether to solvents or various other components, often underlies the key factor in tuning the reactivity of cationic components in NP syntheses. Traditionally in early NP syntheses, highly reactive precursors amenable to forming a supersaturation of active species in solution for inducing swift nucleation were targeted. In a landmark review on NP synthesis from 2005, Yin et al. described promising precursors were those with easily dissociating leaving groups.⁶ Acknowledging the complexity of NP synthetic systems and its major differences with chemical vapor deposition (CVD) techniques, the authors suggested the adaptation of CVD precursors for early solution-based NP synthetic development. As understanding in the field has progressed, simpler metal salts have been more commonly employed. A major factor in this shift comes from a better identification of the active species, specifically how the metal atoms are complexed in solution immediately prior to nucleation. Often, some form of solvent molecules exists as the ultimate metal complexing agent(s) during reaction, and advances in cation precursor selection have occurred via achieving these intermediate, solvent-coordinated metal complexes from more benign starting precursors. This change usually accompanies additional benefits with the use of relatively safer (regarding both human use and environmental impact) and more economical precursors.

One specific example of this cation precursor evolution exists in the history of cadmium chalcogenides. Early work, including the influential study by Murray et al., employed the use of highly reactive dimethylcadmium, targeting swift nucleation for monodisperse particles via pyrolysis of this organometallic compound.⁷ In following works, Cd was found to complex with strong ligands, such as hexylphosphonic acid, prior to NP formation.²⁸ This prompted skepticism of the need for the sensitive, reactive dimethylcadmium precursor. Indeed, syntheses with CdCl₂ and CdO were explored, identifying

high quality NPs formed from CdO alongside the use of phosphonic acids.²⁸ Thus, the initial choice of a highly reactive compound targeting rapid nucleation was replaced by simpler, more stable precursors that afforded the same, or similar, important reactive species.

Another area of NP synthesis in which discoveries parallel this theme lies in the use of metal amides as reactive species, whether directly as precursors or formed in situ. Advantages for the use of metal-nitrogen bonded precursors lie in their increased reactivity and commercial availability or relatively straightforward (albeit typically air-sensitive) production. Historically, these compounds have been favored for thin film deposition methods due to the absence of oxygen and carbon, producing films with lower levels of carbonization compared to metal-carbon bonded precursors.²⁹ In the body of this section, we discuss how cationic mechanism investigations of unary and binary systems led to a general understanding of how lithium amide bases interact with cations in solution. Then we discuss how an extrapolated viewpoint was achieved in ternary systems. This discussion acts as a case study to exemplify the importance of exploring and understanding reaction mechanism with respect to the cationic components and the considerations required. While not intended to be an exhaustive compilation of all NP syntheses involving metal amides, this narrative seeks to illustrate the importance and utility of examining possible alternative hypotheses and the role of seemingly uninvolved components in NP reaction systems.

1.3.2.1 The Hard-Soft Acid-Base Principle

To preface the investigation of metal amides in NP syntheses, the Hard-Soft Acid-Base (HSAB) principle provides a framework for interpreting some of the observations covered in the upcoming discussion. Introduced by Pearson in 1963, its ideas inform many aspects of NP systems: precursor decomposition or stability, reactive monomer complexation, surface-ligand interactions, cation-exchange mechanisms, and ligand exchange mechanisms, etc.³⁰⁻³² Within the HSAB principle, chemical groups are categorized as Lewis acids (electron acceptors) and Lewis bases (electron donors) each on a scale between hard and soft. Hard acids usually exhibit high positive charge and small size with paired valence electrons, while soft acids show the opposite: low positive charge, large size, and often unshared valence

electron pairs. Hard bases have tightly held electrons, while soft bases' electron clouds are easily deformed and oxidation is less difficult. In general, polarizability of components underscores the main difference, with low polarizability in hard acids and bases and high polarizability in soft ones. The key HSAB principle then follows that hard acids prefer to coordinate with hard bases and soft acids with soft bases. Common NP synthetic acids and bases are organized along a hard/soft scale in Fig. 1.7.¹⁵

Acid	Hard	Base	Solvent
H ⁺ , Li ⁺		RNH ₂	H ₂ O
Mg ²⁺ , Sr ²⁺ , Sn ⁴⁺		ROH, RO ⁻	HF
Al ³⁺ , Ga ³⁺ , In ³⁺		OH ⁻	alcohols
Co ³⁺ , Fe ³⁺ , As ³⁺ , Ln ³⁺		RCOO ⁻	carboxylic acids
Si ⁴⁺		F ⁻	
VO ²⁺			
BF ₃ , BCl ₃ , B(OR) ₃			
RPO ²⁺ , ROPO ²⁺			
RSO ²⁺ , ROSO ²⁺ , SO ₃			
R ₃ C ⁺ , RCO ⁺ , NC ⁺			
Fe ²⁺ , Co ²⁺ , Ni ²⁺ , Cu ²⁺		C ₅ H ₅ N	
Zn ²⁺ , Pb ²⁺ , Sn ²⁺		N ₃ ⁻	
SO ₂ , NO ⁺		Cl ⁻	
Cu ⁺ , Ag ⁺ , Au ⁺ , Hg ⁺ , Cs ⁺		CO, R ⁻	dimethyl sulfoxide
Pd ²⁺ , Cd ²⁺ , Pt ²⁺ , Hg ²⁺		R ₃ P, (RO) ₃ P	dimethyl formamide
BH ₃ , I ₂ , Br ₂ , IClN	RSH, RS ⁻	nitroparaffins	
RS ⁺ , RSe ⁺ , RTe ⁺	Br ⁻ , I ⁻	acetone	
M ⁰ (metal atoms)			
bulk metals			
	Soft		

Figure 1.7. Common NP synthetic components categorized as Lewis acids and bases on a qualitative scale of hard to soft, based on the Pearson HSAB principle. Reproduced with permission from ref 15. Copyright 2016 American Chemical Society.

Of course, solution-based NP synthetic systems are inherently complex with many interacting components. Relying on standard, quantitative properties of atoms and compounds may aid explanation of empirical synthetic observations, but syntheses are hardly carried out at standard conditions, and extrapolating to NP synthetic conditions degrades the standard properties' reliability for this use. Thus, the strength of relying on Pearson's HSAB principle may lie in its empirical basis. It suggests how

components might interact, but it is not a quantitative law. Within the principle itself (outside of the world of NP synthesis), Pearson acknowledges there exist important chemical factors determining bond energies that must be taken into account beyond the HSAB principle, such as orbital overlap and steric repulsions, for example. Nonetheless, scientists have benefited from NP synthetic explorations guided by the general trends of the HSAB principle, which is featured in a few examples in this section. Additionally, without explicit referral to HSAB, results from some studies can be interpreted under the context of the HSAB principle.

1.3.2.2 Metal Amides in NP Synthesis: Unary and Binary Systems

Metal amide precursors and related in situ formed species have been used for the synthesis of metal, metalloid, binary, and multinary nanoparticles. Relative to common NP conditions (metal salts in high boiling point solvents), the introduction of a metal amide species often enhances reactivity of the involved components, which can alter nucleation kinetics. Strategically, this has been used as a handle for forming smaller, more monodisperse NPs or for balancing the reactivity of multiple cationic components. This specific field highlights an interesting look into the evolution of scientists' understanding of NP synthetic parameters and their subsequent application to new material systems.

Although metal amide precursors have been seen in the literature from the late '90s and early '00s to form many metals and metalloids³³⁻³⁸, attempts to understand the mechanism causing the increased reactivity were not done until 2008. Kovalenko et al proposed a cation-exchange mechanism, using $\text{Sn}[\text{N}(\text{SiMe}_3)_2]_2$ in the formation of PbSe.³⁹ This hypothesis was based on the alteration of the Sn silylamide precursor amount leading to tunability of the PbSe NPs size. The authors speculated a given reaction pathway based on empirical evidence of the starting materials and the observed end products. Inspired by the PbSe study, in 2011, Yarema et al. synthesized Ag_2Se NPs.⁴⁰ However, it was found that altering the Sn silylamide amount did not induce Ag_2Se NP size tuning. Thus, $\text{LiN}(\text{SiMe}_3)_2$ was substituted for the Sn analogue, and improved NPs were formed with respect to colloidal stability, photoluminescence, quantum efficiency, and synthetic yield. Different from the quasi-seeded cation exchange mechanism proposed in the PbSe work, a metathesis-based reaction mechanism was offered.

Illustrated in Fig 1.8, a short-lived Ag silylamide complex was thought to form before decomposing to a Ag^0 species followed by reaction with the phosphine chalcogenide. Although this study did some control reactions to try and further support this mechanism, the species was never directly characterized and therefore a full picture was still not achieved.

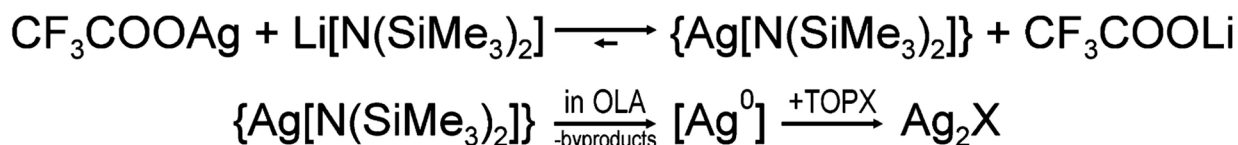


Figure 1.8. Proposed reaction mechanism for the formation of Ag_2E NPs via a metathesis exchange, reduction of Ag^+ , and reaction with phosphine chalcogenides. Reproduced with permission from ref 40. Copyright 2011 American Chemical Society.

In 2013, pivotal work by Kravchyk et al. in the formation of Sn/SnO_2 NPs was inspired by the success of these systems, employing the high reactivity of metal amide compounds to induce swift nucleation.⁴¹ Indeed, the authors were able to produce small, monodisperse Sn NPs, but, more importantly, a better understanding of the active Sn species was observed, allowing a new reaction mechanism to be suggested. Key methodology to this work was ^{119}Sn NMR, displaying the formation of a Sn-oleylamido complex upon the combination of a tin precursor salt, alkylamine solvent, and an organometallic base. Instead of the previously proposed metal silylamide metathesis reaction mechanism, a new role for the organometallic base was suggested. Upon introduction to the alkylamine solvent, it was thought to cause deprotonation, forming an oleylamide moiety, which could then complex with the metal cation. Instead of $\text{Sn}[\text{N}(\text{SiMe}_3)_2]_2$ as the active species for NP nucleation, Sn-oleylamido would then have been reduced to form Sn NPs.

Fig. 1.9 depicts the proposed reaction mechanism and shows the ^{119}Sn NMR spectra for the listed combinations of Sn precursors, OLA, and Brønsted bases, each evidencing the formation of a single, equivalent Sn species. Based on the reaction mechanism proposed, the authors assign this signal ($\delta(^{119}\text{Sn}) = 62.5$ ppm, to the Sn-oleylamido species. In order to eliminate alternative hypotheses for the speciation of Sn in these solutions, various other Sn compounds were characterized. The pure, liquid form of $\text{Sn}[\text{N}(\text{SiMe}_3)_2]_2$, the literature-predicted intermediate, gave signal at $\delta(^{119}\text{Sn}) = 772$ ppm. Further,

solvation effects were ruled out as a possible hypothesis for a shift to 62.5 ppm. The relatively non-coordinating solvent, squalene, with $\text{Sn}[\text{N}(\text{SiMe}_3)_2]_2$ gave signal at $\delta(^{119}\text{Sn}) = 779$ ppm, while the combination of $\text{Sn}[\text{N}(\text{SiMe}_3)_2]_2$ and OLA gave signal at $\delta(^{119}\text{Sn}) = 646$ ppm. A final control solution of SnCl_2 in OLA was ruled out with a characteristic peak at $\delta(^{119}\text{Sn}) = -420$ ppm. Finally, the addition of a Brønsted base to either of the last two solutions, $\text{Sn}[\text{N}(\text{SiMe}_3)_2]_2/\text{OLA}$ or SnCl_2/OLA , resulted in conversion to the Sn-oleylamido complex, as observed by ^{119}Sn NMR. The strength of this work is demonstrated in the experimental evidence eliminating the possibility of the literature-predicted $\text{Sn}[\text{N}(\text{SiMe}_3)_2]_2$ intermediate and in support of a new reaction mechanism possible for amide-assisted NP syntheses.

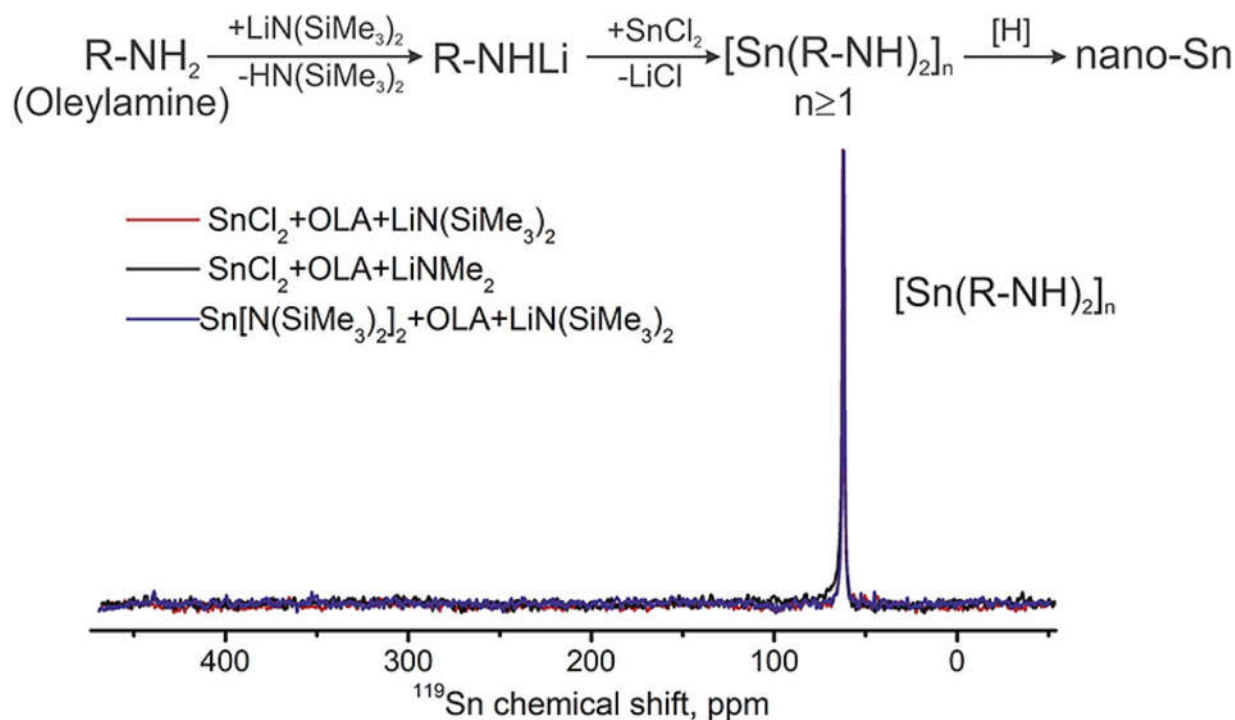


Figure 1.9. Proposed reaction mechanism for the formation of Sn/SnO₂ NPs through the in situ formation of a Sn-oleylamido intermediate. Accompanying ^{119}Sn NMR data for solutions combining Sn precursors, OLA, and Brønsted bases. Reproduced with permission from ref 41. Copyright 2013 American Chemical Society.

Understanding a step in the transformation of the reaction components prior to NP nucleation and growth aided the authors' abilities to extend this reaction scheme to the use of various other Sn salts, organometallic bases, and reducing agents.⁴¹ Further, an impressive collection of metal and metalloid NP

syntheses were developed and characterized by He et al., extending this general reaction scheme to materials including In, Bi, Sn, Sb, Cu, Zn, Ga, and some alloys such as $\text{Bi}_x\text{Sb}_{1-x}$, Cu_6Sn_5 , and Cu_2Sb (Fig 1.10).⁴² The versatility of this NP synthetic strategy emphasizes the necessity for the consideration of this possible reaction mechanism, or a related process, in future studies of NPs developed with similar constituent reagents.

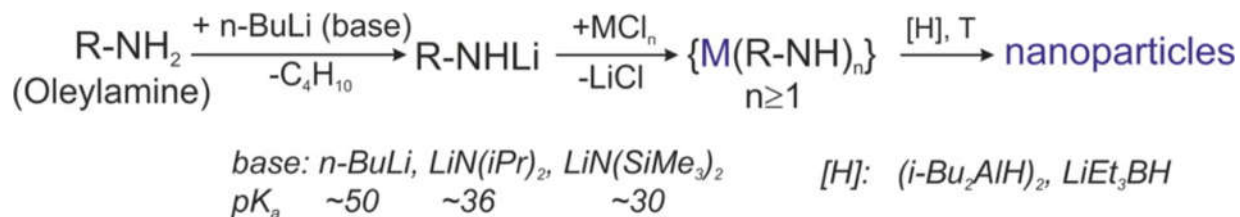


Figure 1.10. General synthetic route proposed by He et al. via the combination of metal and metalloid salts, alkylamines, and Brønsted bases. Metal-oleylamido intermediates are proposed to form, which may then be reduced to metal and metalloid NPs. Reproduced with permission from ref 42. Copyright 2015 American Chemical Society.

1.3.2.3 Metal Amides in NP Synthesis: Ternary Systems

The first silylamide-promoted synthesis for a ternary NP system was published by O. Yarema of the Wood group in the development of Cu-In-Se NP syntheses in 2013.⁴³ Based on previous success in similar systems, oleylamine-based reactions were explored. While small Cu-In-Se NPs could be formed, they lacked photoluminescence. The authors attributed this to the alkylamine's reported role in catalyzing oxidation of NP surfaces.⁴⁴ Thus, altered reactions combined Cu and In halide salts in trioctylphosphine (TOP), and used an injection of $\text{LiN}(\text{SiMe}_3)_2$ and Se dissolved in TOP. Generally, as the silylamide amount was decreased, the NP size was found to increase, with a lessened number of nucleation events offered as an explanation. This work was later extended to the Ag-In-Se system,⁴⁵ utilizing an analogous reaction system; however, in the copper-based system, metal chlorides could be used while iodides were necessary in the silver-based system due to the observed decomposition of AgCl in TOP at >100 °C. Within this reaction space, manipulating the amount of $\text{LiN}(\text{SiMe}_3)_2$ and the ratio of the metal precursors lent control over the NP composition (Fig. 1.11), while both the silylamide amount and the growth time were the key parameters for NP size control (Fig. 1.12).

Interestingly, the authors observed the dependence of the Ag:In composition in the NPs on the $\text{LiN}(\text{SiMe}_3)_2$ amount. When the molar amount of silylamide relative to iodide anions was in excess, the NPs displayed Ag:In molar ratios that reflected the molar ratios of the starting metal precursors. Alternatively, when the silylamide molar amount was deficient relative to the iodide amount, the particles are In-rich, as shown in Fig. 1.11.

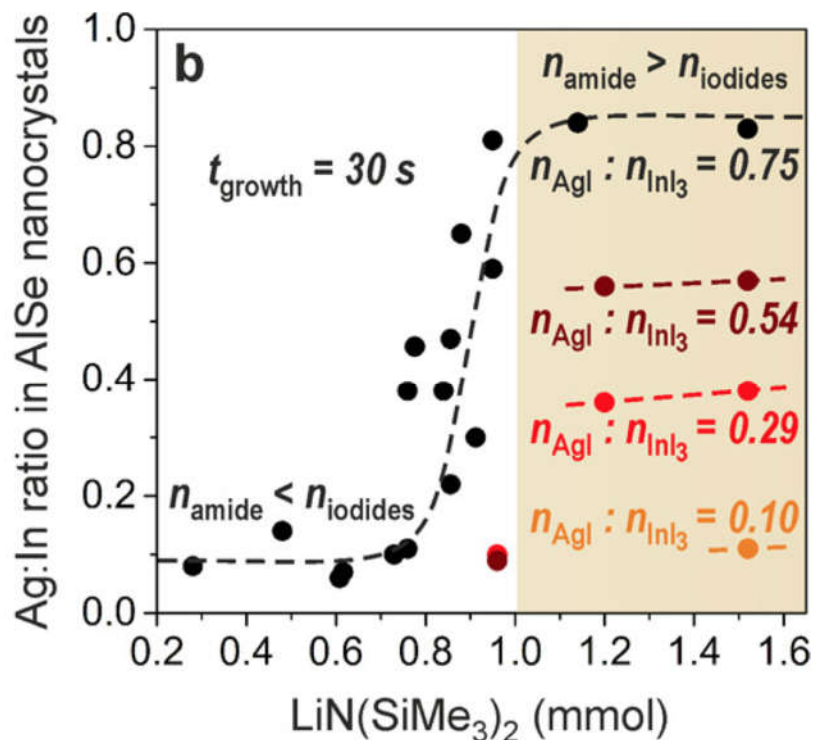


Figure 1.11. Compositions of Ag-In-Se NPs as a function of variable $\text{LiN}(\text{SiMe}_3)_2$ amounts and AgI:InI₃ ratios while the growth time was maintained at 30 s. At high molar $\text{LiN}(\text{SiMe}_3)_2$ amounts relative to the counter Γ^- ions, the NP compositions reflected the starting metal stoichiometries. At low $\text{LiN}(\text{SiMe}_3)_2$ amounts, the NPs were In-rich. Adapted with permission from ref 45. Copyright 2015 American Chemical Society.

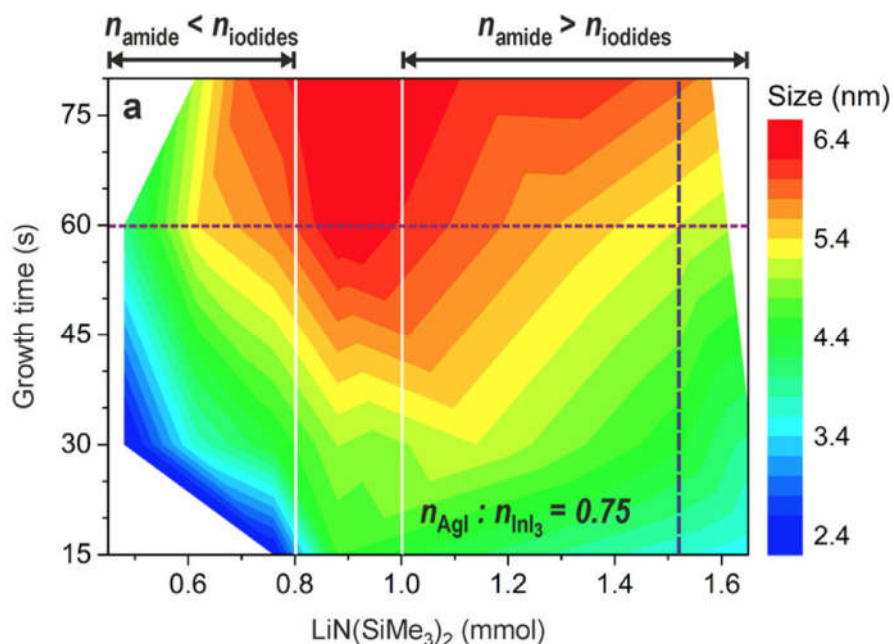


Figure 1.12. Sizes of the Ag-In-Se NPs displayed as a function of the $\text{LiN}(\text{SiMe}_3)_2$ amount and growth time. The $\text{AgI}:\text{InI}_3$ molar ratio was held constant at 0.75. Adapted with permission from ref 45. Copyright 2015 American Chemical Society.

To explain this observation, the authors suggest the following reaction scheme, depicted in Fig. 1.13. Upon interaction of the metal iodide precursors with the Li silylamide, metal amide complexes form. These active species then react with TOPSe in order to form the Ag-In-Se NPs. The key factor here lies in their suggestion of the In-amide having a much higher rate of formation compared to the Ag-amide ($r_{\text{In}} \gg r_{\text{Ag}}$). When the silylamide amount is low, the difference between r_{Ag} and r_{In} is inferred by the In-rich NP compositions. When the silylamide is present in excess, the NP rate of formation is proposed to be the limiting step, and the NPs exhibit Ag:In ratios as supplied in the reaction solution.

The authors connect these observations with the HSAB principle, as the hard base, $[\text{N}(\text{SiMe}_3)_2]^-$ should preferentially coordinate with the hard acid, In^{3+} , relative to the soft Ag^+ . Additionally, we offer support of this connection considering the metal precursors used here are iodides. The soft base, iodide, would preferentially dissociate from In^{3+} over the Ag^+ , which could be an additional factor in the speculated differences in the metal amide rates of formation. This work exemplifies the potential for Li silylamide syntheses to not only be useful for forming smaller, more monodisperse NPs via enhanced

nucleation, but also as a possible handle for balancing the reactivities of multiple cations of varying HSAB character in a ternary compound.

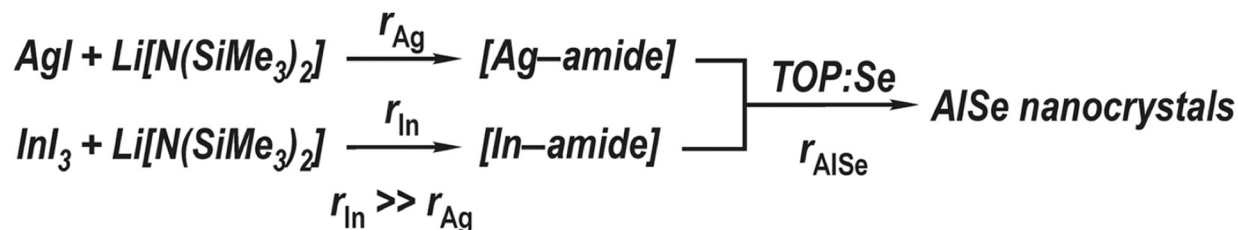


Figure 1.13. Proposed reaction pathway for the formation of Ag-In-Se NPs. Reproduced with permission from ref 45. Copyright 2015 American Chemical Society.

Following, the amide-assisted approach was also applied to attain size and compositional control over the Cu-In-Te and Ag-In-Te NP systems in 2016.⁴⁶ In translating the principles of the selenide system by substituting TOPTe for TOPSe, a difference in the reactivity of the two phosphine chalcogenides was found to be the major factor in the outcome of the reaction. Initially, a bimodal distribution of Cu-In-Te NPs was found to form, which was attributed to TOPTe reacting with both metal amides and unconverted metal halides. The authors cited the higher reactivity of TOPTe relative to TOPSe. In order to promote the transformation of the metal halides to amides, and push the NP formation to be the rate limiting step, the Li silylamide amount was increased. This demonstrated the utility of the proposed reaction mechanism from the Ag-In-Se study. Hypothesizing differences in the reaction rates based on the use of TOPTe, the authors were able to apply a straightforward adaptation and achieve size control over the Te-based NPs.

Additionally, these systems exemplify the sensitivity of controlling aspects such as composition and size dispersion. In the Cu-In-Te reactions, uncontrollable compositional control was observed at temperatures of 280 °C or greater; however, too low of a reaction temperature can also be detrimental for the same parameter, as observed in the Ag-In-Te system. The inactivity of the In-amide complex below 220 °C resulted in Ag-rich ternary NPs as well as the side product, Ag₂Te. Compositional control was achieved in these syntheses by using slightly lower temperatures for the Cu system and by decreasing the initial amount of the Ag precursor for the Ag system. The reaction temperatures also influenced both systems in terms of size distribution. In the Cu system, temperatures at 240 °C or lower gave broad size

distributions and featureless absorption spectra, while the NP nucleation rate in the Ag system was so swift that reducing the reaction temperatures narrowed size distributions. The variations in optimization of these parameters within these two highly related NP reaction systems displays the sensitivity and complex nature of rational design in NP synthesis. For a broader scope on the synthesis and compositional control of I-III-VI NPs, we refer the reader to the comprehensive review by O. Yarema et al.⁴

The demonstrated control over cationic precursor reactivity, nucleation, and particle size with the inclusion of $\text{LiN}(\text{SiMe}_3)_2$ in these I-II-VI ternary systems inspired our group's investigation of $\text{LiN}(\text{SiMe}_3)_2$ in the olivine-structured Fe_2GeS_4 system. Previously, our group reported the first synthesis of Fe_2GeS_4 NP where it was found that the inclusion of hexamethyldisilazane and the sulfur precursor hexamethyldisilathiane were vital for the ternary formation.⁴⁷ However, this reaction took 24 h and formed varying sized particles, with binary impurities forming at early times in the reaction, and dissolving over time. With the recent reports, outlined in this section, making tremendous strides toward understanding the mechanism of metal silylamides in NP syntheses, Miller et al. was able to formulate new hypotheses about our previous study.⁴⁸ Hexamethyldisilazane and hexamethyldisilathiane were likely required due to their decomposition at reaction temperature leading to silylamide moieties. Thus, reactive Ge and Fe silylamide species could form allowing the successful generation of the desired phase. However, as the possible Ge and Fe silylamide is deconvoluted with the S precursor, the poorly understood hexamethyldisilazane and hexamethyldisilathiane precursors were substituted for Li silylamide and sulfur powder. By exploring the Fe-Ge-S phase space and the role of the $\text{LiN}(\text{SiMe}_3)_2$ base, Miller et al. were able to gain mechanistic understanding and produce uniform star-shaped Fe_2GeS_4 particles in 10 min.⁴⁸

From the Kravchyk et al. study on the amide-assisted synthesis of Sn/SnO_2 NPs⁴¹, it was hypothesized that the $\text{LiN}(\text{SiMe}_3)_2$ would deprotonate the OLA to form oleylamide. Further, from the O. Yarema et al. report investigating the role of $\text{LiN}(\text{SiMe}_3)_2$ in the Ag-In-Se NP synthesis⁴⁵, it was hypothesized that the ratio between the cation charge and the base would be important. Therefore, Miller

et al. used these two important ratios to explore the phase space of the Fe-Ge-Se and understand the role of the Li amide base while the ratio of Fe:Ge:S (2:1.25:4) and the total amount of OLA (8mL) were kept constant. Fig. 1.14 shows the plot relating the base:amine and cationic charge:base ratios, as well as the TEM of the resulting particles for each point on the plot.⁴⁸ From this plot, it is easy to observe how trends were elucidated as the movement along different directions (indicated by the dashed lines) would increase the base, the cations, or both together. From exploring this phase space several trends were illuminated. It was found the generally the base aided in balancing the reactivity between Fe²⁺ and Ge⁴⁺, where reactions with low base concentration led to an imbalance and Fe-S binaries formed. Moreover, it was found that increased base, overall increased the system reactivity to favor nucleation over particle growth. From the exploration of this phase space, a phase pure synthesis was realized. Finally, the authors attempted to identify the active species. The injection solution composed of S powder, LiN(SiMe₃)₂, and OLA was analyzed using ¹H NMR and found species similar to previous studies of S powder in OLA.²⁴ The Li amide base was predicted to deprotonate OLA and thus form metal oleylamide species, albeit this was mainly based on end result observations and previous reports as the authors state the difficult in characterizing these precursors after injection.⁴⁸ Overall, this report demonstrates how investigation and depth of understanding reaction mechanisms, such as with the incorporation of LiN(SiMe₃)₂ in NP syntheses, can lead to extrapolation to new systems. Although this does not mean optimization will no longer be required but rather that rational designs of experiments are achievable.

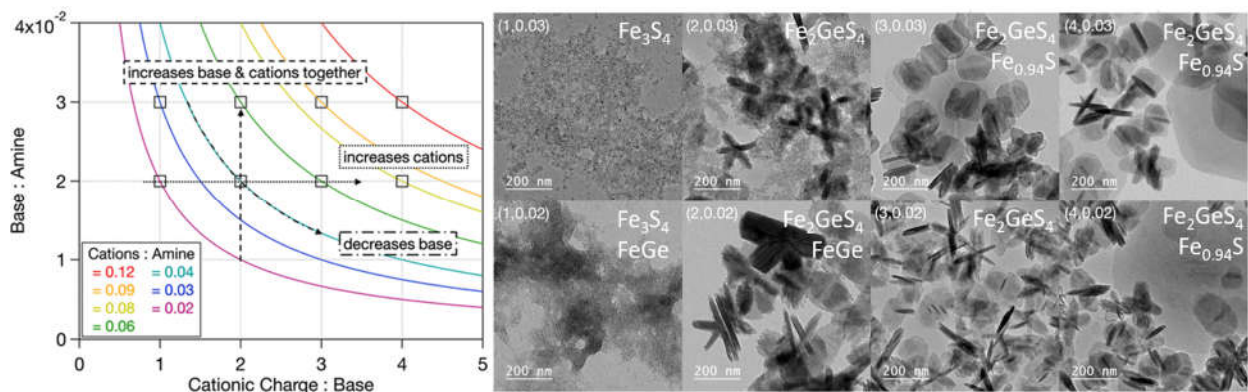


Figure 1.14. The plot represents the reaction phase space of the amide-assisted Fe_2GeS_4 that was investigated by relating the base:amine and cationic charge: base ratios. The TEM, corresponding to a point on the plot, of the resulting particles are shown, where the phases observed by PXRD are written in the right, top corner. Adapted with permission from ref. 48. Copyright 2020 Journal of the American Chemical Society.

1.3.2.4 Outlook on Cationic Speciation and Use of Metal Amides in NP Synthesis

This narrative highlighting the use of metal amides in NP syntheses, whether as precursors or possibly formed in situ, is not intended to be a compendium of all amide-assisted syntheses but rather a demonstration of the impact careful examination and characterization may have on NP synthesis. This has led to a rapid evolution in understanding of the roles of constituent components in these reaction systems, including the cationic species, alkali bases, reducing agents, and the solvent system. While there are still questions to be answered, new possible mechanisms and pathways to be considered have been proposed. This evolution of understanding each of the constituent components, exemplifies how this knowledge of underlying mechanisms can lead to advancements in more complex or novel systems. However, it is important to consider how elucidated processes might possibly have an unintended effect on the development of new NP systems employing similar precursors and solvents. Further, strategies employed and limitations acknowledged are lessons that can be taken into account for the careful understanding and development of all solution-based NP systems.

1.4 Understanding Reaction Pathways

Studies exploring and manipulating reaction pathways widen the available qualitative kinetic and thermodynamic knowledge of a material system. This information can be utilized to access lower energy routes to desired phases, trap metastable phases, and attain novel products. Further, this knowledge can

elucidate possible synthetic strategies for other systems, and as more reaction pathways are explored, patterns across systems could be revealed. Here we will discuss solution-based NP reaction pathways, in reference to the evolution of amorphous and crystalline intermediates formed through the entire duration of a reaction toward an end product.

Reaction pathway studies are traditionally explored for bulk solid-state syntheses to understand the rate-limiting step, diffusion of components, and finally the formation of the desired phase. Although bulk solid-state synthesis and solution-based NP synthesis differ in many ways, the desire to understand fundamental reaction pathway insights such as nucleation and growth exists in both fields. Here we draw parallels from bulk solid-state pathway studies with a non-exhaustive compilation of solution-based NP studies. These solution-based NP studies demonstrate the excitement but also difficulty in exploring these reaction pathways due to the involvement of coinciding concepts drawn from different fields: solid-state chemistry, inorganic chemistry, coordination chemistry, and synthetic organic chemistry. Further, the studies discussed here exemplify the advances toward understanding reaction pathways and where the field can further grow.

1.4.1 Reaction Pathway Studies in Bulk Solid-State Synthesis

Shoemaker et al. have studied reaction pathways of several different systems including K-Cu-S,⁴⁹ K-Sn-S,⁴⁹ Ba-Ru-S,⁵⁰ and Fe-Si-S⁵¹ using in situ XRD techniques. Specifically, Jiang et al. from the Shoemaker group employed in situ XRD to understand and manipulate the reaction pathway to Fe₂SiS₄ with the goal of producing Fe₂SiS₄ at a lower temperature.⁵¹ Analysis of the in situ data for the reaction of the elemental compounds revealed the formation of Fe-S binaries and unreactive Si until the peritectic point of FeS₂ which led to the formation of SiS₂ and the desired ternary. The authors hypothesized that Si sulfurization was the slow step before the production of Fe₂SiS₄. They rationalized that reaction combinations of pre-synthesized binaries with elemental compounds could aid in the navigation of kinetic pathways to bypass low Si reactivity, and thus would require lower energy input for the end formation of Fe₂SiS₄. In support of this hypothesis, the evolution of Fe₂SiS₄ was observed at a lower temperature when pre-synthesized FeS and SiS₂ were reacted, but ultimately, they found the interaction between Fe₃Si and

Fe_5Si_3 with elemental sulfur led to the lowest temperature formation of Fe_2SiS_4 . Jiang et al. speculated the favorability of Fe sulfurization caused the dealloying of the Fe-Si binaries, leaving a defective Si network which allowed faster sulfurization.

Jiang et al. established the value of characterizing reaction pathways both in their interpretation of the system's relative kinetics and thermodynamics and in their subsequent exploitation of this insight for targeted synthesis. In order to visualize these kinetic barriers and thermodynamic sinks en route to the desired product, coordinate plots were constructed (Fig. 1.15).⁵¹ Jiang et al. compared the coordinate plot of the reaction between elemental Fe, Si, and S (Path 1) with the coordinate plot of the reaction between pre-synthesized Fe-Si binaries and S (Path 2). In Path 1, the formation of the Fe-S binaries (B) acts as a thermodynamic sink and the sulfurization of Si exists as a large kinetic barrier forming a trap state before the formation of Fe_2SiS_4 (C). Comparatively, in Path 2 the formation of the Fe-Si binaries (D) exploits the thermodynamic sink of Fe-S binary formation (E) to lower the kinetic barrier of the sulfurization of Si (E) and avoid a trap state. This study outlines a process to investigate reaction pathways and reveals a possible synthesis strategy. The general process of this study was the discovery of all solid-state intermediates followed by the manipulation of a parameter and the observation of the resultant intermediates. By investigating and manipulating the reaction pathway, Jiang et al. gained qualitative kinetic and thermodynamic insight and found improvement of the low Si reactivity by pre-reacting it with Fe. In other words, they changed the reaction combination order to increase the reactivity of a precursor, a strategy that could be applied to other systems.

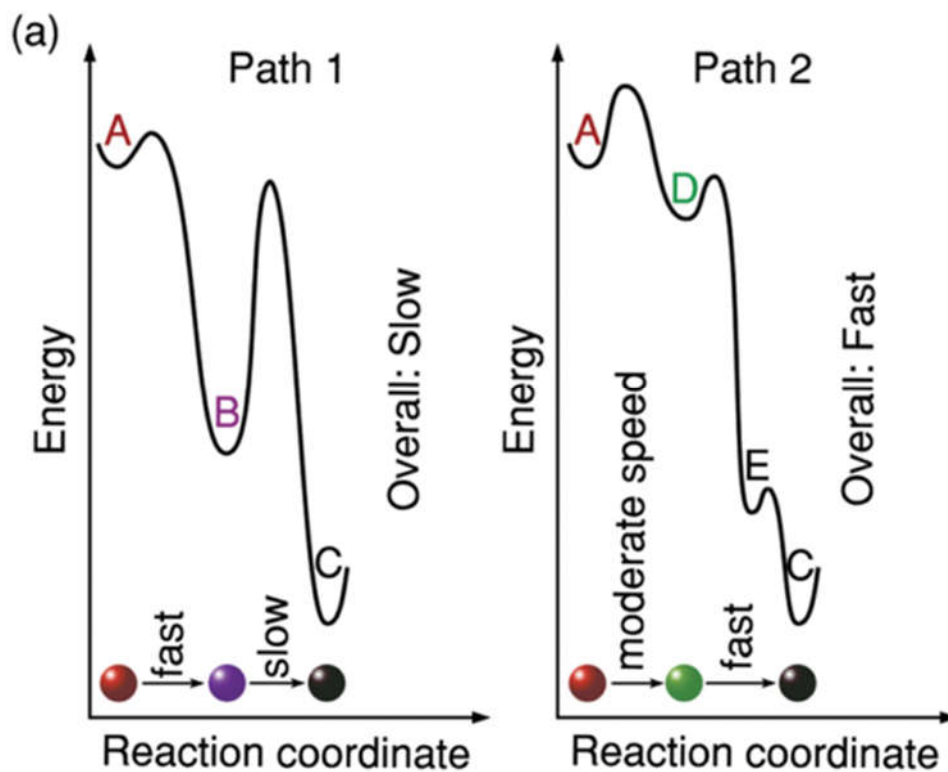


Figure 1.15. Reaction coordinates comparing two Fe-Si-S reaction pathways of the reaction of Fe, Si, and S (A) to ultimately yield Fe_2SiS_4 (C). Following Path 1, the sulfurization of Fe leading to Fe-S binaries (B) is fast, but the sulfurization of Si to allow formation of Fe_2SiS_4 (C) is slow. Following Path 2, the synthesis of Fe-Si binaries (D) first allows fast sulfurization of both Fe and Si to form Fe-S and Si-S binaries (E) and then Fe_2SiS_4 (C). Reprinted with permission from ref 51. Copyright 2017 Royal Society of Chemistry.

Martinolich et al. analyzed the reaction pathway of iron pyrite (FeS_2) using a process similar to the one outlined above.⁵² Here a solid-state method, metathesis, was employed which couples a favorable, low enthalpy of formation product with a less stable product. In this case Na_2S_2 is reacted with FeCl_2 to form NaCl , a favorable product, and FeS_2 , the desired though less favorable product. The FeS_2 reaction pathway was analyzed using in situ XRD and determined to be diffusion limited, where an initial production of NaCl is fast but the diffusion of the resulting Fe and S systems is slow. In an effort to increase diffusion, Martinolich et al. tried mixing the precursors, Na_2S_2 and FeCl_2 , by grinding them. This was carried out in ambient conditions, and a black powder was formed, but was indistinguishable by powder X-ray diffraction (PXRD) with the exception of NaCl . The powder was annealed at low

temperatures (100 - 200 °C) resulting in the desired iron sulfide material. Analysis by PDF of the ground powder before annealing revealed the presence of metal-sulfur bonds but without long-range order. Martinolich et al. concluded this new pathway was limited by nucleation because of the amorphous Fe-S intermediate produced by mixing at RT. Subsequent annealing of the amorphous Fe-S intermediate to form of the crystalline FeS₂ product required a lower temperature than that for the air-free reaction because bonds did not need to be broken and formed, simply rearranged and crystallized.

Similar to the Jiang et al. study, Martinolich et al. gained qualitative kinetic and thermodynamic insight through the investigation of intermediates accessed and the exploration of alternative pathways. Although reaction coordinates were not constructed, they observed a change in the rate-limiting step when the appropriate reaction conditions were altered (Fig. 1.16). Moreover, this pathway understanding was applied in the formation of CuSe₂, both the thermodynamically stable marcasite or the metastable pyrite phase, by reacting Na₂Se₂ with CuCl through the diffusion-limited or nucleation-limited pathways, respectively.^{53,54}

From these solid-state studies, a process to analyze the reaction pathway of a system stands out, and some of the advantages of studying reaction pathways become clear. The studies demonstrate that identification of intermediates along the reaction pathway can allow for strategic variation for targeted synthesis. The value of reaction pathway studies lies in this ability for reaction pathway manipulation. Targeted syntheses could include producing the same product but at a lower temperature (Jiang et al.⁵¹), forming a metastable product (Martinolich et al.⁵³), accessing different products in a system of elements, or a desired morphology, etc. As more reaction pathway information is uncovered by using the process outlined from these solid-state examples, more synthetic strategies and cross system patterns can be discovered.

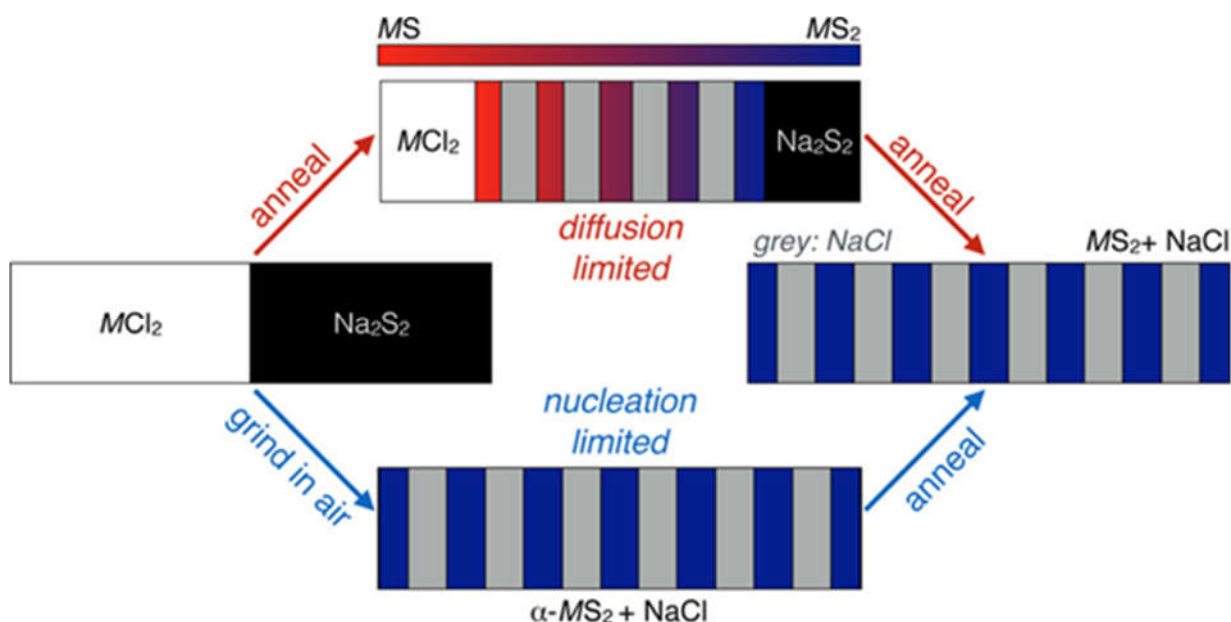


Fig 1.16. Schematic of two accessible metathesis reaction pathways toward the same end products, FeS_2 (labeled here as MS_2) and $NaCl$. The top approach, heating precursors Na_2S_2 and $FeCl_2$ (MCl_2) in a sealed quartz tube under vacuum, was diffusion limited. The bottom approach, grinding the same precursors in ambient air followed by annealing, was nucleation limited. Reprinted with permission from ref 53. Copyright 2017 American Chemical Society.

1.4.2 Reaction Pathway Studies in Nanoparticle Synthesis

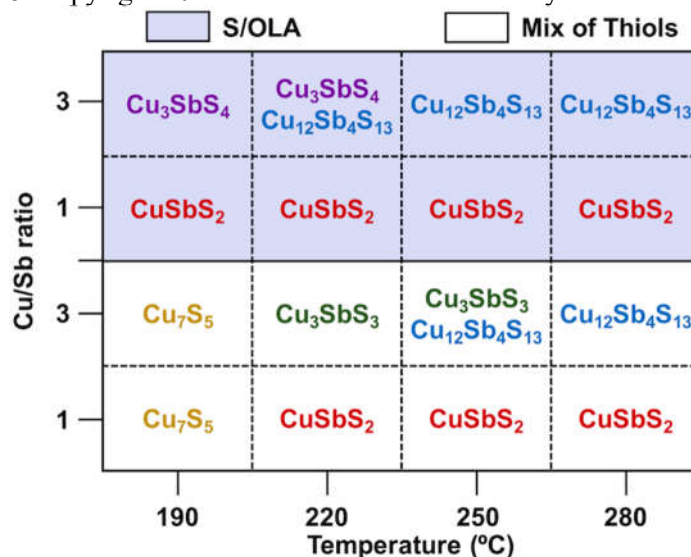
The bulk solid-state examples above outline the manipulation of parameters and the study of intermediate crystalline and amorphous phases as key steps in investigating reaction pathways. These steps are also explored in solution-based NP syntheses, but limitations (primarily in characterization methods readily available) and holes exist within these studies, presenting an exciting area for further exploration. The NP pathway studies we focus on use heat-up and hot injection methods, and for the manipulation of reaction pathway we discuss a few reaction parameters, such as precursor order combination and precursor ratios. We acknowledge that these are not the only approaches toward manipulation of solid-state pathways, but for the scope of this review, we hope these examples can highlight the importance of careful reaction pathway investigation and possible future strategies.

Heat-up and hot injection methods are common for solution-based NP synthesis due to their ability to produce uniform particles, though the nucleation steps for each method differ.⁵⁵⁻⁵⁷ Nucleation in NP syntheses is understood through the models that describe these two methods. In both hot injection and heat-up reactions, historically, the “start” of the reaction is often thought to be nucleation. Specifically, nucleation is perceived as the direct formation of the desired phase. After nucleation, the growth of the desired product is described by the addition of monomers. This commonly-used classical nucleation model often does not describe the entirety of solution-based NP synthesis well. This is due to possible interactions, transformations, or reactions occurring before and/or after the nucleation event of the desired phase (Fig. 1.1). We believe a wider range of possible interactions and transformations should be included in standard NP synthetic models. This is not to say traditional models cannot be used to describe any NP synthesis. Traditional models could be applicable for individual reaction pathway steps (e.g. the formation of an intermediate phase), but models describing full reactions must consider a wider range of possible mechanisms and pathways. For expansion of these models, first NP mechanisms and pathways need to be investigated. Here we will discuss NP pathway studies in a fashion that mirrors the previously discussed solid-state studies. We will first highlight NP studies that explore the phase space of a system of elements to reach various end products, which inherently alters the reaction pathway. Next, we will explain the increased pathway insight gained when NP studies identify intermediates and ultimately, how a more comprehensive understanding of NP syntheses is achieved when both are investigated.

1.4.2.1 Exploring Reaction Phase Space by Altering Synthetic Parameters

In NP synthesis, a common strategy for understanding a material system is to vary parameters and then characterize the end products. These investigations acknowledge that the reaction pathway is altered due to different end products achieved, but the identification of possible solid-phase intermediates is left unknown. Rather, these studies discover the appropriate reaction conditions to achieve various targeted phases and thus elucidate the phase space available for a system of elements.

Table 1.1. Phases of Cu-Sb-S synthesized by systematic changes of parameters. Adapted with permission from ref 58. Copyright 2014 American Chemical Society.



A study by Ramasamy et al. explored the Cu-Sb-S family by keeping the synthesis method, injection order, and cationic precursor identities constant but varying the Cu:Sb ratio, anionic precursor identity, and temperature.⁵⁸ The synthetic parameter changes and the product outcomes were compiled into a table (Table 1.1), making trends easily seen. As long as the temperature was over 190 °C, the evolution of CuSbS_2 was only dependent on one parameter, a 1:1 Cu:Sb ratio. Conversely, synthesis of $\text{Cu}_{12}\text{Sb}_4\text{S}_{13}$ depended on both the Cu:Sb ratio, 3:1, and temperature, which required 150 °C or higher. Finally, production of Cu_3SbS_4 or Cu_3SbS_3 was dependent on all three variables. The synthetic conditions for all four Cu-Sb-Se ternary phases were determined which allowed for trends to be seen. For example, qualitative thermodynamic information was realized due to certain phases (e.g. $\text{Cu}_{12}\text{Sb}_4\text{S}_{13}$) requiring a higher reaction temperature to form compared to others (e.g. Cu_3SbS_4). Additionally, the product dependence on one, two, or all three variables was observed, which illustrates the complexity in optimizing parameters for a desired product. By changing the Cu:Sb ratio, anionic precursor identity, and reaction temperature, Ramasamy et al. determined the phase space of the Cu-Sb-S system. Additionally, synthesizing different desired products inherently allowed the authors to access various reaction pathways, but minimal pathway insight was gained. Further insight about how and why the pathway is

altered when a parameter is changed could have been established by characterizing intermediates for the different reactions.

Some solution-based NP phase space investigations use general chemistry concepts to rationally suggest why manipulating certain reaction parameters results in different products. For example, Wang et al. probed the phase space of Cu_2SnSe_3 NPs.⁵⁹ Optimization of NP synthetic conditions for the cubic (R3) and wurtzite (R1) phases aided in understanding the formation of polytype NPs. Linear (R2) and tetrapod (R4) heterostructures formed via seeded growth of one phase off a core particle of the other. Reaction solution temperature, precursor composition, and order of precursor introduction stood as the most influential parameters for optimizing NP growth; the details are listed in Table 1.2. The metastable wurtzite phase NPs required lower temperatures (220-280 °C) and a Se precursor of higher reactivity (diphenyl diselenide) than for the cubic phase NPs. These reaction conditions were rationalized by their alignment with faster reaction rates, which should favor the dynamically stable wurtzite phase. In contrast, the thermodynamically stable cubic phase required higher reaction temperatures (255-310 °C) and a Se precursor of lower reactivity (elemental Se). Phase-pure cubic NPs additionally required further cation precursor tuning in order to balance reactivities of all components to avoid binary impurities. The optimization of the two polytype heterostructure NPs benefited from the correlation of these reaction conditions and the resulting preferential phases. The majority of the insight gained in this report was identified via manipulation of reaction parameters and careful analysis of the end NP products. The wurtzite NP synthesis was the only synthesis for which the role of an intermediate was mentioned; the NPs were reported to always form by Sn insertion into a Cu-Se binary. However, neither data characterizing this intermediate nor further analysis of this reaction pathway were presented. This report stands as an example of the wide phase space accessible via this strategy of NP synthetic exploration.

Establishing the available phase space of a system allows for control of reaction pathways in that various pure products can be reached. However, without identifying solid-phase intermediates, the majority of the reaction pathway is left unknown. Further, by only characterizing the end products, results can easily be interpreted based on simple models of direct nucleation and growth or lead to non-evidence

based predictions, neither of which should be assumed. Extended insight into material families should include investigating the individual pathways more extensively to elucidate the evolution of possible intermediates en route to the end NP.

Table 1.2. Reaction parameters for the synthesis of wurtzite, cubic, and polytype heterostructures of Cu_2SnSe_3 . Reproduced with permission from ref 59. Copyright 2014 American Chemical Society.

Reaction	Phase	Precursors in Flask	Injected Precursors	Injection Temperature	Growth Temperature	Shape
R1	Wurtzite	Ph_2Se_2 , Cu-Oleate	$\text{Sn}(\text{Ac})_4$	230 °C	240 °C for 30 min	
R2	Polytype 1	Ph_2Se_2 , CuCl, SnCl_2	No injection	No injection	310 °C for 60 min	
R3	Cubic	Se	CuCl, SnCl_2	300 °C	300 °C for 5 min	
R4	Polytype 2	CuCl	Ph_2Se_2 , $\text{Sn}(\text{Ac})_4$	290 °C	280 °C for 15 min	

1.4.2.2 The Evolution of Intermediates in NP Reaction Pathways: A Complex Multinarty (CIGSe) System

Ahmadi et al. used ex situ PXRD plus ex situ transmission electron microscopy (TEM) studies to thoroughly investigate the evolution of solid-phase intermediates toward CIGSe formation.⁶⁰ In their synthesis, CuCl, InCl_3 , and $\text{Ga}(\text{acac})_3$ were mixed in hexadecylamine (HDA) and heated to 130 °C at which point Se in HDA was injected. Following Se injection, the authors initially observed crystalline CuSe and CuGaSe_2 as well as amorphous Se and In_2Se_3 particles. With complementary ex situ TEM, Ahmadi et al. proposed a scheme for the production of CIGSe (Fig. 1.17). The TEM images showed CuSe, the major phase with the largest particle size, transformed into CIGSe as time and temperature increased. Expanding upon simply the observation of solid-phase components present, they reported the transformation occurring in the following way. Initially, CuSe formed due to the reported ability for Cu to complex with two HDA molecules (instead of three, as In and Ga are suggested to do) making it more reactive. Moreover, in this system, Cu and Se are the most compatible HSAB pair. The observation of

In_2Se_3 was also reasoned using HSAB. Since In^{3+} is less electronegative than Ga^{3+} , it is considered softer than Ga and would more readily react with Se. Hence, instead of the formation of a Ga-Se binary, they predicted Ga-HDA reacted with the evolved CuSe to produce CuGaSe_2 . As the temperature rose, In_2Se_3 was said to dissociate while Se and CuSe dissolved to form two quaternary $\text{CuIn}_x\text{Ga}_{1-x}\text{Se}_2$ phases with different In:Ga stoichiometries. Finally, after an additional 60 min at 230 °C, monophasic $\text{CuIn}_{0.5}\text{Ga}_{0.5}\text{Se}_2$ was detected.

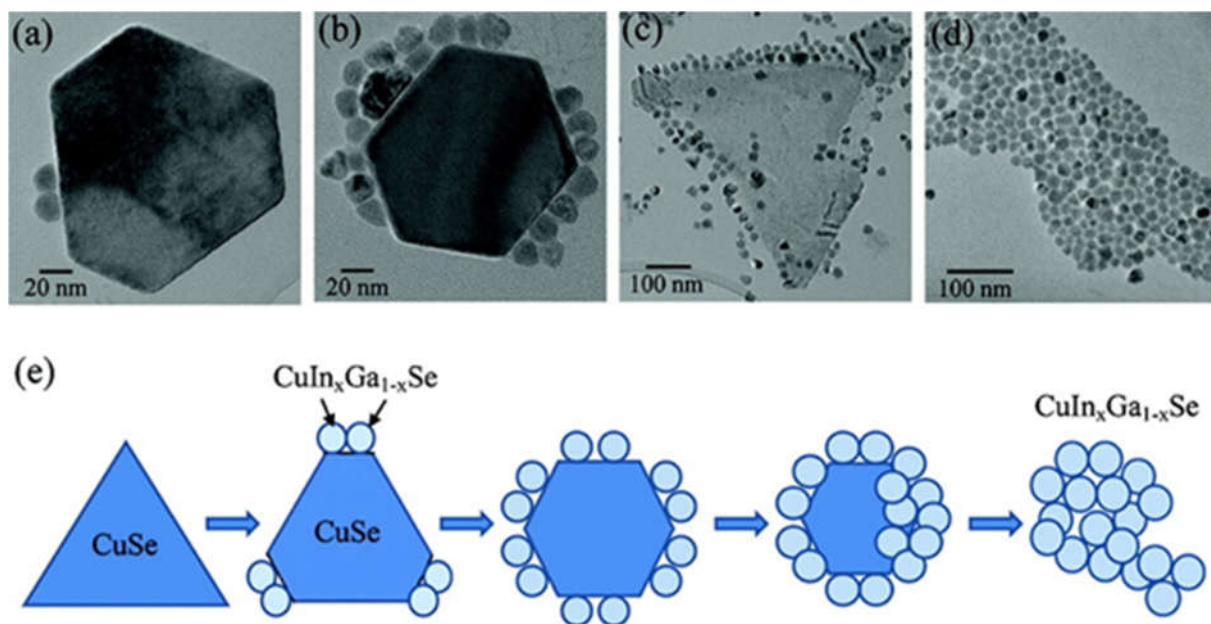


Figure 1.17. TEM images of the reaction pathway evolution of $\text{CuIn}_x\text{Ga}_{1-x}\text{Se}$ at different time and temperature points, (a) 10 min at 130 °C, (b) 20 min at 160 °C, (c) 40 min at 200 °C, and (d) 60 min at 230 °C, which is represented by (e) the pictorial scheme. Reprinted with permission from ref 60. Copyright 2012 American Chemical Society.

This study exemplifies the challenges that multinary systems possess in that intricate pathways do not always proceed by initial nucleation of the desired phase followed by growth. Initially, various crystalline or amorphous intermediate phases can evolve, and then consumption, conversion, coalescence, or a combination of these pathways can occur to finally nucleate the end desired phase (Fig. 1.1). Ahmadi et al. gave vague descriptor words (e.g. dissociate and dissolve) to describe chemical interactions occurring between intermediates to yield CIGSe, but didn't specify whether these transformations occurred through conversion, coalescence, and/or consumption (Fig 1.1). However, controllably ruling out one route versus

another is difficult due to current characterization techniques, modeling, and the understanding of complex nucleation events. Additionally, since these pathways could be occurring simultaneously, deconvoluting the collected data to isolate signatures of a single pathway would be ambitious, but these limitations demonstrate the vast opportunities in further understanding reaction pathways. Moreover, to lend more information to this complex CIGSe system, parameters could be varied to alter the reaction pathway. This would elucidate accessible phase space, possible synthetic strategies, and provide evidence toward the possible qualitative kinetics and thermodynamics at play in this system.

1.4.2.3 Reaction Pathway Studies Through the Identification of Intermediates and Varying Reaction Parameters

Thus far, we have discussed NP studies that have either investigated a systems' phase space by manipulating reaction parameters to elucidate various possible end products or explored the evolution of intermediates. These studies highlight the importance of each in understanding reaction pathways but also the holes left if only one is investigated. Here, we discuss the possibility of expanded reaction pathway knowledge from reports that have studied intermediates and tuned reaction parameters as a result of the knowledge of the intermediates present. Further, we highlight the obstacles and limitations within these NP pathway studies.

1.4.2.3.1 Reaction Pathway Study of In_2O_3

Hutfluss et al. studied a phase transformation for In_2O_3 NPs.⁶¹ This exhibits a relatively simple system compositionally, but the authors identify and study the complexity of the reaction pathway. The In_2O_3 phase transformation proceeded from the metastable, rhombohedral phase (rh- In_2O_3) to the thermodynamically stable, cubic phase (bcc- In_2O_3) and was characterized by ex situ PXRD, extended X-ray absorption fine structure (EXAFS), TEM, and modeling techniques. The phase transformation was observed in NPs prepared by the addition of $\text{In}(\text{acac})_3$ to OLA at various molar ratios (1:20, 1:16, or 1:12) followed by heating to various temperatures over a 60 min time interval. Once the desired temperature was reached, aliquots were removed over time, and the phase content was analyzed. The authors used a

linear combination of reference diffraction patterns for pure rh-In₂O₃, bcc-In₂O₃, and InOOH (a known intermediate) samples to calculate the phase content. This was complemented by EXAFS. We want to bring attention to linear combination of pure rh-In₂O₃ with intermediate InOOH and pure bcc-In₂O₃ being employed over Rietveld refinement. Broadened XRD peaks as a result of smaller crystallite sizes in NPs can be troublesome for fitting data with Rietveld refinement. Hutfluss et al. attempted to account for various particle sizes by compiling reference patterns at various reaction temperatures, but only two temperature data sets were shown and further descriptions of the reference peaks were also limited. The use of linear combination seemed to be successful because the particle sizes determined using linear combination matched the particle sizes measured in TEM. This reiterates the frequent limitations that occur in investigating the chemical interactions and transformations of solution-based NP systems, in this case a phase transformation that must be overcome to fully understand a reaction pathway.

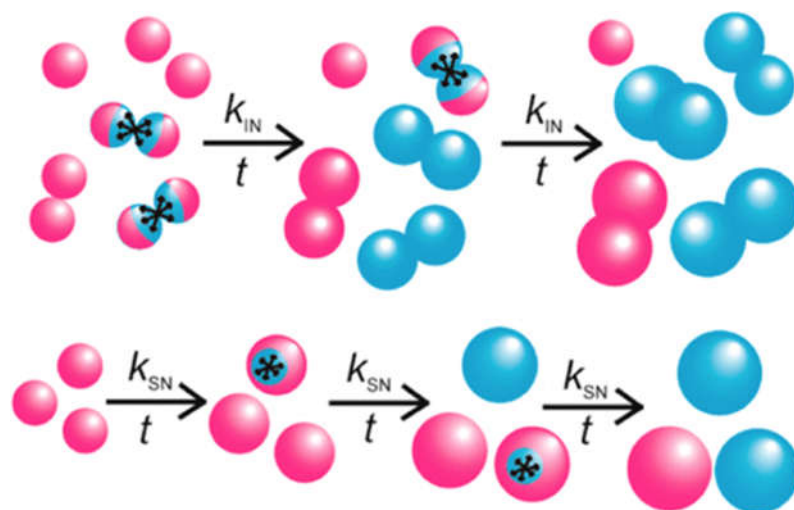


Figure 1.18. Cartoon indicating control over the nucleation pathway of the In₂O₃ phase transformation from rh-In₂O₃ (pink) to bcc-In₂O₃ (blue) depending on the concentration of In(acac)₃ in OLA. High concentration proceeds through interface nucleation (IN) and low concentration proceeds through surface nucleation (SN). Reprinted with permission from ref 61. Copyright 2015 American Chemical Society.

Values related to phase content and crystal size were extracted from the linear combinations of the XRD patterns and fit to two nucleation models to investigate the phase transformation. These included: (1) interface nucleation, where two particles must collide and form a nucleation site, or (2) surface nucleation, where nucleation sites form on individual particle surfaces (Fig. 1.18). From the modeled

fits, they found the phase transformation occurred through two separate mechanisms depending on temperature and precursor concentration. At lower temperature and/or precursor concentration, the phase transformation occurred by surface nucleation, but at higher temperature and/or precursor concentration, the process occurred by interface nucleation, which was attributed to an increased probability of collision. Additionally, the inspection and comparison of TEM images of aliquots taken during each reaction reinforced the hypothesis for the occurrence of the two different mechanisms (Fig. 1.19). Here, Hutfluss et al. noticed the high concentration sample consisted of dumbbell-shaped particles compared to the presence of mostly spherical particles in the low concentration sample. The authors suggested this signified the dominance of interface or surface nucleation depending on high or low precursor concentration, respectively. Interestingly, they stated that a few small dumbbell-shaped, rh-In₂O₃ particles (Fig. 1.19d) were also observed in the low concentration sample. Because these particles were non-transformed, still rhombohedral, and smaller than the critical size at which phase transformation occurs for In₂O₃, they speculated these small dumbbell particles weren't evidence of interaction nucleation occurring at low precursor concentration.

In summary, Hutfluss et al. was able to manipulate the phase transformation nucleation pathway of In₂O₃ by controlling the precursor concentration and/or the temperature of the reaction. We want to highlight the fact that in this system, where only one precursor is used and the same end product is formed, changing a common synthetic parameter can change the chemical interactions of the reaction components. This demonstrates the complexity of understanding the evolution of amorphous and crystalline intermediates in a systems' pathway and the non-innocent impact small changes may have, similar to mechanistic studies. This is not to be a deterrent but rather to point out the vast opportunities for exploration in NP syntheses. Despite the challenging nature of these types of studies, the field of NP synthesis stands to benefit from the application of these characterization and synthetic strategies to other material systems.

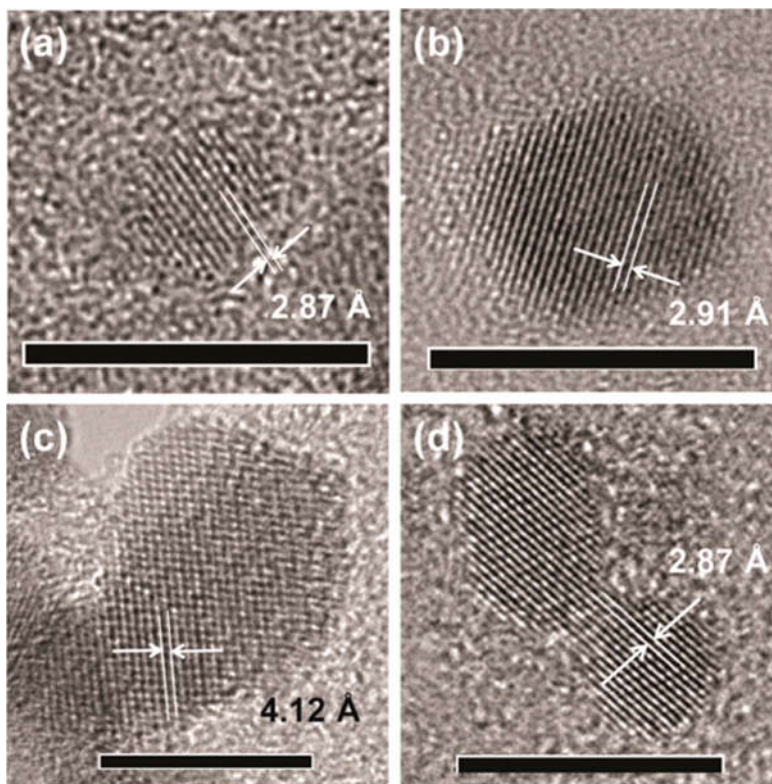


Figure 1.19. TEM images showing single particles observed for (a,b) low precursor concentration (In:OLA molar ratio = 1:20) reaction after 5 h at 200 C and (c) high precursor concentration (In:OLA molar ratio = 1:12) reaction after 2 h at 200 °C. Image (a) was identified as rh-In₂O₃ and (b) was identified as bcc-In₂O₃ supporting surface nucleation. Comparatively, (c) the dumbbell particle was identified as bcc-In₂O₃ supporting interface nucleation. Image (d) is an example of a dumbbell rh-In₂O₃ particle under critical size in the low precursor sample. Reprinted with permission from ref 61. Copyright 2015 American Chemical Society.

1.4.2.3.2 Reaction Pathway Study of CuInSe₂

Kar et al. investigated the evolved solid-state intermediates in the formation of a ternary system, CuInSe₂, and the effect of precursor injection order on the pathway.⁶² Precursors, CuCl, InCl₃, and Se, were individually dissolved in OLA and injected into a separate flask of OLA at 130 °C (original reaction (OR), Table 3). Then, as the reaction was heated to 275 °C, aliquots were removed and analyzed by ex situ PXRD and (field effect scanning electron microscopy) FESEM. Immediately after addition of all three precursors, hexagonal γ -CuSe particles formed and grew, and at 195 °C cubic InSe and chalcopyrite CuInSe₂ particles were observed. The disappearance of the InSe and CuSe peaks correlated to the increase

of the CuInSe_2 peaks above 210 °C, which led the authors to the pathway hypothesis that the dissolution of the InSe and the CuSe particles yield the ternary product.

In an attempt to support their reaction pathway hypothesis, Kar et al. reacted pre-synthesized CuSe and InSe particles in OLA at 275 °C (Control 1 (C1), Table 3). The reaction of the pre-synthesized binaries did lead to CuInSe_2 , but interestingly, it led to the sphalerite CuInSe_2 instead of the chalcopyrite phase, as seen during the original reaction. The system's reaction pathway is more complex than the binary Cu and In selenides reacting, as originally proposed. The authors revised their hypothesis to the evolution of the sphalerite phase from an interaction between In and Cu selenide binaries and the evolution of the chalcopyrite phase from an interaction between CuSe and dissolved InCl_3 in OLA. The authors performed several control experiments (C2-6, Table 1.3) to support this new hypothesis and demonstrate the ability to enable a switch in reaction pathway by varying the precursor injection order to favor different end products. For example, when the In and Se precursors were added to CuCl-OLA together (C5) they believed copper and indium individually reacted with selenium to form binaries before resulting in the formation of the sphalerite phase. Comparatively, given a 30 min dwell time between the injection of the Se and In precursor (C6), Cu/Se binaries were suggested to form first and react with the dissolved InCl_3 precursor to form the chalcopyrite phase.

Table 1.3. Showing reaction conditions and the resulting CuInSe₂ phase for the original reaction (OR) and the six control reactions (C1-6). Adapted with permission from ref 62. Copyright 2011 American Chemical Society.

Reaction	Initial Flask Content	Injection 1	T _{1i}	Injection 2	T _{2i}	T _f	Product
OR	OLA	CuCl-OLA, InCl ₃ -OLA, Se-OLA	130 °C	N/A	N/A	275 °C	Chalcopyrite
C1	OLA	CuSe, InSe	130 °C	N/A	N/A	275 °C	Sphalerite
C2	CuSe-OLA	InCl ₃ -OLA	280 °C	N/A	N/A	280 °C	Chalcopyrite and Cu _{2-x} Se
C3	CuCl-OLA	InCl ₃ -OLA	130 °C	Se-OLA	275 °C	275 °C	Sphalerite
C4	CuCl-OLA	Se-OLA	130 °C	InCl ₃ -OLA	275 °C	275 °C	Chalcopyrite
C5	CuCl-OLA	InCl ₃ -OLA, Se-OLA	275 °C	N/A	N/A	275 °C	Sphalerite
C6	CuCl-OLA	Se-OLA	275 °C	InCl ₃ -OLA	275 °C (30 min later)	275 °C	Chalcopyrite

Similar to the Jiang et al.⁵¹ and Martinolich et al.⁵² solid-state pathway studies, this study first studied the evolution of intermediates, and then altered a parameter to understand how the pathway was affected. Using this process, Kar et al. was able to demonstrate reaction pathway control.⁶² By manipulating the precursor combination order, the majority phase could be switched between sphalerite and chalcopyrite. More importantly, Kar et al. demonstrated the necessity of control reactions and alternative hypotheses in reaction pathway studies. After initially identifying the evolution of intermediates and hypothesizing the interaction occurring to form chalcopyrite CuInSe₂, Kar et al. performed a control experiment that led them to suggest an alternative hypothesis and explore the effect of precursor injection order. Without performing this control reaction, Kar et al. might not have further explored the reaction pathway of CuInSe₂ and found that the pathway can be altered to favor either the chalcopyrite or sphalerite CuInSe₂.

However, we also want to call attention to areas where further studies could enhance the understanding of the reaction pathway. Kar et al. characterized intermediates only by PXRD and FESEM, which alone are inconclusive in confidently determining a truly phase-pure product because the

diffraction patterns for these two CuInSe_2 phases are too similar. Additionally, in reference to the control experiments, the only reported evidence lies in the phase of the end CuInSe_2 product. The intermediates formed during these reaction variations are speculated in the explanation of their results, but it was not evident that aliquots were taken at various stages of the reaction to support the suggested transformations. Therefore, to strengthen their argument, possible future studies could include determination of the control reaction intermediates by *ex situ* TEM, XRD, and complementary characterization studies. These additional studies could lend support or potentially disallow the current reasoning for the observed pathways. Overall, Kar et al. found valuable information about the reaction pathway of CuInSe_2 by carrying out a similar process as outlined in the solid-state examples, and from this study, the importance of thoughtful, meticulous controls which explore alternative hypotheses is exhibited.

1.4.2.3.3 Reaction Pathway Study of the Cu-Sb-Se System

In submitted work from our group, Agocs et al. investigated the reaction pathway to Cu_3SbSe_4 NPs by both the evolution of intermediates and the order of precursor introduction.⁶³ Consequently, a swifter synthesis of smaller Cu_3SbSe_4 NPs was achieved. The procedure of the initial synthesis involved the injection of a CuCl_2/OLA solution into a mixture of Se powder, SbCl_3 , and OLA at 200 °C (Fig. 1.20). After at least a 4 h growth, the products were studied by *ex situ* XRD and TEM. Agocs et al. saw the presence of Sb_2Se_3 prior to and after Cu injection, which initiated the formation of Cu_3SbSe_4 concurrent to the Sb_2Se_3 peaks slowly diminishing. This led to the hypothesis that the incorporation of Cu to form Cu_3SbSe_4 is slow. Similar to the Jiang et al. solid-state study,⁵¹ Agocs et al. explored variations in the precursor introduction order to avoid the formation of the Sb_2Se_3 binary and the slow transformation pathway.⁶³ A double injection of Cu and Se solutions into an Sb solution provided phase-pure Cu_3SbSe_4 NPs accessible in a 5 min growth rather than after at least a 4 h growth (Fig 1.20).

This report focused on the electronic measurements of the resulting NP films and therefore did not detail further investigations of the double injection pathway nor analyze the other injection orders that led to impurities, which are summarized in Fig 1.20. All possible single injection precursor additions were

investigated while temperature and time were kept constant at 200 °C and 5 min. Similar to Ramasamy et al.,⁵⁸ Agocs et al. explored the phase space of a system but other than the initial reaction (Cu injection into the Sb and Se solution) the intermediates were not identified.⁶³ Although the results of these syntheses were not the desired product, their investigation may spark ideas for possible reaction pathway hypotheses. Evidence supporting possible interactions and transformations would result from a multi-faceted analytical approach. If these “failed attempts” were explored, the results could potentially uncover differing intermediate phases. These could then be used to establish a qualitative reaction landscape of this system that might aid in determining a synthetic strategy for another system.

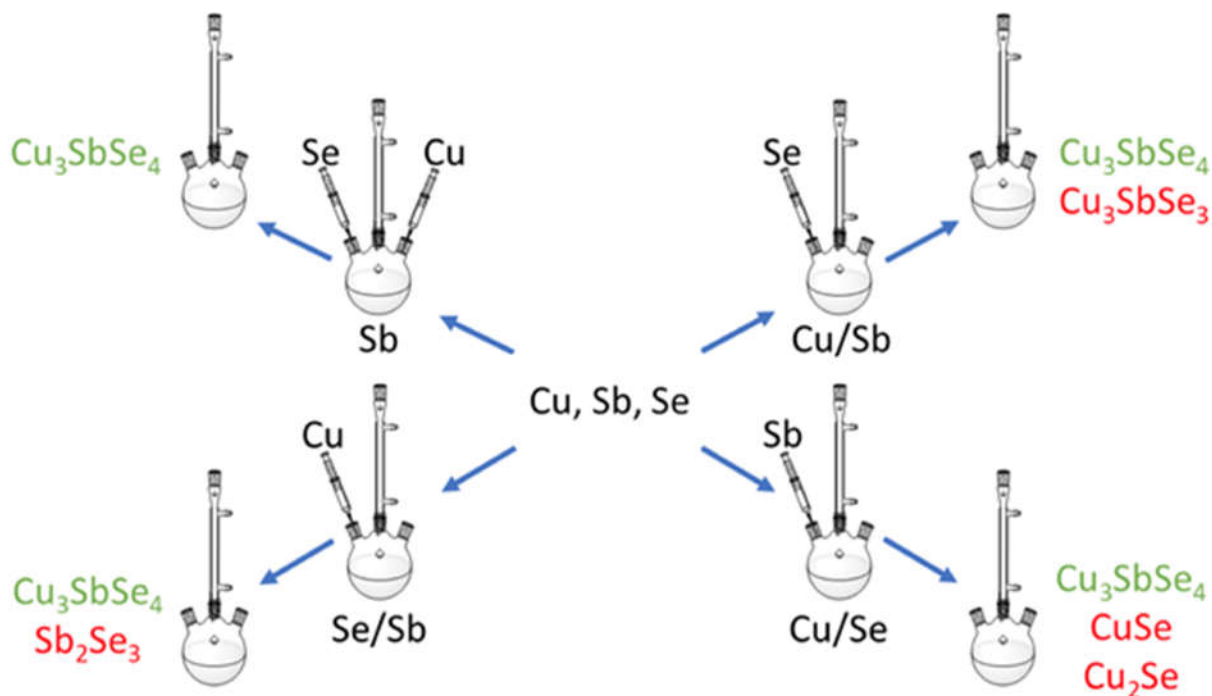


Figure 1.20. Schematic representation of the Cu-Sb-Se system demonstrating the effect of injection order on the reaction pathway by yielding different end products. All reactions were carried out with the same injection temperature and growth time. Green represents the desired phase and red represents the impurity phases observed.

1.4.3 Outlook for Solution-Based NP Reaction Pathways

From the studies discussed in this section, the advantages, gaps in understanding, and limitations of exploring reaction pathways were illuminated. These present an exciting future for the solution-based NP field. Here, we discuss reports that represent the direction we think solution-based NP pathway studies are headed.

1.4.3.1 Pathway Exploration of Li-Zn-Sb Using WANDA

First, the Vela group explored the accessible pathways of the ternary Li-Zn-Sb system⁶⁴ using an automated, high throughput system called WANDA⁶⁵ (Workstation for Automated Nanomaterials Discovery and Analysis). White et al. were able to efficiently explore the effects of a wide range of injection and reaction temperatures, time, precursor concentrations, and precursor injection order as well as remove aliquots mid-reaction for analysis.⁶⁴ The information gained allowed them to produce a phase diagram that accesses five Li-Zn-Sb phases (metal, binary, and ternary) as a function of growth temperature and time (Fig. 1.21). This is an uncommon feat for the NP community but was achieved here due to WANDA providing an outlet for relatively rapid exploration of a wide range of reaction conditions and broad exploration of the material's phase space. Additionally, through this synthetic exploration, White et al. discovered a previously unobserved extended hexagonal LiZnSb structure (h^* -LiZnSb). They delved into understanding the reaction pathway for the formation of this structure by characterizing aliquots with XRD, TEM, and X-ray photoelectron spectroscopy (XPS). Directly after the Sb precursor (triphenylstibine) was injected into a solution of the Li and Zn precursors (n-butyllithium and diethylzinc in ODE and TOP), Zn seeds were observed. An amorphous Sb shell formed around the Zn seeds through interfacial solid-state diffusion. The authors hypothesized that through Li intercalation, h^* -LiZnSb was formed. However, they were straightforward about the inability of the data collected to support this Li intercalation hypothesis. Overall, White et al. were able to use WANDA to probe various reaction conditions which enabled them to produce a phase diagram for the Li-Zn-Sb system and explore the pathway of the previously unobserved h^* -LiZnSb phase. We want to point out that WANDA is a free and

available technique to any researcher who intends to publish results. Proposals to use WANDA can be submitted to the Molecular Foundry research center, located in Lawrence Berkeley National Labs.

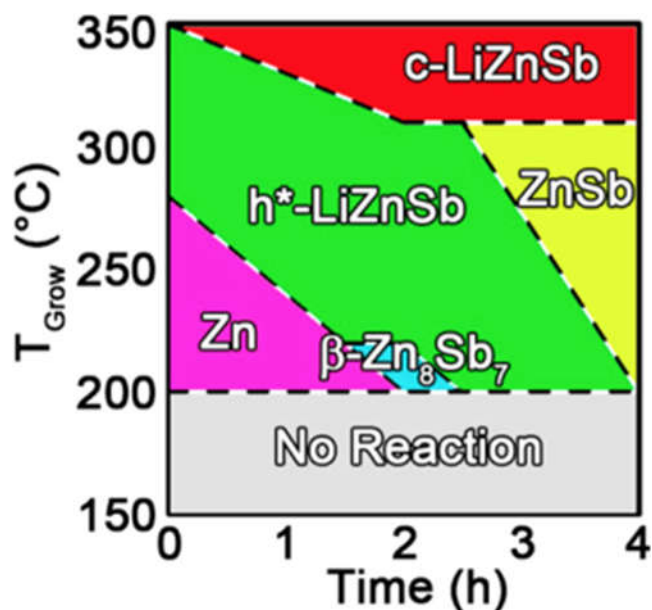


Figure 1.21. The phase space of Li-Zn-Sb as a function of reaction conditions including time and growth temperature. Reproduced with permission from ref 64. Copyright 2018 American Chemical Society.

1.4.3.2 Reaction Coordinate Plot of InP QD Synthesis

Second, the Cossairt group attempted to control nucleation and growth of InP QDs to address poor size dispersity observed in past syntheses of InP.⁶⁶ By optimizing the reactivity of the phosphorus precursors the authors separated nucleation and growth but size distribution was not improved. The authors concluded, “These results are contrary to classical nucleation theory and suggest that control of precursor conversion rate alone is not sufficient to obtain a monodisperse sample of InP.”⁶⁷ This led Gary et al. to investigate and map out the pathway for the formation of InP QDs (Fig. 1.22).⁶⁷ The discrepancy of the InP system with classical nucleation theory was suggested to be due to the formation of magic-sized cluster (MSC) intermediates, which were detected via UV-Vis spectra with lowest energy electronic transition (LEET).

In order to understand the role MSCs played in nucleation and growth of InP, the authors observed the effects of varying the stability of the MSCs on the pathway. To do this, the authors attempted to

synthesize and isolate InP MSCs terminated by carboxylate, amine, or phosphonate ligands (Fig. 1.23 Path A, B, and C, respectively). They found carboxylate-terminated MSCs (Path A) could be isolated and moved toward growth of polydisperse InP QDs. Amine ligands (Path B) bypassed the formation of MSCs to more uniform growth of InP QDs. Phosphonate-terminated MSCs could be isolated, but did not move toward InP QDs. Further, carboxylate-capped MSCs could be replaced by phosphonate ligands but the opposite was not allowed (Path D). This analysis ranked MSC stability as amine-capped < carboxylate-capped < phosphonate-capped and illuminated a reaction landscape toward various products.

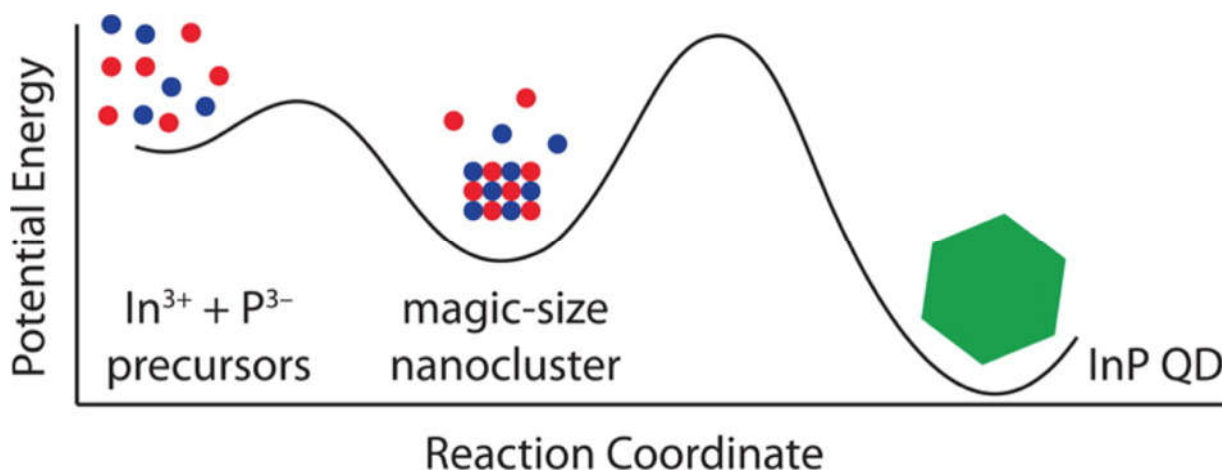


Figure 1.22. General reaction coordinate plot of the two-step nucleation mechanism for the growth of InP QDs from In^{3+} and P^{3-} precursors, depicting the MSC as an isolable intermediate species. Reproduced with permission from ref 67. Copyright 2015 American Chemical Society.

Additionally, Gary et al. investigated the transformation of MSCs to InP QDs by isolating the carboxylate-terminated MSCs and subsequently using them as a single-source precursor (SSP) toward InP QDs (Path E). This decoupled the formation of the MSCs and the nucleation and growth of InP. They observed uniform InP particle shape and InP QD size dependence on concentration. These observations followed classical nucleation theory, and thus, the authors predicted that the reaction pathway of MSCs to InP QDs occurred by monomers created from the dissolution of MSCs rather than an aggregative growth directly from MSCs. Gary et al. demonstrated that NP syntheses can not always be explained by classical nucleation models; this led them to conduct a thorough pathway investigation of the transformation of MSC intermediates to InP QDs. Moving forward, one could imagine that by exploring reaction pathways, a greater understanding of NP syntheses could be achieved and nucleation models could be updated.

Moreover, Gary et al. produced a qualitative reaction coordinate plot, an infrequently used representation for NP syntheses, by studying intermediates and manipulating the stability of the MSCs, allowing them to access various pathways toward monodispersed InP QDs.

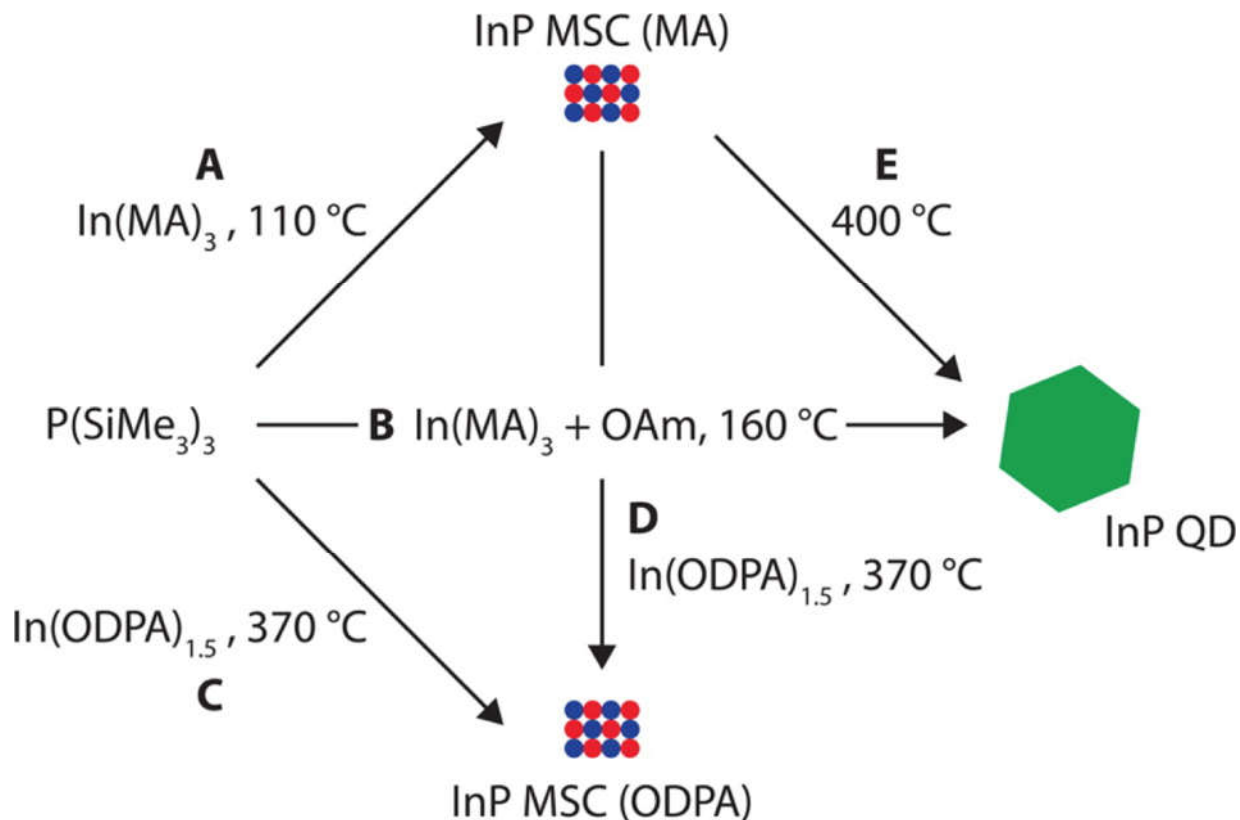


Figure 1.23. Reaction pathways of molecular precursors, indium myristate ($\text{In}(\text{MA})_3$) and indium octadecylphosphonate ($\text{In}(\text{ODPA})_{1.5}$), to InP MSCs and InP QDs in the solvent, octylamine (OAm). Pathways could be tuned by the capping ligands (A and C), carboxylate or phosphonate, as well as the addition of amine (B). Reproduced with permission from ref 67. Copyright 2015 American Chemical Society.

1.4.4 Conclusion for Understanding Reaction Pathways

This section has outlined the process of studying reaction pathways, the possible advantages achieved from exploring reaction pathways, and possible future studies. Further, the importance of control reactions, alternative hypotheses, and the value in reporting failed routes in pathway investigations was demonstrated. The process of studying solution-based NP reaction pathways is progressing to parallel solid-state pathway studies (Jiang et al.⁵¹ and Martinolich et al.⁵²) where intermediates are characterized and the pathway is manipulated by rationally varying a parameter. Moving forward, White et al.

illustrated the ability to efficiently and thoroughly investigate the reaction pathway for h*-LiZnSb and the phase space of the Li-Zn-Sb family using the high throughput system WANDA.⁶⁴ Additionally, Gary et al. demonstrated the InP QD pathway diverging from the classical nucleation model due to an important intermediate, MSCs.^{66,67} By isolating this intermediate, classical nucleation models could describe the transformation to InP QDs. Continuing the thorough investigation of solution-based NP syntheses will improve the understanding of syntheses and allow us to draw conclusions across similar systems, map qualitative thermodynamic and kinetic landscapes, expand nucleation models, as well as lead to the discovery of previously unobserved or metastable products.

1.5 Characterization of NP Syntheses

Represented in Fig. 1.24 are the techniques commonly utilized for characterization of solution-based NP syntheses. The components in the flask depict possible steps from precursors to end products, similarly represented in Fig. 1.1. The green arrows represent possible reaction mechanism transformations, and the black arrows are steps of reaction pathways. Many of these processes occur simultaneously, underscoring the inherent complexity of NP syntheses. However, characterization is commonly carried out on individual components and transformations, which are grouped by similar techniques and are circled within the flask.

Reaction mechanism processes are typically described by NMR, IR, UV-Vis, and MS. These techniques are particularly useful in describing molecular species, and are highly developed for describing the transformation of monomers and ligand coordination. However, their use does not typically extend to the solid-state components, which are commonly characterized by XRD, TEM, Raman, thermal analysis, UV-Vis, and XPS. Traditional characterization is performed on isolated components of NP syntheses. Advancements in characterization move towards providing temporal snapshots of processes via in situ methodology. For a in depth discussion on each of these characterization techniques, we refer the reader to the full written review by J. Lee, R. Miller, L. Moloney, and A. Prieto.⁶⁸

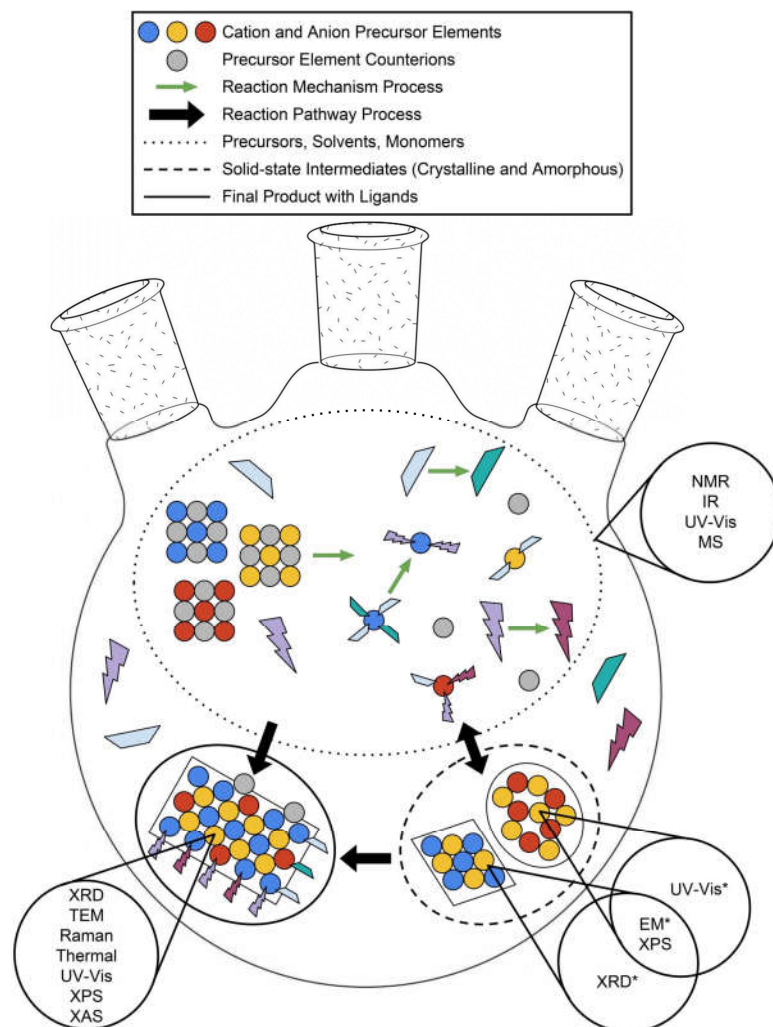


Figure 1.24. A cartoon representation of a dynamic NP synthesis labelled with characterization methods to identify specified reaction species. For example, precursors, solvents, and monomers (encompassed within a dotted circle) can be characterized with NMR, IR, UV-Vis, and MS. Solvent molecules are represented with purple lightning bolts and light blue trapezoids. Subsequent transformations of these species are represented with a color hue change (e.g. purple to magenta and light blue to teal).

1.6 Conclusions

Consistent with the theme of solid-state chemistry over the past fifty years, the aim for NP synthesis is still understanding and designing reactions to ultimately achieve control over a range of thermodynamic and kinetically stable phases. We have highlighted examples here where new insights into reaction mechanisms and pathways and the role of the various components of a synthesis provide new opportunities for elucidating understanding and control over the final products. This is a challenging but

exciting area of chemistry because the perspectives on synthetic approaches draw from solid-state chemistry, organometallics, coordination chemistry, and organic chemistry. Developing new understanding so that we can move toward more predictive schemes continues to be the aspiration of the field, and will lead to new opportunities for materials with novel structures and function, enabling a continually growing group of new technologies.

Traditionally, NP syntheses have involved the characterization of end processes. We challenge the community to characterize dynamic processes so that complete mechanisms and pathways can be proposed (including the identification of intermediates, as well as stoichiometries). While a wide range of techniques are available for characterizing NP synthesis, they tend to be sensitive to single nuclei, solution species, or extended solids (but not necessarily clusters of varying sizes). This challenge then requires that the expectation in the field be that multiple, complimentary characterization methods be used. Moreover, many of the processes depicted here occur simultaneously in a reaction flask, but few characterization methods can describe or deconvolute these simultaneous processes. While some methods have been developed in order to address these limitations, such as the use of mass conservation with FTIR and UV-Vis to characterize growth mechanisms, these techniques are young and have not yet described more complicated systems such as the synthesis of multinary NPs. This leaves room for significant exploratory chemistry to not only develop techniques to answer the questions we pose and to challenge the limits of NP synthesis understanding, but also to optimize these techniques to ensure they reproducibly answer the same questions across different NP systems. We close with challenges and the summary of points that we hope we have described well in this review.

Challenges for Furthering NP Synthetic Strategies:

- adopting more uniform and specific diction
- characterize dynamic processes, not just final products

Important Considerations

- know the limitations of the techniques used, both inherent to the technique and in relation to the materials studied
- use complementary techniques to find evidence in areas for which other techniques are blind
- examine reactions without compromising the replication accuracy of the components and processes as they exist in the original reaction (e.g. in situ capillary experiments, the use of control experiments)
- thoroughly consider all aspects and components present, even if something is traditionally regarded as benign

In particular, if we seek to collaborate with our theory colleagues, we must be able to describe transient species as well as *failed* reactions, so as to contribute useful data for further developing computational methods that can help guide synthetic exploration.

1.7 References

- (1) Feynman, R. P. There's Plenty of Room at the Bottom. *Caltech's Eng. Sci.* **1960**, *23* (5), 22–36.
- (2) Kovalenko, M. V.; Manna, L.; Cabot, A.; Hens, Z.; Talapin, D. V.; Kagan, C. R.; Klimov, V. I.; Rogach, A. L.; Reiss, P.; Milliron, D. J.; Guyot-Sionnest, P.; Konstantatos, G.; Parak, W. J.; Hyeon, T.; Korgel, B. A.; Murray, C. B.; Heiss, W. Prospects of Nanoscience with Nanocrystals. *ACS Nano* **2015**, *9* (2), 1012–1057. <https://doi.org/10.1021/nn506223h>.
- (3) Nasrollahzadeh, M.; Sajadi, S. M.; Sajjadi, M.; Issaabadi, Z. Applications of Nanotechnology in Daily Life. *Interface Sci. Technol.* **2019**, *28*. <https://doi.org/10.1016/B978-0-12-813586-0.00004-3>.
- (4) Yarema, O.; Yarema, M.; Wood, V. Tuning the Composition of Multicomponent Semiconductor Nanocrystals: The Case of I–III–VI Materials. *Chem. Mater.* **2018**, *30* (5), 1446–1461. <https://doi.org/10.1021/acs.chemmater.7b04710>.
- (5) Kumar, S.; Nann, T. Shape Control of II–VI Semiconductor Nanomaterials. *Small* **2006**, *2* (3), 316–329. <https://doi.org/10.1002/sml.200500357>.
- (6) Yin, Y.; Alivisatos, A. P. Colloidal Nanocrystal Synthesis and the Organic–Inorganic Interface. *Nature* **2005**, *437* (7059), 664–670. <https://doi.org/10.1038/nature04165>.
- (7) Murray, C. B.; Norris, D. J.; Bawendi, M. G. Synthesis and Characterization of Nearly Monodisperse CdE (E = S, Se, Te) Semiconductor Nanocrystallites. *J. Am. Chem. Soc.* **1993**, *115* (19), 8706–8715. <https://doi.org/10.1021/ja00072a025>.
- (8) Peng, Z. A.; Peng, X. Formation of High-Quality CdTe, CdSe, and CdS Nanocrystals Using CdO as Precursor [6]. *Journal of the American Chemical Society*. American Chemical Society January 10, 2001, pp 183–184. <https://doi.org/10.1021/ja003633m>.
- (9) Murray, C. B.; Sun, S.; Gaschler, W.; Doyle, H.; Betley, T. A.; Kagan, C. R. Colloidal Synthesis of Nanocrystals and Nanocrystal Superlattices. *IBM J. Res. Dev.* **2001**, *45* (1), 47–56. <https://doi.org/10.1147/rd.451.0047>.
- (10) Bullen, C. R.; Mulvaney, P. Nucleation and Growth Kinetics of CdSe Nanocrystals in Octadecene. *Nano Lett.* **2004**, *4* (12), 2303–2307. <https://doi.org/10.1021/nl0496724>.
- (11) Brutchey, R. L. Diorganyl Dichalcogenides as Useful Synthons for Colloidal Semiconductor Nanocrystals. *Acc. Chem. Res.* **2015**, *48* (11), 2918–2926. <https://doi.org/10.1021/acs.accounts.5b00362>.
- (12) Bullen, C.; van Embden, J.; Jasieniak, J.; Cosgriff, J. E.; Mulder, R. J.; Rizzardo, E.; Gu, M.; Raston, C. L. High Activity Phosphine-Free Selenium Precursor Solution for Semiconductor Nanocrystal Growth. *Chem. Mater.* **2010**, *22* (14), 4135–4143. <https://doi.org/10.1021/cm903813r>.
- (13) Liu, Y.; Yao, D.; Shen, L.; Zhang, H.; Zhang, X.; Yang, B. Alkylthiol-Enabled Se Powder Dissolution in Oleylamine at Room Temperature for the Phosphine-Free Synthesis of Copper-Based Quaternary Selenide Nanocrystals. *J. Am. Chem. Soc.* **2012**, *134* (17), 7207–7210. <https://doi.org/10.1021/ja300064t>.
- (14) García-Rodríguez, R.; Hendricks, M. P.; Cossairt, B. M.; Liu, H.; Owen, J. S. Conversion Reactions of Cadmium Chalcogenide Nanocrystal Precursors. *Chem. Mater.* **2013**, *25* (8), 1233–1249. <https://doi.org/10.1021/cm3035642>.
- (15) Reiss, P.; Carrière, M.; Lincheneau, C.; Vaure, L.; Tamang, S. Synthesis of Semiconductor Nanocrystals, Focusing on Nontoxic and Earth-Abundant Materials. *Chem. Rev.* **2016**, *116* (18), 10731–10819. <https://doi.org/10.1021/acs.chemrev.6b00116>.
- (16) Alvarado, S. R.; Guo, Y.; Ruberu, T. P. A.; Tavasoli, E.; Vela, J. Inorganic Chemistry Solutions to Semiconductor Nanocrystal Problems. *Coord. Chem. Rev.* **2014**, *263–264*, 182–196. <https://doi.org/10.1016/j.ccr.2013.09.001>.
- (17) Steckel, J. S.; Yen, B. K. H.; Oertel, D. C.; Bawendi, M. G. On the Mechanism of Lead Chalcogenide Nanocrystal Formation. *J. Am. Chem. Soc.* **2006**, *128* (40), 13032–13033. <https://doi.org/10.1021/ja062626g>.
- (18) Liu, H.; Owen, J. S.; Alivisatos, A. P. Mechanistic Study of Precursor Evolution in Colloidal

- Group II-VI Semiconductor Nanocrystal Synthesis. *J. Am. Chem. Soc.* **2007**, *129* (2), 305–312. <https://doi.org/10.1021/ja0656696>.
- (19) Frenette, L. C.; Krauss, T. D. Uncovering Active Precursors in Colloidal Quantum Dot Synthesis. *Nat. Commun.* **2017**, *8* (1), 2082. <https://doi.org/10.1038/s41467-017-01936-z>.
 - (20) Ruberu, T. P. A.; Albright, H. R.; Callis, B.; Ward, B.; Cisneros, J.; Fan, H.-J.; Vela, J. Molecular Control of the Nanoscale: Effect of Phosphine–Chalcogenide Reactivity on CdS–CdSe Nanocrystal Composition and Morphology. *ACS Nano* **2012**, *6* (6), 5348–5359. <https://doi.org/10.1021/nn301182h>.
 - (21) Guo, Y.; Alvarado, S. R.; Barclay, J. D.; Vela, J. Shape-Programmed Nanofabrication: Understanding the Reactivity of Dichalcogenide Precursors. *ACS Nano* **2013**, *7* (4), 3616–3626. <https://doi.org/10.1021/nn400596e>.
 - (22) Tappan, B. A.; Barim, G.; Kwok, J. C.; Brutchey, R. L. Utilizing Diselenide Precursors toward Rationally Controlled Synthesis of Metastable CuInSe₂ Nanocrystals. *Chem. Mater.* **2018**, *30* (16), 5704–5713. <https://doi.org/10.1021/acs.chemmater.8b02205>.
 - (23) Mourdikoudis, S.; Liz-Marzán, L. M. Oleylamine in Nanoparticle Synthesis. *Chem. Mater.* **2013**, *25* (9), 1465–1476. <https://doi.org/10.1021/cm4000476>.
 - (24) Thomson, J. W.; Nagashima, K.; Macdonald, P. M.; Ozin, G. A. From Sulfur–Amine Solutions to Metal Sulfide Nanocrystals: Peering into the Oleylamine–Sulfur Black Box. *J. Am. Chem. Soc.* **2011**, *133* (13), 5036–5041. <https://doi.org/10.1021/ja1109997>.
 - (25) Wei, Y.; Yang, J.; Lin, A. W. H.; Ying, J. Y. Highly Reactive Se Precursor for the Phosphine-Free Synthesis of Metal Selenide Nanocrystals. *Chem. Mater.* **2010**, *22* (20), 5672–5677. <https://doi.org/10.1021/cm101308f>.
 - (26) Riha, S. C.; Parkinson, B. A.; Prieto, A. L. Compositionally Tunable Cu₂ZnSn(S_{1-x}Se_x)₄ Nanocrystals: Probing the Effect of Se-Inclusion in Mixed Chalcogenide Thin Films. *J. Am. Chem. Soc.* **2011**, *133* (39), 15272–15275. <https://doi.org/10.1021/ja2058692>.
 - (27) Walker, B. C.; Agrawal, R. Contamination-Free Solutions of Selenium in Amines for Nanoparticle Synthesis. *Chem. Commun.* **2014**, *50* (61), 8331. <https://doi.org/10.1039/c4cc02379j>.
 - (28) Peng, Z. A.; Peng, X. Formation of High-Quality CdTe, CdSe, and CdS Nanocrystals Using CdO as Precursor [6]. *J. Am. Chem. Soc.* **2001**, *123* (1), 183–184. <https://doi.org/10.1021/ja003633m>.
 - (29) Yarema, M.; Caputo, R.; Kovalenko, M. V. Precision Synthesis of Colloidal Inorganic Nanocrystals Using Metal and Metalloid Amides. *Nanoscale* **2013**, *5* (18), 8398–8410. <https://doi.org/10.1039/c3nr02076b>.
 - (30) Pearson, R. G. Hard and Soft Acids and Bases. *J. Am. Chem. Soc.* **1963**, *85* (22), 3533–3539. <https://doi.org/10.1021/ja00905a001>.
 - (31) Parr, R. G.; Pearson, R. G. Absolute Hardness: Companion Parameter to Absolute Electronegativity. *J. Am. Chem. Soc.* **1983**, *105* (26), 7512–7516. <https://doi.org/10.1021/ja00364a005>.
 - (32) Pearson, R. G. *Chemical Hardness*; Wiley-VCH Verlag GmbH: Weinheim, Germany, 1997.
 - (33) Nayral, C.; Ould-Ely, T.; Maisonnat, A.; Chaudret, B.; Fau, P.; Lescouzères, L.; Peyre-Lavigne, A. A Novel Mechanism for the Synthesis of Tin/Tin Oxide Nanoparticles of Low Size Dispersion and of Nanostructured SnO₂ for the Sensitive Layers of Gas Sensors. *Adv. Mater.* **1999**, *4* (1), 61–63. [https://doi.org/10.1002/\(SICI\)1521-4095\(199901\)11:1<61::AID-ADMA61>3.0.CO;2-U](https://doi.org/10.1002/(SICI)1521-4095(199901)11:1<61::AID-ADMA61>3.0.CO;2-U).
 - (34) Cordente, N.; Respaud, M.; Senocq, F.; Casanove, M.-J.; Amiens, C.; Chaudret, B. Synthesis and Magnetic Properties of Nickel Nanorods. *Nano Lett.* **2001**, *1* (10), 565–568. <https://doi.org/10.1021/nl0100522>.
 - (35) Meffre, A.; Lachaize, S.; Gatel, C.; Respaud, M.; Chaudret, B. Use of Long Chain Amine as a Reducing Agent for the Synthesis of High Quality Monodisperse Iron(0) Nanoparticles. *J. Mater. Chem.* **2011**, *21* (35), 13464–13469. <https://doi.org/10.1039/c1jm12127h>.
 - (36) Desvaux, C.; Amiens, C.; Fejes, P.; Renaud, P.; Respaud, M.; Lecante, P.; Snoeck, E.; Chaudret, B. Multimillimetre-Large Superlattices of Air-Stable Iron–Cobalt Nanoparticles. *Nat. Mater.* **2005**, *4* (10), 750–753. <https://doi.org/10.1038/nmat1480>.

- (37) Dumestre, F.; Chaudret, B.; Amiens, C.; Fromen, M. C.; Casanove, M. J.; Renaud, P.; Zurcher, P. Shape Control of Thermodynamically Stable Cobalt Nanorods through Organometallic Chemistry. *Angew. Chemie - Int. Ed.* **2002**, *41* (22), 4286–4289. [https://doi.org/10.1002/1521-3773\(20021115\)41:22<4286::AID-ANIE4286>3.0.CO;2-M](https://doi.org/10.1002/1521-3773(20021115)41:22<4286::AID-ANIE4286>3.0.CO;2-M).
- (38) Pan, C.; Pelzer, K.; Philippot, K.; Chaudret, B.; Dassenoy, F.; Lecante, P.; Casanove, M. J. Ligand-Stabilized Ruthenium Nanoparticles: Synthesis, Organization, and Dynamics. *J. Am. Chem. Soc.* **2001**, *123* (31), 7584–7593. <https://doi.org/10.1021/ja003961m>.
- (39) Kovalenko, M. V.; Talapin, D. V.; Loi, M. A.; Cordella, F.; Hesser, G.; Bodnarchuk, M. I.; Heiss, W. Quasi-Seeded Growth of Ligand-Tailored PbSe Nanocrystals through Cation-Exchange-Mediated Nucleation. *Angew. Chemie - Int. Ed.* **2008**, *47* (16), 3029–3033. <https://doi.org/10.1002/anie.200705604>.
- (40) Yarema, M.; Pichler, S.; Sytnyk, M.; Seyrkammer, R.; Lechner, R. T.; Fritz-Popovski, G.; Jarzab, D.; Szendrei, K.; Resel, R.; Korovyanko, O.; Loi, M. A.; Paris, O.; Hesser, G.; Heiss, W. Infrared Emitting and Photoconducting Colloidal Silver Chalcogenide Nanocrystal Quantum Dots from a Silylamide-Promoted Synthesis. *ACS Nano* **2011**, *5* (5), 3758–3765. <https://doi.org/10.1021/nn2001118>.
- (41) Kravchyk, K.; Protesescu, L.; Bodnarchuk, M. I.; Krumeich, F.; Yarema, M.; Walter, M.; Guntlin, C.; Kovalenko, M. V. Monodisperse and Inorganically Capped Sn and Sn/SnO₂ Nanocrystals for High-Performance Li-Ion Battery Anodes. *J. Am. Chem. Soc.* **2013**, *135* (11), 4199–4202. <https://doi.org/10.1021/ja312604r>.
- (42) He, M.; Protesescu, L.; Caputo, R.; Krumeich, F.; Kovalenko, M. V. A General Synthesis Strategy for Monodisperse Metallic and Metalloid Nanoparticles (In, Ga, Bi, Sb, Zn, Cu, Sn, and Their Alloys) via in Situ Formed Metal Long-Chain Amides. *Chem. Mater.* **2015**, *27* (2), 635–647. <https://doi.org/10.1021/cm5045144>.
- (43) Yarema, O.; Bozyigit, D.; Rousseau, I.; Nowack, L.; Yarema, M.; Heiss, W.; Wood, V. Highly Luminescent, Size- and Shape-Tunable Copper Indium Selenide Based Colloidal Nanocrystals. *Chem. Mater.* **2013**, *25* (18), 3753–3757. <https://doi.org/10.1021/cm402306q>.
- (44) Zhong, H.; Wang, Z.; Bovero, E.; Lu, Z.; Van Veggel, F. C. J. M.; Scholes, G. D. Colloidal CuInSe₂ nanocrystals in the Quantum Confinement Regime: Synthesis, Optical Properties, and Electroluminescence. *J. Phys. Chem. C* **2011**, *115* (25), 12396–12402. <https://doi.org/10.1021/jp204249j>.
- (45) Yarema, O.; Yarema, M.; Bozyigit, D.; Lin, W. M. M.; Wood, V. Independent Composition and Size Control for Highly Luminescent Indium-Rich Silver Indium Selenide Nanocrystals. *ACS Nano* **2015**, *9* (11), 11134–11142. <https://doi.org/10.1021/acs.nano.5b04636>.
- (46) Yarema, O.; Yarema, M.; Lin, W. M. M.; Wood, V. Cu–In–Te and Ag–In–Te Colloidal Nanocrystals with Tunable Composition and Size. *Chem. Commun.* **2016**, *52* (72), 10878–10881. <https://doi.org/10.1039/C6CC05571K>.
- (47) Fredrick, S. J.; Prieto, A. L. Solution Synthesis and Reactivity of Colloidal Fe₂GeS₄: A Potential Candidate for Earth Abundant, Nanostructured Photovoltaics. *J. Am. Chem. Soc.* **2013**, *135* (49), 18256–18259. <https://doi.org/10.1021/ja408333y>.
- (48) Miller, R. C.; Neilson, J. R.; Prieto, A. L. Amide-Assisted Synthesis of Iron Germanium Sulfide (Fe₂GeS₄) Nanostars: The Effect of LiN(SiMe₃)₂ on Precursor Reactivity for Favoring Nanoparticle Nucleation or Growth. *J. Am. Chem. Soc.* **2020**, *142*, 42. <https://doi.org/10.1021/jacs.0c00260>.
- (49) Shoemaker, D. P.; Hu, Y.-J.; Chung, D. Y.; Halder, G. J.; Chupas, P. J.; Soderholm, L.; Mitchell, J. F.; Kanatzidis, M. G. In Situ Studies of a Platform for Metastable Inorganic Crystal Growth and Materials Discovery. *Proc. Natl. Acad. Sci.* **2014**, *111* (30), 10922–10927. <https://doi.org/10.1073/pnas.1406211111>.
- (50) Bhutani, A.; Schiller, J. A.; Zuo, J. L.; Eckstein, J. N.; Greene, L. H.; Chaudhuri, S.; Shoemaker, D. P. Combined Computational and in Situ Experimental Search for Phases in an Open Ternary System, Ba–Ru–S. *Chem. Mater.* **2017**, *29* (14), 5841–5849.

- <https://doi.org/10.1021/acs.chemmater.7b00809>.
- (51) Jiang, Z.; Ramanathan, A.; Shoemaker, D. P. In Situ Identification of Kinetic Factors That Expedite Inorganic Crystal Formation and Discovery. *J. Mater. Chem. C* **2017**, *5* (23), 5709–5717. <https://doi.org/10.1039/C6TC04931A>.
 - (52) Martinolich, A. J.; Kurzman, J. A.; Neilson, J. R. Circumventing Diffusion in Kinetically Controlled Solid-State Metathesis Reactions. *J. Am. Chem. Soc.* **2016**, *138* (34), 11031–11037. <https://doi.org/10.1021/jacs.6b06367>.
 - (53) Martinolich, A. J.; Neilson, J. R. Toward Reaction-by-Design: Achieving Kinetic Control of Solid State Chemistry with Metathesis. *Chem. Mater.* **2017**, *29* (2), 479–489. <https://doi.org/10.1021/acs.chemmater.6b04861>.
 - (54) Martinolich, A. J.; Kurzman, J. A.; Neilson, J. R. Polymorph Selectivity of Superconducting CuSe₂ Through Kinetic Control of Solid-State Metathesis. *J. Am. Chem. Soc.* **2015**, *137* (11), 3827–3833. <https://doi.org/10.1021/ja512520z>.
 - (55) Kwon, S. G.; Hyeon, T. Formation Mechanisms of Uniform Nanocrystals via Hot-Injection and Heat-up Methods. *Small* **2011**, *7* (19), 2685–2702. <https://doi.org/10.1002/smll.201002022>.
 - (56) van Embden, J.; Chesman, A. S. R.; Jasieniak, J. J. The Heat-Up Synthesis of Colloidal Nanocrystals. *Chem. Mater.* **2015**, *27* (7), 2246–2285. <https://doi.org/10.1021/cm5028964>.
 - (57) de Mello Donegá, C.; Liljeroth, P.; Vanmaekelbergh, D. Physicochemical Evaluation of the Hot-Injection Method, a Synthesis Route for Monodisperse Nanocrystals. *Small* **2005**, *1* (12), 1152–1162. <https://doi.org/10.1002/smll.200500239>.
 - (58) Ramasamy, K.; Sims, H.; Butler, W. H.; Gupta, A. Selective Nanocrystal Synthesis and Calculated Electronic Structure of All Four Phases of Copper–Antimony–Sulfide. *Chem. Mater.* **2014**, *26* (9), 2891–2899. <https://doi.org/10.1021/cm5005642>.
 - (59) Wang, J.; Liu, P.; Seaton, C. C.; Ryan, K. M. Complete Colloidal Synthesis of Cu₂SnSe₃ Nanocrystals with Crystal Phase and Shape Control. *J. Am. Chem. Soc.* **2014**, *136* (22), 7954–7960. <https://doi.org/10.1021/ja501591n>.
 - (60) Ahmadi, M.; Pramana, S. S.; Xi, L.; Boothroyd, C.; Lam, Y. M.; Mhaisalkar, S. Evolution Pathway of CIGSe Nanocrystals for Solar Cell Applications. *J. Phys. Chem. C* **2012**, *116* (14), 8202–8209. <https://doi.org/10.1021/jp300187r>.
 - (61) Hutflus, L. N.; Radovanovic, P. V. Controlling the Mechanism of Phase Transformation of Colloidal In₂O₃ nanocrystals. *J. Am. Chem. Soc.* **2015**, *137* (3), 1101–1108. <https://doi.org/10.1021/ja5094056>.
 - (62) Kar, M.; Agrawal, R.; Hillhouse, H. W. Formation Pathway of CuInSe₂ Nanocrystals for Solar Cells. *J. Am. Chem. Soc.* **2011**, *133* (43), 17239–17247. <https://doi.org/10.1021/ja204230d>.
 - (63) Agocs, D. B.; Prieto, A. L. Hot Injection Synthesis and Characterization of Copper Antimony Selenide Non-Canonical Nanomaterials Toward Earth-Abundant Renewable Energy Conversion, Colorado State University, 2018.
 - (64) White, M. A.; Baumler, K. J.; Chen, Y.; Venkatesh, A.; Medina-Gonzalez, A. M.; Rossini, A. J.; Zaikina, J. V.; Chan, E. M.; Vela, J. Expanding the I–II–V Phase Space: Soft Synthesis of Polytypic Ternary and Binary Zinc Antimonides. *Chem. Mater.* **2018**, *30* (17), 6173–6182. <https://doi.org/10.1021/acs.chemmater.8b02910>.
 - (65) Chan, E. M.; Xu, C.; Mao, A. W.; Han, G.; Owen, J. S.; Cohen, B. E.; Milliron, D. J. Reproducible, High-Throughput Synthesis of Colloidal Nanocrystals for Optimization in Multidimensional Parameter Space. *Nano Lett.* **2010**, *10* (5), 1874–1885. <https://doi.org/10.1021/nl100669s>.
 - (66) Gary, D. C.; Glassy, B. A.; Cossairt, B. M. Investigation of Indium Phosphide Quantum Dot Nucleation and Growth Utilizing Triarylsilylphosphine Precursors. *Chem. Mater.* **2014**, *26* (4), 1734–1744. <https://doi.org/10.1021/cm500102q>.
 - (67) Gary, D. C.; Terban, M. W.; Billinge, S. J. L.; Cossairt, B. M. Two-Step Nucleation and Growth of InP Quantum Dots via Magic-Sized Cluster Intermediates. *Chem. Mater.* **2015**, *27* (4), 1432–1441. <https://doi.org/10.1021/acs.chemmater.5b00286>.

- (68) Lee, J. M.; Miller, R. C.; Moloney, L. J.; Prieto, A. L. The Development of Strategies for Nanoparticle Synthesis: Considerations for Deepening Understanding of Inherently Complex Systems. *J. Solid State Chem.* **2019**, *273*, 243–286. <https://doi.org/10.1016/J.JSSC.2018.12.053>.

CHAPTER 2

EXPLORING THE SOLUTION-BASED METATHESIS PATHWAY TOWARD Cu_3Si FORMATION²

2.1 Overview

Copper silicide, Cu_3Si , has a wide range of applications including catalysis, photovoltaics, and energy storage. The complexity of the Cu-Si phase diagram makes synthesizing one phase with control over stoichiometry and high purity challenging. The specific Cu_3Si phase described herein is more typically made using traditional solid-state methods. We demonstrate $\text{Cu}_3\text{Si}@$ Si matrix particles can be successfully synthesized by combining colloidal solution and metathesis methods. The reaction pathway is surprisingly complex and nuanced. The reaction between Mg_2Si and CuCl_2 in OLA was investigated by PXRD, TEM, SEM, and EDS to elucidate the reaction pathway. It was found that rather than the reaction proceeding directly to $\text{Cu}_3\text{Si}@$ Si matrix particles, it proceeds through a two-step process. In the first step, Mg_2Si quickly reduces the Cu-OLA complex fully to Cu^0 , resulting in MgCl_2 and destabilized, amorphous Si matrixes that are capped with OLA. Next, OLA aids in shuttling Cu to the Si matrix and Cu diffuses into the destabilized, amorphous structure to form Cu_3Si particles embedded in a Si matrix. We show that the solvent is critical for controlling this reaction. Finally, the matrix encasing the Cu_3Si particles was selectively analyzed by STEM/EDS, electrochemical cycling, and XPS. This revealed that the matrix contains active Si with minimal amounts of Mg, and the matrix readily oxidizes. This unique synthesis of $\text{Cu}_3\text{Si}@$ Si matrix particles, although still diffusion-limited, combines colloidal solution and metathesis methods to lower the high formation energy barrier commonly observed in solid-state methods.

2.2 Introduction

Transition metal silicides have been a topic of interest for many years as they have a broad range of applications in areas such as catalysis, electronics, photovoltaics, and thermoelectrics.¹⁻³ Specifically, copper silicides (Cu-Si) have long been investigated due to the prominence of Si and Cu in electronics.⁴

²This chapter is a manuscript prepared for submission to Chemistry of Materials with Lily J. Moloney, Leslie A. Kraynak, Jeffery Ma, and Amy L. Prieto. Majority of the data and writing was completed by Lily J. Moloney with guidance from Amy L. Prieto. Leslie A. Kraynak contributed the XPS fitting and Jeffery Ma aided with the cycling data.

Additionally, Cu-Si has applications as a catalyst for the formation of chlorosilanes⁵⁻⁸ and more recently, in Li-ion batteries⁹⁻¹¹, field emitters, and anti-reflective layers¹²⁻¹⁴.

Similar to most silicide phase diagrams, the Cu-Si diagram is complex and has many possible phases.¹⁵ Narrowing in on just the room-temperature, stable phases, there are three different possible compositions within an eight atomic percent range, Cu_3Si (η''), $\text{Cu}_{15}\text{Si}_4$ (ϵ), and Cu_5Si (γ).¹⁶ Between these room-temperature phases, Cu_3Si is the most regularly formed and studied for the previously listed applications.^{3,17} However, the small atomic percentage range between Cu-Si phases causes difficulty in synthesizing Cu_3Si without the formation of other phases. Therefore, the synthesis of Cu_3Si continues to be an area of interest.

Common methods to synthesize and study the solid state reaction to form Cu_3Si include thin film¹⁸⁻²¹, ball-milling with subsequent heat treatment^{22,23} and CVD techniques^{17,24-27}. Some studies have shown that at lower temperatures (100-200 °C) either Cu_3Si precipitates or thin layers can form due to the fast diffusibility of Cu in Si ($2.8 \times 10^{-7} \text{ cm}^2/\text{s}$).^{4,28} However, syntheses attempting to produce a substantial amount of Cu_3Si throughout a sample, or Cu_3Si nanoparticles often require high temperatures, highly reactive precursors, and/or pressure control.

Within the solid-state community, metathesis has gained interest as a tool to combat harsh conditions and/or access kinetic pathways.^{29,30} Additionally, these have long been advantages of solution-based techniques, along with better tunability and control over particle size and shape.^{31,32} For Cu_3Si production, both methods have been investigated but are overall still underdeveloped.

The metathesis reaction between CuCl and Si has been studied since the 1940's as it generates small amounts of Cu_3Si that can catalyze the formation of chlorosilanes.^{3,7,33} Additionally, metathesis reaction methods have been used to successfully synthesize Cu_3Si nanoparticles or significant amounts of Cu_3Si throughout a sample, but these reactions are still limited.^{9,10} This is due to metathesis-based reactions for transition metal silicides, such as Cu_3Si , historically having synthetic difficulties including high initiation temperatures, balancing reaction mechanisms based on the precursors available, and achieving phase control.^{29,34}

Furthermore, to the authors knowledge, only two solution-phase syntheses for Cu_3Si formation have been reported. The Tuan group successfully grew Cu_3Si wires off a copper film with the injection of monophenyl silane into a pressurized (5.5 MPa) and heated (420-475 °C) flow reactor system.^{12,13} Using more traditional solution-based methods, the Schaak group was able to synthesize Cu_3Si as well as Pd_2Si and Ni_2Si , where metal nanoparticles were reacted with monophenyl silane via an injection reaction at 375 °C.³⁵ These two reports established the use of solution-based techniques for Cu_3Si formation, yet general solution-based methods are expansive, and there is still much to be explored for Cu_3Si production. Thus, there is an opportunity to apply known synthetic strategies to this underdeveloped Cu_3Si system, which will lead to an expanded toolkit for further experimental design.³⁶

For instance, the combination of metathesis and solution-based techniques for the synthesis of Cu_3Si could be a way to take advantage of the benefits of both synthesis methods. Solution-based metathesis reactions can use relatively mild precursors and conditions to produce a desired nanoparticle phase plus a thermodynamically favorable alkali metal salt. Additionally, the combination of techniques could give increased control over diffusion rates and growth, and allow for easy post synthesis modification, such as washing away by-products. These advantages have been demonstrated by several reports^{37,38}, but specific to this work, Bley and Kauzlarich reported one of the first solution-based Si nanoparticle syntheses. The authors refluxed the Zintl phase, KSi , and SiCl_4 in glyme (85 °C), diglyme (162 °C), or THF (66 °C) to form the Si nanoparticles.³⁹ As silicon precursors compatible with solution methods are limited, the use of a Zintl phase as a silicon precursor led to the continued development of Zintl phases for solution-based metathesis syntheses of Si nanoclusters/nanoparticles.⁴⁰⁻⁴³

Here we describe a solution-based metathesis reaction between the Zintl phase, Mg_2Si , and CuCl_2 in oleylamine (OLA) to form Cu_3Si particles embedded in a Si matrix. This reaction uses relatively safe precursors and mild reaction conditions, 275 °C reacted overnight (ON). The synthesis is further investigated to understand the reaction pathway and role of the solution within this pathway. The

investigation of this synthesis widens the synthetic toolkit for not only the synthesis of Cu_3Si , but also for solution-based metathesis reactions.

2.3 Experimental Section

Materials. The following reagents were used as bought: anhydrous copper(II) chloride (CuCl_2 , 97%, Riedel-deHaen), magnesium silicide (Mg_2Si , 99.5%, Alfa Aesar), ethylene glycol dimethyl ether (Glyme, 99.5%, anhydrous, sure sealed, Sigma Aldrich), diethylene glycol dimethyl ether (Diglyme, 99%, Fisher Scientific), and reagent grade ethanol, hexanes(mixture of isomers), toluene, and chloroform (all from Fisher Scientific). Squalane (99%, Sigma-Adrich), 1-octadecene (ODE, 90% Technical grade, Sigma Aldrich), and oleylamine (OLA, 70% Technical grade, Sigma Aldrich) were sparged with N_2 for 2 hr; oleylamine was heated at 70 °C during sparging. All reactions were prepared under inert N_2 atmosphere and using standard Schlenk line protocol unless specified otherwise.

Optimized Synthesis of $\text{Cu}_3\text{Si}@$ Si matrix. Reaction conditions were varied including reaction time, ratio of precursors, reaction solvent, and/or reaction temperature (Table S2.1). Presented here is the optimized synthesis which represents the general procedure for all variations. In a 50 mL three-neck round bottom flask, CuCl_2 (1.20 mmol, 162 mg) and Mg_2Si (0.65 mmol, 50 mg) were weighed out. A glass casing that protects the thermocouple was punctured through a rubber septum. This rubber septum was fit to the reaction flask along with a reflux condenser and a glass stir bar. All other open sites were sealed with a rubber septum. OLA (10 mL) was added to the reaction flask, resulting in a bright blue solution with Mg_2Si powder at the bottom. The reaction flask was moved to a Schlenk line and set to stir at a high stir rate (6-7 on a Thermolyne nuova II stir plate). The solution was pump/purged three times and then allowed to degas under vacuum for 45 min at 100 °C, leading to a deep turquoise colored solution. Following degassing, the system was placed under N_2 and heated to 275 °C at a ramp rate of 800 °C/hr. The reaction solution changed from deep turquoise to yellow with “black-looking” solid swirling around at ~165 °C, and then to bright red at ~235 °C (Figure S2.1). Once the reaction reached temperature, it was allowed to react overnight (ON, 17-18 hr), where the solution turned from bright red to a dull red/brown to a black solution with Cu pellets

at the bottom. A gas-tight glass syringe was used to rapidly quench the reaction into toluene (~10 mL), while leaving the Cu pellets at the bottom of the flask.

Particle Washing Procedure. The toluene quenched reaction solution was split into four 15 mL centrifuge tubes, ethanol was added to reach a total volume of 12-15 mL, and the mixture was shaken. Centrifugation at 5800 rpm for 4-5 min separated the particles from a translucent yellow supernatant, which was discarded. An additional toluene (1-2 mL) and ethanol (8-9 mL) wash was done. After centrifuging at 5800 rpm for 4-5 min the clear supernatant was discarded, and a final chloroform (1-2 mL) and ethanol (8-9 mL) wash was performed. The resultant supernatant from the final centrifugation was discarded and the final particles were either suspended in hexanes for characterization or further washed to remove any remnant Cu (see Removal of Excess Cu via Acid Wash). When air-free particle washing was required, dissolved gases in washing solvents were minimized using sparging or freeze-pump-thaw techniques before bringing the solvents into a N₂ glovebox.

Cu Pellets Washing Procedure. The Cu pellets remaining at the bottom of the flask were rinsed with hexanes three times, decanting the solution off between each wash.

Scaled-up Procedure. The same procedure outline for the optimal synthesis was followed except the amount of CuCl₂, Mg₂Si and OLA were all doubled.

Removal of excess Cu via Acid Wash. An additional acid wash was occasionally done to remove any excess Cu and unreacted Mg₂Si. After the general washing procedure, the particles were transferred into a scintillation vial and centrifuged to discard the transfer solution, hexanes. The vial was sealed with a rubber septum before the addition of 3 M nitric acid solution (2 mL). *Caution: NO₂ and minimal amounts of silane gas could form from the dissolution of Cu and Mg₂Si, respectively.* The solution was sonicated for 5-6 min before an excess of DI water (~10 mL) was injected and the headspace of the vial was purged through a water bubbler. Centrifugation for 3 min separated the particles and the supernatant was discarded. The particles were rinsed, centrifuged, and the supernatant discarded two more times, first with DI water and then ethanol. Afterwards, although the particles didn't suspend well likely due to ligand stripping, the

particles were stored in hexanes. If the initial acid wash did not completely remove the excess Cu, the washing steps were either repeated as is or with a slightly more concentrated nitric acid solution (5 M) depending on the amount of Cu still present.

2.4 Characterization

Powder X-Ray Diffraction (PXRD). A concentrated particle suspension in hexanes was dropcast onto a zero-diffraction silicon XRD plate. Analysis was performed on a Cu K α radiation source ($\lambda=1.54 \text{ \AA}$) and a Lynxeye XE-T positron-sensitive detector. PXRD reference patterns used include η'' -Cu₃Si PDF Card 00-059-0263, Si PDF Card 04-001-7247, Cu PDF Card 00-004-0836, Mg_{1.98}Si PDF Card 01-083-5238, and MgCl₂ PDF Card 04-008-7748. It is important to note that the quality marking of the η'' -Cu₃Si pattern is low, albeit there is no high quality pattern available, indicating further the challenge of the Cu₃Si syntheses within the literature.

Transmission Electron Microscopy (TEM). Samples were prepared by making a dilute particle suspension in hexanes and sonicating for 5 min. A carbon-coated, Ni 100 mesh TEM grid was dipped into the solution 2-3 times, allowing the grid to quickly dry between coats. The samples were imaged using a JEOL JEM2100F at a working voltage of 200 keV. Images were collected and analyzed in Digital Micrograph of the Gatan Microscopy Suite software. Scanning transmission electron microscopy (STEM) energy dispersive X-Ray spectroscopy (EDS) was carried out with an Oxford X-Max 80 mm² detector and analyzed using Aztec TEM software.

Scanning Electron Microscopy (SEM). The washed Cu pellets were placed onto double-sided carbon tape that had been placed on an aluminum stub. Analysis was done using a JEOL JSM-6500F microscope equipped with an Oxford 80 X-MAX (80 mm) SDD energy-dispersive X-ray spectroscopy (EDS) detector.

X-Ray Photoelectron Spectroscopy (XPS). Particles were washed air-free in a N₂ glovebox. Afterwards half of the particle solution was removed, and an additional acid wash was done. Then, a concentrated particle suspension in hexanes of both solutions (as-synthesized and acid washed) was dropcast onto a homemade air-free XPS holder.⁴⁴ The holder was sealed by placing the box antechamber under vacuum

before transferring the holder to the instrument where the sample was pumped down overnight. Using a Physical Electronics (PHI) 5800 series Multi-Technique ESCA system with a monochromatic Al K α ($h\nu = 1486.6$ eV) source operating at 350.0 W, high resolution (HRES) spectra of Si 2p, Cu 2p, Mg 2p, Cl 2p, O 1s, N 1s, and C 1s regions were collected. An electron flood gun neutralizer was used during data collection to help with differential charging. Charge correction for the XPS spectra was performed by setting the C 1s peak assigned to adventitious/aliphatic carbon to 285 eV. The spectra were fitted using CasaXPS software (version 2.3.17PR1.1) with a nonlinear Shirley background and 30% Lorentzian/70% Gaussian lineshape, and PHI relative sensitivity factors corrected for angular distribution were used for quantification based on the peak fitting models to obtain atomic percentages.

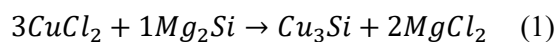
Electrochemical Cycling. Several scaled-up reactions were completed to produce a composite electrode for electrochemical testing of the synthesized particles. To prevent excessive oxidation, the particles from each reaction were washed and stored in a N₂ glovebox. Once an adequate amount of sample was synthesized, the particles were transferred to a Ar glovebox. To make a slurry, consisting of ~67% active material, the synthesized particles were thoroughly mixed with TuBall BATT (0.4% SWCNT/NMP, 2% PVDF Solef 5130 Stabilizer, and OCSiAl mixture) and then casted on Cu foil. It is important to note that the percent active material is a rough estimate as the Cu remaining in the synthesized sample was not washed away and ligands are present. This did not impede observing the lithiation/delithiation events and therefore was not a concern. A coin Li half-cell was assembled with the prepared electrode film, a glass filter separator (Whatman), a 1M LiPF₆ in ethylene carbonate:diethyl carbonate (EC:DEC, 3:7 ratio, BASF, Selectilyte) with 5% by volume fluoroethylene carbonate (FEC, Sigma Aldrich) electrolyte solution, and Li metal. The cell was cycled between 0.1 V-1.5 V vs. Li/Li⁺ at a rate of 500 mA/g on an Arbin battery tester (LBT20084).

2.5 Results and Discussion

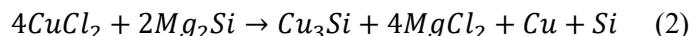
2.5.1 Material Synthesis Overview: Development and Optimization of Cu₃Si@Si matrix Particles. A unique reaction combining solution-based and metathesis techniques was developed for Cu₃Si. The design

and optimization of this synthesis required several considerations, including solvent and precursor identity, solvent/precursor interactions, reaction temperature, and precursor/precursor interactions. The precursors' identity was kept consistent throughout the investigation to observe the interaction between the precursors in different solution and temperature conditions.

Taking inspiration from the solution-based metathesis Si nanoparticle literature⁴⁵, we used the Zintl phase Mg_2Si as our Si precursor. This is a relatively safe precursor and has been successfully employed in solution-based metathesis reactions. In order to form a thermodynamically favorable salt byproduct, a copper salt precursor was required. We chose $CuCl_2$ as it is a common Cu-based nanoparticle precursor and could lead to $MgCl_2$ formation ($E_{\text{formation}} = -2.265 \text{ eV}$)^{46,47}. By solely considering these precursors and the metathesis reaction that would occur, a reaction could be written as:



Although equation (1) is stoichiometrically balanced in terms of the atoms present, the redox reaction is not balanced. The number of electrons available are inadequate to reduce Cu^{2+} to Cu^0 in Cu_3Si . Therefore, a modified reaction can be written as:



As shown in equation (2), excess Cu and Si are required to completely balance the reaction. However, in solution-based reactions, writing balanced reactions are often nontrivial, as the role of the solvent and active monomers may evolve from the initial precursors and the synthesis may occur through a multi-step process. To achieve a detailed understanding of the Cu_3Si solution-based metathesis synthesis, an investigation of the processes occurring in this system was necessary.

In this specific section, we will discuss general observations and considerations about the synthesis system illuminated during initial reaction attempts, synthesis optimization, and analysis of the final product. Rationale from the solvent study and pathway study sections may be interjected to make comprehensive, accurate statements. Further detail and explanation will be described in the sections following, where this section is meant to be a general overview.

During initial reaction attempts in oleylamine (OLA), the optimization of the reaction was nearly impossible because reproducible results were not being achieved. Two factors within the system were found to be the reason for this initial irreproducibility. First, the Mg_2Si precursor initially used was bought in high purity (99.99%) pellets and then quickly ball milled down to smaller grains. However, grain size was not actively controlled, and since Mg_2Si does not dissolve in OLA, but rather disperses, it was hypothesized that ball milling produced various Mg_2Si grain sizes causing irreproducible results. To eliminate this concern slightly less pure (99.5%) powdered Mg_2Si was bought. Second, Cu was observed plating onto

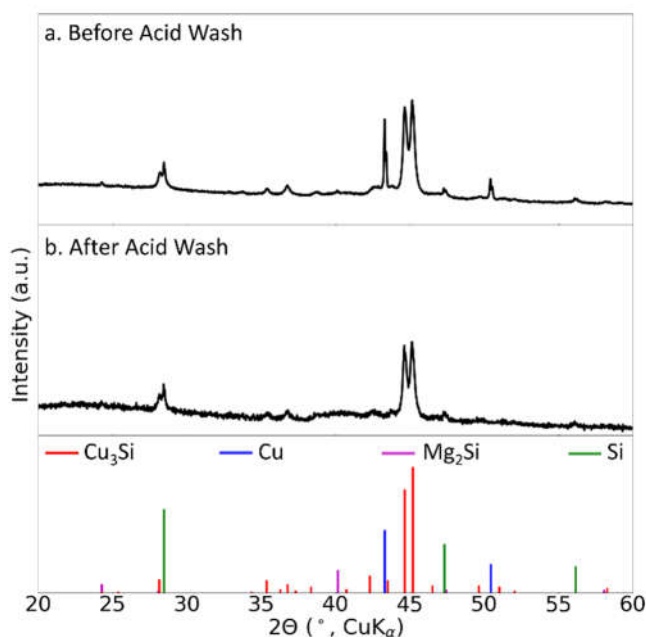


Figure 2.1. PXRD patterns of the as-synthesized particles produced under optimal reaction conditions a. before an acid wash and b. the particles remaining after the removal of excess Cu and unreacted Mg_2Si via acid washing.

the thermocouple in solution, which would cause differing Cu concentration in the reaction solution. This was remedied by placing a glass casing around the thermocouple to prevent plating. These alterations led to reproducible results, and thus the reaction could be optimized for Cu_3Si formation. Precursor ratio, time, and temperature were all manipulated to achieve the consumption of Mg_2Si , while avoiding Cu_5Si formation, Figure S2.2. The Cu-Si phase diagram illustrates that within a small range, 8%, of Cu content, three different Cu-Si stoichiometries are accessible, Cu_3Si , $\text{Cu}_{15}\text{Si}_4$, and Cu_5Si .¹⁶ Therefore, accessing Cu_3Si without forming other Cu-Si binaries has been problematic.^{16,48} Generally, we observed that increasing the

time or temperature of the reaction aided in Cu_3Si formation. However, at the commonly used 2:1 Cu:Si precursor ratio, it was difficult to get a significant amount of Cu_3Si without also observing the formation of Cu_5Si . Therefore, lower $\text{CuCl}_2\text{:Mg}_2\text{Si}$ ratios were tested, including 1.5:1, 1.75:1, and 1.85:1. It was found that a significant amount of Mg_2Si was left unreacted for the 1.5:1 and 1.75:1 reaction, but not the 1.85:1 reaction.

Therefore, optimal conditions for the synthesis of Cu_3Si were found to be $\text{CuCl}_2\text{:Mg}_2\text{Si}$ in a 1.85:1 ratio reacted in OLA at 275 °C overnight (ON, 17-18 hr). As shown in Figure 2.1a, PXRD shows Cu_3Si is formed along with Cu and Si. It should be noted that although the reaction was optimized for Cu_3Si formation, nominal amounts of unreacted Mg_2Si was observed and on rare occasion Cu_5Si was observed. We attribute these occasional impurities to Cu diffusion being slightly uncontrollable, which will be further discussed in the pathway section. The Cu and any small Mg_2Si remaining could be removed using a nitric acid wash, Figure 2.1b, where special care was taken when this was necessary since this could form NO_2 gas and small amounts of silane gas. Despite the ability to remove these impurities, an acid wash was rarely utilized because the goal of this study was to gain a comprehensive understanding of the synthesis. Herein, unless otherwise noted, all samples were characterized without the extra acid wash.

TEM imaging of the product showed particles of varying size and shape are produced within a large matrix, Figure 2.2a. The composition of the particles and matrix were analyzed using STEM EDS. A line scan across several particles, Figure 2.2b and c, elucidated that the particles are rich in Cu, there is negligible amounts of Cu within the matrix, and Si is present over the entire line scan. Additionally, counts of Mg, O, and Cl are present across the scan, suggesting that the Cu_3Si particles are encased in a Si matrix, which oxidized easily, and contains small amounts of Mg and Cl.

The encasement of the particles caused difficulty in exclusively analyzing the Cu/Si ratio of the Cu_3Si particles and thus, the ratio uniformity between the particles. The Si counts vary across the line scan, but there is overall no clear pattern between the Si counts and the particles. In this line scan, one exception is

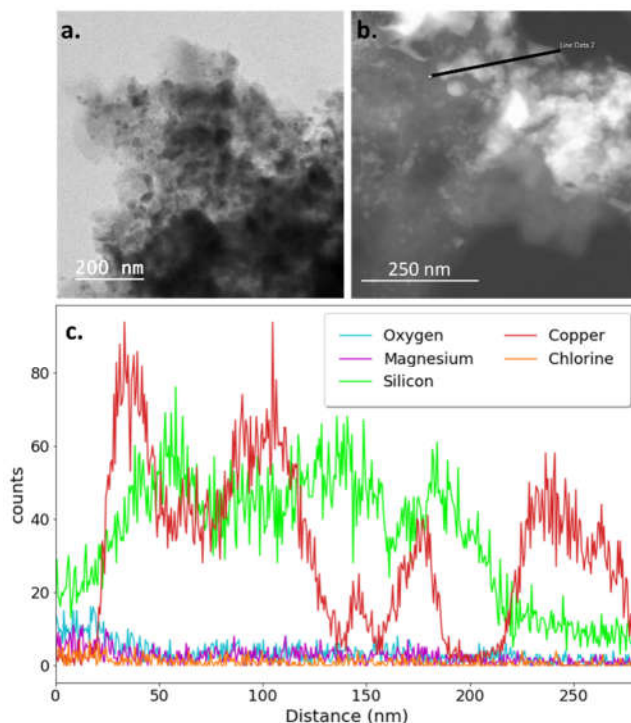


Figure 2.2. The resulting particles from the optimal synthesis conditions (1.85:1 $\text{CuCl}_2:\text{Mg}_2\text{Si}$ reacted in OLA at 275°C , ON) were imaged by a. TEM and b. STEM, with c. the associated EDS line scan. These shows the sample is composed of varying sized Cu_3Si particles encased in a Si matrix ($\text{Cu}_3\text{Si}@\text{Si}$ matrix).

the last particle at the edge of the matrix, where there is a decrease of Si corresponding with the increase of Cu as it scans across the particle. This could suggest that the particle has a higher Cu/Si ratio, yet the overall randomness of the Si counts across the scan suggest it is instead likely due to the matrix thickness varying. While it is difficult to discern the Cu/Si ratio on a small scale, PXRD confirms that the majority of particles have a 3:1 Cu/Si ratio (Figure 2.1) and TEM validates that the particles within the matrix are Cu-rich and illuminated the presence of the Si matrix. To investigate and understand the formation of these $\text{Cu}_3\text{Si}@\text{Si}$ matrix particles through this unique solution-based metathesis method, solution and pathway studies were performed.

2.5.2 Examining the Effect of the Solvent Employed. OLA is a commonly used solvent for solution-based nanoparticle synthesis as it has a high boiling point, acts as a ligand, and has reducing power.⁴⁹ In this study it was found that the use of OLA aided in the production of Cu₃Si. To understand the role of OLA, information was gathered by both studying each individual precursor in OLA as well as investigating the effect of different solvents on the reaction.

As the reaction between CuCl₂ and Mg₂Si in OLA proceeded, several color changes were realized to correlate to the reduction of Cu. The reaction solutions starts as a deep blue solution due to the copper(II) chloride dissolving in solution. After the reaction is degassed at 100 °C the solution is a turquoise color, likely the result of partial reduction to Cu¹⁺. Next, as the reaction heats to 275 °C, the solution turns yellow as all the Cu²⁺ is reduced to Cu¹⁺, and then around 235 °C the solution turns bright red, indicative of Cu⁰ formation. Finally, the solution turns black overnight as Cu₃Si forms. As stated previously, OLA does have reducing ability and therefore could be contributing to this Cu reduction. To investigate solely the OLA role in the reduction of the copper precursor, just CuCl₂ was heated in OLA. Similar color changes were observed, except the final reduction of Cu¹⁺ (yellow) to Cu⁰ (bright red). Even after the solution dwelled at reaction temperature, 275 °C, for 4 hr, the bright red color was absent. This suggests that OLA is not the sole reducing agent, but rather that Mg₂Si aids in the reduction of Cu. The Mg₂Si precursor does have reducing abilities, as it is a Zintl salt with Si as the anionic component, (Mg²⁺)₂Si⁴⁻, which is an unfavorable state for Si. Although Mg₂Si does not dissolve in OLA, similar to Mg₂Si in other solvent systems^{41,50}, the visible presence of Mg₂Si solid vanishes when Cu¹⁺ reduces to Cu⁰. We hypothesize that Mg₂Si assists to quickly reduce copper resulting in either 1) a destabilized Mg-Si species with Cl⁻ in solution or 2) MgCl₂ and some Si species. As the production of MgCl₂ is extremely favorable, it is presumed that the latter is occurring.

Investigating Various Solvents. To delve deeper into elucidating the role of the solvent in this solution-based metathesis reaction of $\text{Cu}_3\text{Si}@\text{Si}$ matrix, other solvents were explored (Figure 2.3). Although these studies led to “failed” reactions, where little to no Cu_3Si formed, they were important for understanding this synthetic system. Drawing inspiration from the solution-based metathesis Ge and Si nanoparticle

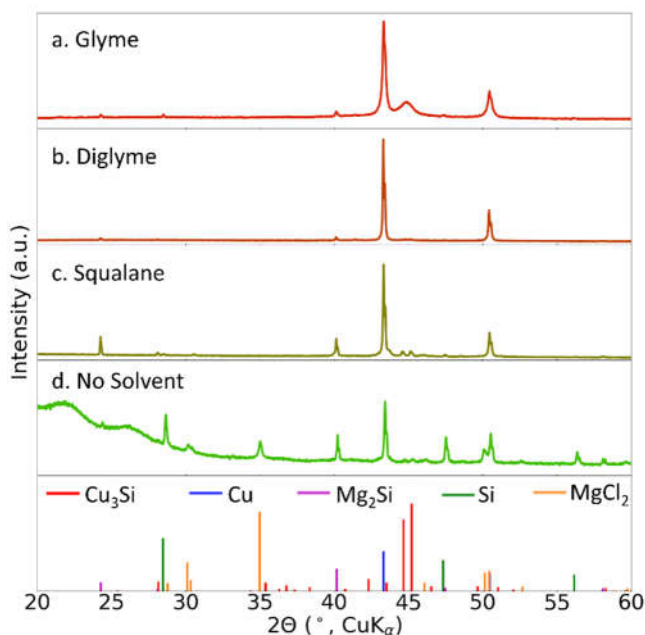


Figure 2.3. PXRD patterns of the metathesis reaction between Mg_2Si and CuCl_2 in coordinating solvents (a. glyme and b. diglyme), non-coordinating solvent (c. squalane), and neat (d. no solvent) illuminated the importance of the coordination strength of the solvent. These represent the extremes and indicate the balanced coordinating strength oleylamine provides in the optimized synthesis. The two amorphous peaks present at low 2θ , in pattern d, are from the use of Kapton tape.

literature^{39,41,42}, glyme was initially tested. Figure 2.3a, shows that Cu_3Si was formed when Mg_2Si and CuCl_2 were reacted at reflux ($82\text{ }^\circ\text{C}$) overnight (17-18 hr). The formation of Cu_3Si at this low temperature demonstrates the solvent’s importance in aiding Cu_3Si production. However, based on relative intensities, only a moderate amount of Cu_3Si was produced compared to the decent amount of crystalline Cu. Additionally, the two distinctive, high intensity peaks in the PXRD pattern of Cu_3Si , at 44.6 and $45.2\ 2\theta$, were instead represented as one very broad peak. This could be due to smaller Cu_3Si particles forming or the particles having amorphous character. As the reaction was performed at a low temperature ($82\text{ }^\circ\text{C}$), we hypothesize that the Cu_3Si particles formed likely are amorphous. This has been seen in other solution-

based metathesis reactions, where a high temperature post-synthesis anneal (500-800 °C) can be performed to crystallize the amorphous product.^{37,51} However, the Cu₃Si reaction in glyme also had a distinguishable amount of Mg₂Si leftover, and the purpose of a solution-based metathesis reaction was to avoid harsh conditions, such as an extreme high temperature post-synthesis anneal. Thus, to promote increased amounts of crystalline Cu₃Si, solvents allowing slightly greater reaction temperatures (100-300 °C) were tested.

The most obvious higher boiling point solvent, as a next step up from glyme, is diglyme with a boiling point of 162 °C. Surprisingly, reacting Mg₂Si and CuCl₂ in diglyme at reflux (170 °C) ON did not lead to improved Cu₃Si formation. Instead, PXRD shows minimal Cu₃Si formation with a large amount of Cu and a small fraction of unreacted Mg₂Si, Figure 2.3b. This “failed” reaction elucidated the importance of coordination strength of the solvent. Diglyme compared to glyme is a tridentate ligand rather than a bidentate ligand and previous reports have observed improved Mg₂Si dissolution in diglyme.^{41,52} Therefore, it was hypothesized that diglyme coordinates too strongly with copper and silicon species in solution preventing the interaction between Cu and the Si species.

To avoid this problem, non-coordinating solvents with high boiling points were tested, such as squalane and 1-ocadecene (ODE). When these solvents were applied to the reaction system, similar results were produced, and therefore only the exemplary results of squalane will be discussed (ODE result shown in Figure S2.3). The PXRD of Mg₂Si and CuCl₂ reacted ON at 275 °C in squalane, Figure 2.3c, shows significant amounts of unreacted Mg₂Si and Cu formation, with a minimal amount of Cu₃Si. In this case, the low production of Cu₃Si could be due to two aspects: the solvent’s inability to stabilize Si species remaining after Mg₂Si reduces CuCl₂, and/or its inability to aid in shuttling Cu to the Si species. In other words, the non-coordinating solvents are only acting as a diffusion medium, leading to low Cu₃Si production. To exaggerate this point further, the precursors in the optimal conditions were reacted without any solvent. Similar to the reactions done in non-coordinating solvents, unreacted Mg₂Si and an insignificant amount of Cu₃Si was observed by PXRD, Figure 2.3d. Since a washing procedure is not required for the solid-state synthesis, the formation of MgCl₂ could also be observed. This validates a

metathesis-type reaction is occurring and supports the hypothesis that Mg_2Si aids in fully reducing Cu, leading to MgCl_2 and a Si species. The collective solvent data demonstrates that this step is relatively fast, and the interaction between the Si and Cu species is slow.

Overall, from these “failed” solution studies, the role of OLA was further understood. The coordination strength of OLA is a compromise between the strongly coordinating diglyme and the non-coordinating solvents. We hypothesize that this allows OLA to promote the interaction between Cu and the Si species in two ways 1. by capping the Si species as it forms, further supported by N 1s and C 1s binding environments observed by XPS (Figure S2.15), and 2. by aiding in shuttling the Cu from the initially formed Cu particles to the surface of the Si species, discussed further in the pathway study.

Additionally, from these solution controls and “failed” syntheses studies, we can hypothesize that the metathesis reaction proceeds through a two-step reaction where Cu and some Si species form alongside the thermodynamically favorable salt, MgCl_2 . Then, the Cu and Si species react to form $\text{Cu}_3\text{Si} @\text{Si}$ matrix particles. These hypotheses were further evaluated through reaction pathway studies.

2.5.3 Pathway Study of $\text{Cu}_3\text{Si}@\text{Si}$ matrix: Confirming a Two-Step reaction. The formation pathway of Cu_3Si has not been investigated for solution-phase syntheses to date, though a number of pathway studies exist for solid-state systems.^{17,18,24,53–55} While the complexities of the Cu-Si phase diagram, the physical properties of Cu and Si (e.g diffusion constants and solubility of the elements within each other), and the synthetic method can cause slight discrepancies between solid-state systems, there are commonalities that remain.^{4,16,18} Often pitting or Kirkendall voids in the Cu source are observed due to the fast diffusion of Cu. The Cu diffusion energy barrier at the surface is found to be greater than the bulk. Finally, as Cu_3Si has a significantly larger lattice than Si, often imperfections within the Si lattice, such as Si vacancies, are sites where Cu_3Si forms. The elucidation of the solution-based metathesis Cu_3Si pathway will allow the system to be compared to previous nonsolution-based reactions. Therefore, this solution-based metathesis system will be understood in perspective of other studies. This ability to compare different synthetic systems is necessary to continue to build synthetic toolkits.

PXRD Pathway Analysis. The pathway was explored by fully quenching separate syntheses after proceeding for 1.5, 3, and 6 hr at 275 °C, and subsequently the samples were analyzed by PXRD, TEM, STEM/EDS and SEM. The resulting particles were washed and stored in a N₂ glovebox until characterization, albeit none of the characterization methods are completely air-free. Additionally, PXRD was done on aliquots taken while the reaction was ramping to temperature. One was taken at ~235 °C, when the solution first turns red, and the second, as soon as the reaction reached its final temperature. As stated in the solution study section, Mg₂Si promotes the reduction of Cu, becoming no longer visible by eye as the solution turns red. Agreeably, the PXRD of these early time aliquots show Mg₂Si quickly diminishes as Cu grows in (Figure S2.4). Other than nominal amounts of pristine Si, no new crystalline Si compound is observed at these early times, supporting that either an amorphous or solubilized Si species is formed. The PXRD patterns of the continued time quenched reactions (1.5, 3, 6 hr) as well as the final ON reaction are shown in Figure 2.4. Following the trend of the early aliquots, after only 1.5 hr at reaction temperature (Figure 2.4a), minimal Mg₂Si remains and an abundance of Cu is detected. Additionally, a small amount of Cu₃Si can already be observed. Generally, as the time increases, Cu₃Si peaks grow in as the always prevalent Cu peaks slowly diminish. At later times crystalline Si peaks have grown more distinguishable but are still relatively small.

One discrepancy in the growth of Cu_3Si can be seen between the 3 hr reaction and the 6 hr reaction (Figure 2.4b and 2.4c, respectively) where, based on intensities relative to the Cu peaks, the two major Cu_3Si peaks at 44.6 and 45.2 2θ are lower in the 6 hr reaction compared to the 3hr. One hypothesis for this discrepancy is Cu_3Si formation could require Cu diffusion, and despite the solution providing some control over this diffusion, it might not be consistent. Alternatively, excess Cu always remains in the reaction which temporally agglomerates into large pellets, but the amount of free Cu vs pelletized is inconsistent. Thus, this discrepancy could be due to the effectiveness of Cu agglomeration. Both propositions could be occurring to cause the discrepancy between the 3 hr and 6 hr time sample, and these could be a reason longer reaction times are beneficial. Overall, from the PXRD time studies, it was confirmed that Mg_2Si is quickly consumed during the reduction of Cu, forming a solvated or amorphous Si species. Then, the transformation to $\text{Cu}_3\text{Si}@\text{Si}$ matrix is slow suggesting this solution-based reaction still has a large energy barrier to overcome.

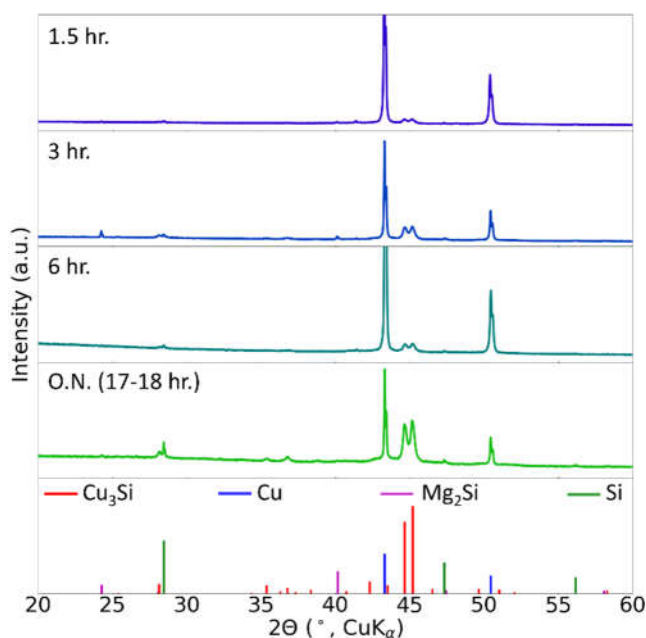


Figure 2.4. PXRD patterns of separate syntheses under optimal conditions fully quenched at 1.5 hr, 3 hr, 6 hr, and ON demonstrating the progression of the crystalline species during the synthesis of the $\text{Cu}_3\text{Si}@\text{Si}$ matrix particles. The patterns show the quick consumption of Mg_2Si and the slow increase of Cu_3Si as the Cu peak intensities decrease with extended reaction times.

TEM and STEM/EDS Pathway Analysis. To compliment the PXRD data and further inspect the formation pathway of the $\text{Cu}_3\text{Si}@\text{Si}$ matrix particles, the particles from each time sample (1.5 hr, 3 hr, 6 hr, and ON) were imaged by TEM and STEM/EDS, Figure 2.5. In all time samples, three morphologies were observed with their composition verified by STEM/EDS (Figure 2.5, row 2&3): 1. large matrixes, with no defined shape, edge, or lattice (Si matrix) 2. smaller particles within this matrix (Cu_3Si) and 3. well defined, often circular, particles (Cu). From TEM imaging (Figure 2.5, row 1), general trends for each morphology were

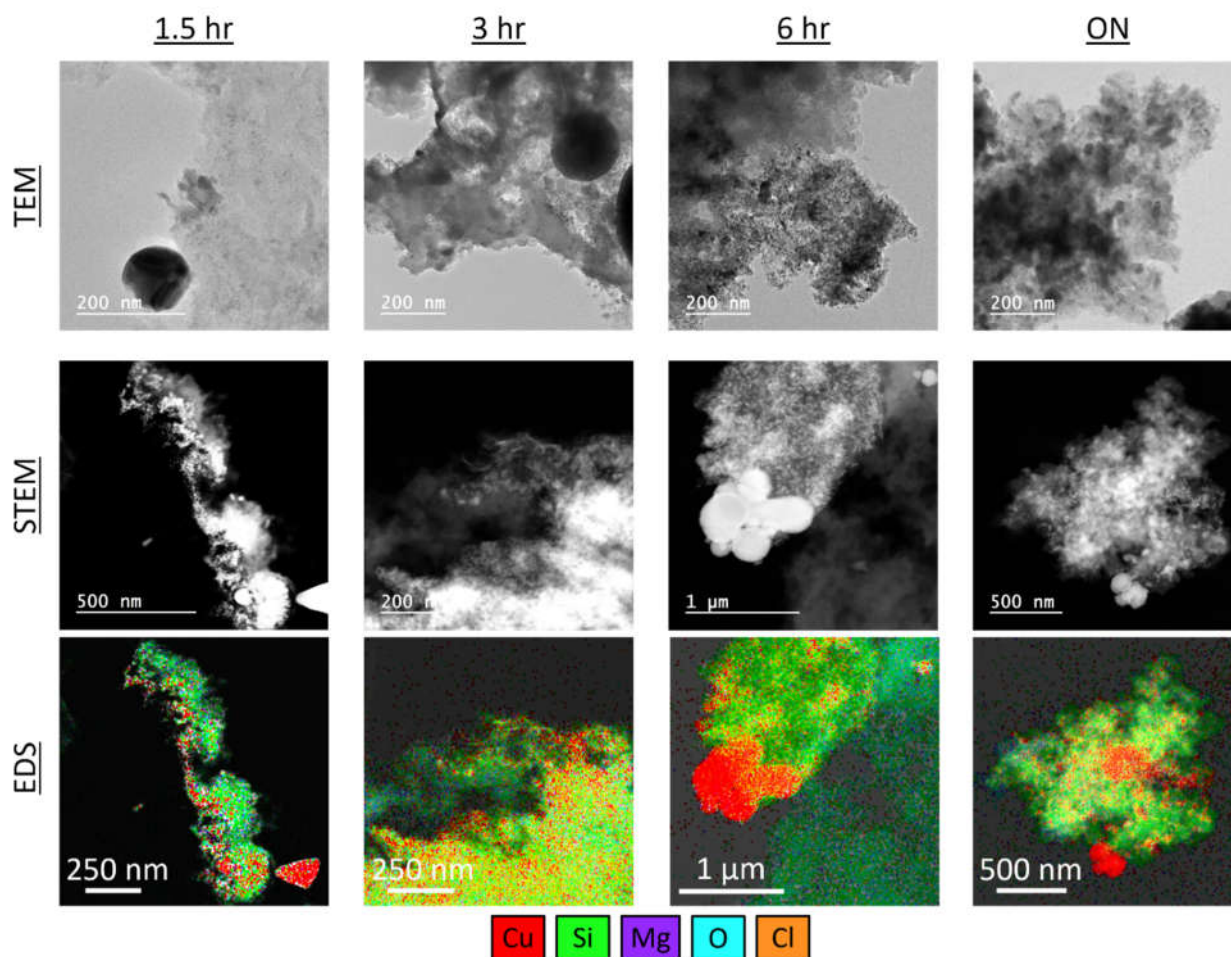


Figure 2.5. TEM (row 1), STEM (row 2), and EDS mapping (row 3) of separate syntheses under optimal conditions, fully quenched at 1.5 hr, 3 hr, 6 hr, and ON following the diffusion growth of Cu_3Si particles inside the Si matrix as the reaction progresses. found. At 1.5 hr, Si matrixes without Cu_3Si particles and Cu particles are in an abundance. Additionally, when Cu_3Si particles were detected, they were often small and consolidated (Figure 2.5, col 1). As the reaction time increases to 3 hr and 6 hr, more Cu_3Si particles are observed, while Cu particles and empty Si

matrixes start becoming less prominent (Figure 2.5, col 2&3). Finally, in the ON sample, most Si matrixes have Cu_3Si particles within them. The Cu_3Si particles have become larger and more densely packed, possibly agglomerated in areas (Figure 2.5, col 4). Lattice spacings at the edge of the Si matrix could also occasionally be detected, meaning pockets of crystalline Si are present.

The trends in TEM and STEM/EDS data corroborates the PXRD time study and new information can be deduced. The detection of the Si matrix at early times revealed that as Mg_2Si reacted with CuCl_2 to form MgCl_2 and Cu^0 , an amorphous Si matrix was left behind rather than a soluble Si species. The lattice parameter of Mg_2Si , 6.37 Å, is larger than Si, 5.43 Å, therefore, it makes sense that as Mg diffuses out, the Si matrix remaining is amorphous and possibly destabilized. Furthermore, the small, infrequent Cu_3Si particles progressing to a sample with more Cu_3Si particles densely packed within the Si matrix demonstrated that Cu diffusion is required for the formation of the Cu_3Si particles. However, as exemplified in previous solid-state Cu_3Si pathway studies, the destabilized, amorphous Si matrix likely lowers the nucleation energy barrier of Cu_3Si formation.

Several additional findings from STEM/EDS are important to note. As stated briefly in the Materials Synthesis Overview section, there is a small amount of Mg and Cl detected within the Si matrix. The atomic percent (at%) of the Mg and Cl show no clear pattern and stay relatively consistent for these temporal reactions (Figure S2.6-9 and Table S2.2), supporting that the Cu reduction by Mg_2Si to form destabilized, amorphous Si matrixes and MgCl_2 is mostly complete by 1.5 hr. The speed of this reaction likely causes small amounts of Mg and Cl to become trapped in the Si matrix. Alternatively, small amounts of MgCl_2 could persist on the surface of the matrix even after particle washing. These hypotheses were further tested and are discussed in the Characterization of the Matrix Section. Besides the presence of Mg and Cl, there is also consistently large amounts of oxygen present. It is known that Si will quickly oxidize in air and this process is further catalyzed in the presence of Cu_3Si , therefore the high at% of oxygen in these samples is unsurprising.^{14,56} Finally, in certain areas, the Cu particles seem to be caught in the Si matrix, for example see the 3 hr TEM and the 6 hr STEM/EDS images. From the Solvent Studies it was predicted that OLA

aided in shuttling the initially formed Cu to the Si species (Si matrix). Alternatively, the presences of these stuck Cu particles could indicate that as Cu reduces, particles become stuck in the Si matrix allowing for diffusion. However, the low frequency of these caught Cu particles would suggest both pathways are occurring. This will be further discussed in the following section. Overall, the XRD, TEM, and STEM/EDS analysis of the $\text{Cu}_3\text{Si}@\text{Si}$ matrix synthesis fully quenched at different times showed that the formation of Cu_3Si occurs in two steps: the quick formation of reduced Cu, Si matrix, and MgCl_2 , then the slow diffusion of Cu into the Si matrix.

SEM/EDS Analysis of the Cu Pellets. To further investigate the Cu diffusion, the Cu remaining at the bottom of the reaction flask, after each time reaction, was imaged by SEM/EDS. Fortunately, the excess Cu pelletizes with increased reaction time (Figure 2.6, insets) allowing for it to be easily separated from the

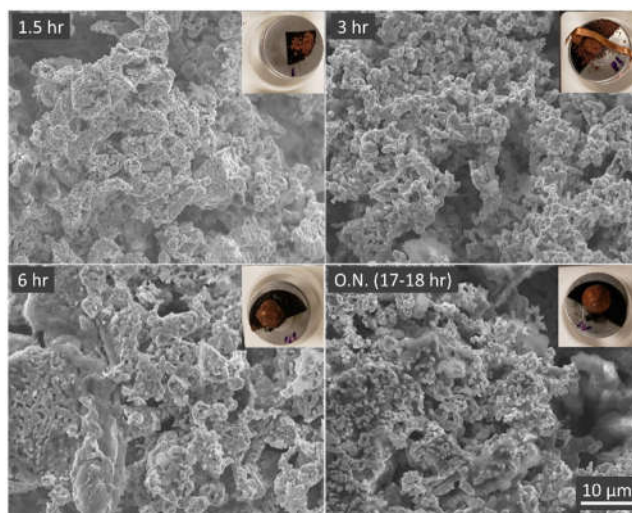


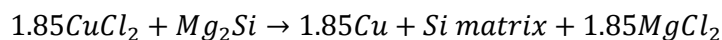
Figure 2.6. SEM images of the Cu pellet (insets) remaining in the flask after separate optimal reactions were quenched at 1.5 hr, 3 hr, 6 hr, and ON showing the pitted globular shaped samples, indicative of Cu out diffusion. The images also show the Cu samples becoming more agglomerated at longer reaction time.

rest of the reaction, washed with hexanes, and analyzed. A SEM image of each sample is shown in Figure 2.6, with the macroscopic image shown in the insets. Comparing the SEM images for each time reaction, there does not seem to be much variation between the samples. All have a globular-shaped morphology with pitted surfaces, which is indicative of Cu diffusion. One slight difference between the time samples is this globular shape is not as defined in the 1.5 hr sample, albeit still present, and as the reaction time

increases to 6 hr and ON, we can observe more dense, agglomerated areas. These signs of Cu diffusion from the Cu pellets further substantiates that OLA could aid in shuttling the Cu from these bulk Cu pellets to the Si matrix, which would further lower the energy barrier of Cu diffusion.

At lower magnification, particles with more angular edges could be seen scattered on the surface of the Cu pellets. Elemental analysis determined that these particles were just the reaction particles, Si matrixes transforming to Cu₃Si@Si matrix particles, that had not been fully rinsed away (Figure S2.10-11). Interestingly, since the pellets were only rinsed with hexanes and no ethanol, a correlation between Mg and Cl was detected, verifying MgCl₂ production during this reaction.

Summary of Pathway Studies. Investigating the progression of the solution-based metathesis reaction route to Cu₃Si@Si matrix particles illuminated the complexities of the reaction and provided perspective of this synthesis compared to the common solid-state Cu₃Si routes. From these studies, an updated two-step synthesis equation could be written:



Equation (3) only shows the solid components, not the solution, and is balanced to the best of our knowledge/ability, based on the data collected. It was found that Mg₂Si aids in the full reduction of Cu, and as Mg diffuses out to form MgCl₂ it leaves an amorphous, destabilized Si matrix behind. This process is fast and nearly complete after only 1.5 hr. It was found that small amounts of Mg and Cl are correlated with the Si matrix, where Mg and Cl could be combined within the matrix or MgCl₂ persisting on the surface. Moreover, imaging of the Cu pellets and the Cu₃Si@Si matrix particles demonstrated that Cu diffusion into the Si matrix is required for Cu₃Si production. Seldomly, small Cu particles were found to be caught in the Si matrix, presumably from the initial reduction step. Although an exact mechanism is not known, based on our current understanding, it is thought Cu diffusion from both the Cu pellets in solution and these attached particles is occurring. When comparing this reaction to common solid-state syntheses we see that both are limited by the diffusion process and subsequently, the nucleation of Cu₃Si. However, the initial

step of this reaction is unique, and the production of the amorphous, destabilized Si matrix could be one reason the overall energy barrier is lowered for this reaction.

2.5.4 Further Characterization of the Matrix. Although, TEM and STEM/EDS provided an initial examination of the Si matrix, complimentary characterization was needed for further understanding. The matrix composition, by EDS, was found to be majorly Si with smaller amounts of Mg and Cl as well as a relatively high oxygen content, due to rapid oxidation. To compliment the observations from STEM/EDS analysis, the $\text{Cu}_3\text{Si}@\text{Si}$ matrix particles were cycled against lithium and XPS was performed.

Silicon is a well-studied anode material for Li-ion batteries and Cu_3Si , albeit not Li active itself, has been reported to improve the electrical conductivity and reduce size expansion issues.⁹⁻¹¹ Thus, cycling our optimized $\text{Cu}_3\text{Si}@\text{Si}$ matrix particles against Li can probe the Si matrix specifically. It is important to note

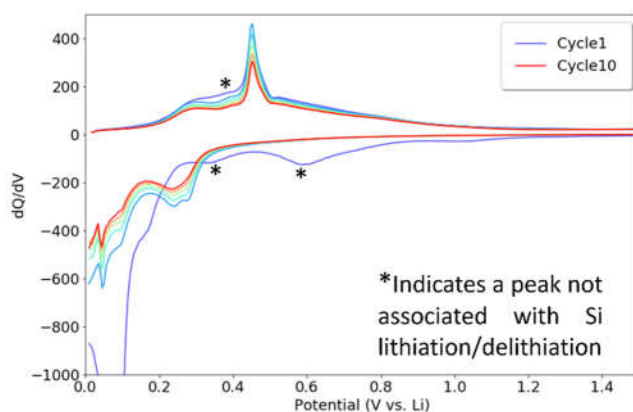


Figure 2.7. The dQ/dV plot of a prepared $\text{Cu}_3\text{Si}@\text{Si}$ matrix film cycled between 0.1V-1.5V at a rate of 500mA/g. The cycling data selectively investigated the Si matrix encasing the Cu_3Si particles and shows the electrochemical events match Si lithiation/delithiation events previously identified in literature, where only the peaks labeled with a * are not associated with Si lithiation/delithiation.

that it was not our goal to achieve optimal capacity or cycling performance. Rather, cycling was used as a tool to further characterize the matrix surrounding the Cu_3Si particles. A Li half-cell was assembled with the as synthesized particles and cycled between 0.1 V-1.5 V vs. Li/Li^+ at a rate of 500 mA/g. To easily observe the electrochemical events occurring during lithiation and delithiation, differential capacity (dQ/dV) was plotted for the 1st-10th cycle, Figure 2.7. The presence of well-defined lithiation/delithiation events indicates that unsurprisingly the matrix surrounding the particles is active to lithiation. Specifically, the lithiation/delithiation activity in the material matches with literature studies investigating Si or a

Cu₃Si/Si alloy as a Li-battery anode material.^{9-11,57} Based on these previous studies, careful assignment of the electrochemical events represented by each peak has been identified and are shown in the SI (Figure S2.12). Overall, the electrochemical events detected for the synthesized particles reinforces the STEM/EDS data, demonstrating the matrixes surrounding the Cu₃Si particles contain active Si.

To corroborate the findings from STEM/EDS and cycling against Li, the surface sensitive technique, XPS, was performed. Particles synthesized using optimal conditions were quenched and washed air-free, then half of the sample was removed from the glovebox and washed with nitric acid. For XPS analysis, the as synthesized as well as acid washed particles were drop-casted on a homemade air-free XPS holder.⁴⁴ The acid washed sample will be mainly discussed, as this insured no excess Cu or unreacted Mg₂Si was present, and therefore, specifically the matrix of the particles could be analyzed. The as-synthesized XPS results were consistent with the acid wash data and are discussed further in the SI (Figures S2.13-15).

The acid wash XPS results overall coincided with the STEM/EDS and electrochemical cycling observations, where Si (30 At%) and O (47.2 At%) were major components and Mg (1.7 At %), and Cu (0.6 At%) were present at lower percentages. The Cu binding environments located at high energies are more surface sensitive which could be contributing to the extremely low Cu content, and this also supports the morphology observed by TEM (Cu₃Si particles encased in a Si matrix). The high resolution (HRES) Cu 2p spectrum (Figure 2.8a) has bands at 933.7 and 953.6 eV, representing the Cu_{3/2} and Cu_{1/2} components, respectively. The peaks are relatively narrow and a good fit was achieved with one environment, Cu-Si.^{11,58} The HRES spectrum of Si 2p (Figure 2.8b) consists significantly of Si-O environments at 102.9 and 103.8 eV. Interestingly, in the air-free as-synthesized sample, major Si-O environments were also detected, demonstrating the ease of Si oxidation with Cu₃Si present. This could also be a sign of poor ligand coverage, as the N and C HRES spectra do have binding energies indicative of OLA (Figure S2.15). Additionally, environments at 99.5 and 101.6 eV in the Si 2p HRES spectrum indicate Cu-Si and Si-Si bonding, respectively, are present.^{11,22} Although a Mg-Si binding site, ~98 eV,⁵⁹ was not observed in the Si 2p HRES spectrum, a Mg 2p HRES spectra was still detected in the acid wash sample (Figure S2.14). As any remnant

Mg₂Si would have been removed during the acid wash, this supports slight Mg remaining in the destabilized, amorphous Si matrix. Finally, negligible amounts of Cl were detected in the acid washed sample by XPS. This refutes the hypothesis that the Cl is present throughout the Si matrix. However, as Cl was detected in the as-synthesized XPS spectrum (in agreement with the STEM/EDS data), we believe a Cl species was likely persisting on the surface of the Cu₃Si@Si matrix particles after the normal washing procedure, and the extra acid wash was able to fully remove the species.

In summary, electrochemical cycling and XPS provided secondary characterization of the Si matrixes surrounding the Cu₃Si particles. Taking advantage of Si being Li active where Cu₃Si is not, cycling the as-synthesized particles against Li probed the Si matrix and confirmed the matrix content indeed has active Si present. Furthermore, by analyzing the acid washed particles by XPS, again the Si matrix could be investigated. Similar to the STEM/EDS data it was found that Si and O are major components of the matrix and small amounts of Mg was detected. Additionally, it was found that the Cl content detected by

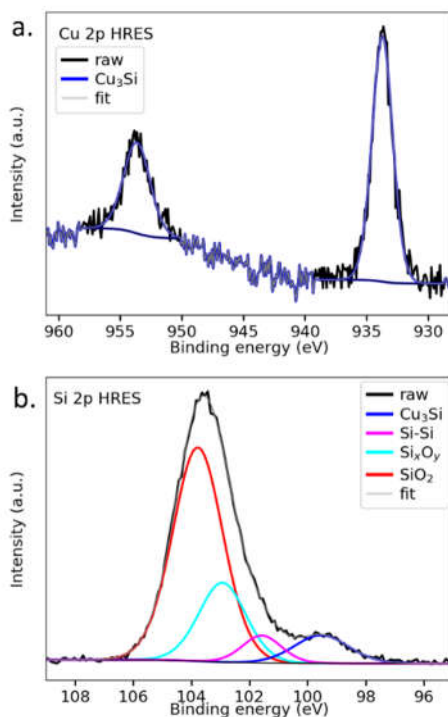


Figure 2.8. XPS analysis of acid washed Cu₃Si@Si matrix particles. a. The HRES Cu 2p spectrum was best fit with one environment matching Cu-Si. b. The HRES Si 2p spectrum was best fit with four environments, including two Si-O environments, Si-Si, and Cu-Si.

STEM/EDS was likely a Cl species persisting on the surface of the $\text{Cu}_3\text{Si}@\text{Si}$ matrix particles, as negligible amounts of Cl were detected by XPS after the additional acid wash.

2.6 Conclusions

$\text{Cu}_3\text{Si}@\text{Si}$ matrix particles were successfully synthesized with mild conditions (275 °C, ON) and precursors (Mg_2Si and CuCl_2 in OLA) by combining colloidal solution and metathesis methods. During optimization, it was found that temperature, time, and precursor ratios could be tuned to achieve $\text{Cu}_3\text{Si}@\text{Si}$ matrix formation without excessive unreacted Mg_2Si or production of Cu_5Si . Generally, an increase in time, temperature, or the $\text{CuCl}_2:\text{Mg}_2\text{Si}$ ratio increased the amount of Cu_3Si produced, however, any extreme could also lead to the presence of the Cu_5Si phase.

Further, the fundamentals of this synthesis system were explored to gain a more in-depth understanding. The role of OLA was investigated by reacting the precursors in differing solvents and conducting controls of the precursors in OLA. From these studies, OLA's intermediate coordination strength was demonstrated to be a refined balance between extremely non-coordinating and extremely coordinating solvents, and its high boiling point allowed for increased reaction temperatures. It was hypothesized that OLA supports the formation of the Si matrix by acting as a labile capping ligand. Further, it is thought that OLA could help shuttle the initially formed Cu in solution, and therefore aid the Cu and Si matrix interaction. It was found that although OLA acts as a reducing agent to CuCl_2 , it is not able to reduce Cu^{1+} to Cu^0 on its own, and therefore Mg_2Si promotes the full reduction of Cu^{1+} to Cu^0 . These hypotheses were further confirmed in the reaction pathway study.

The reaction pathway was elucidated by fully quenching reactions at 1.5 hr, 3 hr, 6 hr, and ON and examining both the resulting particles and the excess Cu pellet. These studies showed that indeed Mg_2Si is quickly consumed during the reduction of Cu^{1+} to Cu^0 and this results in an amorphous, destabilized Si matrix and MgCl_2 . Next, Cu diffuses into the Si matrix, subsequently leading to Cu_3Si particles within the Si matrix. The investigation of the Si matrix illuminated that the matrix is active Si with small amounts of

Mg, which presumably got trapped during the initial reaction step. Unsurprisingly, the matrix is very susceptible to oxidation, leading to a high O content in the matrix.

Overall, from the thorough examination of this solution-based metathesis reaction, it appears the Cu_3Si formation energy barrier was lowered. Although the reaction still proceeds through a diffusion-limited pathway, two factors aid in lowering the energy barrier commonly associated with diffusion pathways. 1) The solvent supports the formation of the intermediates and promotes the diffusion of Cu to the Si matrixes. 2) Starting with the Mg_2Si and CuCl_2 precursors leads to Si matrixes that are amorphous and destabilized. This disordered Si structure likely provides sites for easy nucleation of Cu_3Si particles.

2.7 References

- (1) Schmitt, A. L.; Higgins, J. M.; Szczech, J. R.; Jin, S. Synthesis and Applications of Metal Silicide Nanowires. *J. Mater. Chem.* **2010**, *20*, 223–235. <https://doi.org/10.1039/B910968D>.
- (2) Zhang, S.-L.; Östling, M. Metal Silicides in CMOS Technology: Past, Present, and Future Trends. *Crit. Rev. Solid State Mater. Sci.* **2003**, *28* (1), 1–129. <https://doi.org/10.1080/10408430390802431>.
- (3) Chen, X.; Liang, C. Transition Metal Silicides: Fundamentals, Preparation and Catalytic Applications. *Catal. Sci. Technol.* **2019**, *9*, 4785–4820. <https://doi.org/10.1039/c9cy00533a>.
- (4) Istratov, A. A.; Weber, E. R. Physics of Copper in Silicon. *J. Electrochem. Soc.* **2002**, *149* (1), G21–G30. <https://doi.org/10.1149/1.1421348>.
- (5) Gillot, B.; Weber, G.; Souha, H.; Zenkour, M. Reactivity of Commercial Silicon and Silicides towards Copper(I) Chloride. Effect of Aluminium, Calcium and Iron on the Formation of Copper Silicide. *J. Alloys Compd.* **1998**, *270*, 275–280. [https://doi.org/10.1016/S0925-8388\(98\)00527-1](https://doi.org/10.1016/S0925-8388(98)00527-1).
- (6) Acker, J.; Köther, S.; Lewis, K. M.; Bohmhammel, K. The Reactivity in the System CuCl-Si Related to the Activation of Silicon in the Direct Synthesis. *Silicon Chem.* **2003**, *2*, 195–206. <https://doi.org/10.1023/B:SILC.0000046751.05300.d4>.
- (7) Ding, W. J.; Wang, Z. B.; Yan, J. M.; Xiao, W. De. CuCl-Catalyzed Hydrogenation of Silicon Tetrachloride in the Presence of Silicon: Mechanism and Kinetic Modeling. *Ind. Eng. Chem. Res.* **2014**, *53*, 16725–16735. <https://doi.org/10.1021/ie503242t>.
- (8) Yadav, S.; Singh, C. V. First Principles Investigation of HCl, H₂, and Chlorosilane Adsorption on Cu₃Si Surfaces with Applications for Polysilicon Production. *J. Phys. Chem. C* **2018**, *122*, 20252–20260. <https://doi.org/10.1021/acs.jpcc.8b04460>.
- (9) Zhou, J.; Lin, N.; Han, Y.; Zhou, J.; Zhu, Y.; Du, J.; Qian, Y. Cu₃Si@Si Core–Shell Nanoparticles Synthesized Using a Solid-State Reaction and Their Performance as Anode Materials for Lithium Ion Batteries. *Nanoscale* **2015**, *7*, 15075–15079. <https://doi.org/10.1039/C5NR04456A>.
- (10) Zhang, Y.; Du, N.; Jiang, J.; Chen, Y.; Lin, Y.; He, Y.; Lei, Y.; Zhu, S.; Yang, D. Enhanced Electrochemical Properties of Cu₃Si-Embedded Three-Dimensional Porous Si Synthesized by One-Pot Synthesis. *J. Alloys Compd.* **2019**, *792*, 341–347. <https://doi.org/10.1016/j.jallcom.2019.04.082>.
- (11) Guo, J.; Pei, S.; He, Z.; Huang, L.-A.; Lu, T.; Gong, J.; Shao, H.; Wang, J. Novel Porous Si-Cu₃Si-Cu Microsphere Composites with Excellent Electrochemical Lithium Storage. *Electrochim. Acta* **2020**, *345*, 136334–136343. <https://doi.org/10.1016/j.electacta.2020.136334>.
- (12) Yuan, F.-W.; Wang, C.-Y.; Li, G.-A.; Chang, S.-H.; Chu, L.-W.; Chen, L.-J.; Tuan, H.-Y. Solution-Phase Synthesis of Single-Crystal Cu₃Si Nanowire Arrays on Diverse Substrates with Dual Functions as High-Performance Field Emitters and Efficient Anti-Reflective Layers. *Nanoscale* **2013**, *5*, 9875–9881. <https://doi.org/10.1039/c3nr03045h>.
- (13) Wang, C.-Y.; Yuan, F.-W.; Hung, Y.-C.; Su, Y.-W.; Tuan, H.-Y. *In-Situ* TEM and XRD Analysis of Microstructures Changes in Solution-Grown Copper Silicide Nanowires Array for Field Emitters. *J. Alloys Compd.* **2018**, *735*, 2373–2377. <https://doi.org/10.1016/J.JALLCOM.2017.12.032>.
- (14) Chen, L.-J. Nanoscale Copper and Copper Compounds for Advanced Device Applications. *Metall. Mater. Trans. A* **2016**, *47*, 5845–5851. <https://doi.org/10.1007/s11661-016-3477-8>.
- (15) Okamoto, H.; Schlesinger, M.E.; Mueller, E. M. *Alloy Phase Diagrams*, 3rd ed.; ASM International, 2016.
- (16) Chromik, R. R.; Neils, W. K.; Cotts, E. J. Thermodynamic and Kinetic Study of Solid State Reactions in the Cu–Si System. *J. Appl. Phys.* **1999**, *86* (8), 4273–4281. <https://doi.org/10.1063/1.371357>.
- (17) Li, S.; Cai, H.; Gan, C. L.; Guo, J.; Dong, Z.; Ma, J. Controlled Synthesis of Copper-Silicide Nanostructures. *Cryst. Growth Des.* **2010**, *10* (7), 2983–2989. <https://doi.org/10.1021/cg1000232>.

- (18) Buchin, E. Y.; Naumov, V. V.; Vasilyev, S. V. Formation of Nanoporous Copper-Silicide Films. *Semiconductors* **2019**, *53* (3), 395–399. <https://doi.org/10.1134/S1063782619030059>.
- (19) Dodony, E.; Radnóczy, G. Z.; Dódony, I. Low Temperature Formation of Copper Rich Silicides. *Intermetallics* **2019**, *107*, 108–115. <https://doi.org/10.1016/j.intermet.2019.01.010>.
- (20) Jung, S. J.; Lutz, T.; Bell, A. P.; Mccarthy, E. K.; Boland, J. J. Free-Standing, Single-Crystal Cu₃Si Nanowires. *Cryst. Growth Des.* **2012**, *12*, 3076–3081. <https://doi.org/10.1021/cg300273d>.
- (21) Ibrahim, M.; Balogh-Michels, Z.; Stender, P.; Baither, D.; Schmitz, G. Nucleation Controlled Reaction of Cu₃Si in the Field of Sharp Concentration Gradient. *Acta Mater.* **2016**, *112*, 315–325. <https://doi.org/10.1016/j.actamat.2016.04.041>.
- (22) Lu, G. L.; Liu, F. H.; Chen, X.; Yang, J. F. Cu Nanowire Wrapped and Cu₃Si Anchored Si@Cu Quasi Core-Shell Composite Microsized Particles as Anode Materials for Li-Ion Batteries. *J. Alloys Compd.* **2019**, *809*, 151750–151757. <https://doi.org/10.1016/j.jallcom.2019.151750>.
- (23) Bernard, F.; Souha, H.; Gaffet, E. Enhancement of Self-Sustaining Reaction Cu₃Si Phase Formation Starting from Mechanically Activated Powders. *Mater. Sci. Eng. A* **2000**, *284*, 301–306. [https://doi.org/10.1016/S0921-5093\(00\)00749-8](https://doi.org/10.1016/S0921-5093(00)00749-8).
- (24) Zhang, Z.; Wong, L. M.; Ong, H. G.; Wang, X. J.; Wang, J. L.; Wang, S. J.; Chen, H.; Wu, T. Self-Assembled Shape- and Orientation-Controlled Synthesis of Nanoscale Cu₃Si Triangles, Squares, and Wires. *Nano Lett.* **2008**, *8* (10), 3205–3210. <https://doi.org/10.1021/nl8015208>.
- (25) O'Donoghue, Richard; Teiskersis, Arunas; Gun'ko, Y. Pulsed-Injection Metal Organic Chemical Vapour Deposition for the Development of Copper Silicate and Silicide Nanostructures. *Adv. Mater. Lett.* **2017**, *8* (8), 830–840. <https://doi.org/10.5185/amlett.2017.1465>.
- (26) Klementová, M.; Krabáč, L.; Brázda, P.; Palatinus, L.; Dřínek, V. Cu-Si Nanoobjects Prepared by CVD on Cu/Cu₃Si-Substrates Using Various Precursors (SiH₄, EtSiH₃, BuSiH₃) with Added H₂ or Air. *J. Cryst. Growth* **2017**, *465*, 6–11. <https://doi.org/10.1016/j.jcrysgro.2017.02.019>.
- (27) Johnson, D. C.; Mosby, J. M.; Riha, S. C.; Prieto, A. L. Synthesis of Copper Silicide Nanocrystallites Embedded in Silicon Nanowires for Enhanced Transport Properties. *J. Mater. Chem.* **2010**, *20*, 1993–1998. <https://doi.org/10.1039/b919281f>.
- (28) Parditka, B.; Zaka, H.; Erdélyi, G.; Langer, G. A.; Ibrahim, M.; Schmitz, G.; Balogh-Michels, Z.; Erdélyi, Z. The Transition from Linear to Parabolic Growth of Cu₃Si Phase in Cu/a-Si System. *Scr. Mater.* **2018**, *149*, 36–39. <https://doi.org/10.1016/j.scriptamat.2018.01.035>.
- (29) Parkin, I. P. Solvent Free Reactions in the Solid State: Solid State Metathesis. *Transit. Met. Chem.* **2002**, *27*, 569–573. <https://doi.org/10.1023/A:1019885916386>.
- (30) Martinolich, A. J.; Neilson, J. R. Toward Reaction-by-Design: Achieving Kinetic Control of Solid State Chemistry with Metathesis. *Chem. Mater.* **2017**, *29*, 479–489. <https://doi.org/10.1021/acs.chemmater.6b04861>.
- (31) Kovalenko, M. V.; Manna, L.; Cabot, A.; Hens, Z.; Talapin, D. V.; Kagan, C. R.; Klimov, V. I.; Rogach, A. L.; Reiss, P.; Milliron, D. J.; Guyot-Sionnest, P.; Konstantatos, G.; Parak, W. J.; Hyeon, T.; Korgel, B. A.; Murray, C. B.; Heiss, W. Prospects of Nanoscience with Nanocrystals. *ACS Nano* **2015**, *9* (2), 1012–1057. <https://doi.org/10.1021/nn506223h>.
- (32) Coughlan, C.; Ibáñez, M.; Dobrozhan, O.; Singh, A.; Cabot, A.; Ryan, K. M. Compound Copper Chalcogenide Nanocrystals. *Chem. Rev.* **2017**, *117*, 5865–6109. <https://doi.org/10.1021/acs.chemrev.6b00376>.
- (33) Rochow, E. G. The Direct Synthesis of Organosilicon Compounds. *J. Am. Chem. Soc.* **1945**, *67* (6), 963–965. <https://doi.org/10.1021/ja01222a026>.
- (34) Parkin, I. P. Solid State Metathesis Reaction for Metal Borides, Silicides, Pnictides and Chalcogenides: Ionic or Elemental Pathways. *Chem. Soc. Rev.* **1996**, *25*, 199–207. <https://doi.org/10.1039/cs9962500199>.
- (35) McEnaney, J. M.; Schaak, R. E. Solution Synthesis of Metal Silicide Nanoparticles. *Inorg. Chem.* **2015**, *54*, 707–709. <https://doi.org/10.1021/ic502394u>.

- (36) Lee, J. M.; Miller, R. C.; Moloney, L. J.; Prieto, A. L. The Development of Strategies for Nanoparticle Synthesis: Considerations for Deepening Understanding of Inherently Complex Systems. *J. Solid State Chem.* **2019**, *273*, 243–286. <https://doi.org/10.1016/J.JSSC.2018.12.053>.
- (37) Chianelli, R. R.; Dines, M. B. Low-Temperature Solution Preparation of Group 4B, 5B and 6B Transition-Metal Dichalcogenides. *Inorg. Chem.* **1978**, *17* (10), 2758–2762. <https://doi.org/10.1021/ic50188a014>.
- (38) Kher, S. S.; Wells, R. L. *A Straightforward, New Method for the Synthesis of Nanocrystalline GaAs and GaP*; 2056; Vol. 6.
- (39) Bley, R. A.; Kauzlarich, S. M. A Low-Temperature Solution Phase Route for the Synthesis of Silicon Nanoclusters. *J. Am. Chem. Soc.* **1996**, *118* (49), 12461–12462. <https://doi.org/10.1021/ja962787s>.
- (40) Beekman, M.; Kauzlarich, S. M.; Doherty, L.; Nolas, G. S. Zintl Phases as Reactive Precursors for Synthesis of Novel Silicon and Germanium-Based Materials. *Materials (Basel)*. **2019**, *12*, 1139–1161. <https://doi.org/10.3390/ma12071139>.
- (41) Kauzlarich, S. M.; Liu, Q.; Yin, S. C.; Lee, H. W. H.; Taylor, B. The Novel Synthesis of Silicon and Germanium Nanocrystallites. *Mater. Res. Soc. Symp. - Proc.* **2001**, *638*, 651–656. <https://doi.org/10.1557/proc-638-f6.5.1>.
- (42) Taylor, B. R.; Kauzlarich, S. M.; Delgado, G. R.; Lee, H. W. H. Solution Synthesis and Characterization of Quantum Confined Ge Nanoparticles. *Chem. Mater.* **1999**, *11* (9), 2493–2500. <https://doi.org/10.1021/cm990203q>.
- (43) Taylor, B. R.; Fox, G. A.; Hope-Weeks, L. J.; Maxwell, R. S.; Kauzlarich, S. M.; Lee, H. W. H. Solution Preparation of Ge Nanoparticles with Chemically Tailored Surfaces. *Mater. Sci. Eng. B* **2002**, *96*, 90–93. [https://doi.org/10.1016/S0921-5107\(02\)00297-0](https://doi.org/10.1016/S0921-5107(02)00297-0).
- (44) Schneider, J. D.; Agocs, D. B.; Prieto, A. L. Design of a Sample Transfer Holder to Enable Air-Free X-Ray Photoelectron Spectroscopy. *Chem. Mater.* **2020**, *32*, 8091–8096. <https://doi.org/10.1021/acs.chemmater.0c01895>.
- (45) Yang, C. S.; Bley, R. A.; Kauzlarich, S. M.; Lee, H. W. H.; Delgado, G. R. Synthesis of Alkyl-Terminated Silicon Nanoclusters by a Solution Route. *J. Am. Chem. Soc.* **1999**, *121* (22), 5191–5195. <https://doi.org/10.1021/ja9828509>.
- (46) De Jong, M.; Chen, W.; Angsten, T.; Jain, A.; Notestine, R.; Gamst, A.; Sluiter, M.; Ande, C. K.; Van Der Zwaag, S.; Plata, J. J.; Toher, C.; Curtarolo, S.; Ceder, G.; Persson, K. A.; Asta, M. Charting the Complete Elastic Properties of Inorganic Crystalline Compounds. *Sci. Data* **2015**, *2* (1), 1–13. <https://doi.org/10.1038/sdata.2015.9>.
- (47) Jain, A.; Ong, S. P.; Hautier, G.; Chen, W.; Richards, W. D.; Dacek, S.; Cholia, S.; Gunter, D.; Skinner, D.; Ceder, G.; Persson, K. A. Commentary: The Materials Project: A Materials Genome Approach to Accelerating Materials Innovation. *APL Materials*. American Institute of Physics Inc. July 18, 2013, p 11002. <https://doi.org/10.1063/1.4812323>.
- (48) Hong, S. Q.; Comrie, C. M.; Russell, S. W.; Mayer, J. W. Phase Formation in Cu-Si and Cu-Ge. *J. Appl. Phys.* **1991**, *70* (7), 3655–3660. <https://doi.org/10.1063/1.349213>.
- (49) Mourdikoudis, S.; Liz-Marza, L. M. Oleylamine in Nanoparticle Synthesis. *Chem. Mater.* **2013**, *25*, 1465–1476. <https://doi.org/10.1021/cm4000476>.
- (50) Pettigrew, K. A.; Liu, Q.; Power, P. P.; Kauzlarich, S. M. Solution Synthesis of Alkyl- and Alkyl/Alkoxy-Capped Silicon Nanoparticles via Oxidation of Mg₂Si. *Chem. Mater.* **2003**, *15* (21), 4005–4011. <https://doi.org/10.1021/cm034403k>.
- (51) Carmalt, C. J.; Morrison, D. E.; Parkin, I. P. Liquid-Mediated Metathetical Synthesis of Binary and Ternary Transition-Metal Pnictides. *Polyhedron* **2000**, *19*, 829–833. [https://doi.org/10.1016/S0277-5387\(00\)00323-5](https://doi.org/10.1016/S0277-5387(00)00323-5).
- (52) Tang, S.; Zhao, H. Glymes as Versatile Solvents for Chemical Reactions and Processes: From the Laboratory to Industry. *RSC Adv.* **2014**, *4*, 11251–11287. <https://doi.org/10.1039/c3ra47191h>.
- (53) Ibrahim, M.; Balogh, Z.; Stender, P.; Schlesiger, R.; Greiwe, G.-H.; Schmitz, G.; Parditka, B.; Langer, G. A.; Csik, A.; Erdélyi, Z. On the Influence of the Stacking Sequence in the Nucleation

- of Cu₃Si: Experiment and the Testing of Nucleation Models. *Acta Mater.* **2014**, *76*, 306–313. <https://doi.org/10.1016/j.actamat.2014.05.006>.
- (54) Wen, C.-Y.; Spaepen, F. *In Situ* Electron Microscopy of the Phases of Cu₃Si. *Philos. Mag.* **2007**, *87* (35), 5581–5599. <https://doi.org/10.1080/14786430701675829>.
- (55) Jung, S. J.; O’kelly, C. J.; Boland, J. J. Position Controlled Growth of Single Crystal Cu₃Si Nanostructures. *Cryst. Growth Des.* **2015**, *15*, 5355–5359. <https://doi.org/10.1021/acs.cgd.5b00947>.
- (56) Stolt, L.; Charai, A.; D’Heurle, F. M.; Fryer, P. M.; Harper, J. M. E. Formation of Cu₃Si and Its Catalytic Effect on Silicon Oxidation at Room Temperature. *J. Vac. Sci. Technol. A* **1991**, *9* (3), 1501–1505. <https://doi.org/10.1116/1.577653>.
- (57) Ogata, K.; Salager, E.; Kerr, C. J.; Fraser, A. E.; Ducati, C.; Morris, A. J.; Hofmann, S.; Grey, C. P. Revealing Lithium-Silicide Phase Transformations in Nano-Structured Silicon-Based Lithium Ion Batteries via *in Situ* NMR Spectroscopy. *Nat. Commun.* **2014**, *5*, 3217–3227. <https://doi.org/10.1038/ncomms4217>.
- (58) Kim, I. C.; Byun, D.; Lee, S.; Lee, J. K. Electrochemical Characteristics of Copper Silicide-Coated Graphite as an Anode Material of Lithium Secondary Batteries. *Electrochim. Acta* **2006**, *52*, 1532–1537. <https://doi.org/10.1016/j.electacta.2006.02.055>.
- (59) Kohandehghan, A.; Kalisvaart, P.; Kupsta, M.; Zahiri, B.; Amirkhiz, B. S.; Li, Z.; Memarzadeh, E. L.; Bendersky, L. A.; Mitlin, D. Magnesium and Magnesium-Silicide Coated Silicon Nanowire Composite Anodes for Lithium-Ion Batteries. *J. Mater. Chem. A* **2013**, *1*, 1600–1612. <https://doi.org/10.1039/c2ta00769j>.

CHAPTER 3

CONTROLLING THE CHALCOGEN REACTIVITY IN THE $\text{Fe}_2\text{GeS}_{4-x}\text{Se}_x$ System with LiHMDS³

3.1 Overview

The Brønsted base, lithium bis(trimethylsilyl)amide (LiHMDS), has been shown to increase the reactivity in unary and binary systems as well as some ternary systems. However, LiHMDS has mainly been studied for controlling cation reactivities. Here, we use the olivine $\text{Fe}_2\text{GeS}_{4-x}\text{Se}_x$ system as a model system to investigate the role of the LiHMDS base when the chalcogen reactivity is altered (S vs Se). It is demonstrated that incorporation of LiHMDS allows for the first nanoparticle synthesis of Fe_2GeSe_4 and the controlled synthesis of the solid-solution $\text{Fe}_2\text{GeS}_{4-x}\text{Se}_x$, $x=0.8, 1$. The synthesis parameters, the pre-injection chalcogen speciation, and the reaction pathways are investigated to understand the role of LiHMDS when the precursor reactivity is inherently altered.

3.2 Introduction

Nanoparticle technology is driven by the vast number of viable applications, including but not limited to photovoltaics, thermoelectrics, drug delivery, and LEDs.^{1,2} Current advances in these technologies depend critically on the ability to control structure/property relationships. Specifically, solution-based ternary and quinary nanoparticle (NP) systems have synthetic handles to tune composition, structure, morphology, and size.³ Yet, synthesizing a structure with more than two elements is challenging, making the controllability of these systems underdeveloped compared to binary and unary systems.

To synthesize the desired ternary phase over the associated binaries, precursor reactivities must be balanced. To explain the challenge in balancing reactivities, Hard-Soft Acid-Base (HSAB) theory is often referenced, where metal cations with different valency need to synchronously react with chalcogen anions to compose the ternary.^{3,4} HSAB theory gives a simplified understanding of the challenge, but reactivity is intertwined with the various interactions (i.e. organic, solid-state, inorganic) involved in solution-based NP

³This Chapter is a manuscript for submission to the Journal of the American Chemical Society with Lily J. Moloney, Rebecca C. Miller, and Amy L. Prieto as Authors. Lily J. Moloney carried out majority of the experiments and writing. Rebecca C. Miller performed preliminary data to establish the research. Rebecca C. Miller and Amy L. Prieto provided discussion and edits.

synthesis. For this reason, synthesis methods that can be broadly applied to a variety of systems and lead to high yield and purity are limited.

The development of reagents that can be used to control a broad range of reactive monomers could be a solution. One reagent investigated thoroughly in unary and binary systems is Li bis(trimethylsilyl)amide ($\text{LiN}(\text{SiMe}_3)_2$, LiHMDS).⁵ These studies found that the reactivity of the metal cation is increased as the metal-HMDS complex that is formed is easily decomposed to release an active metal monomer. This allows for the nucleation of phase pure, small nanoparticles. In alkylamine (i.e. OLA) solvent systems, the Brønsted base is hypothesized to deprotonate the alkylamine solvent to form a highly reactive metal-alkylamide complex.⁶ Moreover, LiHMDS has been shown to balance the reactivity of multiple cation precursors in ternary systems.⁷⁻⁹ Recently, we demonstrated that LiHMDS assisted in rapidly producing phase-pure Fe_2GeS_4 .¹⁰ By exploring the phase space of Fe-Ge-S and the role of the LiHMDS base, it was found that manipulation of the ratio between the precursors as well as the ratio of the cations, amine, and base were necessary to afford the desired phase. Further, it was shown that the base not only tuned precursor reactivity but also particle nucleation vs growth, where the balance led to triplets of twinned particles, or trillings.

However, to our knowledge, LiHMDS has mainly been studied for controlling cation reactivities towards a single chalcogen. The chalcogens S and Se, albeit from the same family, have differing solution chemistries. Simply by examining the calculated energies of formations for Fe-Ge-S and Fe-Ge-Se, we can see the Se containing compounds are less enthalpically favorable to form compared to the corresponding S compounds (Table S3.2).^{11,12} This could be explained in terms of HSAB principals. Chalcogens are generally termed soft bases, but Se is more polarizable compared to S. Additionally, Ge^{4+} is considered hard and Fe^{2+} is borderline hard, meaning the interaction with the less polarizable S would be more favorable. Finally, the choice of Se precursor is more limited, compared to S, due to solubility issues in common NP synthesis solvents.¹³⁻¹⁵ Here the olivine $\text{Fe}_2\text{GeS}_{4-x}\text{Se}_x$ system, a possible photovoltaic or thermoelectric material^{16,17}, is used as a model system to investigate the role of LiHMDS when the chalcogen reactivity is

altered (S vs Se) and the cations are kept constant (Fe^{2+} , Ge^{4+}). We report the first solution-based NP synthesis of Fe_2GeSe_4 as well as the controlled synthesis of the solid-solution $\text{Fe}_2\text{GeS}_{4-x}\text{Se}_x$, $x=0.8, 1$. Therefore, further demonstrating the versatility of the reagent, LiHMDS, in multivariable material systems, where precursor reactivities are vastly different.

3.3 Results and Discussion

Herein, we report the synthesis of $\text{Fe}_2\text{GeS}_{4-x}\text{Se}_x$ ($x=0.8, 1$, and 4) for the first time using a hot-injection method adapted from our previous report.¹⁰ Briefly, for the synthesis of Fe_2GeSe_4 , FeCl_2 (2 eq, 41 mg), GeI_4 (1.5 eq, 141 mg), and oleylamine (OLA, 6 mL) were degassed under vacuum at 120 °C for 1 hr before heating to 340 °C under N_2 . Simultaneously, Se powder (3.5 eq, 45 mg), $\text{LiN}(\text{SiMe}_3)_2$ (3 eq, 81 mg), and OLA (2 mL) were placed in a scintillation vial and sonicated for ~1hr 40min. The Se/LiHMDS/OLA solution was injected into the Fe/Ge/OLA solution at 320 °C, before the end temperature (340 °C) was reached. After reacting for 15 min, the reaction contents were quickly quenched into toluene. For the two solid-solution reactions, a similar procedure was followed except the equivalence of GeI_4 was lowered to 1.4 eq, the chalcogen/LiHMDS/OLA solution was injected at 330 °C, and allowed to react at 330 °C for 10 min. For the full experimental detail, see the Supporting Information.

Previous exploration of the LiHMDS-assisted Fe-Ge-S phase space provided a reasonable starting point for the Fe_2GeSe_4 synthesis. However, replacing elemental S with Se and following the optimized synthesis conditions for Fe_2GeS_4 , resulted in Fe-Se and Ge-Se binaries along with some Fe_2GeSe_4 (Fig. S3.1). The presence of these binaries highlighted that the system reactivity was indeed changed when Se replaced S. Additionally, the presence of the Fe_2GeSe_4 phase illuminated that LiHMDS could aid in balancing this reactivity change.

It was found that the manipulation of temperature, time, amount of base, and precursor stoichiometry were important for tuning the resulting nanoparticle composition and morphology. These parameters are interrelated and thus, although each parameter is discussed here in a linear fashion, often multiple factors have to be considered. The $\text{Fe}_2\text{GeS}_{4-x}\text{Se}_x$ ($x=0.8, 1$, and 4) NPs composition and morphology were analyzed

mainly by powder X-ray diffraction (PXRD) with Rietveld refinement, as well as transmission electron microscopy with energy dispersive spectroscopy (EDS).

3.3.1 Describing the Resulting Fe_2GeSe_4 , $x=0.8, 1, 4$ Particles. Conditions for Fe_2GeSe_4 generation required a higher reaction temperature (340 °C vs. 320 °C) and time (15 min vs. 10 min) compared to Fe_2GeS_4 . The refinement of the resulting $x=4$ PXRD pattern fits well with the reference Fe_2GeSe_4 pattern (ICSD Coll. Code 87086), showing the synthesis produced high purity Fe_2GeSe_4 (Fig. 3.1a). However, minimal amounts of Fe-Se binary (10.44%) are present, indicated by the small, broad peak at ~ 33 2 θ . The best fit was achieved with the inclusion of an off stoichiometric Fe_7Se_8 pattern, $Fe_{0.8}Se$. Generally, the refinement parameters included unit cell, profile terms, and background. Additionally, the refinement indicates some anisotropic growth favored in the 200 and 020 directions. Using TEM and EDS mapping (Fig. S3.2) the Fe_2GeSe_4 particles were found to be large (Ave. particle width:length = 710:880) hexagonal or rounded Fe_2GeSe_4 particles (Fig. 3.1b), periodically decorated with small Fe-Se plate particles (Fig 3.1c).

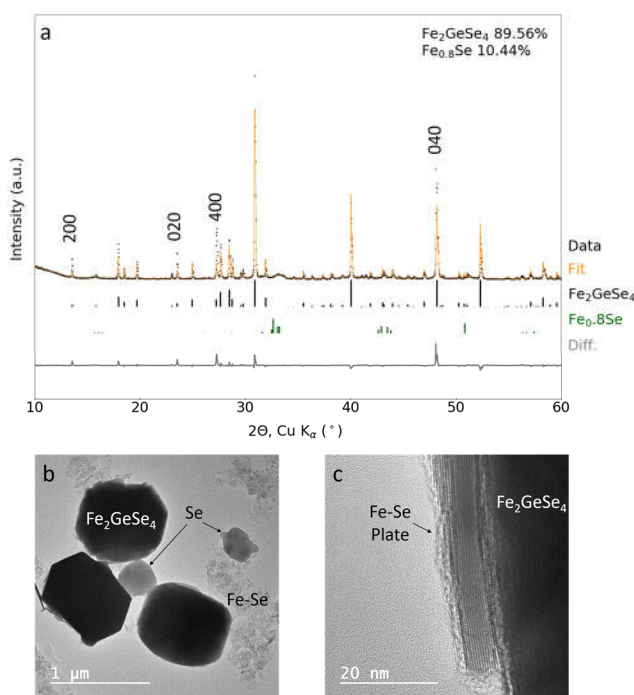


Figure 3.1. a. The Rietveld refinement of the resulting Fe_2GeSe_4 particles showing a good fit with the Fe_2GeSe_4 reference pattern (ICSD Coll. Code 87086 and slight $Fe_{0.8}Se$). TEM images showing the a. Fe_2GeSe_4 morphology and the slight presence of Fe-Se flakes and amorphous Se, as well as b. the Fe-Se plates that decorated the sides of the Fe_2GeSe_4 particles.

Additionally, Fe-Se flakes, and occasionally amorphous, globular Se particles were observed. In agreement with the anisotropy indicated in the refinement, the Fe_2GeSe_4 particles do have a slightly skewed aspect ratio (Fig 3.1b).

As it was discovered the LiHMDS could balance the system reactivity when the chalcogen was replaced, the next step was to test the chalcogen solid solution, $\text{Fe}_2\text{GeS}_{4-x}\text{Se}_x$. The successful solid-solution synthesis ($x=0.8$ or 1) was achieved by using temperature conditions between the S and Se systems (330°C) reacted for 10 min. Additionally, slightly a lower GeI_4 equivalence (1.4 vs. 1.5 eq) was required. For both the $x=0.8$ and $x=1$ sample, the $\text{Fe}_2\text{GeS}_{4-x}\text{Se}_x$ particles had mixed morphologies of single plates as well as twinned plates (Fig. 3.2a and b). Interestingly, the $x=1$ particles were larger than the $x=0.8$ particles. Refinements of the solid-solution PXRD patterns (Fig. S3.3), where $x=0.8$ and 1 , matched the Fe_2GeS_4 reference pattern (ICSD Coll. Code 333), but the peaks are slightly shifted to lower 2θ due to the slight

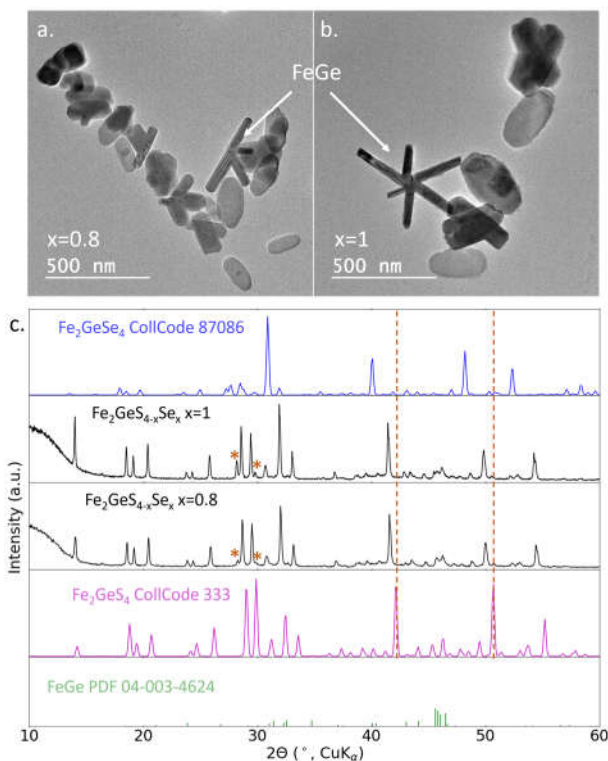


Figure 3.2. TEM images showing a similar morphology of the solid-solution $\text{Fe}_2\text{GeS}_{4-x}\text{Se}_x$ a. $x=0.8$ and b. $x=1$. c. The PXRD patterns of the $x=0.8$ and 1 plotted between the Fe_2GeS_4 and Fe_2GeSe_4 reference patterns to illustrate the peaks shifting and the increasing intensity of the peaks representing the 400 and 002 planes (indicated by the red *).

lattice expansion from Se incorporation. Moreover, the peaks at 27.2 and 28.7 2θ in the Fe_2GeSe_4 reference pattern, associated to the 400 and 002 plane, become more prevalent in the $x=0.8$ and 1 pattern (Fig 3.2c, indicated by *). Comparatively, the intensity of these peaks is almost non-existent in the Fe_2GeS_4 reference pattern.

In addition to the previously listed refinement parameters, for the solid-solution refinement, Se atoms were added to the Fe_2GeS_4 unit cell at all three S sites. The calculated x values were $x=0.78$ and 1.16, agreeing with the experimental imputed values of the chalcogen precursors. Further, from the EDS composition analysis of the $\text{Fe}_2\text{GeS}_{4-x}\text{Se}_x$ ($x=0.8$ and 1) samples, the x -value was found to be $x=0.76$ and 0.98, respectively. This would suggest that the reactivity of S and Se are balanced. Yet, these samples did also have a slight FeGe (twinned, rod-shaped particles) impurity (13.5-14%) present, revealing that, although LiHMDS helps balance reactivity, complete balance in this complex system is difficult to achieve.

3.3.2 Altering the LiHMDS Amount. To further test LiHMDS's effect on the system reactivity, the amount of LiHMDS was altered in the $x=4$ system. Without LiHMDS present, Fe_2GeSe_4 particles were not observed, rather yellow GeSe_2 particles were formed (Fig. S3.6). This reaction highlights the importance of LiHMDS in the generation of Fe_2GeSe_4 particles. When the equivalence of LiHMDS was increased to 3.5 eq compared to 3 eq, the Fe_2GeSe_4 particle size significantly decreased (Ave. particle width:length = 450 nm:540 nm), however GeSe and $\text{Fe}_{0.8}\text{Se}$ binaries were also observed (Fig 3.3 a). The inclusion of the HMDS moiety has been reported to produce small uniform particles through increased reactivity and/or capping.^{5,18,19} In agreeance with the literature, we hypothesize the base either itself or a transformed species is capping the Fe_2GeSe_4 particles as well as allowing the Fe_2GeSe_4 formation through increased precursor reactivity. When the base was further increased to 4 eq, the Fe_2GeSe_4 particle size again significantly decreased (Ave. particle width:length = 150 nm:180 nm), supporting this hypothesis (Fig 3.3 b). Similar to the 3.5 eq LiHMDS reaction, the 4 eq LiHMDS reaction also led to GeSe and $\text{Fe}_{0.8}\text{Se}$ binaries. Thus, although smaller Fe_2GeSe_4 particles could be achieved, the presence of these binaries means the system reactivity was unfavorably tipped as the amount of LiHMDS was increased. In an effort to avoid these

binaries, the 3.5 eq LiHMDS reaction time was increased to 20 min. Although the GeSe particles were no longer present and minimal $\text{Fe}_{0.8}\text{Se}$ was observed, the Fe_2GeSe_4 particles seemed to start decomposing. This was indicated by the resulting black solution having a slight yellow tint. The amount of decomposition seemed to vary in the reproduced reactions but generally the Fe_2GeSe_4 particles started to agglomerate, and amorphous fragments formed (Fig 3.3 c).

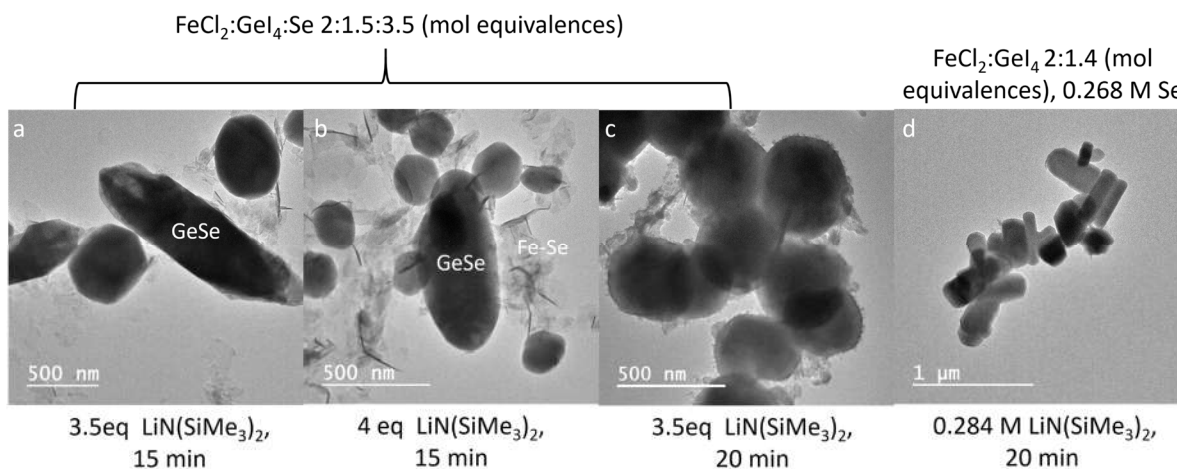


Figure 3.3. TEM images demonstrating the change in Fe_2GeSe_4 morphology and size as the LiHMDS base, reaction time, and precursor stoichiometry is altered, where the alterations are as follows a. 3.5 eq LiHMDS, b. 3.5 eq LiHMDS and 20 min, c. 4 eq LiHMDS, and d. 1.4 eq GeI_4 , 3.3 eq Se, 3.5 eq

Overall, the manipulation of the base amount demonstrates the importance of LiHMDS for balancing reactivity as well as controlling the morphology of the particles. However, we know the role of LiHMDS is intertwined with many factors (i.e. amounts of amine, cations, chalcogens, temperature, etc.). For instance, thinner plates with occasional twinning could be observed (Fig 3.3 d) when 1.8 mL of a stock solution with less Se (0.268 M) and more LiHMDS base (0.284 M) was injected into the reaction flask with 2 eq FeCl_2 and 1.4 eq GeI_4 and then reacted for 20 min. Therefore, to fully understand the parameters controlling morphology and this twinning, further studies are required.

Generally, although temperature, time, and stoichiometry were important, we found the inclusion of LiHMDS to be imperative for promoting the synthesis of high purity $\text{Fe}_2\text{GeS}_{4-x}\text{Se}_x$ ($x=0.8, 1, \text{ and } 4$) phases. Yet, complete phase-purity was difficult to achieve. The $x=4$ phase had minimal Fe-Se and the $x=0.8$ and 1

phases had minimal FeGe present. To understand the origin of the impurities, the chalcogen speciation and the pathway were investigated.

3.3.3 Investigating the Chalcogenide Speciation. As stated previously, S and Se precursors have differing solution chemistries, and Se-based precursors are limited due to their insolubility in commonly used long-chain organic solvents for NP syntheses. In this system, elemental S and Se are used and, unlike S, Se does not dissolve in OLA. However, previous studies have shown the inclusion of a reducing agent or solvent with Se in an alkylamine solvent causes a transformation to a soluble alkylammonium selenide species.^{13,20,21} This soluble selenide species has also been said to be similar to the alkylammonium sulfide species observed in OLA.^{13,22} As LiHMDS is a reducing agent, in this study we see a homogeneous solution is achieved after the Se/LiHMDS/OLA mixture is sonicated (Fig S3.7). Thus, in addition to balancing reactivity through the formation of active alkylamide-metal complexes, LiHMDS also aids in creating a soluble selenide species. From ¹H NMR studies we observed that the Se/LiHMDS/OLA, S/Se/LiHMDS/OLA, and S/LiHMDS/OLA do have similar species present (Fig S3.8). Although similar species seem to be present in the injection solution, this does not equate to similar reactivities nor does it confirm the speciation present after injection.

3.3.4 Elucidating the Reaction Pathway. For each reaction, aliquots were taken at 2 and 7 min and then analyzed by PXRD (Fig. S3.9) and TEM to gain pathway understanding. For the x=4 synthesis, the time study elucidated that after 2 min mostly Fe-Se flakes with crystalline Fe-Se plates are present. Additionally, by TEM and EDS analysis, amorphous Se particles were observed (Fig. 3.4a). After 7 min, large GeSe rods and Fe₂GeSe₄ particles are detected, alongside the Fe-Se flakes and plates (Fig. 3.4b). A diversity of pathway combinations could be hypothesized from the collected data. The Se particles could lead to the onset of GeSe, or possibly be an artifact of quenching. The Fe-Se and GeSe binaries could possibly redissolve, coalesce or a combination of both to form the desired Fe₂GeSe₄ phase. We hypothesize the binaries transform to Fe₂GeSe₄ by a combination of redissolving and coalescence. The resulting Fe₂GeSe₄ particles do not share a similar morphology to either binary, suggesting the redissolving of species

is occurring. However, the small Fe-Se plate particles become less frequently observed in association with the flakes of Fe-Se as the reaction proceeds, and instead can be observed on the sides of the Fe_2GeSe_4 particles, suggesting possible coalescence. Future pathway studies would elucidate the details of the Fe_2GeSe_4 pathway, but that is out of the scope of this report.

Importantly for this study, we discovered the generation of Fe_2GeSe_4 is not direct and instead proceeds through binary intermediates. This means the precursors needed to lead to a balance of the two binaries in order to react to form a Fe_2GeSe_4 without any leftover intermediate binaries. Additionally, it was found that extended times lead to GeSe_2 formation, likely due to the decomposition of Fe_2GeSe_4 . Therefore, to achieve phase pure Fe_2GeSe_4 , the precursor reactivity would need to lead to balanced binary intermediates. Then, the binaries need to react at a rate that forms Fe_2GeSe_4 before the degradation of the ternary begins. The complexity of the pathway illuminated why slight Fe-Se impurity likely remains in the optimized Fe_2GeSe_4 synthesis.

In contrast to the multi-step pathway for the $x=4$ system, $\text{Fe}_2\text{GeS}_{4-x}\text{Se}_x$ ($x=0.8$) particles were already present after 2 min, and the morphology matched that of the end particles (Fig. 3.4c). At this very early time aliquot, small (~4-8 nm), round particles were also observed. Based on elemental analysis these particles seem to be small Fe-Ge-S species. However, the size of these particles made elemental analysis difficult. After 7min, these small particles are absent and the FeGe impurity particles appear (Fig. 3.4d). Similar to the previously reported Fe_2GeS_4 synthesis, the solid solution reaction $\text{Fe}_2\text{GeS}_{4-x}\text{Se}_x$ NPs seems to directly or very rapidly nucleate. The FeGe impurity was found to form in the Fe_2GeS_4 system at conditions where the system reactivity was high and nucleation was favored.¹⁰ However, here attempts to completely avoid the FeGe impurity were unsuccessful. Therefore, this impurity represents the slight imbalance in the mixed chalcogen system.

These different pathways elucidated that, although LiHMDS aids in balancing reactivities to reach the desired end product, the S and Se interactions during the reaction must differ. Interestingly, attempts of

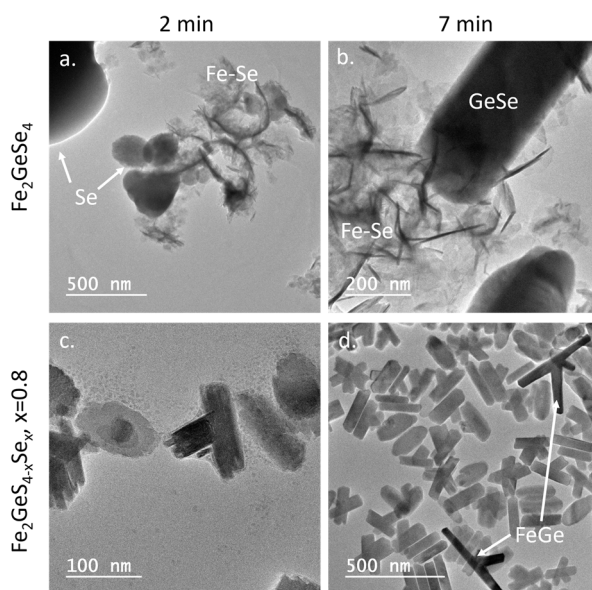


Figure 3.4. TEM images of the aliquots taken to understand the reaction pathway of a, b. Fe_2GeSe_4 and c, d. $\text{Fe}_2\text{GeS}_{4-x}\text{Se}_x$, $x=0.8$. a. After 2 min, the Fe_2GeSe_4 synthesis has mostly Fe-Se flakes and plates as well as some amorphous Se. b. After 7 min, the Fe-Se flakes and plates are still present as well as GeSe and Fe_2GeSe_4 (not shown), these transform to form the final Fe_2GeSe_4 particles shown in Fig. 3.1. c. After 2 min, the $\text{Fe}_2\text{GeS}_{4-x}\text{Se}_x$, $x=0.8$ synthesis has $\text{Fe}_2\text{GeS}_{4-x}\text{Se}_x$ particles already present as well as very small particles thought to be composed of Fe-Ge-S. d. After 7 min, the $\text{Fe}_2\text{GeS}_{4-x}\text{Se}_x$ particles are still present and FeGe particles are observed, a very similar composition and morphology as the final $\text{Fe}_2\text{GeS}_{4-x}\text{Se}_x$ particles shown in Fig. 3.2.

higher x -values (increased Se amount) led to binaries, even when the Fe_2GeSe_4 synthesis conditions were used. This could suggest that direct or rapid nucleation is favorable to achieve the full range of solid-solutions. To achieve this, likely the investigation of other chalcogen precursors would be required. Diphenyl diselenide was quickly tested instead of Se powder for $\text{Fe}_2\text{GeS}_{4-x}\text{Se}_x$, $x=0.8$ and 4. Surprisingly, for the $x=4$ synthesis, ternary formation was not achieved; however, for the $x=0.8$ synthesis, twinned quaternary particles with a composition closer to $x \sim 3.2$ (based on Rietveld refinement and EDS (Fig S3.15)) as well as FeS impurity particles were produced. This highlights that precursor reactivity greatly affects the end composition, where here diphenyl diselenide is more reactive than Se powder, leading to a higher end x -value compared to the imputed value for the $x=0.8$ synthesis. Yet, this increased precursor reactivity in the $x=4$ system caused the binaries to be favored over any ternary formation, illuminating the difficulty in finding reactivity balance.

3.4 Conclusions

In conclusion, we demonstrated that the reagent LiHMDS is a versatile reagent for balancing the reactivity of multiple cationic and anionic species in a multinary NP system by successfully synthesizing $\text{Fe}_2\text{GeS}_{4-x}\text{Se}_x$ ($x=0.8, 1, \text{ and } 4$). Additionally, LiHMDS leads to the dissolution of Se in OLA. From previous literature and ^1H NMR analysis this is likely due to the reductive nature of LiHMDS causing the formation of a soluble alkylammonium selenide species. Thus, S and Se form similar species upon reaction with LiHMDS and OLA in the injection solution. However, from a quick pathway study it was discovered that the formation of Fe_2GeSe_4 is a multistep pathway compared to the direct $\text{Fe}_2\text{GeS}_{4-x}\text{Se}_x$, $x=0.8$ and 1 formation. This suggests either differing reactivity of the analogous S or Se species or the active chalcogen species differ during the reaction. Nonetheless, the dissimilarity means slight binary formation was seen in these syntheses, and higher x -value solid-solutions were difficult to achieve. However, these initial syntheses elucidate a wealth of future investigations, including further pathway studies, testing varying chalcogen precursors, and expanded use of LiHMDS for ternary and quaternary metal chalcogenide solid solutions.

3.5 References

- (1) Lohse, S. E.; Murphy, C. J. Applications of Colloidal Inorganic Nanoparticles: From Medicine to Energy. *Journal of the American Chemical Society*. American Chemical Society September 26, 2012, pp 15607–15620. <https://doi.org/10.1021/ja307589n>.
- (2) Kovalenko, M. V.; Manna, L.; Cabot, A.; Hens, Z.; Talapin, D. V.; Kagan, C. R.; Klimov, V. I.; Rogach, A. L.; Reiss, P.; Milliron, D. J.; Guyot-Sionnest, P.; Konstantatos, G.; Parak, W. J.; Hyeon, T.; Korgel, B. A.; Murray, C. B.; Heiss, W. Prospects of Nanoscience with Nanocrystals. *ACS Nano* **2015**, *9* (2), 1012–1057. <https://doi.org/10.1021/nn506223h>.
- (3) Yarema, O.; Yarema, M.; Wood, V. Tuning the Composition of Multicomponent Semiconductor Nanocrystals: The Case of I-III-VI Materials. *Chemistry of Materials*. American Chemical Society March 13, 2018, pp 1446–1461. <https://doi.org/10.1021/acs.chemmater.7b04710>.
- (4) Reiss, P.; Carrière, M.; Lincheneau, C.; Vaure, L.; Tamang, S. Synthesis of Semiconductor Nanocrystals, Focusing on Nontoxic and Earth-Abundant Materials. *Chem. Rev.* **2016**, *116* (18), 10731–10819. <https://doi.org/10.1021/acs.chemrev.6b00116>.
- (5) Yarema, M.; Caputo, R.; Kovalenko, M. V. Precision Synthesis of Colloidal Inorganic Nanocrystals Using Metal and Metalloid Amides. *Nanoscale* **2013**, *5* (18), 8398–8410. <https://doi.org/10.1039/c3nr02076b>.
- (6) Kravchyk, K.; Protesescu, L.; Bodnarchuk, M. I.; Krumeich, F.; Yarema, M.; Walter, M.; Guntlin, C.; Kovalenko, M. V. Monodisperse and Inorganically Capped Sn and Sn/SnO₂ Nanocrystals for High-Performance Li-Ion Battery Anodes. *J. Am. Chem. Soc.* **2013**, *135* (11), 4199–4202. <https://doi.org/10.1021/ja312604r>.
- (7) Yarema, O.; Yarema, M.; Lin, W. M. M.; Wood, V. Cu–In–Te and Ag–In–Te Colloidal Nanocrystals with Tunable Composition and Size. *Chem. Commun.* **2016**, *52* (72), 10878–10881. <https://doi.org/10.1039/C6CC05571K>.
- (8) Yarema, O.; Bozyigit, D.; Rousseau, I.; Nowack, L.; Yarema, M.; Heiss, W.; Wood, V. Highly Luminescent, Size- and Shape-Tunable Copper Indium Selenide Based Colloidal Nanocrystals. *Chem. Mater.* **2013**, *25* (18), 3753–3757. <https://doi.org/10.1021/cm402306q>.
- (9) Yarema, O.; Yarema, M.; Bozyigit, D.; Lin, W. M. M.; Wood, V. Independent Composition and Size Control for Highly Luminescent Indium-Rich Silver Indium Selenide Nanocrystals. *ACS Nano* **2015**, *9* (11), 11134–11142. <https://doi.org/10.1021/acsnano.5b04636>.
- (10) Miller, R. C.; Neilson, J. R.; Prieto, A. L. Amide-Assisted Synthesis of Iron Germanium Sulfide (Fe₂GeS₄) Nanostars: The Effect of LiN(SiMe₃)₂ on Precursor Reactivity for Favoring Nanoparticle Nucleation or Growth. *J. Am. Chem. Soc.* **2020**, *142*, 42. <https://doi.org/10.1021/jacs.0c00260>.
- (11) De Jong, M.; Chen, W.; Angsten, T.; Jain, A.; Notestine, R.; Gamst, A.; Sluiter, M.; Ande, C. K.; Van Der Zwaag, S.; Plata, J. J.; Toher, C.; Curtarolo, S.; Ceder, G.; Persson, K. A.; Asta, M. Charting the Complete Elastic Properties of Inorganic Crystalline Compounds. *Sci. Data* **2015**, *2* (1), 1–13. <https://doi.org/10.1038/sdata.2015.9>.
- (12) Jain, A.; Ong, S. P.; Hautier, G.; Chen, W.; Richards, W. D.; Dacek, S.; Cholia, S.; Gunter, D.; Skinner, D.; Ceder, G.; Persson, K. A. Commentary: The Materials Project: A Materials Genome Approach to Accelerating Materials Innovation. *APL Materials*. American Institute of Physics Inc. July 18, 2013, p 11002. <https://doi.org/10.1063/1.4812323>.
- (13) Walker, B. C.; Agrawal, R. Contamination-Free Solutions of Selenium in Amines for Nanoparticle Synthesis. *Chem. Commun.* **2014**, *50* (61), 8331–8334. <https://doi.org/10.1039/c4cc02379j>.
- (14) Prodanov, M.; Diakov, M.; Vashchenko, V. A Facile Non-Injection Phosphorus-Free Synthesis of Semiconductor Nanoparticles Using New Selenium Precursors. *CrystEngComm* **2020**, *22* (4), 786–

793. <https://doi.org/10.1039/c9ce01467e>.
- (15) Ke, B.; Bai, X.; Wang, R.; Shen, Y.; Cai, C.; Bai, K.; Zeng, R.; Zou, B.; Chen, Z. Alkylthiol-Enabled Se Powder Dissolving for Phosphine-Free Synthesis of Highly Emissive, Large-Sized and Spherical Mn-Doped ZnSeS Nanocrystals. *RSC Adv.* **2017**, *7* (71), 44867–44873. <https://doi.org/10.1039/c7ra06873e>.
- (16) Gudelli, V. K.; Kanchana, V.; Vaitheeswaran, G. Predicted Thermoelectric Properties of Olivine-Type Fe₂GeCh₄ (Ch = S, Se and Te). *J. Phys. Condens. Matter* **2016**, *28*, 025502. <https://doi.org/10.1088/0953-8984/28/2/025502>.
- (17) Yu, L.; Lany, S.; Kykyneshi, R.; Jieratum, V.; Ravichandran, R.; Pelatt, B.; Altschul, E.; Platt, H. A. S.; Wager, J. F.; Keszler, D. A.; Zunger, A. Iron Chalcogenide Photovoltaic Absorbers. *Adv. Energy Mater.* **2011**, *1* (5), 748–753. <https://doi.org/10.1002/aenm.201100351>.
- (18) Deng, Z.; Han, D.; Liu, Y. Colloidal Synthesis of Metastable Zinc-Blende IV-VI SnS Nanocrystals with Tunable Sizes. *Nanoscale* **2011**, *3* (10), 4346–4351. <https://doi.org/10.1039/c1nr10815h>.
- (19) Huang, P. C.; Huang, J. L.; Wang, S. C.; Shaikh, M. O.; Lin, C. Y. Photoelectrochemical Properties of Orthorhombic and Metastable Phase SnS Nanocrystals Synthesized by a Facile Colloidal Method. In *Thin Solid Films*; Elsevier, 2015; Vol. 596, pp 135–139. <https://doi.org/10.1016/j.tsf.2015.09.081>.
- (20) Liu, Y.; Yao, D.; Shen, L.; Zhang, H.; Zhang, X.; Yang, B. Alkylthiol-Enabled Se Powder Dissolution in Oleylamine at Room Temperature for the Phosphine-Free Synthesis of Copper-Based Quaternary Selenide Nanocrystals. *J. Am. Chem. Soc.* **2012**, *134* (17), 7207–7210. <https://doi.org/10.1021/ja300064t>.
- (21) Wei, Y.; Yang, J.; Lin, A. W. H.; Ying, J. Y. Highly Reactive Se Precursor for the Phosphine-Free Synthesis of Metal Selenide Nanocrystals. *Chem. Mater.* **2010**, *22* (20), 5672–5677. <https://doi.org/10.1021/cm101308f>.
- (22) Thomson, J. W.; Nagashima, K.; Macdonald, P. M.; Ozin, G. A. From Sulfur-Amine Solutions to Metal Sulfide Nanocrystals: Peering into the Oleylamine-Sulfur Black Box. *J. Am. Chem. Soc.* **2011**, *133*, 5036–5041. <https://doi.org/10.1021/ja1109997>.

CHAPTER 4

EXPLORING SOLUTION PHASE SYNTHESSES EN ROUTE TO Cu_3SiSe_3 : A POTENTIAL PHOTOVOLTAIC MATERIAL

4.1 Overview

The near infinite amount of solar energy available makes photovoltaics an attractive energy alternative, but the use of environmentally friendly, earth-abundant materials could further enable the large-scale adoption of PV technology. A developing group of materials that has gained much attention is copper chalcogenide nanoparticles due to their exemplary intrinsic and structural properties including direct, optimal band gaps and low tolerances to defect formation. One such earth-abundant material is Cu_2SiSe_3 , which is predicted to have a direct band gap with near optimum energy for solar spectrum absorption. However, experimental reports are limited and previous synthetic reports require elevated temperatures. An investigation of hot injection, metathesis, and solvothermal solution phase syntheses are reported herein. Common precursors from literature were employed in hot injection and solvothermal methods and resulted in binary Cu/Se phases. In the metathesis reactions, a Zintl salt Si precursor was employed leading to Si incorporation by way of an intermediate binary Cu/Si phase. Finally, a future direction is described, with a focus on understanding the reactivity of group IV elements, Si, Ge, and Sn, in an amide-assisted synthesis of the Cu_2IVSe_3 materials.

4.2 Introduction

The combustion of fossil fuels produces carbon dioxide as a byproduct, which is the most abundant greenhouse gas contributing to climate change.¹ Photovoltaics offer an emission-free energy alternative by converting sunlight into electricity, avoiding the need to burn fossil fuels. Ternary copper chalcogenide materials have increasingly become of interest due to their earth-abundant and non-toxic nature, excellent electronic conductivity, and tunability of composition and properties.² Specifically, the exploration of multinary copper chalcogenides has contributed greatly to the advancement of photovoltaics, producing materials such as CZTS and CIGS.

One copper chalcogenide that has been named in theoretical studies, that examine materials with similar properties to the I-III-VI₂ chalcogenides and calculated their potential for use in solar cell applications, is Cu₂SiSe₃.^{3,4} The ternary compound Cu₂SiSe₃ is predicted to have a direct band gap of 1.34 eV with a diamond-like crystal structure (Fig. 4.1), and is composed of all environmentally friendly, earth abundant

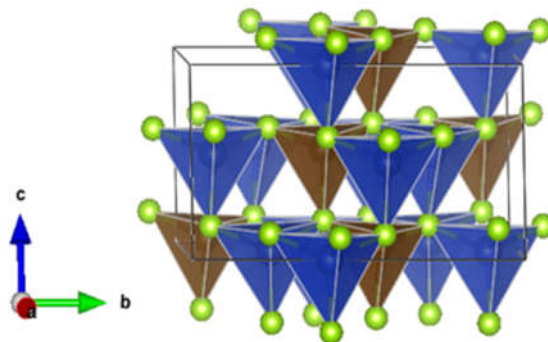


Figure 4.1. Crystal structure of Cu₂SiSe₃.

elements.⁴ Chen et al. first synthesized Cu₂SiSe₃ using a solid state method in which Cu₂Se, Si, and Se were placed in an evacuated silica tube along with the eutectic mixture KCl/LiCl and held at 550°C for 6 weeks.⁵ In 2015, El Anzeery et al. claimed to synthesize a Cu₂SiSe₃ thin film using a multi-step deposition and annealing technique.⁶ However, on closer inspection of their data, we believe a Cu-Se binary was formed rather than the desired ternary. Overall, synthesis methods for Cu₂SiSe₃ are lacking, which is intriguing as the ternary copper chalcogenides of the other group IV elements, Cu₂GeSe₃ and Cu₂SnSe₃, are well studied.² The work presented here is a compilation of attempts to synthesize Cu₂SiSe₃ through low temperature, solution phase synthetic routes. The work described here led to the research described in Chapter 2 of this dissertation. Therefore, for this chapter, the original thought processes are described with additional commentary based on what we learned in subsequent work. We then discuss possible future studies that examine the copper group IV chalcogenides as a whole, to understand reactivity differences and trends. This exploration could not only lead to the synthesis of Cu₂SiSe₃, but more interestingly lead to versatile synthesis methods.

Three solution methods for synthesis of Cu_2SiSe_3 nanocrystals are explored herein: hot injection, solvothermal, and metathesis reactions. Each of these methods have previously been used for nanocrystal synthesis and provide different modes of control.^{2,7-9} The hot injection solution method provides control over morphology and composition with good size monodispersity.¹⁰ Metathesis reactions take advantage of Le Chatelier's principle by forming an insoluble salt which causes equilibria to shift toward desired products. Solvothermal methods allow for increased reactivity and precursor solubility giving access to differently shaped, high quality nanoparticles.² The investigation of these three methods provided a scope of the distribution of products available.

4.3 Experimental

Materials and Methods. Anhydrous copper (II) chloride (CuCl_2 , 97%, Ridel-deHaën), copper (I) chloride (CuCl , 97%, Strem), silicon tetrachloride (SiCl_4 , 99%, Aldrich), magnesium granules (Mg, 99.8%, Alfa Aesar, -12+50 mesh), silicon powder (Si, 99%, Strem), selenium powder (Se, 99.99%, Strem), magnesium silicide (Mg_2Si , 99.99%, Aldrich) selenium dioxide (SeO_2 , 99.9%, Aldrich), selenium tetrachloride (SeCl_4 , Johnson Matthey Catalog Company, 99.5%), trioctylphosphine (TOP, 97%, Aldrich), trioctylphosphine oxide (TOPO, 99%, Aldrich), octyldecylphosphonic acid (ODPA, PCI synthesis), and ethylenediamine (En, 99%, Alfa Aesar) were used as packaged and received. Oleylamine (OLA, 70% Technical grade, Aldrich), 1-dodecanethiol (DDT, $\geq 98\%$, Aldrich), diphenyl ether (99%, Acros Organics) and octadecene (ODE, 90% Technical grade, Aldrich) were sparged with N_2 before use. OLA and DDT were sparged for 2 hr under gentle heating before use. Tetrahydrofuran (THF) was dried and deoxygenated using standard procedures with a MBraun solvent-purification system. Anhydrous dimethoxyethane (Glyme, 99.5%, Sigma-Aldrich) was distilled over potassium metal (K, 99.95%, Sigma-Aldrich) and phenanthrene (98%, Aldrich). All reactions were performed under inert N_2 atmosphere unless specified otherwise.

Materials characterization. The structure of the resulting nanoparticles was characterized using powder X-ray diffraction (PXRD). Samples were suspended in chloroform and drop cast onto a p-type

boron-doped Si Zero Diffraction Wafer. Samples were then exposed to a Cu K α radiation ($\lambda=1.54 \text{ \AA}$) source on a Bruker D8 Discover Powder X-ray Diffractometer to obtain X-Ray patterns.

The morphology of the nanoparticles was explored with a JEOL JSM-6500F scanning electron microscope (SEM) with the ability to also examine the composition of the nanoparticles through energy dispersive X-ray spectroscopy (EDS).

Cu₂SiSe₃ Nanocrystal Hot-Injection Synthesis. These reactions were modified from the synthesis of CuSbS₂ nanoparticles reported by Yan et al.¹² Both double injection and single injection methods were tried with various precursors. For a general double injection procedure, 0.118 g of CuCl₂ (0.873 mmol) was measured into a 50 mL three-neck round bottom flask. The reaction flask was fitted with a reflux condenser, a glass stir bar, and a thermocouple. The CuCl₂ was dissolved in OLA (4 mL) and attached to a Schlenk line under N₂ gas. The reaction was then heated to 110°C, pumped and purged three times, and finally left under vacuum for 15-60 minutes to ensure the solution was fully degassed. The reaction temperature was then raised to 150-160°C to allow OLA to reduce Cu, seen by the reaction changing from a blue color to an orangish-yellow color. The CuCl₂ solution was cooled to 50°C before the Se precursor and 0.05 mL SiCl₄ (0.436 mmol) were rapidly and simultaneously injected. The Se precursor was formed by sonicating 0.108 g Se powder (1.309 mmol) with OLA (1mL) and DDT (1mL) until it was fully dissolved. After the injection, a nucleation and growth period of 10 min was allowed followed by cooling and transferring of the reaction solution into glass vials to quench particle growth. The resulting particles were subsequently washed then centrifuged until the supernatant was clear. Each wash consisted of toluene (~1mL) to suspend the particles and ethanol (~4mL) to flocculate the particles. The final pellet was placed in chloroform and sonicated to fully disperse the product. For a single injection both the Cu precursor and SiCl₄ were initially added to the 50 mL three-neck round bottom flask. Once the reaction was added to the Schlenk line under N₂, it was immediately heated to 150-160°C rather than degassing at 110°C due to the low boiling point of SiCl₄. Finally, for a single injection, the Se precursor, Se/OLA/DDT, was injected at 150°C rather than 50°C.

Mg₂Si Solid State Synthesis. This procedure was modified from the Li et al. synthesis of Mg₂Si.¹¹ Elemental silicon (0.348 g, 12.34 mmol) and elemental magnesium (0.607 g, 24.69 mmol) in a ~1% stoichiometric excess were placed in a carbon coated silica tube. The tube was then evacuated, sealed, and heated to 700°C at a rate of 10°C/min. The temperature was maintained for three days and then allowed to naturally cool to room temperature. The resulting pellet was a deep blue color which was ground into a fine powder. The PXRD confirmed the Mg₂Si phase had been made, but unreacted Si was also present.

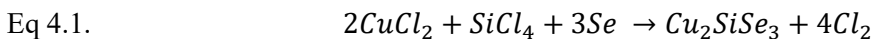
Cu₂SiSe₃ Nanocrystal Metathesis Synthesis. This method was modified from the silicon nanoparticle synthesis designed by Yang et al.⁸ Reaction conditions were varied including reaction time, amounts of precursors, precursor identities, and reaction solvent which subsequently determines the reaction temperature due to different boiling points. General procedure includes the addition of 0.175 g CuCl₂ (1.3 mmol) and 0.050 g Mg₂Si (0.65 mmol) in a 2:1 molar ratio to a 50 mL three-necked round bottom flask which was fitted with a Teflon stir bar, reflux condenser, and thermocouple. Glyme, diphenyl ether, THF, OLA or En (20 mL) was added to the reaction flask which was then moved to a Schlenk line and either purged with N₂ for approximately 5 minutes or pumped and purged three times before heating to reflux or a specified temperature. Temperature was maintained for either 24 or 48 hr, unless otherwise noted. To monitor the intermediate products, 1.5 mL aliquots were removed with a glass luer lock syringe. The aliquots were washed in the same fashion as stated for the hot injection reactions and were washed until the supernatant was clear. Next, a Se precursor was injected into the Cu/Si solution with a glass luer lock syringe and allowed to react for 5, 10, or 60 min. The Se precursors were prepared by placing 0.153 g Se powder (1.95 mmol) or 0.217 g SeO₂ (1.95 mmol), OLA (1 mL) and DDT (1 mL) into a scintillation vial and sonicated until Se was fully dissolved. After the given time, the reaction solution was quenched through quick cooling by the removal of the solution to glass vials. The washing procedure was duplicated from the hot injection synthesis. This procedure was further varied for the additional Se precursors: TOPSe, ODESe, and SeCl₄. These procedure variations are explained in the results and discussion section.

Cu₂SiSe₃ Nanocrystal Solvothermal Synthesis. The synthesis described here was adapted from Liang Shi et al. literature protocol for Cu₂ZnSnSe₄ nanosheets.⁹ Stoichiometric equivalents 2:1:3 of CuCl₂, SiCl₄, and Se powder, respectively, were either premixed in a beaker or placed directly into a 23 mL Teflon liner with ethylenediamine (10 mL). The liner was then sealed in a stainless steel autoclave and heated to 200-210°C for either 18, 24, or 44.5 hr. After the specified reaction time, the autoclave was allowed to naturally cool to room temperature. The resulting particles were washed with distilled water and then ethanol. Particles were washed twice with each solvent and centrifuged between every wash. The particles were then dried in air overnight and finally suspended in chloroform.

4.4 Results and Discussion

4.4.1 Cu₂SiSe₃ Nanocrystal Hot-Injection Synthesis. Hot injection syntheses instantaneously administer a high precursor concentration into a hot organic surfactant, allowing a quick nucleation and a slow nanoparticle growth. The separation of these steps is the reason hot injections afford excellent monodispersity and size control.^{2,12} Important factors to be considered include precursor reactivity, the organic solvent, and the capping surfactant. The reactions reported here originally adopted the high boiling point and commonly used organic surfactant oleylamine, which also acted as a solvent for the Cu and Se precursors. Electron donating amines coordinate well with Cu and the long fatty chain prevents the agglomeration of particles making OLA a good capping agent.¹³ For the Cu precursor, Cu²⁺ is more shelf stable than Cu⁺ and OLA is known to act as a reducing agent at elevated temperatures^{13,14}, therefore a Cu precursor in the 2+ oxidation state, CuCl₂, was first heated in OLA to afford the active Cu⁺ species. For the Se precursor, a mixture of OLA and DDT was used to fully dissolve Se powder into Se₈²⁻ and avoid introducing a phosphine to the system, as is common in similar reactions.¹⁵ Finally, SiCl₄ was selected as a Si precursor because it is a liquid at room temperature which avoids complicating the system with another solvent, and Si is already in the correct oxidation state, Si⁴⁺. Excluding any solvent interactions, the chosen precursors should react and form Cu₂SiSe₃ and Cl₂ gas (Equation 4.1). However, in solution-based nanoparticle syntheses many interactions contribute to the end result, including the solvents

present, the transformation of precursors to active monomers, and the reaction thermodynamic and kinetic pathways.¹⁶



Initially, a double injection was performed to ensure an instantaneous concentration increase of all precursors. CuCl_2 was heated in OLA to 160°C allowing the reduction and subsequent coordination of Cu, signified by color changes from blue (Cu^{2+}) to green (Cu^+) and then to orange (Cu^+/OLA complex). To avoid evaporation of SiCl_4 upon injection, the reaction temperature was reduced to 50°C before Se and SiCl_4 were injected. The resulting PXRD pattern of the black particles was inconclusive due to the analogous powder patterns of Cu_2SiSe_3 and $\text{Cu}_{1.8}\text{Se}$ (Fig. 4.2a). Further analysis of the particle composition was done by EDS which revealed less than 1% Si was present. This amount is within error of the instrument and it was concluded that the particles produced were $\text{Cu}_{1.8}\text{Se}$. To favor Si incorporation, another double injection was completed with 20 times more SiCl_4 precursor. Upon quenching the reaction, the black solution turned to an aliphatic solid, requiring an extra warming step for the washing procedure. The PXRD showed that Si had not been incorporated and CuSe had formed. It was hypothesized that SiCl_4 was either evaporating upon injection, seen by white vapor appearing, or the reaction energy was insignificant for a ternary phase to form.

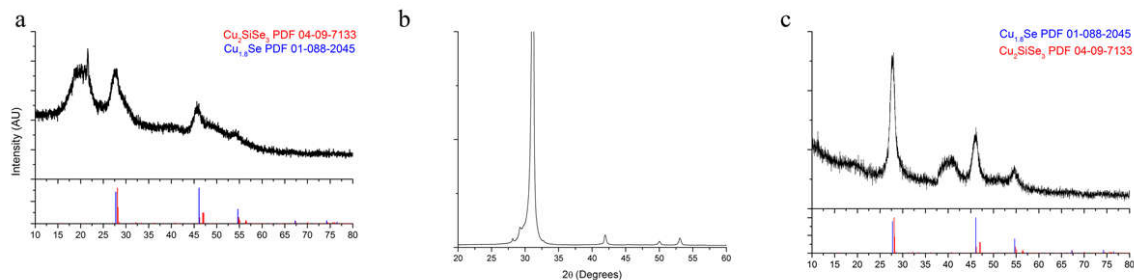
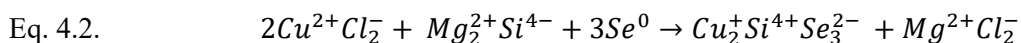


Figure 4.2. Hot injection PXRD patterns of a. double injection resulting in the production of $\text{Cu}_{1.8}\text{Se}$ and b. single injection resulting in a non-indexable pattern both made with stoichiometric equivalences of CuCl_2 , SiCl_4 , and Se powder. c. Single injection using stoichiometric equivalences of CuCl , SiCl_4 , and Se powder producing $\text{Cu}_{1.8}\text{Se}$.

To avoid SiCl_4 evaporation and to enable increased reaction temperatures, single injection methods were explored. It was speculated that premixing SiCl_4 with OLA and CuCl_2 before heating would allow the Si precursor to either solvate and coordinate with OLA or react with CuCl_2 . The solvation of Si could preserve the high concentration of each monomer at the point of nucleation, similar to a double injection. An initial reaction between Si and Cu could promote Si incorporation and still allow the desired Cu chalcogenide ternary to form when Se is injected since the bond dissociation energy of Cu-Si, 217 kJ/mol, is lower than that of Cu-Se, 255 kJ/mol, or Se-Si, 531 kJ/mol.^{5,6} A white vapor formed when SiCl_4 was mixed with the blue CuCl_2 and OLA solution which then changed from blue to a brownish red color when heated and finally black after Se was injected. Unfortunately, the PXRD of the product did not index to any known binary or ternary phase of Cu, Si, and Se (Fig. 4.2b). Moreover, by adding only SiCl_4 into OLA it was found that SiCl_4 reacts to form a white aliphatic solid. In an effort to avoid the undesired reaction between SiCl_4 and OLA, DDT was used as the organic surfactant and solvent. Without the presence of OLA the reduction of Cu^{2+} to its active species, Cu^+ , was no longer observed. A different Cu precursor in the 1+ oxidation state, CuCl , was chosen. The mixture of CuCl , SiCl_4 , and DDT was a white solution which turned yellow when heated and black after the injection of Se. From PXRD and EDS it was determined that yet again a Cu/Se phase, $\text{Cu}_{1.8}\text{Se}$, had formed (Fig. 4.2c). The hot injection experiments continually favored the production of Cu/Se phases and thus no further analysis of the solvent role was done, and a new method was explored.

4.4.2 Cu_2SiSe_3 Nanocrystal Metathesis Synthesis. The incorporation of Si has proven to be a difficult task, necessitating a search for a different Si precursor. A report by the Kauzlarich group on Zintl salts gave insight to a new Si precursor. The salts, which are composed of an alkali or alkaline earth metal and a post-transition metal or main group metalloid, were used to synthesize Si nanoparticles.⁸ The salts can display both ionic and covalent bond behavior¹⁷, leading to interesting compounds such as Mg_2Si . A metathesis reaction using Mg_2Si is proposed here en route to the ternary Cu chalcogenide Cu_2SiSe_3 . In the proposed reaction, Si is oxidized from the Si^{4-} to Si^{4+} oxidation state, allowing 8 electrons to reduce 2Cu^{2+}

to 2Cu^+ and 3Se^0 to 3Se^{2-} (Equation 4.2). Modeling the Yang et al. synthesis, distilled glyme acts as a non-coordinating solution for Mg_2Si , CuCl_2 and Se powder to react.⁸ The precursors were heated to reflux and allowed to react for 48 hr. The initial solution was grey with undissolved solid but after the 48 hr it turned into black particles suspended in solution. The PXRD of the particles revealed CuSe had been made along with unreacted Mg_2Si , Si and Se (Fig. 4.3). It is unclear if the Si observed is a product of the reaction or unreacted Si from the synthesis of Mg_2Si .



The products of this synthesis suggest that Cu/Se phases are still acting as extreme kinetic traps that prevent the reaction from reaching the desired thermodynamic equilibrium. The enthalpies of formation calculated by the Materials Project for CuSe, Cu_3Si and Cu_2SiSe_3 are -0.128, -0.055, and -0.283 eV/atom, respectively.^{18,19} These enthalpies show Cu_2SiSe_3 as the thermodynamic product which supports the experimental hypothesis that CuSe is acting as a kinetic trap. Although these enthalpy calculations assume

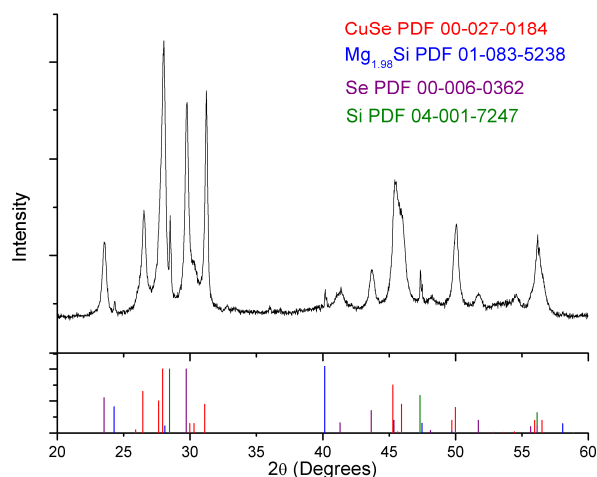


Figure 4.3. PXRD pattern of one pot metathesis reaction in which CuCl_2 , Mg_2Si , and Se powder were refluxed in distilled glyme for 48 hr. The resulting undesired particles consisted of CuSe, Si, and unreacted Mg_2Si and Se.

that the reactants are the elemental components, they aid in understanding the possible reaction pathways and led to the exploration of a different pathway in order to try and avoid Cu/Se binaries. The Shoemaker

group found that, through solid state methods, Fe_2SiS_4 formed at a lower temperature if the intermediate phases Fe_3Si and Fe_5Si_3 were reacted with elemental Se compared to the just the elements reacting.²⁰ Further, Lee et al. from our group found that the formation of Cu_3P intermediate before introducing Se, led to the successful synthesis of Cu_3PSe_4 .²¹ Based on these literature reports, a synthesis of a Cu/Si phase intermediate product was attempted before the Se precursor was introduced. CuCl_2 and Mg_2Si were refluxed in distilled glyme for two days. The reaction mixture started as a grey solution with solid present (Fig. 4.4a), then around 65°C the solution turned yellow with black solid on the sides of the flask which is predicted to be Cu^+ species in solution with solid Mg_2Si (Fig 4.4b), and finally at reflux the solution turned a reddish brown (Fig 4.4c) which darkened over the two days (Fig 4.4d). As Mg_2Si and CuCl_2 were refluxed in glyme, 1.5 mL aliquots were taken at 45 min, 5 hr, 22.5 hr, 48.5 hr, and 72 hr. Comparing the PXRD patterns reveals that after 22.5 hr Mg_2Si had fully reacted and the formation of two Cu/Si phases, Cu_3Si and $\text{Cu}_{0.9}\text{Si}_{0.1}$, was observed, with the $\text{Cu}_{0.9}\text{Si}_{0.1}$ appearing first and the Cu_3Si phase growing in (Fig 4.4e). We now understand that the Mg_2Si aids in the reduction of Cu^{2+} to Cu^0 which then will slowly react with the Si to form Cu_3Si . Although the resulting particles from the Mg_2Si and CuCl_2 reaction in glyme were never imaged, from our studies described in Chapter 2 of this dissertation, the

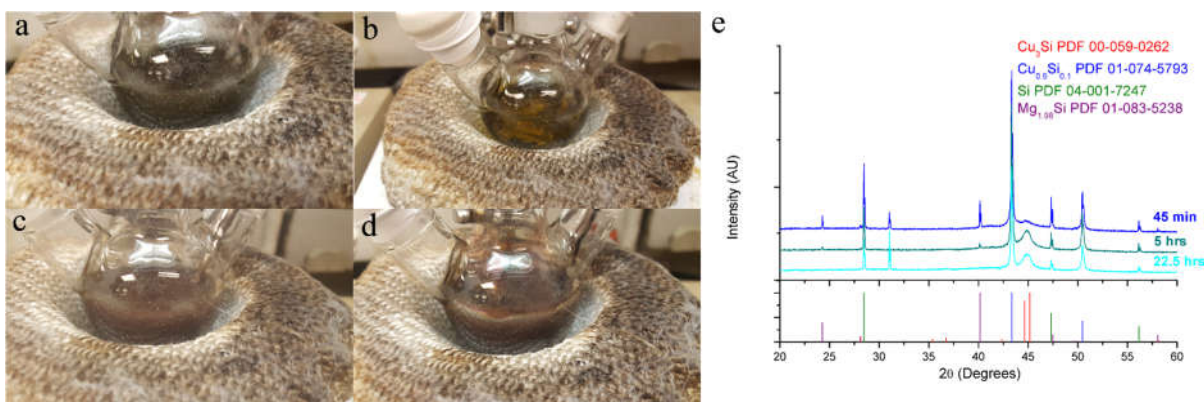
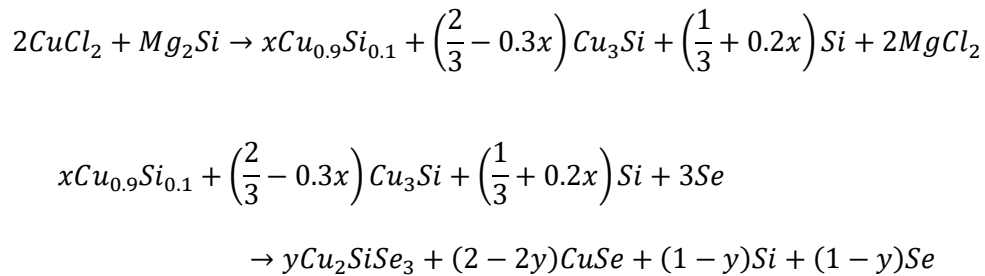


Figure 4.4. A Step-wise metathesis synthesis was performed by refluxing CuCl_2 and Mg_2Si in glyme for 48 hr. The reaction a. started as a grey solution with undissolved precursor then b. at 65°C the solution turned yellow with clumps of black solid and finally c. as the solution reached reflux it turned a brownish-red color which d. darkened over the reflux period. e., During the reaction aliquots were removed at 45 min, 5 hr, and 22.5 hr revealing in the PXRD that the Cu_3Si peak growing in and the Mg_2Si peak disappearing.

Cu₃Si particles are likely encased in a Si matrix. Further the Cu_{0.9}Si_{0.1} species may have a small amount of Si, however it should be considered as unreacted Cu.

After discovering the formation of Cu/Si phases was possible, the reaction was repeated with the added step of injecting Se powder dissolved in OLA and DDT. From the PXRD pattern, it was uncertain if the black solid formed was CuSe or Cu₂SiSe₃ (Fig 4.5a). From EDS, the Si atomic percent was 25-30% but the ratio of Cu:Si:Se was not 2:1:3 and thus it was hypothesized that both CuSe and Cu₂SiSe₃ were present. From these results, an updated reaction equation was formed to include the Cu/Si intermediates (Equation 4.3). There is still some uncertainty about the exact equivalents and in order to balance the final equation unreacted Se was added to the equation. Unreacted Se would not be seen in the PXRD because the dissolved excess Se would have been removed during the washing steps.

Eq. 4.3.



Particles synthesized in glyme (glyme NPs) seem to be a mixture of Cu₂SiSe₃ and CuSe. Comparatively, the particles synthesized in THF (THF NPs) seem to be comprised mostly of CuSe and Si particles. The PXRD pattern of the glyme NPs (Fig. 4.5a) has two broadly defined peaks between 52° and 57° 2θ that match the Cu₂SiSe₃ pattern. In contrast, there is only one broad peak present in this 2θ range in the PXRD pattern of the THF NPs (Fig. 4.5b) which matches the pattern of CuSe. The THF NP pattern had clear, sharp Si peaks at 28.5°, 47.3°, and 56.1° 2θ which were nonexistent in the glyme NP pattern. From the glyme NP EDS map (Fig. 4.5c) it seems that Si (red color) is incorporated but in the THF NP

EDS map (Fig. 4.5d) it appears that Si (pink color) is segregated into Si clusters. The two large Si clusters in the glyme EDS map are assumed to be unreacted Si from the synthesis of Mg_2Si .

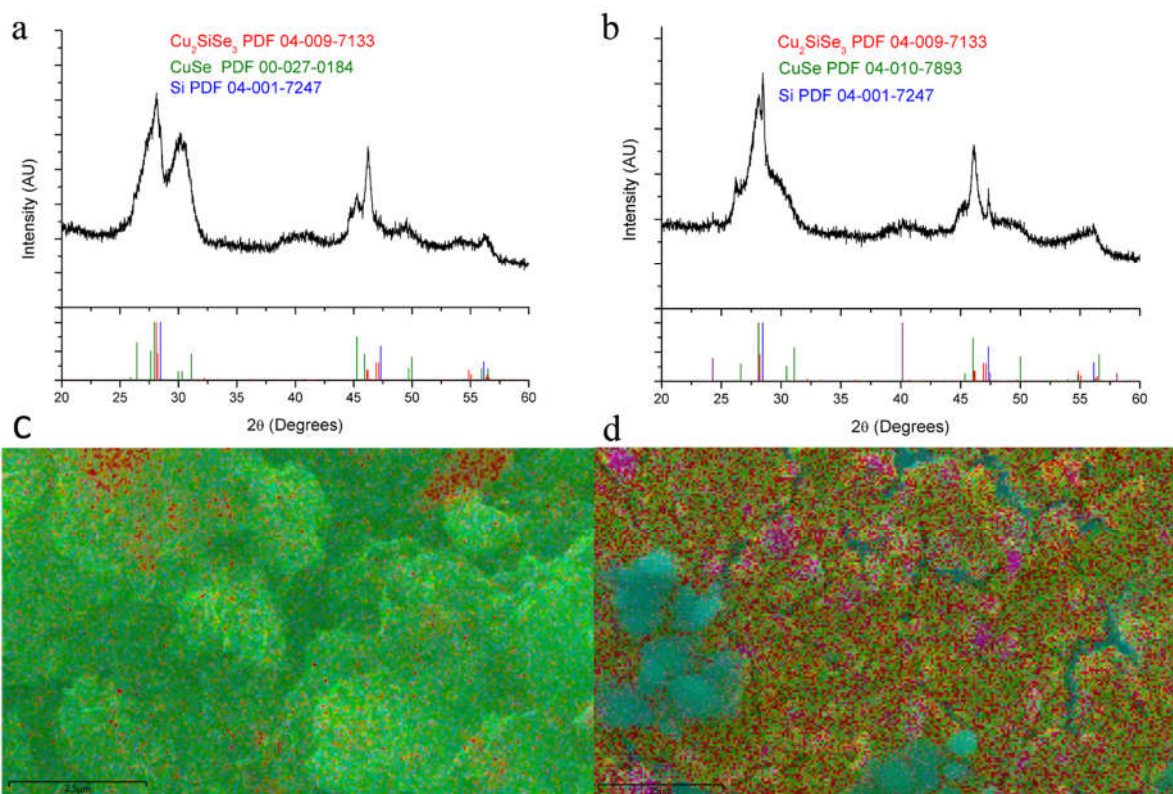


Figure 4.5. Comparison of step-wise metathesis reactions refluxed in (a/c) glyme and (b/d) THF with Se precursor injected. The XRD of the a. refluxed in glyme particles reveals Si was likely incorporated due to the lack of elemental Si peaks and more Cu_2SiSe_3 characteristic peaks but the b. refluxed in THF particles have more $CuSe$ characteristic peaks and elemental Si is present. This is further supported by the SEM-EDS maps of c. the glyme particles showing Si dispersed throughout the image (shown in red), and d. the THF particles showing Si isolated in small clumps (shown in pink). The two isolated red spots in c. are assumed to be unreacted Si powder from the Mg_2Si reaction.

Analyzing this data with a new perspective, the original hypothesis that the injection of Se/OLA/DDT into the reaction solution ($Cu_3Si/Cu_{0.9}Si_{0.1}$ in glyme) leads to Cu_2SiSe_3 and $CuSe$, is likely not true. We now know that the reaction between $CuCl_2$ and Mg_2Si produces Cu particles and an amorphous Si species, which Cu diffuses into to form Cu_3Si particle with a Si matrix. As glyme has such a low boiling point, a large amount of unreacted Cu (or $Cu_{0.9}Si_{0.1}$) remains, as seen in the XRD (Fig. 4.4e). Additionally, the Mg_2Si precursor has been consumed meaning amorphous Si is likely present, which is

not detectable by PXRD. Therefore, when the Se/OLA/DDT solution is injected, it would react with the Cu in solution to form CuSe, and the amorphous Si would still be present. Obviously, it is difficult to know exactly how the reaction is proceeding without attempting to directly investigate the speciation. However, from our study on the CuCl₂ and Mg₂Si reaction to form Cu₃Si it is unlikely that Cu₂SiSe₃ had been formed. As further evidence of this, both the optimized Cu₃Si@Si matrix particles described in Chapter 2 as well as Cu₃Si particles described by the Schaak group²² were reacted with Se/OLA/DDT and neither generated Cu₂SiSe₃.

Yet, as it was originally hypothesized that some Cu₂SiSe₃ had been formed, further studies to produce Cu₃Si over the Cu_{0.9}Si_{0.1} species were done. These studies included increasing the starting amount of Mg₂Si as well as injecting SiCl₄, with the hypothesis that this would result in less unreacted Cu. Additionally, other solvents such as diphenyl ether, ethylene diamine, and OLA were investigated. This is how the research reported in Chapter 2 began, and for more information, we refer the reader to Chapter 2 of this dissertation.

Simultaneously to investigating the solvent system and Si precursors, the identity of the Se precursor was also explored. The reactivity of the Se precursor could influence the incorporation of Si into the system. The reaction time after the Se precursor, Se/OLA/DDT, was injected was investigated by both shortening the reaction time to 5 min and extending it to 60 min. When the Se precursor has an abbreviated growth time the resulting PXRD pattern shows that the formation of CuSe and Si occurs relatively quickly (Fig 4.6a). According to the PXRD pattern and EDS of the particles (Fig 4.5a and 4.5c, respectively) allowed a 10 min growth time, Cu₂SiSe₃ may start to grow in, but with an extended growth time an additional Cu/Se phase, Cu_{1.82}Se, begins to form (Fig 4.6b). This time experiment shows that although there is evidence that Cu₂SiSe₃ is formed after the 10 min growth time, Cu/Se binary phases are always present and therefore the investigation of different Se precursors is necessary to find a different reaction pathway to Cu₂SiSe₃.

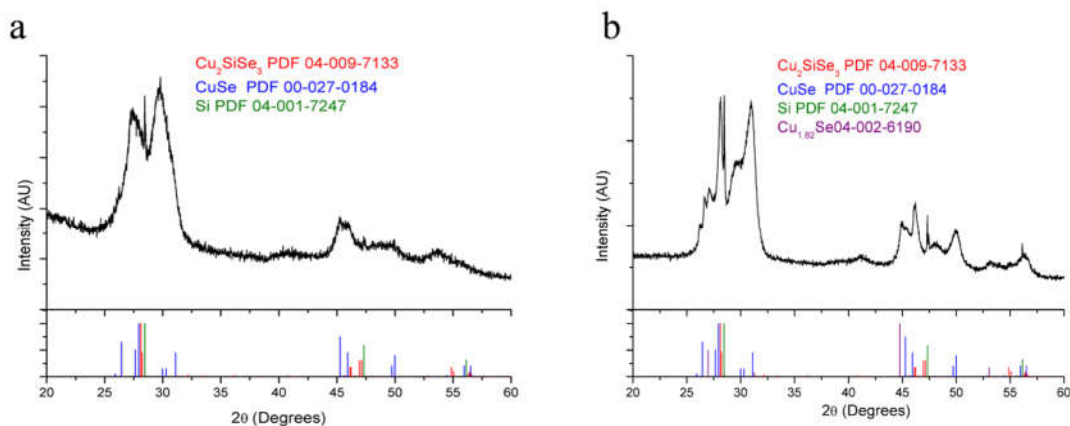


Figure 4.6. The reaction time allowed after injection of the Se precursor was varied from the originally chosen 10 min to a. 5 min and b. 60 min. The PXRD of the shortened reaction period is more characteristic of CuSe and PXRD of the lengthened period seems to have more Cu_2SiSe_3 , characteristics but also CuSe and $\text{Cu}_{1.82}\text{Se}$.

A common Se precursor in I-III-VI nanoparticle syntheses is TOPSe.^{23,24} In comparison to the Se/OLA/DDT precursor, TOPSe should be a less reactive precursor because in order for Se to be released, a phosphorus/selenium double bond (dissociation energy=364 kJ/mol) must be broken compared to Se-Se single bonds (dissociation energy=172 kJ/mol) of the Se/OLA/DDT active species, Se_8^{2-} .^{15,25,26} A less reactive Se precursor would slow the release of Se, which could avoid the CuSe byproduct by slowing the reaction of Se with the Cu formed after Se reacts with Cu_3Si and $\text{Cu}_{0.9}\text{Si}_{0.1}$. The procedure was adapted from Ruberu et al. synthesis.²³ The glyme metathesis products, Cu_3Si and $\text{Cu}_{0.9}\text{Si}_{0.1}$, were put into a three-neck round bottom flask with ODPa and TOPO then heated to 100°C where the system was placed under vacuum for 15 min. After being degassed for 15 min, the solution was heated to 320°C under N_2 gas, then cooled to 120°C where a second 15 min degas was done. Finally, the solution was placed under N_2 gas and heated to 320°C where TOP (1 mL) was injected then a pre-dissolved 1:1 molar ratio of Se in TOP was injected and allowed to react for 85 min. Contrary to what was predicted, the PXRD of the resulting particles showed that the TOPSe precursor led to the production of Cu_2Se .

Another common Se precursor, ODESe, was examined due to its success in forming Cu_3PSe_4 nanoparticles from Cu_3P intermediate nanoparticles.²⁸ Although it is difficult to compare Se precursor

reactivity across Se precursor types, Bullen et al. were able to compare the reactivity of ODE-Se and TOPSe precursors in a model CdSe system, and they supported their findings with the bond dissociation energies associated with these precursors²⁵, a common method to explain chalcogenide precursor reactivities.^{23,25,27} It was found that ODE-Se precursor, which due to its speciation requires the breaking of both Se-Se (172 kJ/mol) and Se=Se (272 kJ/mol) bonds, is more reactive than TOPSe, which requires the breaking of P=Se (364 kJ/mol) bonds. Therefore, we hypothesized this increased reactivity would increase the chances of the Cu and Si in the Cu/Si binaries to simultaneously react with Se to form the desired ternary. Using an adopted procedure from Bullen et al. synthesis²⁵, a 0.1 molar solution of Se powder in ODE was put in a three-neck round bottom flask along with the glyme metathesis products, Cu₃Si and Cu_{0.9}Si_{0.1}, and heated for 5 hr at 180°C. Unfortunately, the PXRD showed that this reaction, similar to TOPSe, resulted in various Cu/Se binaries.

These common Se precursors for nanoparticle syntheses consistently reacted selectively with Cu, omitting Si from the structure, thus a couple of nonconventional Se precursors were selected in the hope that they would afford better results. The zero oxidation state of Cu and Si in Cu₃Si and Cu_{0.9}Si_{0.1} means that both Cu and Si need to be oxidized in order to form Cu₂SiSe₃. The Se precursor SeO₂ requires Se to be reduced to form Cu₂SiSe₃ and therefore was selected as a possible unconventional Se precursor. Similar to Se powder, SeO₂ was dissolved in DDT (1 mL) and OLA (1 mL) then injected into Cu₃Si and Cu_{0.9}Si_{0.1} particles suspended in glyme and allowed to react for 10 min. Again, Si was expelled from the particles and CuSe and Se were the only patterns seen by PXRD. Finally, it was thought that if the reactivity of the Se precursor was increased specifically toward Si, then Si would be incorporated into the final structure. The Se precursor, SeCl₄, would, similarly to CuCl₂, react with Mg₂Si to produce the insoluble salt, MgCl₂, making it more reactive towards the Si precursor. All three precursors, CuCl₂, Mg₂Si, and SeCl₄, were placed in glyme in a 2:1:3 molar ratio, respectively, and heated to reflux, 82°C, for 24hr. Devastatingly, the resulting particles were a mix of various Cu/Se binaries, Se, and MgCl₂. Table 4.1 shows all the Se precursors screened along with the reason they were chosen, the reaction conditions,

the active species, and the results. From differing the Se precursor it was found that Se powder dissolved in OLA and DDT is the only precursor that leads to possible Si incorporation and further, even if Si was incorporated in the intermediate product, the addition of the Se precursor consistently leads to Cu/Se binaries.

Table 4.1. Se precursor Scope Reacted with the Cu/Si Binaries Produced in the Glyme Reaction.

Precursor	Reaction Conditions	Active Species	Reason	Results
Se powder	Step-wise metathesis in glyme	Se_8^{2-}	Starting point	CuSe and Cu_2SiSe_3
TOPSe	Step-wise metathesis in glyme then ODPa and TOPO	$\begin{array}{c} \text{Se} \\ \\ \text{R}-\text{P}-\text{R} \\ \\ \text{R} \\ \text{R}=\text{C}_8\text{H}_{17} \end{array}$	Slower release of Se due to Se=P having a larger bond dissociation energy than Se-Se.	Cu_2Se
ODESe	Step-wise metathesis in glyme then ODE	Alkane and alkenes bridged by Se short chains	Similar reaction produced Cu_3PSe_4 from Cu_3P	Various Cu/Se binaries
SeO_2	Step-wise metathesis in glyme	Unknown	Oxidizing agent	CuSe and Se
SeCl_4	One-pot metathesis in glyme	Unknown	Can react with Mg_2Si	Various Cu/Se binaries, Se, and MgCl_2

4.4.3 Cu_2SiSe_3 Nanocrystal Solvothermal Synthesis. Solvothermal syntheses are not limited by a solvent's boiling point, making increased reaction temperatures and pressures possible, causing elevated precursor solubility and reactivity.² The ability to increase the reactivity of the Cu, Si, and Se precursors could in turn produce Cu_2SiSe_3 and avoid any Cu/Se phases. The precursors, CuCl_2 , SiCl_4 , and Se powder were either pre-mixed or placed directly into an autoclave with ethylenediamine, a common solvothermal solvent. The autoclave was then heated to 200-210°C for 18, 24, or 44.5 hr. Every time trial's PXRD pattern had Cu_2Se and Cu_3Si peaks along with some unidentified peaks (Fig. 4.7a and b). For further identification, EDS was done on the 24 and 44.5 hr trials, revealing an insignificant amount of Si present. The 24 hr trial was not premixed, resulting in a diversity of particle morphology and size as seen in SEM (Fig. 4.7c). In contrast the 44.5 hr trial was premixed and resulted in hexagonal-shaped particles (Fig.

4.7d). Overall, it was concluded that solvothermal reaction conditions were ineffective in synthesizing Cu_2SiSe_3 and instead the production of the binary Cu_2Se was favored.

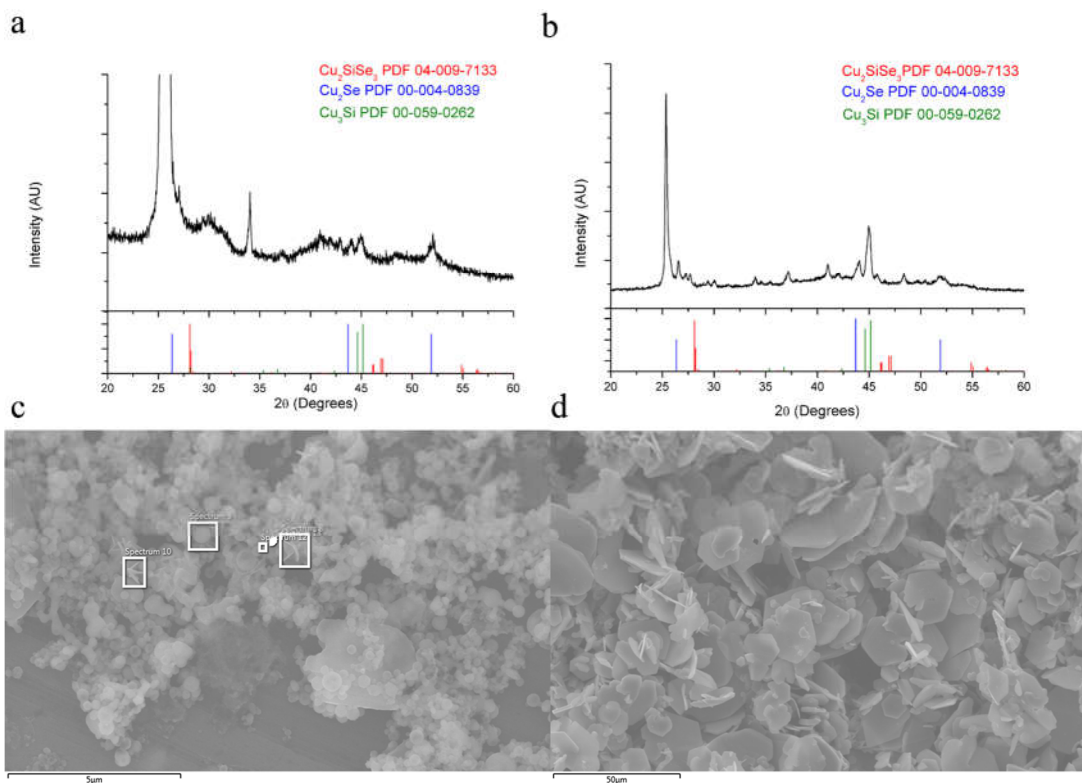


Figure 4.7. Solvothermal reactions in which the reaction mixture was a. and c. not premixed and heated at 200-210°C for 24 hr or b. and d. premixed and heated for 44.5 hr. The PXRDs for both the a. not premixed, 24 hr reaction and b. the premixed, 44.5 hr reaction showed Cu_2Se and Cu_3Si present along with various unindexed peaks. Further analysis by SEM-EDS determined there was no Si present and the c. morphology of the sample without premixing was very diverse compared to the d. hexagonal morphology found from the premixed sample.

4.5 Conclusions

Three solution methods were investigated in pursuit of a lower temperature synthesis of Cu_2SiSe_3 , a potential photovoltaic material. These syntheses were chosen due to the great size and morphology control that hot injection offers and the elevated precursor reactivity that solvothermal offers, but unfortunately both resulted in poor Si incorporation and produced Cu/Se alloy phases. The metathesis route reacted the Zintl salt Mg_2Si and CuCl_2 to yield the formation of two intermediate Cu/Si phases, Cu_3Si and $\text{Cu}_{0.9}\text{Si}$, which appeared to react with injected Se/OLA/DDT to form the desired product.

However, with further investigation of the Cu_3Si synthesis, it is now known that Cu_2SiSe_3 likely was not formed. Other efforts, including exploring Se precursors and adding an additional Si precursor, to selectively synthesize Cu_2SiSe_3 failed signifying a need for further exploration.

4.6 Outlook and Possible Future Directions

It is not uncommon for the incorporation of main group elements into ternary systems to be a difficult task as compared to the relatively soft transition metal cations because main group elements can adopt high oxidation states making them relatively hard cations.^{24,28} Thus, it is more favorable for the soft chalcogenides anions to react with the transition metal cation. For the successful production of a ternary compound, these metal cations with differing valency need to synchronously react with the chalcogenide. In other words, the reactivity of the system needs to be balanced. This can be very difficult as speciation in solution-based nanoparticle synthesis is complex and therefore elucidating the active monomer, determining its reactivity, and further how to tune that reactivity can be daunting.

There have been a multitude of reports investigating chalcogenide reactivity using model binary systems, leading to ranked precursors and a foreseeable continuum of precursors with varying reactivity.^{23,25,27,29,30} Additionally, several of these reports have compared different chalcogen (S vs Se) precursors to make solid solution or core/shell particles. Contrary to this, tuning main group element reactivity is limited and further understanding how that reactivity varies in a family of main group element is unclear.

This presents a gap in literature that the Cu_2IVSe_3 materials could fill. As stated at the beginning of this chapter, Cu_2GeSe_3 and Cu_2SnSe_3 have several reported nanoparticle syntheses², yet the nanoparticle synthesis of Cu_2SiSe_3 has not been achieved. By studying these materials in an environment where a similar group IV active species is present, trends between the group IV elements could be elucidated and reactivity tuned. One technique that has been used to increase the reactivity of a variety of metals and metalloids is the utilization of LiHMDS as a versatile reagent.^{31,32} Studies have shown that either metal-

silylamide species or, if an amine is present, a metal-alkylamide species forms, which easily decompose to release an active metal monomer. Therefore, investigating the speciation of the group IV elements when LiHMDS is included in the synthesis of the Cu_2IVSe_3 materials could be a method to understand the reactivity differences between this family of elements and possibly lead to the first nanoparticle synthesis of Cu_2SiSe_3 . Preliminary studies including LiHMDS in the synthesis of the Cu_2IVSe_3 compounds revealed that unsurprisingly the Cu_2GeSe_3 and Cu_2SnSe_3 syntheses were successful but the Cu_2SiSe_3 synthesis was not. This sets up a comparison between the systems, to elucidate why the Ge and Sn ternaries are successful but the Si ternary is not. Additionally, further variations in the synthesis parameters should be explored to reveal the fundamental interactions, transformations, and energies at play.

4.7 References

- (1) How Much Carbon Dioxide is Produced by Burning Gasoline and Diesel Fuel?-FAQ-U.S. Energy Information Administration (EIA) Eia.gov.
- (2) Coughlan, C.; Ibáñez, M.; Dobrozhan, O.; Singh, A.; Cabot, A.; Ryan, K. M. Compound Copper Chalcogenide Nanocrystals. *Chem. Rev.* **2017**, *117*, 5865–6109. <https://doi.org/10.1021/acs.chemrev.6b00376>.
- (3) Yu, L.; Kokenyesi, R. S.; Keszler, D. A.; Zunger, A. Inverse Design of High Absorption Thin-Film Photovoltaic Materials. *Adv. Energy Mater.* **2013**, *3* (1), 43–48. <https://doi.org/10.1002/aenm.201200538>.
- (4) Zhang, Y.; Wang, Y.; Zhang, J.; Xi, L.; Zhang, P.; Zhang, W. Pinning down High-Performance Cu-Chalcogenides as Thin-Film Solar Cell Absorbers: A Successive Screening Approach. *J. Chem. Phys.* **2016**, *144* (19), 194706. <https://doi.org/10.1063/1.4950818>.
- (5) Chen, X. –; Wada, H.; Sato, A.; Nozaki, H. Synthesis, Structure, and Electronic Properties of Cu₂SiQ₃ (Q=S, Se). *J. Alloys Compd.* **1999**, *290* (1), 91–96. [https://doi.org/10.1016/S0925-8388\(99\)00208-X](https://doi.org/10.1016/S0925-8388(99)00208-X).
- (6) Elanzeery, H.; Buffière, M.; Messaoud, K. Ben; Oueslati, S.; Brammertz, G.; Daif, O. El; Cheyns, D.; Guindi, R.; Meuris, M.; Poortmans, J. Multistep Deposition of Cu₂Si(S,Se)₃ and Cu₂ZnSiSe₄ high Band Gap Absorber Materials for Thin Film Solar Cells. *Phys. Status Solidi - Rapid Res. Lett.* **2015**, *9* (6), 338–343. <https://doi.org/10.1002/pssr.201510125>.
- (7) Yan, C.; Su, Z.; Gu, E.; Cao, T.; Yang, J.; Liu, J.; Liu, F.; Lai, Y.; Li, J.; Liu, Y. Solution-Based Synthesis of Chalcostibite (CuSbS₂) Nanobricks for Solar Energy Conversion. *RSC Adv.* **2012**, *2* (28), 10481–10484. <https://doi.org/10.1039/c2ra21554c>.
- (8) Yang, C. S.; Bley, R. A.; Kauzlarich, S. M.; Lee, H. W. H.; Delgado, G. R. Synthesis of Alkyl-Terminated Silicon Nanoclusters by a Solution Route. *J. Am. Chem. Soc.* **1999**, *121* (22), 5191–5195. <https://doi.org/10.1021/ja9828509>.
- (9) Shi, L.; Li, Q. Thickness Tunable Cu₂ZnSnSe₄ Nanosheets. *CrystEngComm* **2011**, *13* (21), 6507–6510. <https://doi.org/10.1039/c1ce05746d>.
- (10) Kwon, S. G.; Hyeon, T. Formation Mechanisms of Uniform Nanocrystals via Hot-Injection and Heat-up Methods. *Small* **2011**, *7* (19), 2685–2702. <https://doi.org/10.1002/smll.201002022>.
- (11) Li, G.; Gill, H. S.; Varin, R. A. Magnesium Silicide Intermetallic Alloys. *Metall. Trans. A* **1993**, *24* (11), 2383–2391. <https://doi.org/10.1007/BF02646518>.
- (12) Yin, Y.; Alivisatos, A. P. Colloidal Nanocrystal Synthesis and the Organic-Inorganic Interface. *Nature*. Nature Publishing Group September 29, 2005, pp 664–670. <https://doi.org/10.1038/nature04165>.
- (13) Mourdikoudis, S.; Liz-Marza, L. M. Oleylamine in Nanoparticle Synthesis. *Chem. Mater.* **2013**, *25*, 1465–1476. <https://doi.org/10.1021/cm4000476>.
- (14) Thomson, J. W.; Nagashima, K.; Macdonald, P. M.; Ozin, G. A. From Sulfur-Amine Solutions to Metal Sulfide Nanocrystals: Peering into the Oleylamine-Sulfur Black Box. *J. Am. Chem. Soc.* **2011**, *133*, 5036–5041. <https://doi.org/10.1021/ja1109997>.
- (15) Walker, B. C.; Agrawal, R. Contamination-Free Solutions of Selenium in Amines for Nanoparticle Synthesis. *Chem. Commun.* **2014**, *50* (61), 8331–8334. <https://doi.org/10.1039/c4cc02379j>.
- (16) Lee, J. M.; Miller, R. C.; Moloney, L. J.; Prieto, A. L. The Development of Strategies for Nanoparticle Synthesis: Considerations for Deepening Understanding of Inherently Complex Systems. *J. Solid State Chem.* **2019**, *273*, 243–286. <https://doi.org/10.1016/J.JSSC.2018.12.053>.
- (17) Kauzlarich, S. M. Zintl Phases with D-Metal. In *Comprehensive Inorganic Chemistry II*; Elsevier Ltd, 2013; pp 103–110.
- (18) Jain, A.; Ong, S. P.; Hautier, G.; Chen, W.; Richards, W. D.; Dacek, S.; Cholia, S.; Gunter, D.; Skinner, D.; Ceder, G.; Persson, K. A. Commentary: The Materials Project: A Materials Genome Approach to Accelerating Materials Innovation. *APL Materials*. American Institute of Physics Inc.

- July 18, 2013, p 11002. <https://doi.org/10.1063/1.4812323>.
- (19) De Jong, M.; Chen, W.; Angsten, T.; Jain, A.; Notestine, R.; Gamst, A.; Sluiter, M.; Ande, C. K.; Van Der Zwaag, S.; Plata, J. J.; Toher, C.; Curtarolo, S.; Ceder, G.; Persson, K. A.; Asta, M. Charting the Complete Elastic Properties of Inorganic Crystalline Compounds. *Sci. Data* **2015**, *2* (1), 1–13. <https://doi.org/10.1038/sdata.2015.9>.
 - (20) Jiang, Z.; Ramanathan, A.; Shoemaker, D. P. In Situ Identification of Kinetic Factors That Expedite Inorganic Crystal Formation and Discovery. *J. Mater. Chem. C* **2017**, *5* (23), 5709–5717. <https://doi.org/10.1039/C6TC04931A>.
 - (21) Lee, J. M.; Kraynak, L. A.; Prieto, A. L. A Directed Route to Colloidal Nanoparticle Synthesis of the Copper Selenophosphate Cu_3PSe_4 . *Angew. Chemie Int. Ed.* **2020**, *59* (8), 3038–3042. <https://doi.org/10.1002/anie.201911385>.
 - (22) McEnaney, J. M.; Schaak, R. E. Solution Synthesis of Metal Silicide Nanoparticles. *Inorg. Chem.* **2015**, *54*, 707–709. <https://doi.org/10.1021/ic502394u>.
 - (23) Ruberu, T. P. A.; Albright, H. R.; Callis, B.; Ward, B.; Cisneros, J.; Fan, H. J.; Vela, J. Molecular Control of the Nanoscale: Effect of Phosphine-Chalcogenide Reactivity on CdS-CdSe Nanocrystal Composition and Morphology. *ACS Nano* **2012**, *6* (6), 5348–5359. <https://doi.org/10.1021/nn301182h>.
 - (24) Yarema, O.; Yarema, M.; Wood, V. Tuning the Composition of Multicomponent Semiconductor Nanocrystals: The Case of I-III-VI Materials. *Chemistry of Materials*. American Chemical Society March 13, 2018, pp 1446–1461. <https://doi.org/10.1021/acs.chemmater.7b04710>.
 - (25) Bullen, C.; Van Embden, J.; Jasieniak, J.; Cosgriff, J. E.; Mulder, R. J.; Rizzardo, E.; Gu, M.; Raston, C. L. High Activity Phosphine-Free Selenium Precursor Solution for Semiconductor Nanocrystal Growth. *Chem. Mater.* **2010**, *22* (14), 4135–4143. <https://doi.org/10.1021/cm903813r>.
 - (26) Liu, H.; Owen, J. S.; Alivisatos, A. P. Mechanistic Study of Precursor Evolution in Colloidal Group II-VI Semiconductor Nanocrystal Synthesis. *J. Am. Chem. Soc.* **2007**, *129* (2), 305–312. <https://doi.org/10.1021/ja0656696>.
 - (27) Guo, Y.; Alvarado, S. R.; Barclay, J. D.; Vela, J. Shape-Programmed Nanofabrication: Understanding the Reactivity of Dichalcogenide Precursors. *ACS Nano* **2013**, *7* (4), 3616–3626. <https://doi.org/10.1021/nn400596e>.
 - (28) Reiss, P.; Carrière, M.; Lincheneau, C.; Vaure, L.; Tamang, S. Synthesis of Semiconductor Nanocrystals, Focusing on Nontoxic and Earth-Abundant Materials. *Chem. Rev.* **2016**, *116* (18), 10731–10819. <https://doi.org/10.1021/acs.chemrev.6b00116>.
 - (29) Smith, D. K.; Luther, J. M.; Semonin, O. E.; Nozik, A. J.; Beard, M. C. Tuning the Synthesis of Ternary Lead Chalcogenide Quantum Dots by Balancing Precursor Reactivity. **2011**. <https://doi.org/10.1021/nn102878u>.
 - (30) Hamachi, L. S.; Yang, H.; Jen-La Plante, I.; Saenz, N.; Qian, K.; Campos, M. P.; Cleveland, G. T.; Rreza, I.; Oza, A.; Walravens, W.; Chan, E. M.; Hens, Z.; Crowther, A. C.; Owen, J. S. Precursor Reaction Kinetics Control Compositional Grading and Size of CdSe_{1-x}S_x Nanocrystal Heterostructures. *Chem. Sci.* **2019**, *10* (26), 6539–6552. <https://doi.org/10.1039/c9sc00989b>.
 - (31) Yarema, M.; Caputo, R.; Kovalenko, M. V. Precision Synthesis of Colloidal Inorganic Nanocrystals Using Metal and Metalloid Amides. *Nanoscale* **2013**, *5* (18), 8398–8410. <https://doi.org/10.1039/c3nr02076b>.
 - (32) Kravchyk, K.; Protesescu, L.; Bodnarchuk, M. I.; Krumeich, F.; Yarema, M.; Walter, M.; Guntlin, C.; Kovalenko, M. V. Monodisperse and Inorganically Capped Sn and Sn/SnO₂ Nanocrystals for High-Performance Li-Ion Battery Anodes. *J. Am. Chem. Soc.* **2013**, *135* (11), 4199–4202. <https://doi.org/10.1021/ja312604r>.

APPENDIX A
SUPPLEMENTAL INFORMATION FOR CHAPTER 2: EXPLORING THE SOLUTION-BASED
METATHESIS PATHWAY TOWARD Cu_3Si FORMATION

Experimental for the Variations of Reaction Conditions: The experimental for the optimized $\text{Cu}_3\text{Si}@\text{Si}$ matrix particles can be found in the main text. The reaction conditions varied were the time, temp, precursor ratio, and solvent, see Table S1. Most variation follow the same procedure as the optimized reaction. However, in some cases, such as low boiling point solvents and the neat reaction, the procedure was slightly altered. Here we describe the slight alteration of the procedure, where other than the information stated here, the reactions follow the procedure for the optimal synthesis reported in the main text.

For low boiling point solvents, including glyme and diglyme, the degas step and the final reaction temperature were altered. After adding the reaction flask to the Schlenk line, instead of placing the reaction under vacuum for 45 min at 100 °C, the degas step included three quick oscillations between vacuum and N_2 . Additionally, as the boiling points of glyme and diglyme are much lower than 275 °C, instead these reactions were heated to reflux, 82 °C and 170 °C respectively.

For the neat or “no solvent” reaction, the optimal conditions were mimicked to the best of our ability. In an N_2 glovebox, CuCl_2 and Mg_2Si were weighed out. Using an agate mortar and pestle, the precursors were ground together until a visibly homogeneous powder, a bluish grey colored powder, was achieved. The powder was transferred air-free to an Ar glovebox, where the sample was split approximately in half. Half of the powder was pressed into a pellet and then placed into a quartz tube, and the other half was placed into a separate quartz tube as loose powder. Both tubes were sealed under a partial N_2 environment. Afterwards, both samples were placed in a furnace and heated to 275 °C at a ramp rate of 600 °C/hr, and then held at 275 °C for 18 hr before furnace cooling to room temperature. The resulting samples were a redish black color with white flecks. The sealed tubes were pumped back into a N_2 glovebox before cracking them open for characterization.

Table S2.1. Variations of reaction conditions with the optimal conditions highlighted.

Solvent	CuCl ₂ :Mg ₂ Si ratio	Degas Step	Reaction Temperature	Ramp Rate	Time
Oleylamine	2:1, 1.85:1, 1.75:1, 1.5:1	Under vacuum for 45 min at 100°C	275°C, 300°C	800°C/hr	8 hr or O.N. (17-18 hr), quenched into Toluene
Glyme	1.85:1	Quick 3 cycle pump/purge at room temp.	Refluxed at 82°C	800°C/hr	O.N. (17-18 hr), quenched into Toluene
Diglyme	1.85:1	Quick 3 cycle pump/purge at room temp.	Refluxed at 170°C	800°C/hr	O.N. (17-18 hr), quenched into Toluene
Squalane	1.85:1	Under vacuum for 45 min at 100°C	275°C	800°C/hr	O.N. (17-18 hr), quenched into Toluene
Octadecene	1.85:1	Under vacuum for 45 min at 100°C	275°C	800°C/hr	O.N. (17-18 hr), quenched into Toluene
No Solvent	1.85:1	Sealed in a quartz tube under partial N ₂	275°C	600°C/hr	O.N. (18 hr), furnace cooled

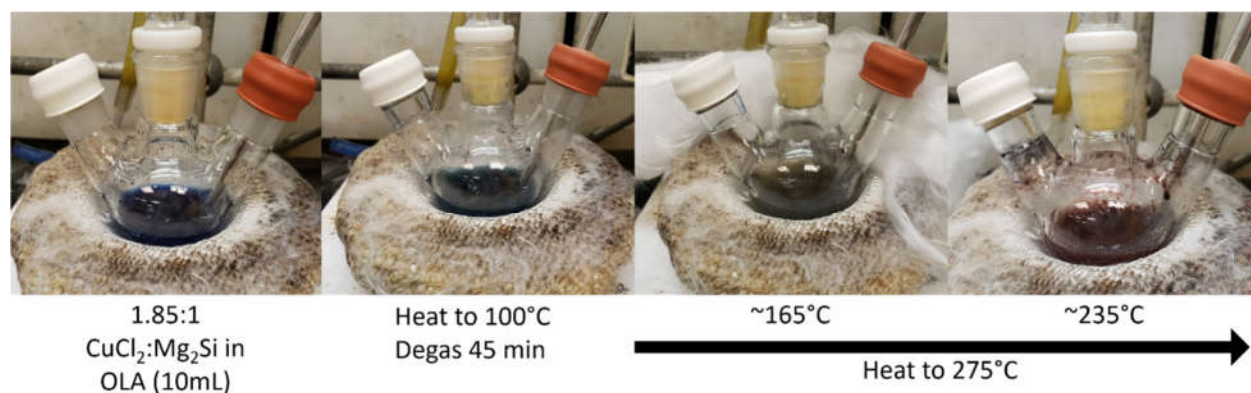


Figure S2.1. Color changes during the reaction between Mg₂Si with CuCl₂ in OLA. The solution starts as a deep blue color which transforms into a deep green/blue color after the solution is degassed at 100 °C for 45 min. As the solution is heated to the reaction temperature of 275 °C, the solution changes to a yellow solution with “black-looking” solid around 165 °C and then to a bright red solution around 235 °C. These color changes were found to correlate with the color changes seen for Cu²⁺ reduction to Cu⁺ and then to Cu⁰ in OLA.

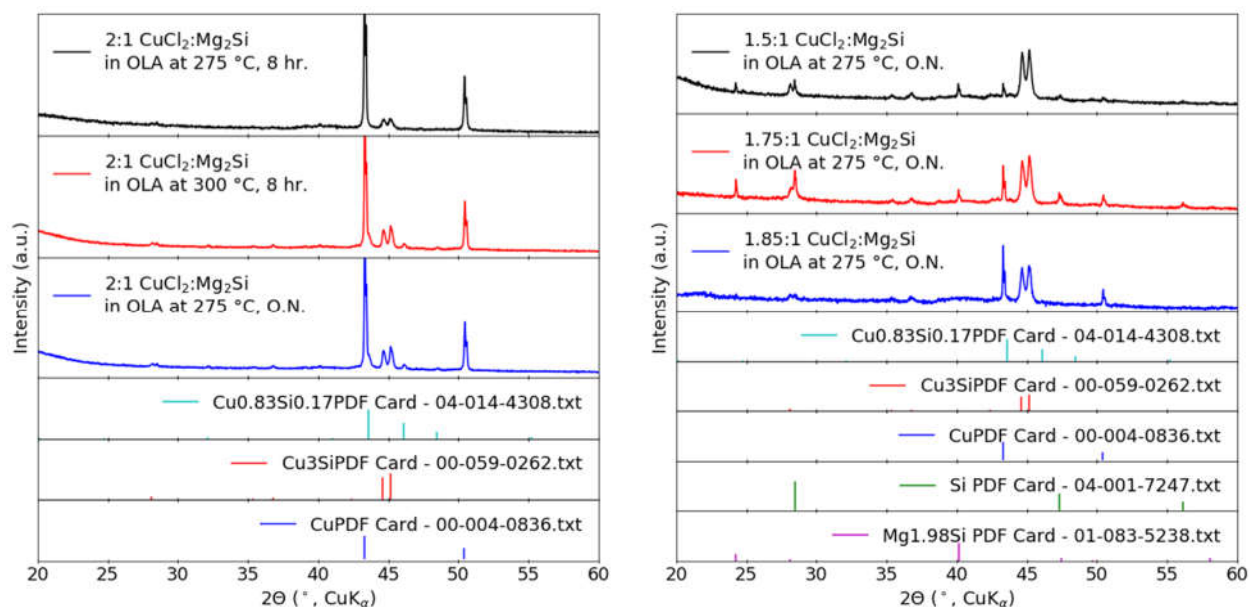


Figure S2.2. PXRDs of the optimization of the reaction between Mg_2Si and CuCl_2 in OLA by altering the precursor ratio, as well as the reaction time, and temperature. a. The ratio of $\text{CuCl}_2:\text{Mg}_2\text{Si}$ was held constant at 2:1 while the temperature and time were altered between 275 $^\circ\text{C}$ or 300 $^\circ\text{C}$ and 8 hr or overnight (ON), respectively. The increase in time or temperature increased Cu_3Si formation but Cu_5Si was also observed. b. The temperature and time were held constant at 275 $^\circ\text{C}$ and ON, while the ratio of $\text{CuCl}_2:\text{Mg}_2\text{Si}$ was varied from 1.5:1, 1.75:1, and 1.85:1. At lower ratios, relevant amounts of unreacted Mg_2Si was observed. Optimal conditions were found to be 1.85:1 $\text{CuCl}_2:\text{Mg}_2\text{Si}$ reacted at 275 $^\circ\text{C}$, ON.

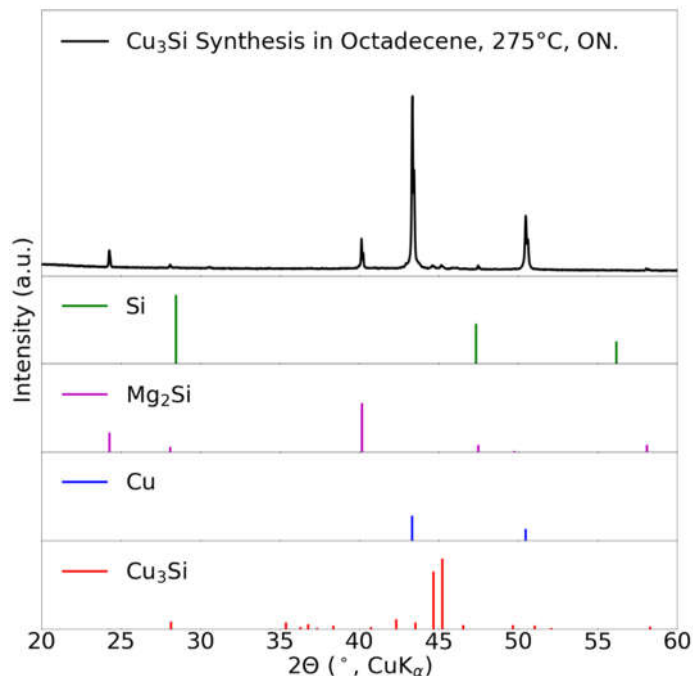


Figure S2.3. PXRD of the particles formed when CuCl_2 and Mg_2Si were reacted in 1-Octadecene at 275 °C, ON (17-18hr). Similar to the reaction in squalane, Figure 2.3c, minimal amounts of Cu_3Si were observed along with large amounts of Cu and a significant amount of unreacted Mg_2Si .

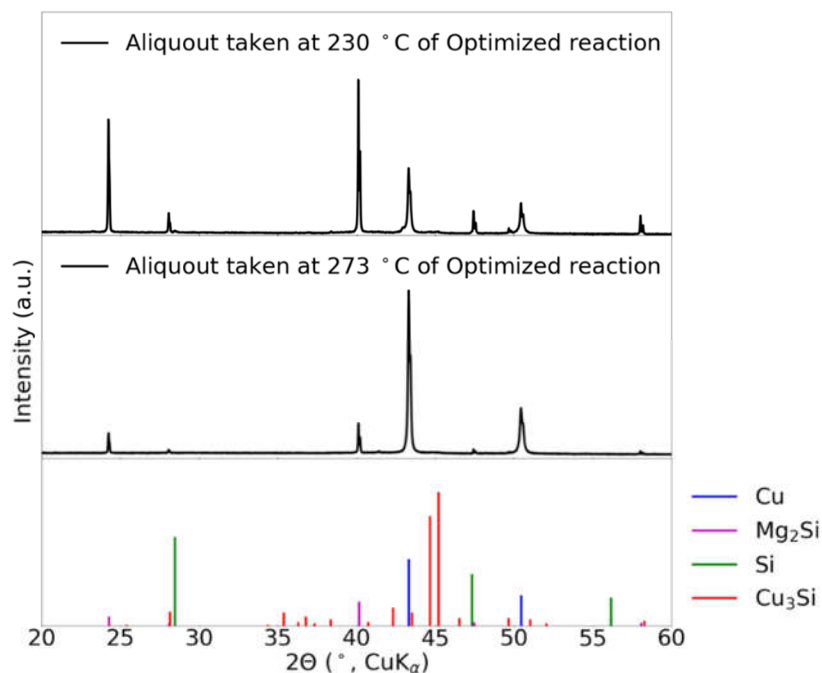


Figure S2.4. Aliquots were taken as the optimized $\text{Cu}_3\text{Si}@/\text{Si}$ matrix synthesis ramped to 275 °C a. The PXRD of the aliquot taken when the solution turned to bright red, around 230 °C. b. PXRD of the aliquot taken right before the final reaction temperature was reached, at 273 °C. These show the rapid decrease of Mg_2Si as Cu^0 is formed.

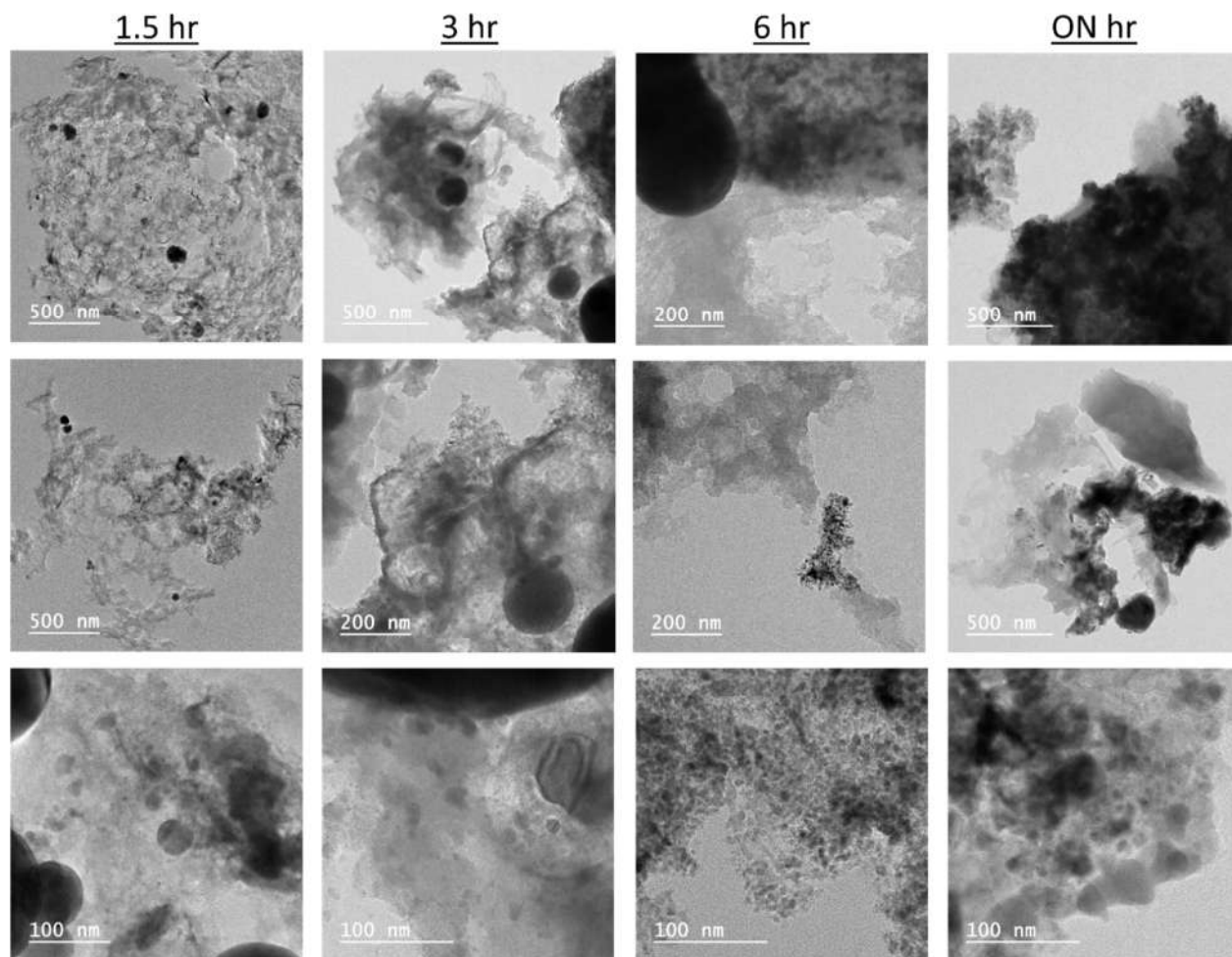


Figure S2.5. Representative TEM images at each of the reaction times. Col 1. Images of the 1.5 hr reaction showing large areas of Si matrix without Cu_3Si particles inside, Cu particles, and where Cu_3Si is present, it is densely packed. Col 2. Images of the 3 hr reaction showing mostly similar results as the 1.5 hr reaction, however slightly more Cu_3Si particles within Si matrixes could be found. Col 3. Images of the 6 hr reaction showing areas of more Cu_3Si particle within the Si matrixes. Areas of Si matrixes without Cu_3Si were still observed along with large Cu particles. Col 4. Images of the ON. reaction demonstrating the Cu_3Si particles within the Si matrixes are frequent throughout the sample. These particles have varying size and shape and in certain areas look agglomerated. Small areas of Si matrix without Cu_3Si particles and Cu particles were still observed.

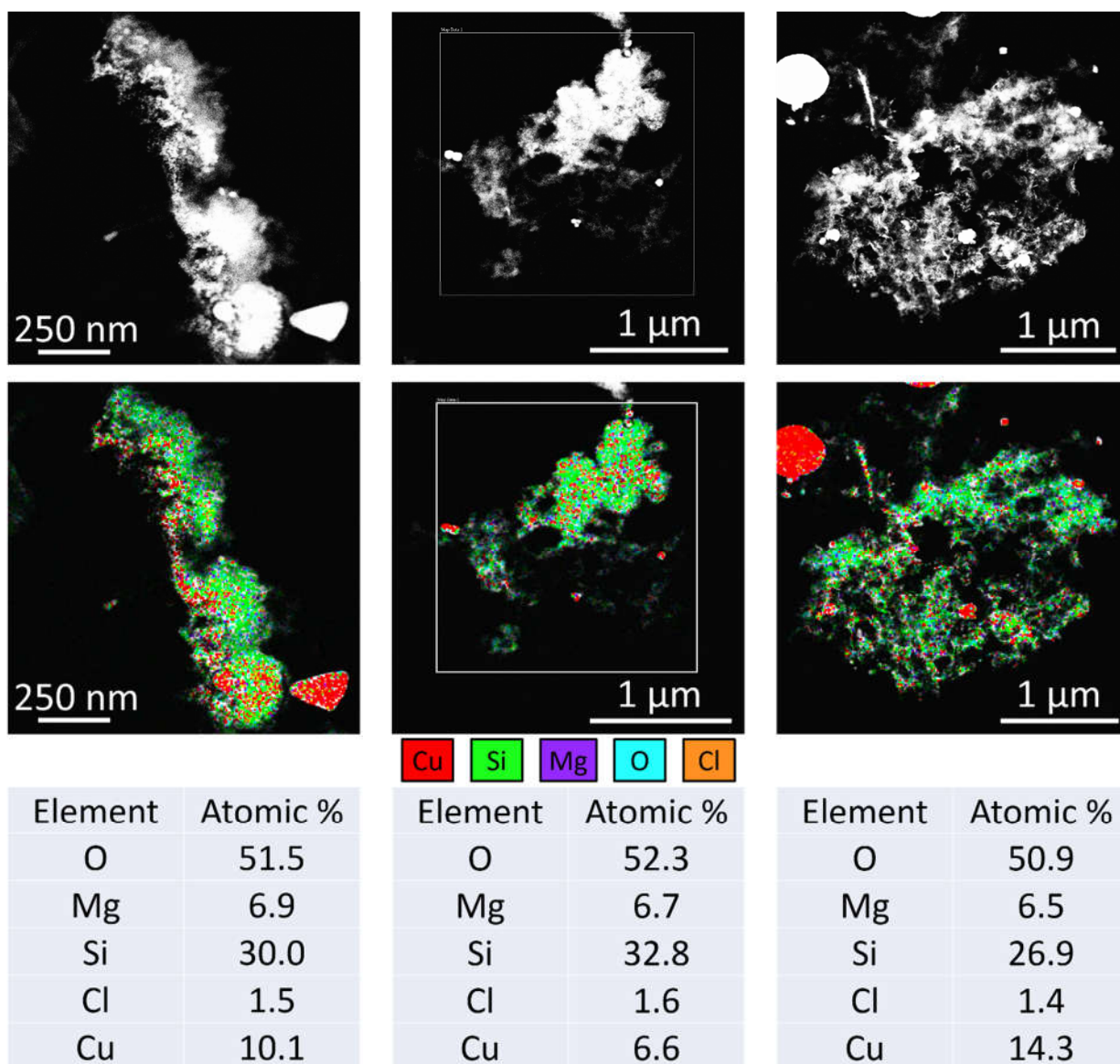


Figure S2.6. STEM images, row 1, and corresponding EDS maps, row 2, with atomic percentages, row 3, from the 1.5 hr reaction.

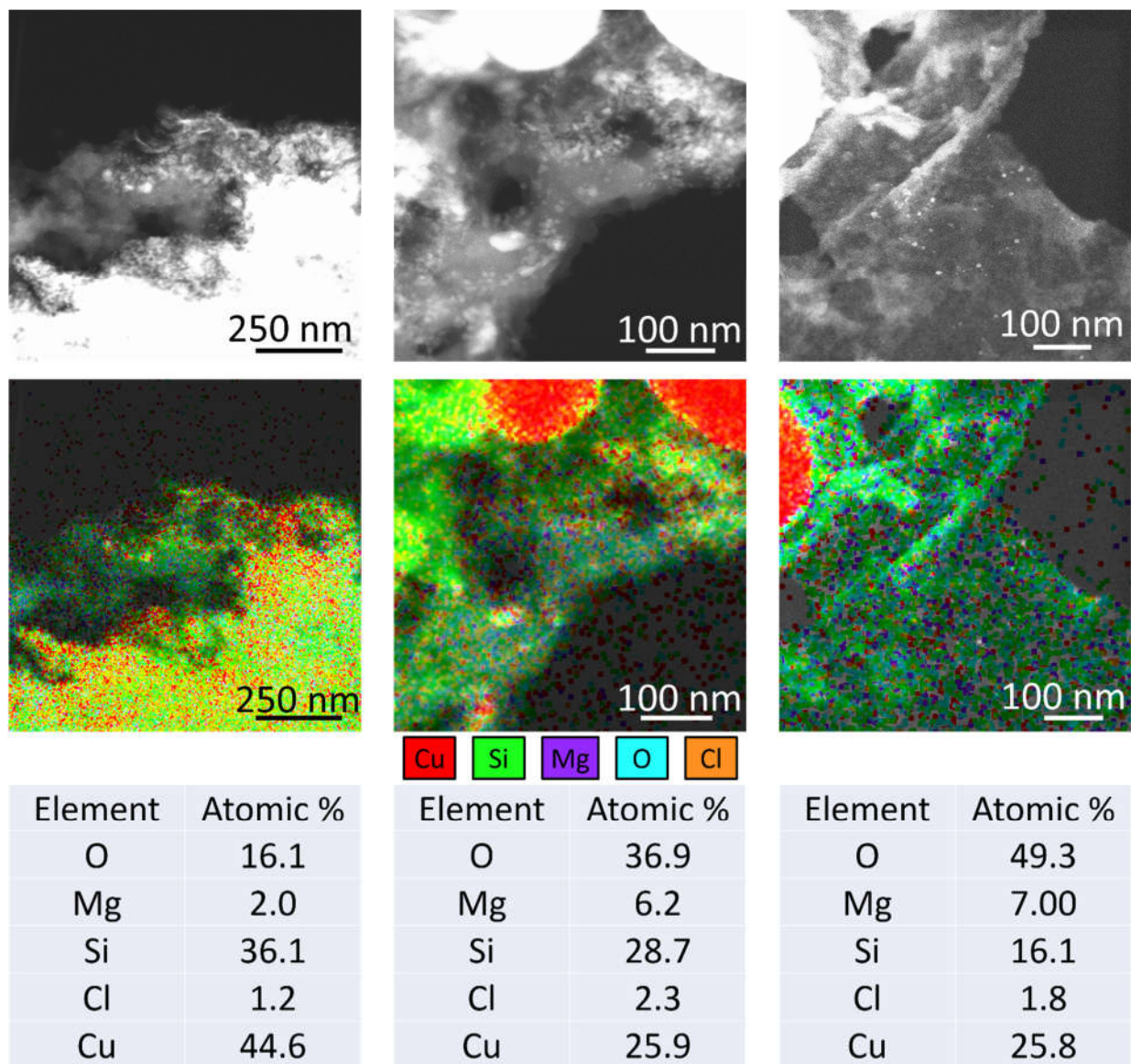


Figure S2.7. STEM images, row 1, and corresponding EDS maps, row 2, with atomic percentages, row 3, from the 3 hr reaction.

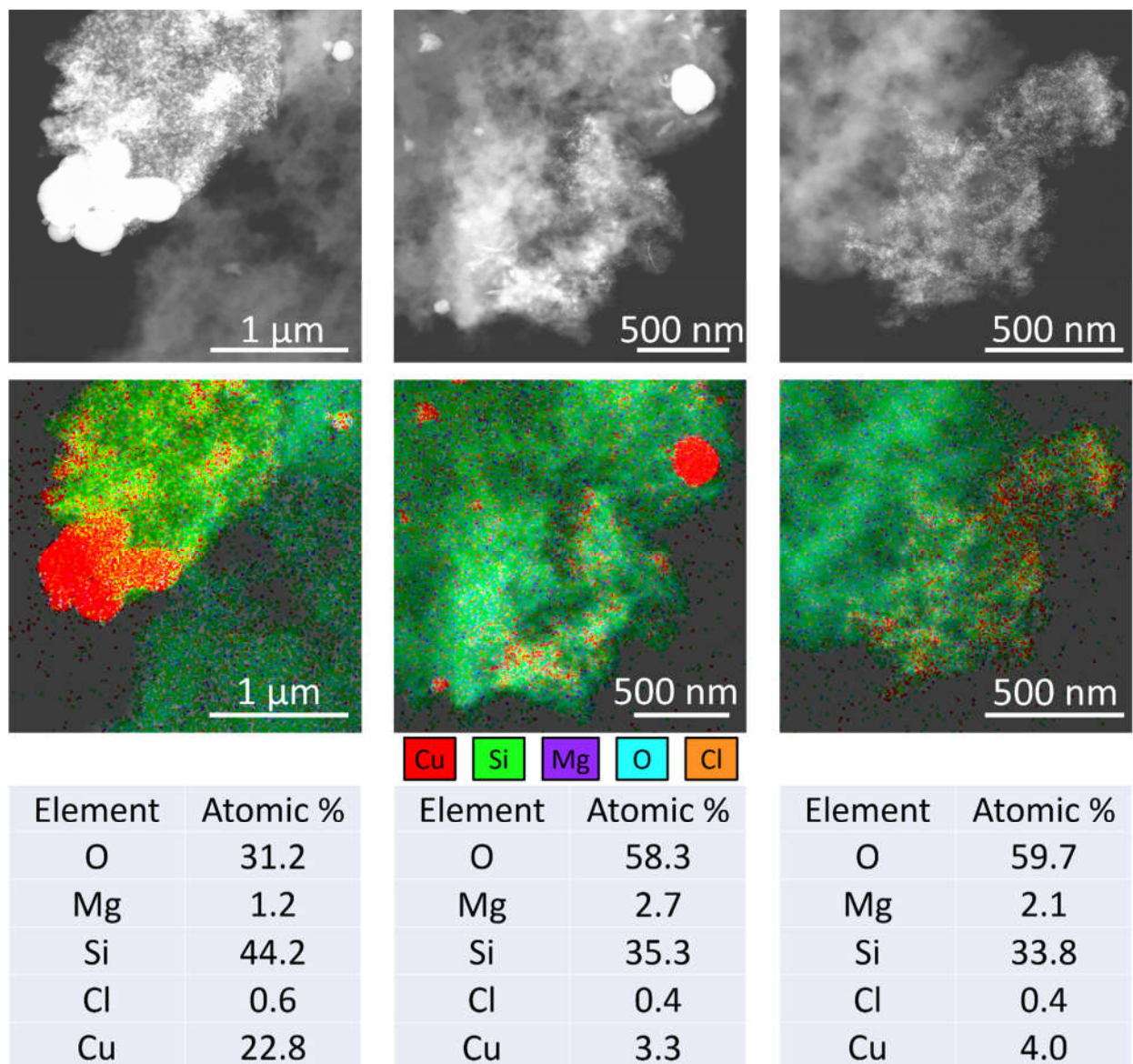


Figure S2.8. STEM images, row 1, and corresponding EDS maps, row 2, with atomic percentages, row 3, from the 6 hr reaction.

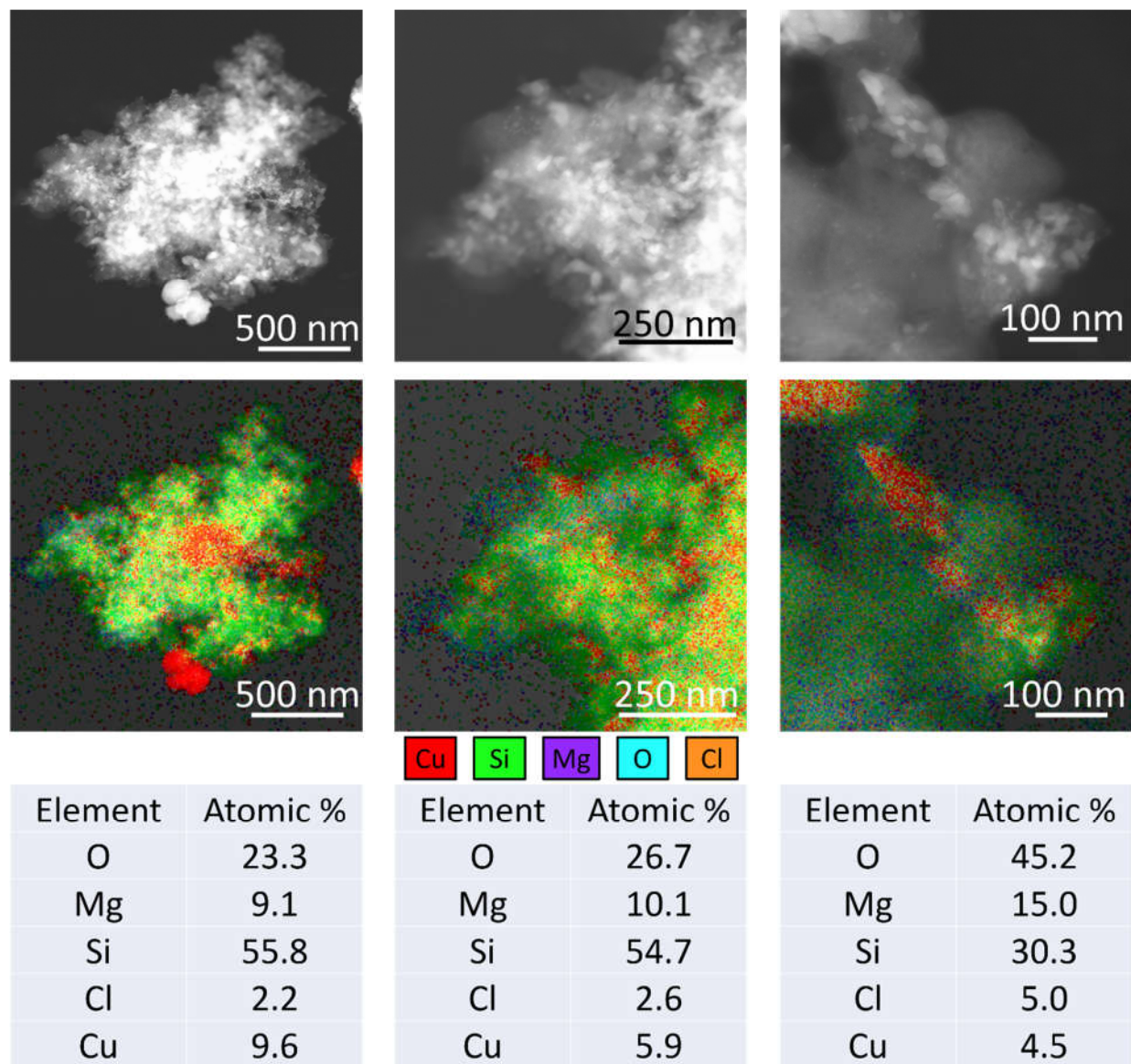


Figure S2.9. STEM images, row 1, and corresponding EDS maps, row 2, with atomic percentages, row 3, from the ON reaction.

Table S2.2. Average Atomic Percent for Each Fully Quenched Time Reaction (1.5 hr, 3 hr, 6 hr, and ON) using STEM/EDS

Element	1.5 hr Ave. At.%	3 hr Ave. At.%	6 hr Ave. At.%	ON Ave At.%
O	52.8	36.6	53.9	34.0
Mg	7.1	5.1	2.4	10.5
Si	29.7	27.2	35.8	39.1
Cl	1.7	1.7	0.5	3.0
Cu	8.7	29.4	7.4	13.4

Brief Discussion about Qualitative STEM/EDS Data: In this report, EDS maps were used qualitatively, as the ability to gather quantitative EDS spectra and atomic percentages requires sample features and preparation that are difficult to achieve in this system, i.e. flat and homogeneous samples. Thus, qualitative trends, such as determining the composition of different morphologies observed in TEM and the general percent of the elements present, were gathered. Several STEM, corresponding EDS maps, and the atomic percentages from each time sample (1.5 hr, 3 hr, 6 hr, and ON) are shown in Figure S2.6-2.9. Additionally, the average atomic percentages from all STEM/EDS maps collect, all not shown, were calculated and are shown in Table S2.2. These atomic percentages, although not quantitative, still are important for gaining an understanding of the elements present and an overall sense of percentage. However, as discussed in the main text, the $\text{Cu}_3\text{Si}@\text{Si}$ matrix time samples have three different particle types present, Cu particles, Si matrixes, and Cu_3Si particles within the Si matrixes. Therefore, when looking at these atomic percentages, it is important to keep in mind that depending on the area being analyzed, the atomic percent of the elements can vary, even within the same sample, as shown from Figures S2.6-2.9.

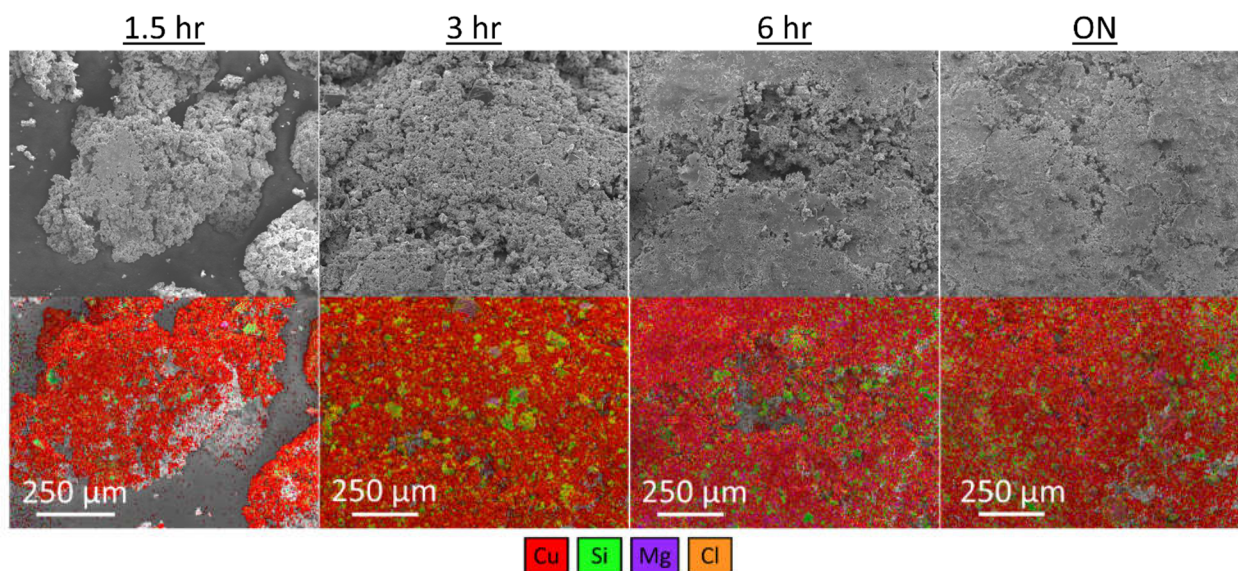


Figure S2.10. SEM/EDS layered mapping of the Cu pellet at the bottom of the reaction flask for each time reaction (1.5 hr, 3 hr, 6 hr, and ON). The pellets are majorly Cu but reaction particles can also be observed showing the increase of Cu_3Si particles within the Si matrix at longer times.

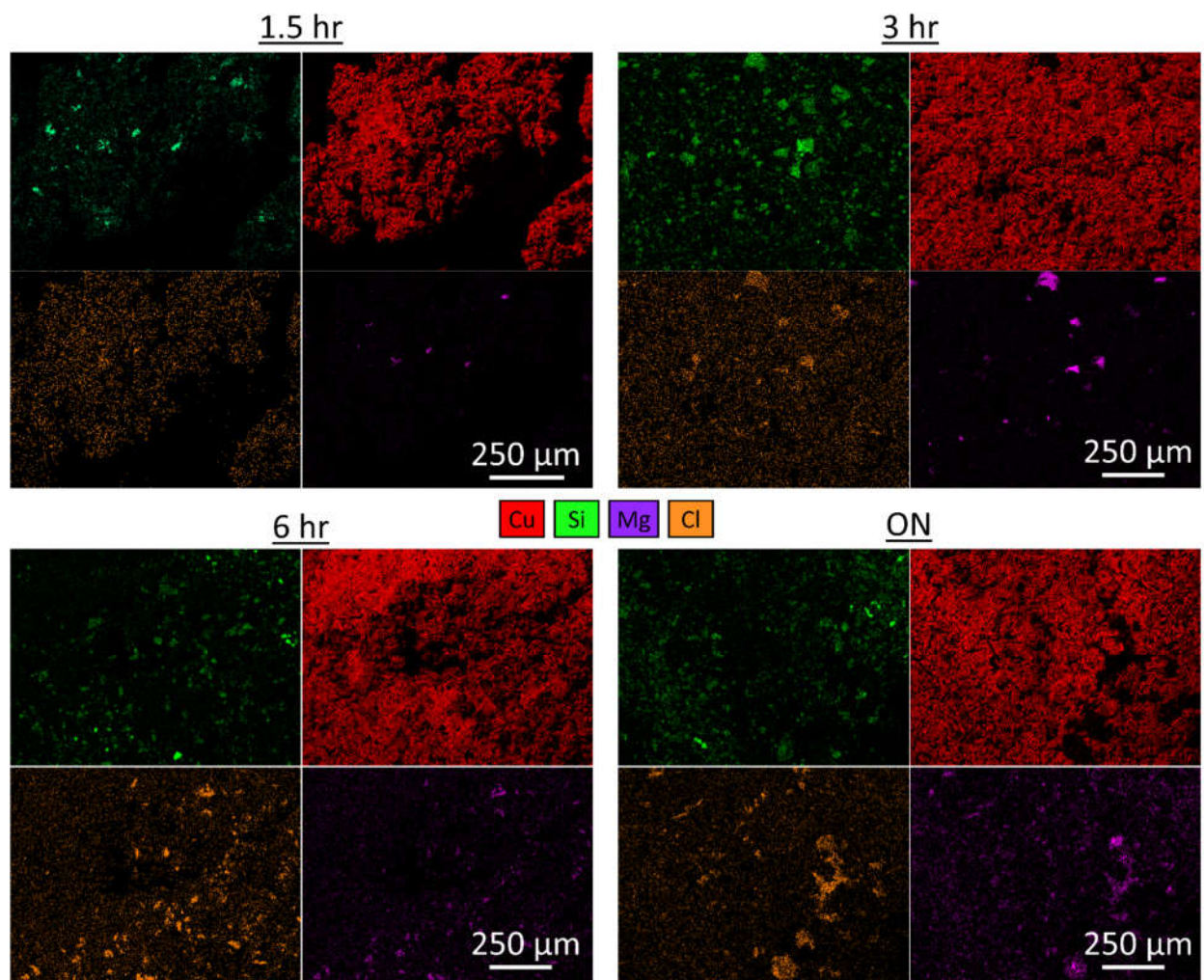


Figure S2.11. SEM/EDS individual element images from the layered map in Fig. S2.10. of the Cu pellet at bottom of the reaction flask for each time reaction (1.5 hr, 3 hr, 6 hr, and ON). As the Cu pellets were only rinsed with hexanes, a clear correlation between Mg and Cl can be seen, suggesting MgCl_2 formation.

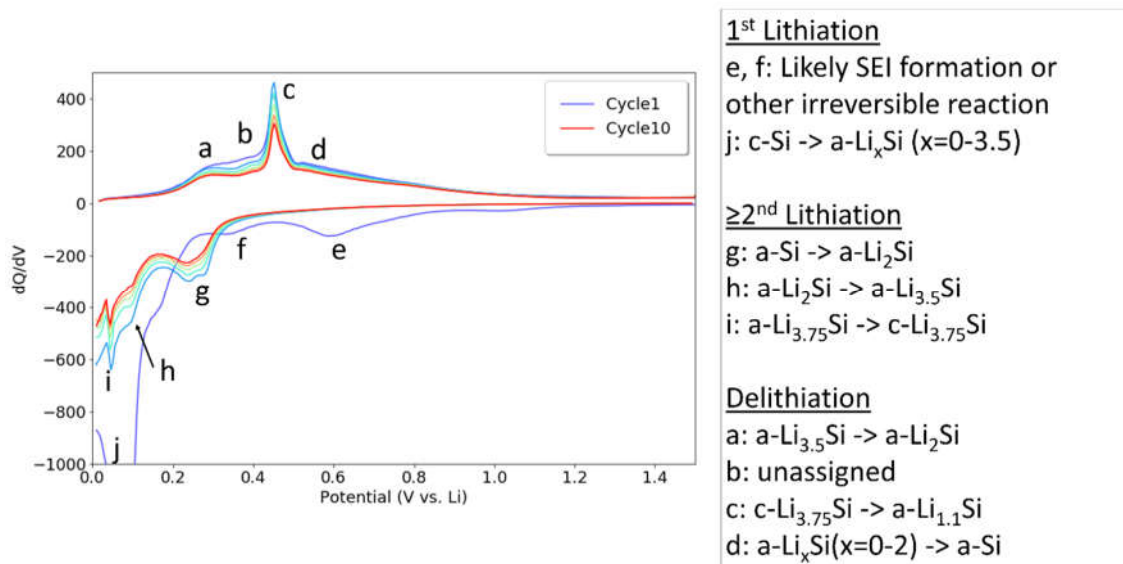


Figure S2.12. Identification of the electrochemical events observed in the dQ/dV plot of the Cu₃Si@Si matrix cycled against Li/Li⁺. The events were assigned based on a previous report studying the lithiation/delithiation mechanism of Si nanowires.⁵⁵

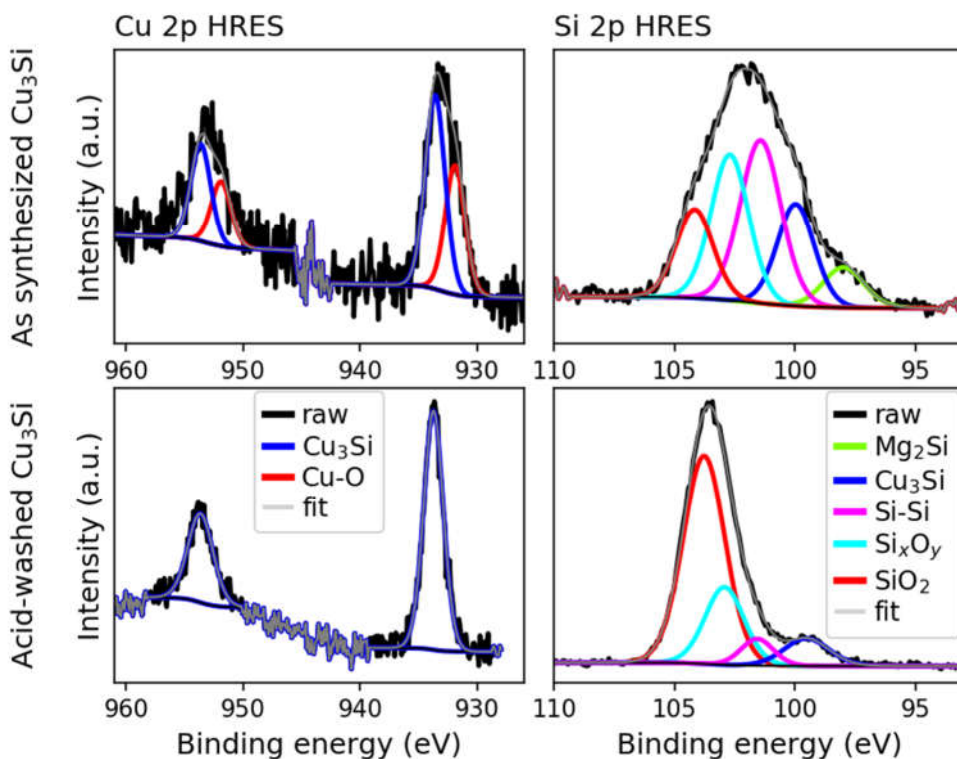


Figure S2.13. XPS HRES Cu 2p and Si 2p spectra of both the acid washed and as synthesized Cu₃Si@Si matrix particles.

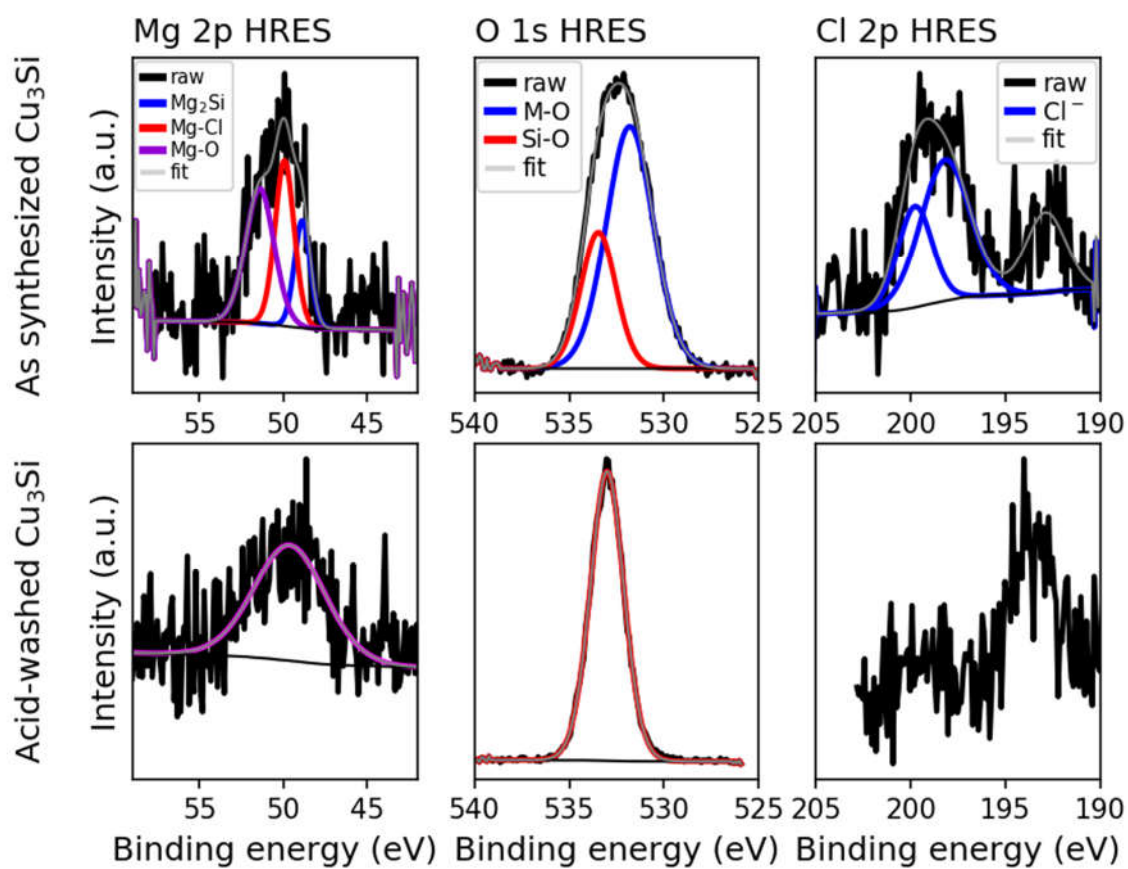


Figure S2.14. XPS HRES Mg 2p, O 1s, and Cl 2p spectra of both the acid washed and as synthesized Cu₃Si@Si matrix particles.

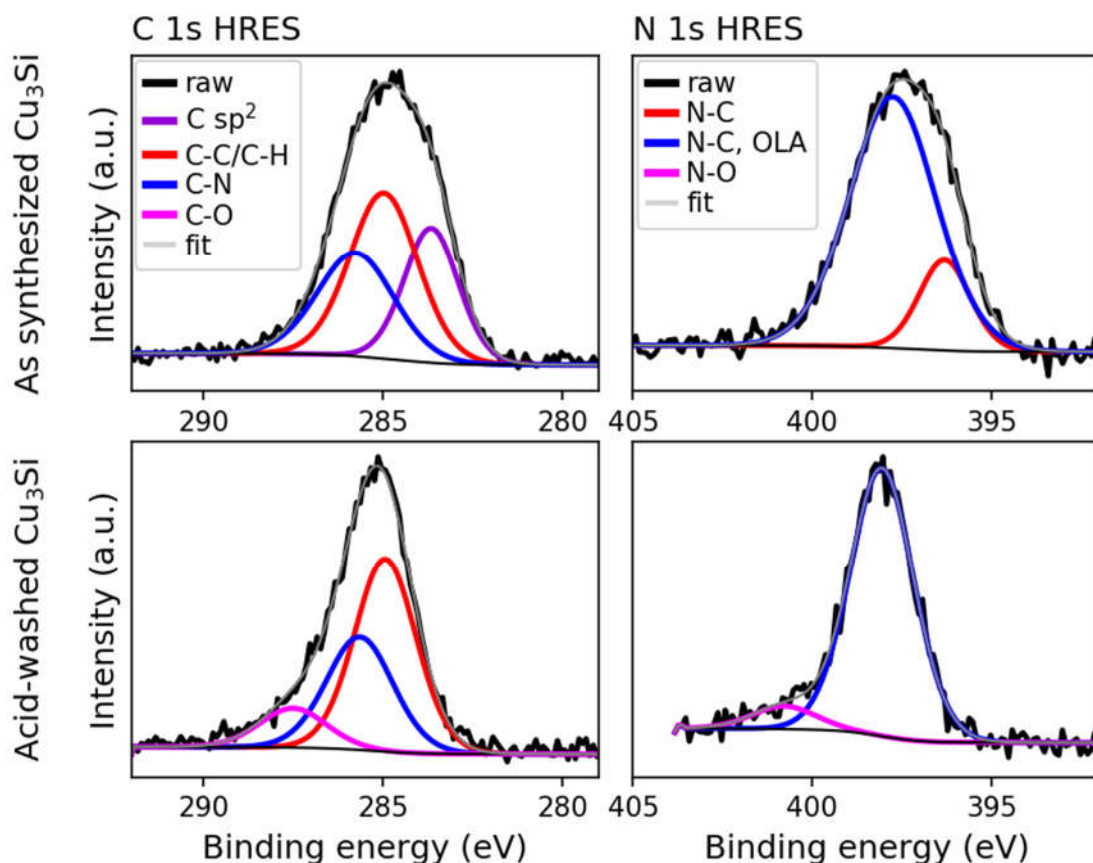


Figure S2.15. XPS HRES C 1s and N 1s spectra of both the acid-washed and as-synthesized $\text{Cu}_3\text{Si}@\text{Si}$ matrix particles.

Comparing the XPS Data of the Acid-washed and As-synthesized Particles: Most characterizations were performed on the as-synthesized $\text{Cu}_3\text{Si}@\text{Si}$ matrix particles to best describe the synthesis process. However, to specifically analyze the Si matrix without interference from the excess Cu or possible unreacted Mg_2Si , particles synthesized using optimal conditions were analyzed by XPS both with (acid-washed) and without (as-synthesized) the extra nitric acid wash. The XPS analysis of the two samples overall agreed with each other, yet some differences were observed. Here, we will describe the differences and discuss why these differences were observed.

The differences seen between the as-synthesized and acid-washed XPS HRES Cu 2p and Si 2p spectra (Figure S2.13) were mainly due to the excess Cu particles and the minimal amounts of unreacted Mg_2Si present at the end of the reaction. The broadness of the Cu peaks observed in the as-synthesized spectra

indicate two Cu environments are present, a Cu-Si environment and a Cu-O environment.^{12,56} The Cu-O environment is assumed to be due to slight surface oxidation occurring on the excess Cu remaining in the sample. Comparatively, the peaks are narrowed in the acid washed spectra, indicating the acid wash successfully washed away the excess Cu and therefore only the Cu-Si environment persists. Similarly, the main difference between the as-synthesized and the acid-washed HRES Si 2p spectra is a low energy environment (~98 eV) associated with Mg-Si.⁵⁷ Since the acid wash will remove any remnant Mg₂Si in the resulting particles, the as-synthesized spectra includes this Mg-Si environment but the acid-washed spectra does not.

Comparing the HRES Mg 2p, O 1s, and Cl 2p XPS spectra of the as-synthesized and acid-washed sample (Figure S2.14) we can see correlations to the Cu 2p and Si 2p spectra. The Mg 2p as-synthesized spectra was best fit with three environments (Mg-Si, Mg-O, and Mg-Cl). After the acid-wash the Mg signal is significantly decreased likely due to the wash removing any remnant Mg₂Si and MgCl₂. Thus, it was difficult to fit this small peak to know the specific binding environment(s). However, it shows Mg is still present in the Si matrix after the acid wash. There is also a significant decrease in the Cl 2p spectra after the acid wash, suggesting the Cl species (either MgCl₂ or Cl⁻ capping) is washed away from the acid wash, rather than it being incorporated in the Si matrix. Additionally, we observe the XPS O 1s HRES spectra narrow after the acid wash which corresponds to the removal of the previously mentioned Cu-O and Mg-O species.

Finally, the HRES C 1s and N 1s XPS spectra of the as-synthesized and acid-washed sample are shown in Figure S2.15. These spectra show C-N binding environments indicative of OLA capping. The C-N binding environments are at a slightly lower binding energy than what is expected for an allylic nitrogen compound. We hypothesize that this is either from the capping interaction or an artifact of the electron flood beam. The peaks in the acid wash sample do narrow due to the C-N environments decreasing, which is unsurprising as the acid wash could strip the ligands. This is further supported by the post acid washed

particle no longer suspending well in hexanes. Additionally, similar to the other HRES spectra the acid wash sample shows oxidation.

Table S2.3. XPS fitting information for the as-synthesized Cu₃Si@Si matrix sample

Name	Position	FWHM	Area/(RSF _x T _x MFP*)	%At Conc	Total
C 1s	283.65	1.79	117.5	10.4	37.7
C 1s	284.97	2.23	180.6	16.0	
C 1s	285.76	2.5	126.1	11.2	
O 1s	531.8	2.92	195.9	17.4	24.7
O 1s	533.46	2.17	82.0	7.3	
N 1s	396.32	1.68	22.4	2.0	11.3
N 1s	397.76	2.83	105.0	9.3	
Cu 2p	931.86	2	2.0	0.2	0.7
Cu 2p	951.87	2	1.0	0.1	
Cu 2p	933.56	2	3.0	0.3	
Cu 2p	953.6	2	1.5	0.1	
Si 2p	97.99	2	18.6	1.7	21.0
Si 2p	99.97	1.81	42.9	3.8	
Si 2p	101.43	2	75.6	6.7	
Si 2p	102.71	1.85	62.3	5.5	
Si 2p	104.17	1.8	36.9	3.3	
Mg 2p	48.87	1.11	8.5	0.8	3.9
Mg 2p	49.93	1.34	15.8	1.4	
Mg 2p	51.41	2	19.2	1.7	
Cl 2p	198.18	3.08	6.1	0.5	0.8
Cl 2p	199.78	2.14	3.1	0.3	

Table S2.4. XPS fitting information for the acid-washed Cu₃Si@Si matrix sample

Name	Position	FWHM	Area/(RSF _x T _x MFP*)	%At Conc	Total
C 1s	284.9	2.0	186.4	9.1	16.9
C 1s	285.6	2.2	118.1	5.8	
C 1s	287.5	2.2	41.3	2.0	
O 1s	533.0	2.1	964.4	47.2	47.2
Si 2p	103.8	2.0	385.9	18.9	30.0
Si 2p	102.9	1.9	134.2	6.6	
Si 2p	99.5	2.2	54.8	2.7	
Si 2p	101.6	1.6	38.5	1.9	
N 1s	398.1	2.1	67.1	3.3	3.6
N 1s	400.8	2.1	5.8	0.3	
Cu 2p 3/2	933.7	2.0	8.2	0.4	0.6
Cu 2p 1/2	953.6	2.5	3.9	0.2	
Mg 2p	49.6	5.0	34.1	1.7	1.7

*RSF: Relative Sensitivity Factor; MFP: Mean Free Path; T: Transmission

APPENDIX B

SUPPLEMENTAL INFORMATION FOR CHAPTER 3: EXAMINING THE ROLE OF LiHMDS IN THE $\text{Fe}_2\text{GeS}_{4-x}\text{Se}_x$ SYSTEM WHERE PRECURSOR REACTIVITY IS INHERENTLY ALTERED

Experimental

Materials. All syntheses were set up and executed under inert N_2 conditions and using standard Schlenk line methods unless otherwise stated. The chemicals used as bought include: iron (II) chloride (FeCl_2 , anhydrous, 99.99%, Sigma Aldrich), germanium (IV) iodide (GeI_4 , 99.99%, Sigma Aldrich), sulfur powder (purified by sublimation, -100 mesh, Sigma Aldrich), selenium powder (99.99%, STREM chemicals), lithium bis(trimethylsilyl)amide ($\text{LiN}(\text{SiMe}_3)_2$, >98%, Sigma Aldrich), and reagent grade toluene, isopropanol, chloroform, hexanes (mixture of isomers), and ethanol (all from Fisher Scientific). Oleylamine (OLA, 70% Technical grade, Sigma Aldrich) was sparged with N_2 for 2 hr while gently heating to 70 °C before use.

Synthesis A of Fe_2GeSe_4 Particles. All syntheses were adapted from a report by Miller et al.¹⁰ Variations of the synthesis are represented in Table S3.1 and follow this general procedure. In a three-neck round bottom flask, FeCl_2 (0.32 mmol, 41 mg) and GeI_4 (0.24 mmol, 141 mg) were weighed out before a Teflon stir bar was added. This reaction flask was sealed off with a condenser, a thermocouple, and rubber septa before OLA (6 mL) was added. Separately, in a scintillation vial, Se powder (0.57 mmol, 45 mg) and $\text{LiN}(\text{SiMe}_3)_2$ (0.49 mmol, 81 mg) were weighed out and sealed off with a septa before OLA (2 mL) was added. Next, the reaction flask was added to a N_2 Schlenk line and cycled between vacuum and N_2 three times before leaving under vacuum. The flask was heated to 120 °C and left to degas for 1 hr. Simultaneously, the Se/ $\text{LiN}(\text{SiMe}_3)_2$ /OLA solution was sonicated until the injection step. After the 1 hr degas period, the reaction flask was placed under N_2 and heated to 340 °C. When the reaction flask reached 300 °C, the Se/ $\text{LiN}(\text{SiMe}_3)_2$ /OLA solution was placed on the Schlenk line under N_2 . A gas-tight syringe was purged with N_2 before collecting the Se/ $\text{LiN}(\text{SiMe}_3)_2$ /OLA solution, which was then injected into the reaction flask when the temperature reached 320 °C. A temperature drop to 275-278°C was observed before the temperature ramped to the final 340 °C. After 15 min, where a timer was started immediately after the

injection, a 10 mL glass luer lock syringe was used to quench the reaction solution into a 25 mL Erlenmeyer flask containing toluene (10 mL). *Caution: Take care when quenching the 340 °C reaction solution as the temperature and pressure could cause the syringe plunger to pop off, causing the escape of a hot solution and risk of burns.* The resulting particles were washed using the procedure described below.

Table S3.1. Variations in reaction parameters for the Fe₂GeSe₄ synthesis.

	Synthesis A	Synthesis B	Synthesis C	Synthesis D	Synthesis E
Reaction Flask	2 eq FeCl ₂ , 1.5 eq GeI ₄ , OLA (6 mL)	2 eq FeCl ₂ , 1.5 eq GeI ₄ , OLA (6 mL)	2 eq FeCl ₂ , 1.5 eq GeI ₄ , OLA (6 mL)	2 eq FeCl ₂ , 1.5 eq GeI ₄ , OLA (6 mL)	2 eq FeCl ₂ , 1.4 eq GeI ₄ , OLA (6 mL)
Injection Vial	3.5 eq Se, 3 eq LiHMDS, OLA (2 mL)	3.5 eq Se, 3.5 eq LiHMDS, OLA (2 mL)	3.5 eq Se, 3.5 eq LiHMDS, OLA (2 mL)	3.5 eq Se, 4 eq LiHMDS, OLA (2 mL)	0.268 M Se, 0.284 M LiHMDS, OLA (3 mL), Inject 1.8 mL
Injection Temperature	320 °C				
Reaction Temperature	340 °C				
Reaction Time	15 min	15 min	20 min	15 min	20 min

Synthesis of Fe₂GeS_{4-x}Se_x (x=0.8). The same general procedure outlined in Synthesis A was followed here, except for a couple of alterations. Into the three-neck round bottom flask, FeCl₂ (0.32 mmol, 41 mg) and GeI₄ (0.23 mmol, 132 mg) were weighed out. In the scintillation vial, Se (0.117 mmol, 9 mg), S (0.467 mmol, 15 mg) and LiN(SiMe₃)₂ (0.486 mmol, 81 mg) were weighed out. Finally, the injection solution in the scintillation vial was injected at 330 °C and reacted at 330 °C for 10 min.

Particle Washing Procedure. After the reaction solution was quenched into toluene (10 mL), it was split evenly between four, 15 mL centrifuge tubes. Isopropanol was added to each tube to reach the 10 mL mark. The tubes were shaken vigorously and then centrifuged at 3200 rpm for 2-3 min. The redish orange supernatant was discarded before chloroform (~1 mL) was added to disperse the particles. The anti-solvent, ethanol was added and again the tubes were shaken vigorously before centrifuging. After centrifuging at 3200 rpm for 2-3 min, the clear supernatant was removed. Finally, the particles were washed with hexanes

(10 mL) and then centrifuged for 2-3 min at 3200 rpm to separate the cleaned particles. The particles were stored in chloroform until characterization.

Characterization.

Powder X-Ray Diffraction (PXRD). A concentrated particle suspension in chloroform was drop casted onto a zero-diffraction silicon XRD plate. Analysis was performed on a Cu K α radiation source ($\lambda=1.54 \text{ \AA}$) and a Lynxeye XE-T positron-sensitive detector. Rietveld refinement was done using TOPAS v6 software.

Transmission Electron Microscopy (TEM). A concentrated particle suspension in chloroform was heavily diluted in hexanes. Then, a carbon-coated, Cu 100 mesh TEM grid was dipped into the solution 2-3 times, allowing the grid to quickly dry between coats. The samples were imaged using a JEOL JEM2100F at a working voltage of 200 keV. Images were collected and analyzed in Digital Micrograph of the Gatan Microscopy Suite software. *Scanning transmission electron microscopy (STEM) energy dispersive X-Ray spectroscopy (EDS)* was carried out with an Oxford X-Max 80 mm² detector and analyzed using AZtecTEM software.

Nuclear Magnetic Resonance (NMR). Proton nuclear magnetic resonance (¹H NMR) spectra were recorded at ambient temperature on a Bruker Ultrashield-400 (400 MHz) spectrometer. Samples were prepared by taking 0.02 mL of each injection solution and diluting it in 0.6 mL deuterated benzene.

Table S3.2. The Energy of Formation, calculated by Materials Project, for different phases in the Fe-Ge-Se and Fe-Ge-S phase space.^{11,12}

Material	E of formation (eV)	Material	E of formation (eV)
Fe ₂ GeSe ₄	-0.082	GeS	-0.585
Fe ₇ Se ₈	-0.135	Fe ₂ GeS ₄	-0.664
GeSe	-0.209	Fe ₇ S ₈	-0.725
GeSe ₂	-0.254	GeS ₂	-0.769
FeSe	-0.272	FeS	-0.839
FeSe ₂	-0.355	FeS ₂	-0.955

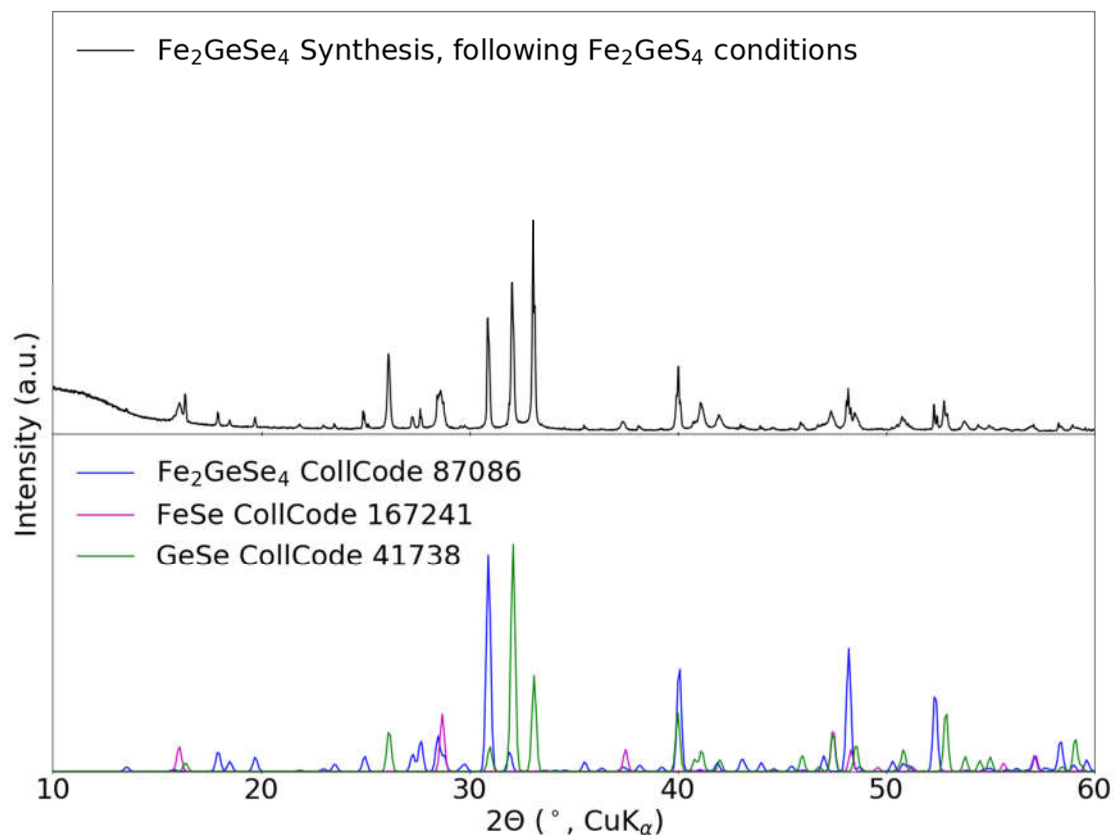


Figure S3.1. PXRD pattern resulting from using the optimized Fe_2GeSe_4 conditions, found in our previous paper (cite), to attempt to synthesize Fe_2GeSe_4 .

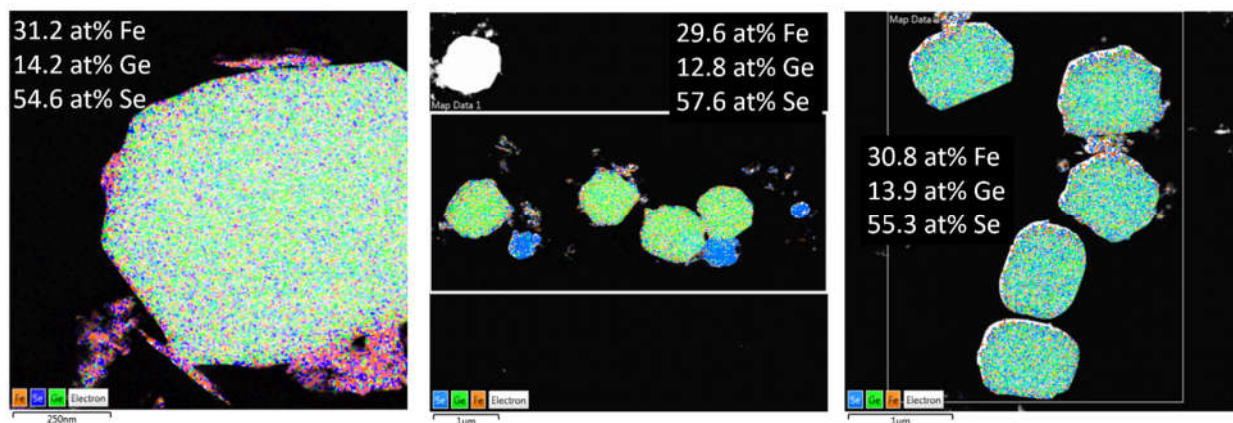


Figure S3.2. Representative EDS maps of the Fe_2GeSe_4 reaction, illustrating the composition of different morphologies observed in the TEM. These also show the successful synthesis of Fe_2GeSe_4 , as the atomic percentages are close to the expected values of 28.57 at% Fe, 14.29 at% Ge, and 57.14 at % Se.

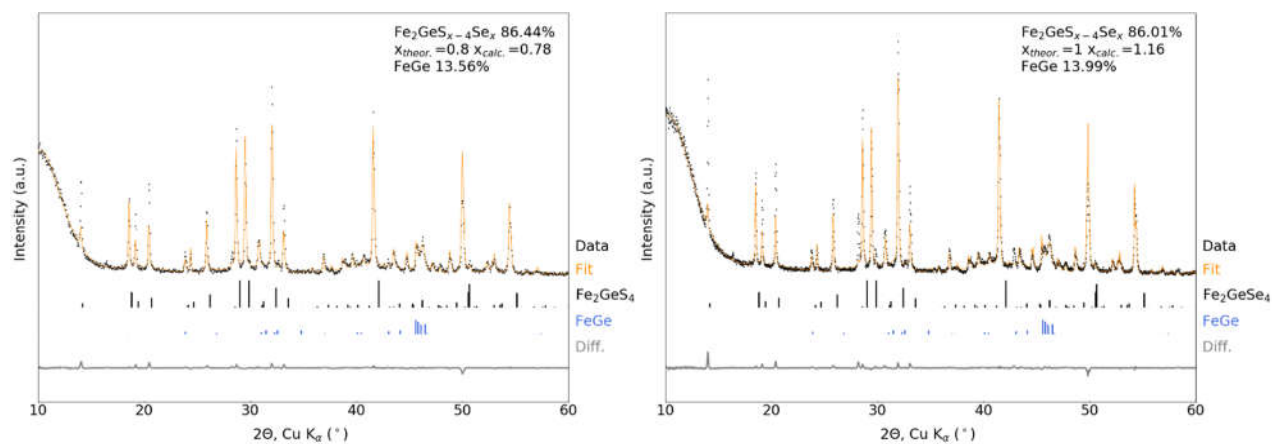


Figure S3.3. The Rietveld refinements for the solid solutions $\text{Fe}_2\text{GeS}_{4-x}\text{Se}_x$, $x=0.8$ (left) and $x=1$ (right), showing the percentage of $\text{Fe}_2\text{GeS}_{4-x}\text{Se}_x$ and FeGe present as well as the calculated x -value.

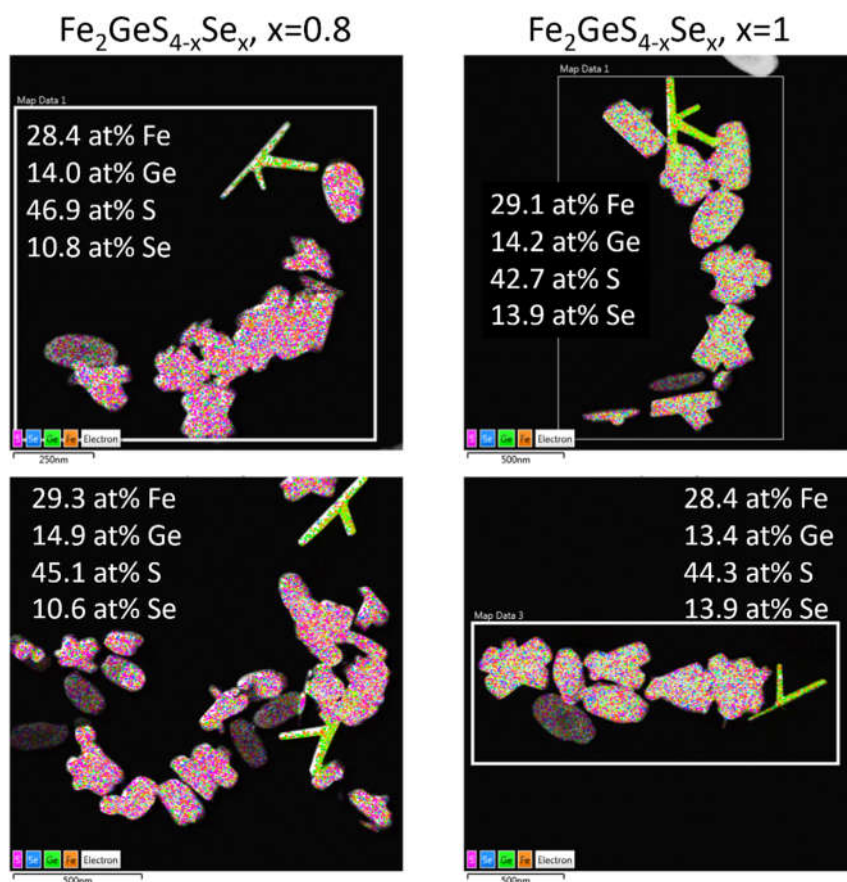


Figure S3.4. Representative EDS maps of the $\text{Fe}_2\text{GeS}_{4-x}\text{Se}_x$, $x=0.8$ and 1 reactions, illustrating the composition of different morphologies observed in the TEM. These also show the successful synthesis of $\text{Fe}_2\text{GeS}_{4-x}\text{Se}_x$, $x=0.8$ and 1, as the atomic percentages are close to the expected values for $x=0.8$: 28.57 at% Fe, 14.29 at% Ge, 45.71 at% S and 11.43 at % Se and $x=1$: 28.57 at% Fe, 14.28 at% Ge, 42.86 at% S and 14.29 at % Se.

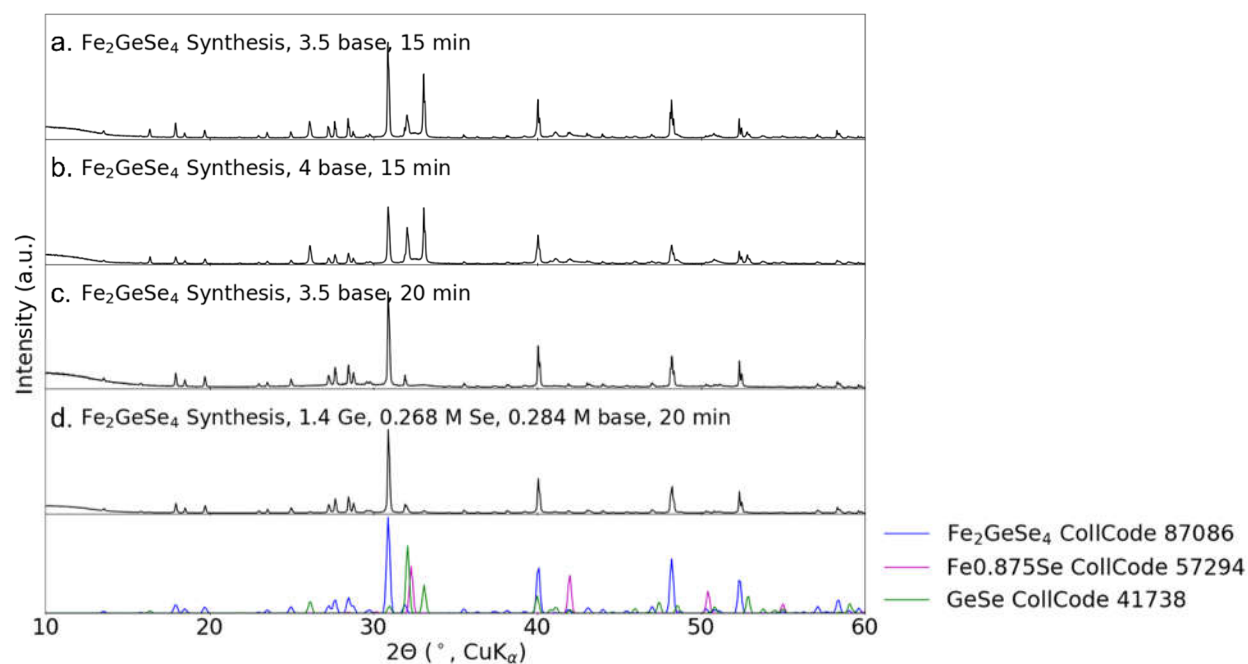


Figure S3.5. The PXR D patterns of the resulting particles when the LiHMDS base equivalence, reaction time, or precursor stoichiometry was altered. If not specifically stated then the stoichiometry is 2:1.5:3.5:3 FeCl₂:GeI₄:Se:LiHMDS (mol equivalence) and the reaction time is 15 min. The alterations include: a. 3.5 eq. LiHMDS, b. 4 eq LiHMDS, c. 3.5 eq LiHMDS and 20 min, and d. 1.4 eq GeI₄, 1.8 mL injected of a 0.268 M Se and 0.284 M LiHMDS solution, and 20min.

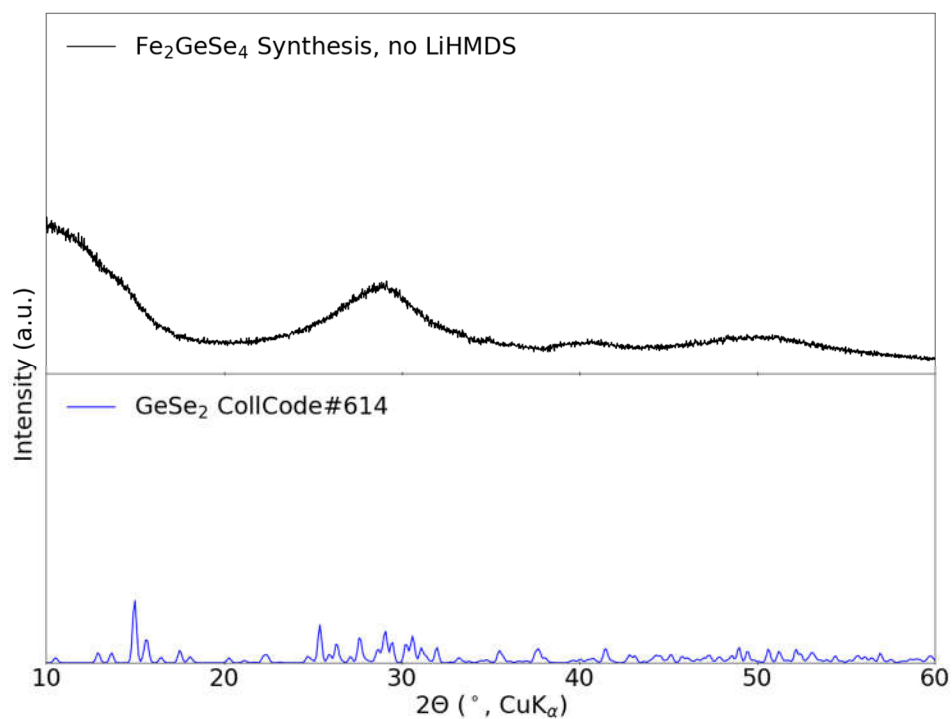


Figure S3.6. PXR D of the Fe₂GeSe₄ synthesis when no LiHMDS base is included, showing the resulting yellow powder is GeSe₂.

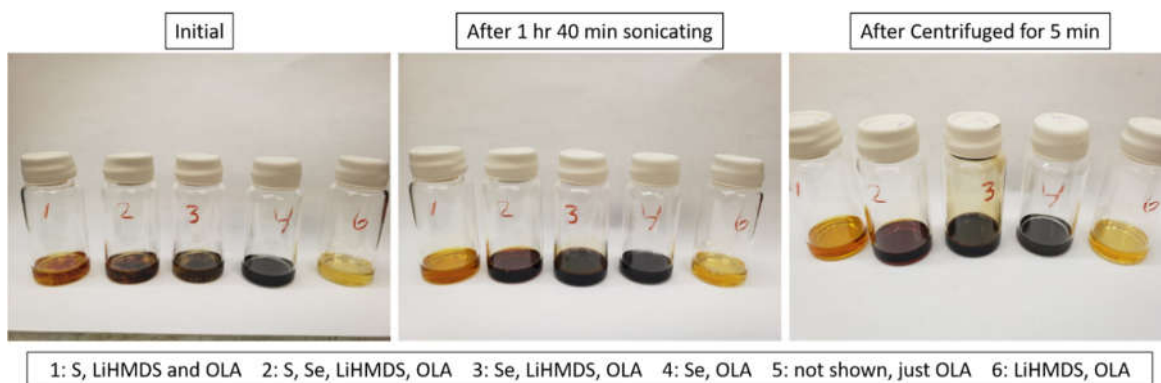


Figure S3.7. Pictures of the injection solutions of different combinations of Se, S, and LiHMDS in OLA, showing that after sonication, at first glance, all look like homogeneous solutions, but after centrifuging it becomes clear that Se is not soluble in OLA.

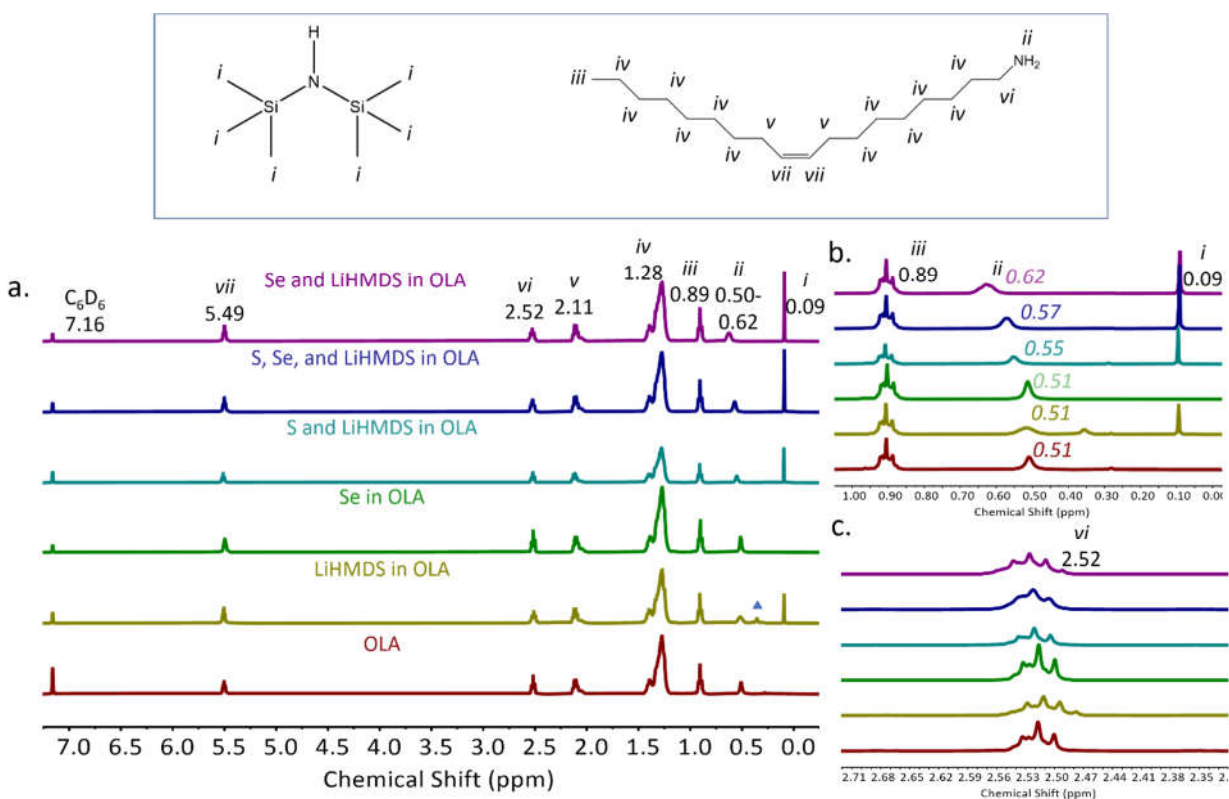


Figure S3.8. a. ^1H NMR spectra of the different injection solutions shown in Fig. S3.7. Each peak is labeled with the associated ^1H on HMDS or OLA. The peak labeled with the blue triangle is thought to be the LiHMDS-OLA solvate. b. Zoomed in range of the ^1H NMR spectra to highlight the shift of peak *ii* (N-H), indicating the OLA-chalcogen species forming.²² It is also shown that Se does not form this species without the presence of LiHMDS. c. Zoomed in range of the ^1H NMR spectra to highlight the broadening of peak *vi* (α -amino protons) in the injection solutions with LiHMDS present. This broadening could be caused by the equilibrium of OLA and LiHMDS deprotonating OLA to form the oleylamide species.

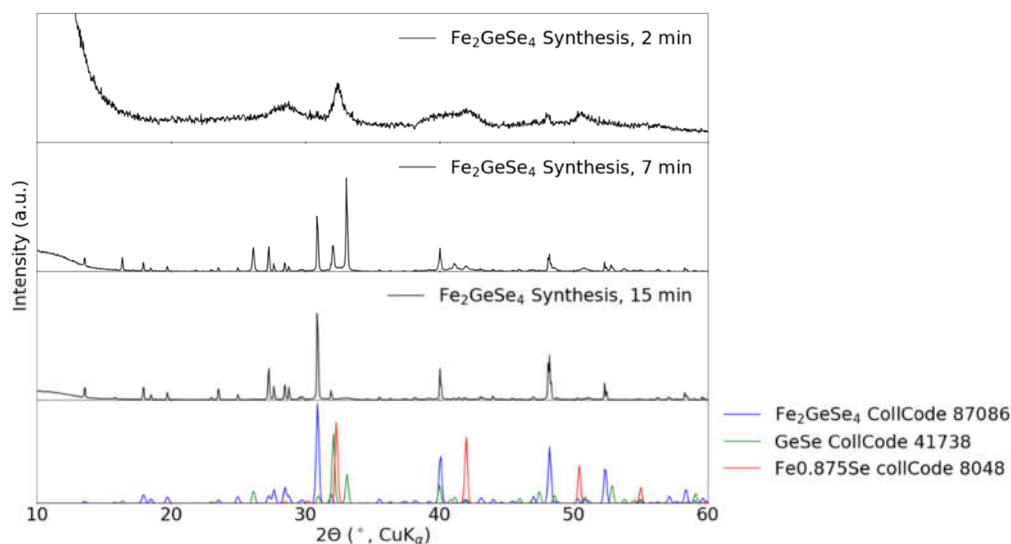


Figure S3.9. Aliquots were taken at 2 min and 7 min and then the reaction fully quenched at 15 min for the Fe_2GeSe_4 reaction. The PXRD of the resulting particles from each time quench are shown demonstrating the formation of Fe-Se and GeSe binaries before the formation of Fe_2GeSe_4 .

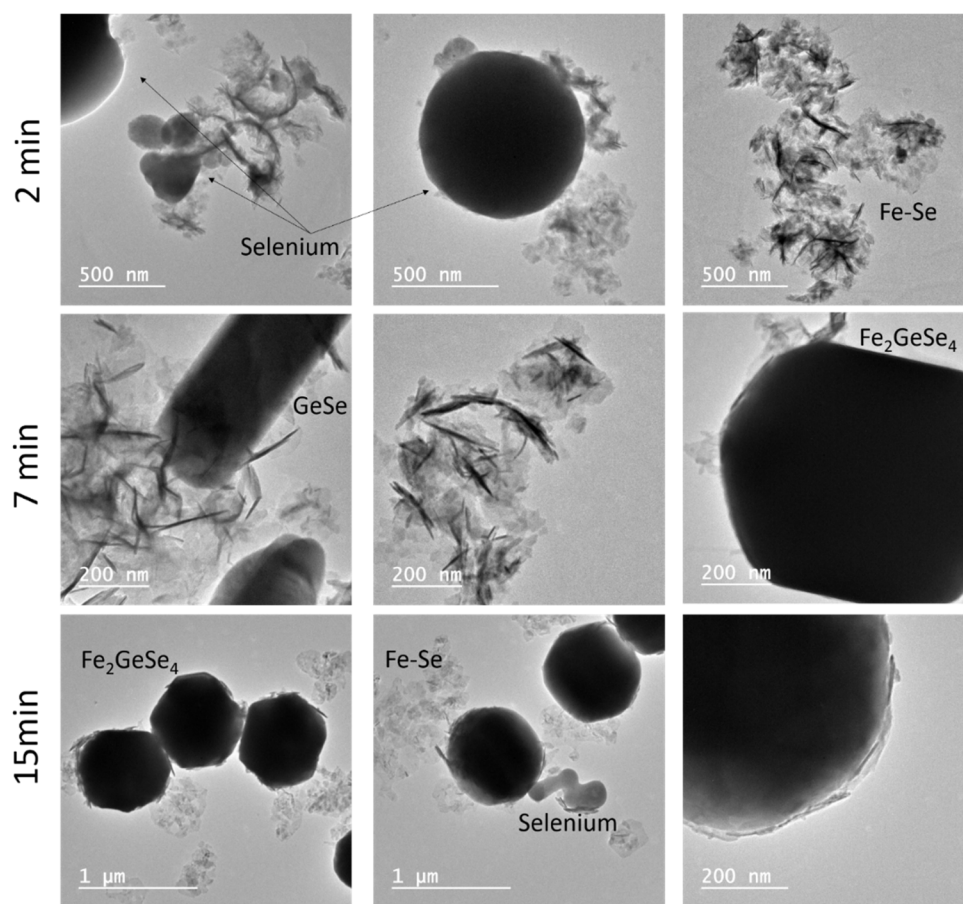


Figure S3.10. Aliquots were taken at 2 min and 7 min and then the reaction fully quenched at 15 min for the Fe_2GeSe_4 reaction. Shown here are representative TEM images of the resulting particles from each time quench illustrating the morphologies present.

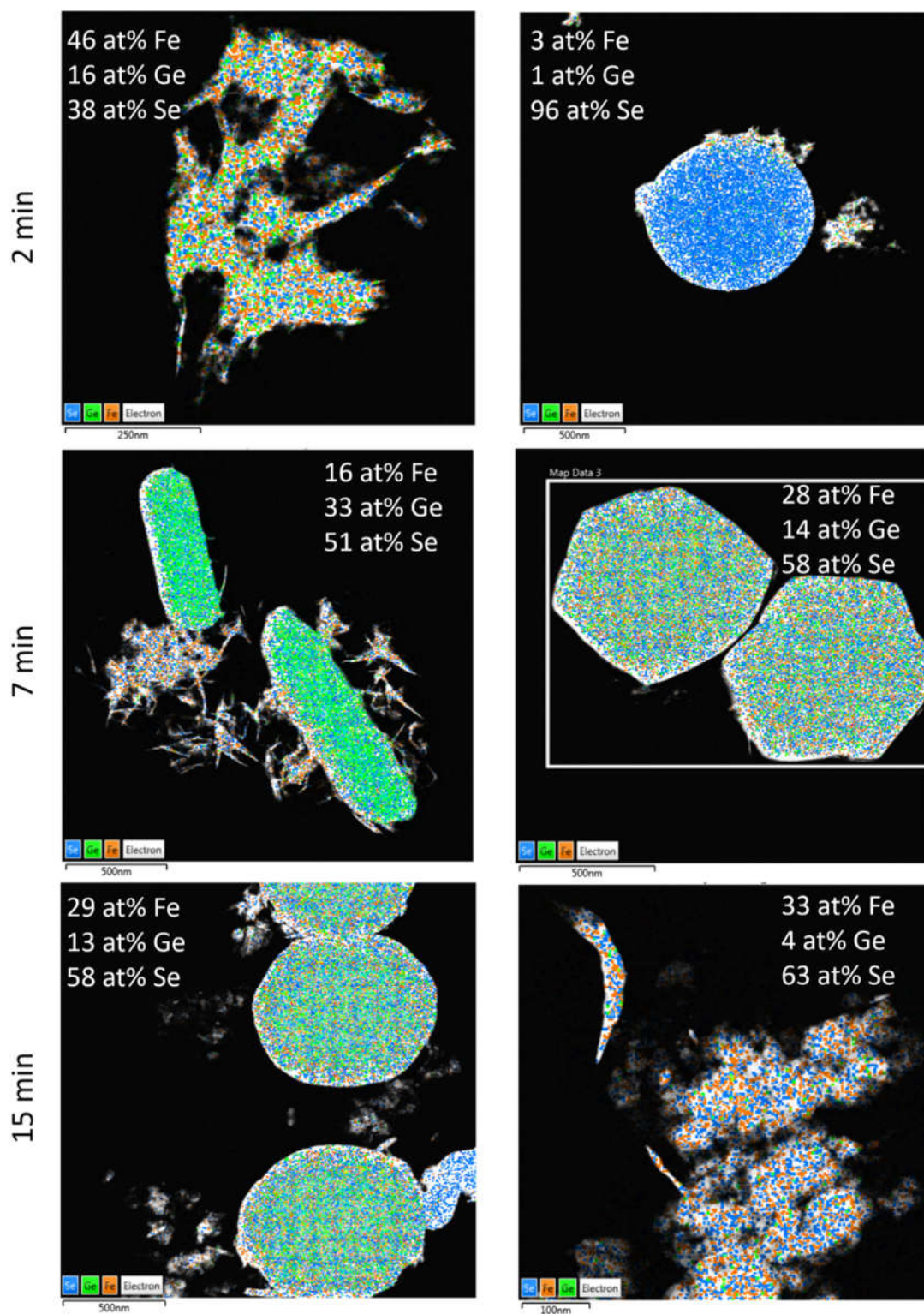


Figure S3.11. Aliquots were taken at 2 min and 7 min and then the reaction fully quenched at 15 min for the Fe_2GeSe_4 reaction. Representative EDS maps of the resulting particles for each time quench are shown. The composition of the morphologies observed in TEM (Fig. S3.10) were determined.

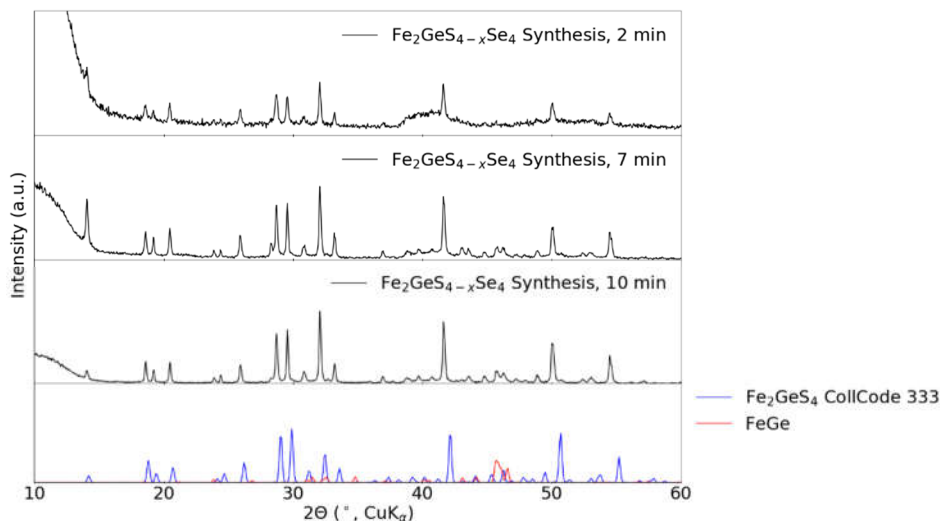


Figure S3.12. Aliquots were taken at 2 min and 7 min and then the reaction fully quenched at 10 min for the $\text{Fe}_2\text{GeS}_{4-x}\text{Se}_x$, $x=0.8$ reaction. The PXRD of the resulting particles from each time quench are shown demonstrating the rapid formation of $\text{Fe}_2\text{GeS}_{4-x}\text{Se}_x$, $x=0.8$.

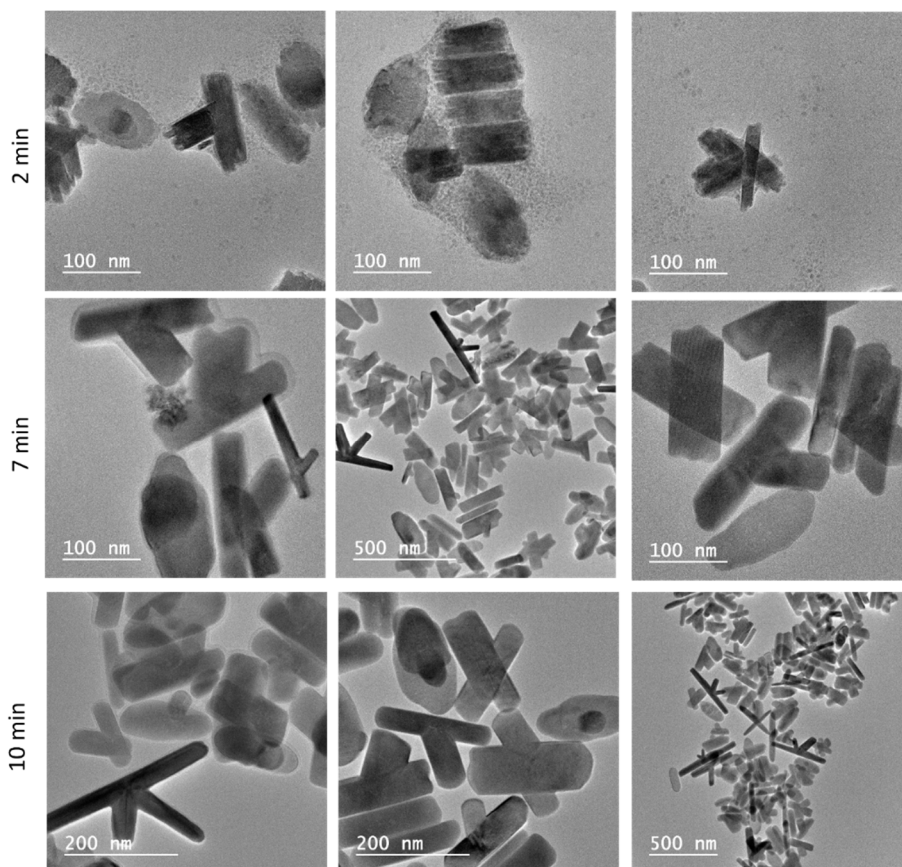


Figure S3.13. Aliquots were taken at 2 min and 7 min and then the reaction fully quenched at 10 min for the $\text{Fe}_2\text{GeS}_{4-x}\text{Se}_x$ reaction. Shown here are representative TEM images of the resulting particles from each time quench illustrating the morphologies present. Here we observe $\text{Fe}_2\text{GeS}_{4-x}\text{Se}_x$ particles with a similar morphology throughout as well as very small particles at 2 min and FeGe at 7 and 10 min.

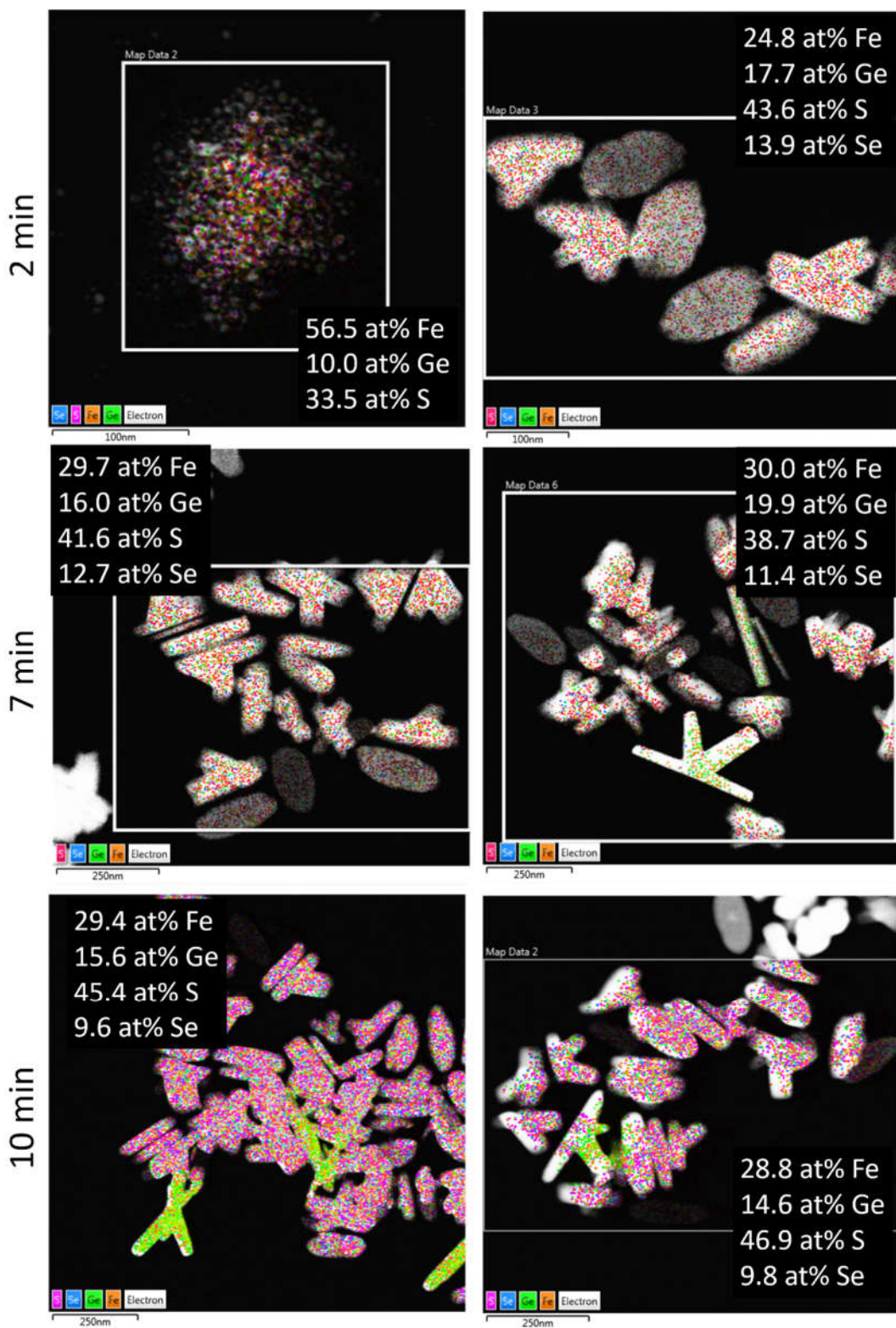


Figure S3.14. Aliquots were taken at 2 min and 7 min and then the reaction fully quenched at 10 min for the $\text{Fe}_2\text{GeS}_{4-x}\text{Se}_x$ reaction. Representative EDS maps of the resulting particles for each time quench are shown. The composition of the morphologies observed in TEM (Fig. S3.13) were determined.

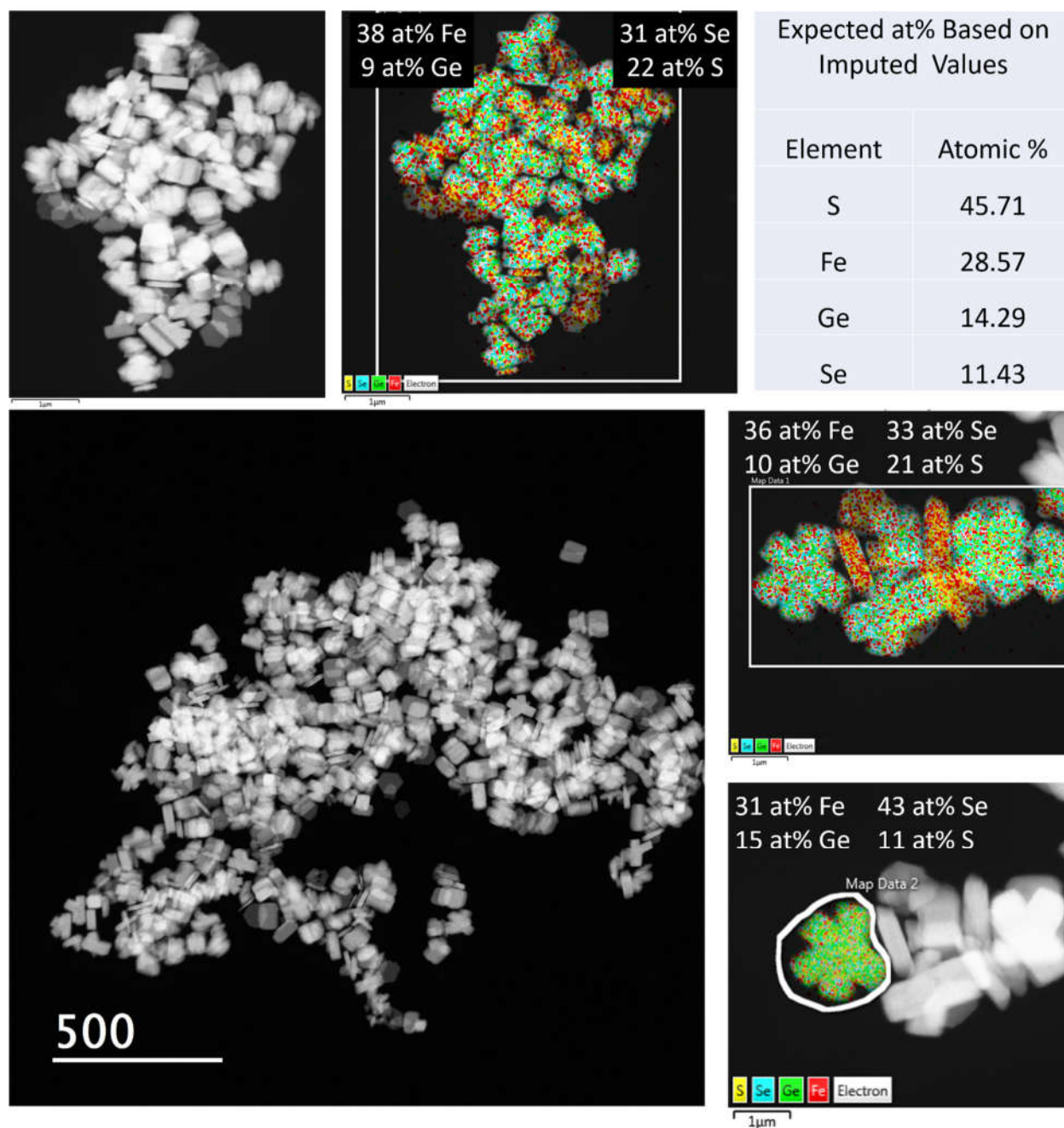


Figure S3.15. The Se precursor, Se powder, was exchanged for diphenyl diselenide in the $\text{Fe}_2\text{GeS}_{4-x}\text{Se}_x$, $x=0.8$ synthesis resulting in $\text{Fe}_2\text{GeS}_{4-x}\text{Se}_x$ and Fe-S particles. Here, the EDS mapping shows that the $\text{Fe}_2\text{GeS}_{4-x}\text{Se}_x$ particles have a much higher Se content than what was imputed into the system.